Radicals and Radical Pairs in Chemical and Biological Systems

Thesis submitted for the degree of
Doctor of Philosophy
at the University of Leicester

by

Raminder Shergill MChem

Department of Chemistry
University of Leicester

March 2010

University of Leicester

STATEMENT OF ORIGINALITY

The accompanying thesis submitted for the degree of doctor of philosophy entitled;

Radicals and Radical Pairs in Chemical and Biological Systems

is based on work conducted by the author in the Department of Chemistry at the University of Leicester during the period between October 2005 and October 2009. All the work recorded in this thesis is original unless otherwise acknowledged in the text or by references. None of the work has been submitted for another degree at this or any other university.

Signed: ..... Date: .....

Name: .....

Radicals and Radical Pairs in Chemical and Biological Systems

Raminder Shergill

Abstract

Magnetic fields of different strengths can be applied to chemical and biological systems to study processes involving radicals or radical pairs. This work uses two such techniques, electron paramagnetic resonance (EPR) spectroscopy ($\geq$ 150 mT) in addition to time resolved EPR spectroscopy and time resolved infrared (TRIR) spectroscopy ($\leq$ 37 mT). The former are used to monitor metalloproteins, and the photochemistry of phosphorus oxides, while TRIR spectroscopy is used to record the magnetic field effects on the reaction kinetics of neutral radical pairs.

The thesis begins with an introduction and an overview of the experimental techniques and developments. This is followed by an EPR study of the Fe(III) binding proteins, transferrin and lactoferrin and the effect thereon of catecholamine stress hormones. Catecholamines mediate bacterial growth by sequestering iron from the iron binding proteins. The mechanism of iron capture is unknown, however, the current work reveals Fe(III) binding by the catecholamine and supports subsequent reduction as the most likely route. Since catecholamines are also administered therapeutically, the validity of EPR as a diagnostic technique is examined and iron loss from human serum transferrin is observed.

Also within this work, experiments are presented in which TRIR spectroscopy is used to investigate factors that affect the development of magnetic field effects for radical pairs in different solutions. This initially involves studies on acylphosphine oxides. In addition to the reported photoprocesses, alternative chemistry is uncovered, which occurs when bisacylphosphine oxide is in solutions where the solvent is sufficiently nucleophilic. The photochemistry is investigated using time resolved EPR and density functional theory calculations to suggest three possible structures that are responsible for the additional radicals observed. Furthermore, encapsulated organic radical pairs in reverse micelles are studied. These experiments, in combination with dynamic light scattering measurements provide insight into the magnitude of the observed magnetic field effects and the differing kinetics of the radical pair in the reverse micelles.

Acknowledgements

I've dreamt of this day, and finally it's here….

I would like to begin by thanking the bosses, without whom I'm sure I wouldn't have made it out of the dark days of writing. My supervisor Jonny, for his never-ending enthusiasm, advice and ideas, thanks for introducing me to spin chemistry all those years ago. Hmm, well, it didn't run smoothly, but I am now quite content in knowing that I'll never have to see that beastly FTIR ever again! Equally I'd like to say a massive thanks to Corey, for being so generous with his time and his knowledge, which I've come to realise was very important when I was lacking in motivation. Thanks for being supportive/sarcastic at the same time and available all so often when I needed help (which was perhaps too often for your liking?). You'll no longer have to put up with me cackling from next door. I am also grateful to Primrose, for welcoming me in to her microbiological world, for the explanations, encouragement and for the supply of snacks; she shares my love of biscuits, which can only mean great things. I did enjoy and value working with you all and hopefully am a bit wiser for it.

To the workshop, John, Carlos, Roy and Keith; I am in awe of your skills, I really appreciated your help with technical stuff and your abilities for storytelling. I would also like to acknowledge Richard and Dawn for being my 'go to' people for equipment.

My spin chemistry buddy Timmah! your two moods of relaxed and super-relaxed make you an inspiration. To Claire, I'm sure I wasn't the best mentee, I'm fortunate that by nature you are kind, patient and generally lovely. Thanks to Micheal (blond), Hollie, Rem, Mark, Adrian, Michael (O), and Niccy for their individual contributions to my work.

To everyone in the lab; Tom, Nika, Matt, Ginelli, Eko, the Stud (superben), & Rozo, you kept me entertained-always. I'll miss our inappropriate conversations and the day to day drama, you are all incredibly funny. I value your friendship and am sad to no longer be seeing you every day.

I would also like to thank Kiran, Kerry and John for another enjoyable four years. It has flown by, again, and wouldn't have been anywhere near as fun without you.

Other fantastic individuals, Kelvin (fatty), what can I say; you came through like a true friend. Thanks to James for his speedy proof reading skills, and Alan, for being my writing up buddy and sharing my despair.

A special thanks to my family, for their love and support over these difficult few months. This especially means my mum, who has always had faith in me, and is the most selfless person I know.

To anyone else who has made my life easier along the way, I haven't forgotten you, my memory just isn't what it used to be…..

Contents

Acronyms

αhp	2-hydroxy-4-(2-hydroxyethoxy)-2-methylpropiophenone
6-OHDA	6-hydroxydopamine
AO	Atomic Orbital
AOT	Sodium bis(2-ethylhexyl)sulfosuccinate
Apo-Tf	Iron free Transferrin
B3LYP	Becke three parameter Lee, Yang, Parr Hybrid Exchange Functional
BAPO	Bis(2,4,6-trimethylbenzoyl)phenylphosphine Oxide
CA	Catecholamine
CIDEP	Chemically Induced Dynamic Electron Polarisation
cmc	Critical Micelle Concentration
CW	Continuous Wave
$\boldsymbol{D}$	Diffusion coefficient
$\boldsymbol{d_H}$	Hydrodynamic diameter
$\boldsymbol{d_w}$	Water pool diameter
DFT	Density Functional Theory
DLS	Dynamic Light Scattering
Dob	Dobutamine
Dop	Dopamine
E . coli	*Escherichia coli*
Epi	Epinephrine
EPR	Electron Paramagnetic Resonance
f-pair	Freely diffuse pairs
Fe	Iron
Fe-Tf	Iron(III)-Transferrin
FT	Fourier Transform
FTIR	Fourier Transform Infrared
Fz	Ferrozine

g-pair	Geminate pair
He-Ne	Helium-Neon
HF	Hartree-Fock
hfc	Hyperfine Coupling
hfcc	Hyperfine Coupling Constant
HFM	Hyperfine Coupling Mechanism
Holo-Tf	Iron-replete Transferrin
HOMO	Highest Occupied Molecular Orbital
HS	Human Serum
ICU	Intensive Care Unit
IR	Infrared
ISC	Intersystem Crossing
J	Electron exchange interaction
L-dopa	L- Dihydroxyphenylaniline
Lf	Lactoferrin
LFE	Low Field Effect
LFP	Laser Flash Photolysis
MAPO	(2,4,6-trimethylbenzoyl)diphenylphoshine Oxide
MARY	MAgnetic affect on Reaction Yield
MCT	Mercury Cadmium Telluride
MFE	Magnetic Field Effect
mhp	2-hydroxyethoxy-2-methylpropiophenone
MO	Molecular Orbital
MP2	Second order Møller-Plesset Perturbation theory
MW	Molecular Weight
N_{agg}	Aggregation number
Nd:YAG	Neodymium: Yttrium Aluminium Garnet
NE	Norepinephrine

NIBS	Non-Invasive Back Scatter
NMR	Nuclear Magnetic Resonance
PAGE	Polyacrymide Gel Electrophoresis
PI	Polydispersity Index
psTf	Partially Saturated Transferrin
Q	Quality factor
RP	Radical Pair
rpm	Revolutions Per Minute
RPM	Radical Pair Mechanism
S^2TRS	Step Scan Time Resolved FTIR Spectroscopy
SAM	Spin Angular Momentum
SAPI	Salt Supplemented Medium
SAXS	Small Angle X-ray Scattering
SCF	Self Consistent Field
SCRP	Spin Correlated Radical Pair
SD	Standard Deviation
SNS	Sympathetic Nervous System
S/N	Signal to Noise
SO	Spin-Orbit
SOMO	Singly Occupied Molecular Orbital
SP	Single Point
STO	Slater Type Orbitals
R	Correlation Function
TBP	Trigonal Bipyramid
Tbps	Transferrin-binding Proteins
Td	Tetrahedral
Tf	Transferrin
TREPR	Time Resolved Electron Paramagnetic Resonance

TRIR	Time Resolved Infrared
Tris-HCL	Tris(hydroxymethyl)aminomethane-hydrochloride
UV	Ultraviolet
w	Water pool size
ZPE	Zero Point Energy

List of Figures

Chapter 1

Chapter 2

Chapter 3

Chapter 4

Chapter 5

List of Tables

1. Introduction

1.1 Spin of an Electron

Following a series of experiments conducted in the early 1900s that disobeyed predictions based on classical mechanics, came a pivotal discovery termed electron *spin*.

In 1921 Stern and Gerlach[1] aimed to prove the quantisation of angular momentum by demonstrating that a single beam of silver atoms would be divided into specific orientations when directed through an inhomogeneous magnetic field. The results displayed overlapping bands, showing a constant deviation from the central beam position; this outcome was different from the random distribution anticipated from classical behaviour. The two bands were, however, also in conflict with quantum mechanical predictions of the time. Since l (angular momentum quantum number) gives rise to $2l + 1$ orientations of angular momentum, it may only be equal to 2 under the condition that $l = ½$, contrary to the understanding that l must be an integer.[2] The explanation of this result was proposed some four years later, when the physicists Gouldsmit and Uhlenbeck[3] suggested the existence of a half integral inherent angular momentum. This was in order to aid their explanation of the *fine structure* that was detected in atomic hydrogen emission spectra. The appearance of these spectra was such that an additional splitting of lines was observed, arising due to the doubling of states available to the valence electron. The pair concluded that the angular momentum observed was therefore not due to orbital angular momentum brought about by electron rotation about the nucleus, as initially suspected, but rather from an innate angular momentum of an electron, which became known as spin.

Further support of this theory arose through a repeat of the Stern-Gerlach experiment using hydrogen atoms, which was performed by Philips and Taylor.[4] Hydrogen atoms exhibit no orbital angular momentum ($l = 0$), yet the deviation was still present. This implied that the previously unrealised magnetic moment of the atom could adopt two defined orientations with respect to the field, thus providing clear evidence for the inclusion of an intrinsic angular momentum to an electron.

In 1928 Dirac[5] confirmed that relativistic effects and quantum mechanics could only be linked if the electron had an internal degree of freedom possessing the properties of angular momentum. This natural outcome of his workings allowed the

construction of the relativistic formulation, which remains the origin of the spin angular momentum of an electron.

1.1.1 Spin Angular Momentum

The origin of the electron's angular momentum is quantum mechanical. For convenience it is illustrated as precessing around an internal axis. The associated quantum number for this spinning motion, s, maintains a constant value of ½, for all electrons. The square of the Hamiltonian operator, $\hat{S}$, for the spin angular momentum (SAM) gives the magnitude and this can be described by a vector of length $\sqrt{\{s\ (s\ +\ 1)\}}\hbar$. m_s is the projection of the angular momentum in a defined direction, and the component of the angular momentum along the z-axis can be determined from $m_s\,\hbar$. The values of m_s are limited by the same boundaries that apply to other quantised angular momenta, where $2s + 1$ sub-states are allowed. Thus m_s can have values of $-s, (-s + 1), \ldots (s - 1), .. + s$, in integer steps, allowing m_s to occupy discrete values of $\pm$½.[6]

As a consequence of internal SAM, the force of magnetism is induced. Expression [1.1], details the proportional and antiparallel nature of the generated magnetic dipole moment and the intrinsic spin of an electron.

$$\mu_e = -\,g_e\mu_B s = -\,\gamma s \quad [1.1]$$

Here, g_e is the Landé g-value, this describes the ratio of the magnetic moment to the angular momentum of the electron and for a free electron this is equal to 2.002319304.[7] $\mu_B = e\hbar/2m_e$ is the Bohr magneton, where e and m_e are the charge and mass of an electron respectively. The formulation on the right hand side of Equation [1.1] is also commonly used for simplification and for this γ is called the gyromagnetic ratio.

Like electrons, protons and neutrons are fermions and therefore they each possess a spin of ½. If unequal numbers of protons and/or neutron exist within a given nucleus, that nucleus will also possess net spin. A nucleus with net spin is referred to as spin active. Nuclear spins can exist in integral or half integral states, and $\hat{I}$ is used to represent the SAM operator, where the vector $\sqrt{\{I(I + 1)\}}\hbar$ gives the magnitude. Following the same reasoning as described earlier, the spin projection in a given direction is m_I, again running in integral steps from $-I$ through to $+I$.

$$\mu_I = g_N \mu_N I \quad [1.2]$$

Unlike the electron, the magnetic moments and nuclear spins are in general parallel. Though there are examples for which the magnetic moments and nuclear spins are opposite, this occurrence is governed by a negative gyromagnetic ratio.

1.2 Radicals, Generation and Reaction

Any chemical species containing an unpaired electron, including those with an odd number of valence electrons in an orbital, is defined as a *radical*. Much of a radical's behaviour is governed by the high reactivity of the unpaired electron(s), which leads to instability and short lifetimes (~ nanoseconds). Due to radical reactions occurring so rapidly, radical concentrations in solution are typically low (μM), making them both difficult to detect and study.[8]

Radicals are formed when a parent molecule becomes structurally unstable through excitation and electron movement processes, which can occur in a variety of ways as summarised in Table 1.1.[8] These processes specifically include:

- *Homolysis*, where a covalent bond is cleaved using either heat (thermolysis) or radiation (photolysis) and each fragment inherits a single electron from the bond.
- *Atom abstraction*, where an excited molecule abstracts an atom, commonly hydrogen, from second molecule.
- *Electron transfer*, where an electron is lost from a donor, D, and/or gained by an acceptor molecule, A.
- *Radiolysis*, where the removal of an electron is triggered by high energy X- or γ-ray radiation.

Once formed, the *propagation* of these radicals is primarily governed by the stability of the radicals and their thermodynamic drive to gain additional stability. This allows the likely sequence of reactions to be categorised into four distinct groups, as shown in Table 1.2.

Radical abstraction (or transfer);-

Here the radical attack occurs on a weak σ-bond of the target molecule from which the non-radical atom is to be abstracted. The outcome is a regenerated radical and a new molecule with a stronger covalent bond than was present in the original molecule.

Table 1.1 Possible pathways for producing radical species.

Initiation process	Radical formation route
Homolysis	$R_1 - R_2 \longrightarrow R_1^{\bullet} + R_2^{\bullet}$
Atom abstraction	$R_1 - R_2^{*} + R_3H \rightarrow R_1 - R_2^{\bullet}H + R_3^{\bullet}$
Electron transfer	$R_1 - R_2 + D \rightarrow [R_1 - R_2]^{-\bullet} + D^{+\bullet}$ $R_1 - R_2 + A \rightarrow [R_1 - R_2]^{+\bullet} + A^{-\bullet}$
Radiolysis	$R_1 - R_2 \rightarrow [R_1 - R_2]^{+\bullet} + e^{-} \rightarrow R_1^{+} + R_2^{\bullet}$

Radical addition;-

This involves the carbon centred radical attack on a weak π-bond of an unsaturated molecule, which selectively creates a more stable σ-bond. Both intra and intermolecular reactions are common, with the rate of reaction governed by the individual radical and the π-system.

Table 1.2 Possible pathways for propagating a chain reaction.

Propagation process	Radical formation route	
Radical abstraction	$R_1^{\bullet} + X - R_2 \longrightarrow R_1 - X + R_2^{\bullet}$	X = H, Cl, I, etc.
Radical addition	$R_1^{\bullet} + H_2C = CH_2 \longrightarrow H_2C^{\bullet} - CH_2R_1$	
Radical fragmentation	$H_2C^{\bullet} - CH_2R_1 \longrightarrow R_1^{\bullet} + H_2C = CH_2$ $R_1C^{\bullet} = O \longrightarrow R_1{}^{\bullet} + C = O$	β-elimination α-elimination
Radical rearrangement	$R_1(X) - R_2^{\bullet} \rightarrow R_1^{\bullet} - R_2(X)$	X = Ar, C = C, C = O

Radical fragmentation;-

Driven by an increase in entropy, this process frequently involves β-elimination, or less frequently α-elimination, and results in the formation of an unsaturated molecule and a radical. For elimination to occur it is necessary to have correct overlap of the participating orbitals to form the new π-bond.

In the case of benzoyl radicals, which are of particular interest in this work, the rate of decarboxylation of the radical is relatively slow due to the additional stabilisation provided by the electron rich phenyl group. The typical reaction rate (tens of microseconds) of the benzoyl radical is therefore more rapid than the usually

competitive decarboxylation process. This along with additional reasons discussed in Chapters **2** and **5**, makes the benzoyl moiety suitable for investigation using the TRIR spectrometer.

Radical Rearrangement;-

This intramolecular process often occurs in cyclic systems and involves an electron initiating the breaking and reforming of bonds to produce a more stable structure.

An alternative to propagation is for two radicals to encounter one another and react to form a diamagnetic molecule; a process called *termination*. This can only occur *via* one of two pathways. The first possible pathway is by combination, where two radicals form a covalent bond. This reaction is fast (~ 10^9 dm^3 mol^{-1} s^{-1}) and results in the simultaneous release of the bond dissociation energy.[8] A second equally competitive route, disproportionation involves the production of one saturated and one unsaturated product, *via* the transfer of a β-hydrogen atom, to again produce the most thermodynamically stable products (see Table 1.3).

Table 1.3 Possible pathways for terminating a radical reaction.

Termination process	Molecule formation route
Combination	$R_1^{\bullet} + R_2^{\bullet} \longrightarrow R_1 - R_2$
Disproportionation	$R_1HC^{\bullet} - CH_2R_2 + R_3HC^{\bullet} - CH_2R_4$ $\downarrow$ $R_1HC = CHR_2 + R_3CH_2 - CH_2R_4$

More than 100 years after the chemist Moses Gomberg[9] identified the first organic *free radical* reaction, it is clear that radicals are involved in many aspects of life. From peroxy radicals within the atmosphere, driving the chemistry of the boundary layer, to use and applications in the plastics and coatings industry, where organic radicals formed from molecules such as aryl ketones and aryl phosphine oxides have become widely used to initiate polymerisation reactions. Further discussion of industrial reactions involving the radicals formed from such molecules can be found in Chapter **4**.

The next section considers the effects of the inherent spin of an unpaired electron, in a magnetic field and how this property can be used to reveal information on the immediate chemical environment of an electron.

1.3 Spins in a Magnetic Field

The energy of a magnetic moment, μ_e, of an unpaired electron in a static magnetic field, B, is classically defined as $E = -\mu_e B$.[6] A quantum mechanical system requires the construction of a Zeeman spin Hamiltonian, $\hat{\mathcal{H}}$, and modification *via* the inclusion of a spin operator, $\hat{S}$,

$$\hat{\mathcal{H}}_s = g_e \mu_B \hat{S} \cdot B \quad [1.3]$$

When considering the application of a strong external field to a system containing a lone electron, the direction parallel to the field, B_0, is defined as the quantisation axis, commonly referred to as the z-axis. This allows simplification of the above expression to give,

$$\hat{\mathcal{H}}_z = g_e \mu_B \hat{S}_z B_0 \quad [1.4]$$

and alters the energy of the system to be,

$$E = g_e \mu_B m_s B_0 \quad [1.5]$$

Recalling that m_s can have values of ±½, there exist only two possible eigenstates for the electron to occupy, α ($m_s = +½$) or β ($m_s = -½$), and without any other influences these two are initially degenerate. Upon the introduction of a magnetic field the two $m_s = +½$ and $m_s = -½$ electron levels, become separated in energy.

$$\Delta E = h\nu = g_e \mu_B B_0 \quad [1.6]$$

The extent of the separation is proportional to the magnitude of the applied field, B_0, as given by the relationship [1.6] and shown in Figure 1.1.[10]

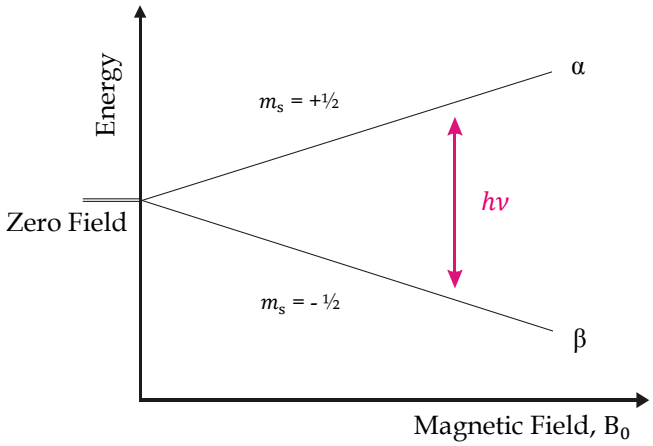

Figure 1.1 The Zeeman splitting of two initially degenerate spin-states of an electron in an applied magnetic field of increasing magnitude (B_0).

Under this imposed strong field the electron precesses about the applied field direction rather than around its *internal axis* and the magnetic moment of the electron can therefore align either parallel or anti-parallel to the z-axis (see Figure 1.2). If the spin is parallel with B_0, the energy of the electron increases and if antiparallel it decreases.

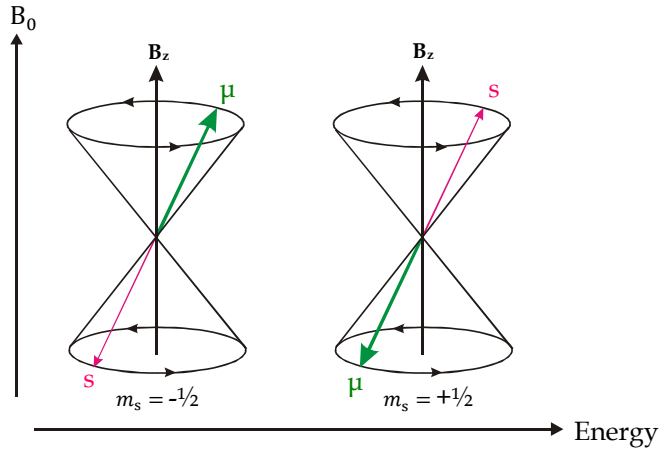

Figure 1.2 The alignment of electron spin-states, $m_s = \pm ½$, in a strong magnetic field, with the electron shown circling the z-axis.

The rate of precession around the z-axis for the unpaired spin is governed by its unique Larmor frequency, ω. This frequency is linked to g and is proportional to the external field, B_0.

$$\omega = \frac{g\mu_B \mathrm{B}_0}{\hbar} \quad [1.7]$$

It is appropriate to mention at this stage that spin active nuclear energy levels are also subject to splitting *via* the analogous nuclear Zeeman Effect, though this is often neglected as its magnitude is several orders lower than the equivalent electronic value.

The Landé g_e factor is the value for a free electron. This, by definition, is measured for an electron in the gas phase in the absence of neighbouring nuclei. In reality unpaired electrons reside within atoms and molecules (radicals) as discussed, and the g-value for these yield information on the effective magnetic field experienced by the electron in the sample. Alterations in g occur due to differing resultant magnetic moments arising from the immediate environment. The effective field, B_{eff}, felt by a particular electron therefore has two components; the value from the applied field, B_0, and the induced fields, B_{ind}.

$$\mathrm{B}_{eff} = \mathrm{B}_0 + \mathrm{B}_{ind} \quad [1.8]$$

This effective field is accounted for by an effective g factor giving the relationship in [1.9] rather than [1.8]. Here, g deviates from g_e according to B_{ind}.

$$\Delta \mathrm{E} = h\nu = g\mu_B \mathrm{B}_0 \quad [1.9]$$

Transition metals with unpaired electrons, such as iron (Chapter **3**) normally reveal large deviations from g_e, due to the magnetic moment arising from the electron's orbital motion around the nucleus, in addition to the usual SAM.[2] The interaction between the spin and angular magnetic moments is accounted for by spin-orbital (SO) coupling. The magnitude of SO coupling depends on the orientation of the electron and nucleus in relation to the applied magnetic field, and is therefore a measure of the anisotropy of a particular sample. Under these circumstances g should be replaced with a 3-dimensional tensor, $\boldsymbol{g}$. Only truly isotropic solutions will have $g = g_e$. This is very nearly demonstrated by organic free radicals in solution, since contributions from the orbital angular momentum are averaged and consequently the g-values only differ from g_e by up to 10^{-3}.[11]

1.3.1 Hyperfine Coupling

The Hamiltonian describing the interaction of an electron with a single nuclear centre in an applied field may be written as,[12]

$$\widehat{\mathcal{H}}_s = g\mu_B \hat{\mathrm{S}} \cdot \mathrm{B} - g_N \mu_N \hat{\mathrm{I}} \cdot \mathrm{B} + \mathrm{A}\hat{\mathrm{S}} \cdot \hat{\mathrm{I}} \quad [1.10a]$$

$$= g\mu_B \hat{\mathrm{S}}_z \mathrm{B}_0 - g_N \mu_N \hat{\mathrm{I}}_z \mathrm{B}_0 + \sum_i \mathrm{A}\hat{\mathrm{S}}_i \hat{\mathrm{I}}_i \quad [1.10b]$$

The first two components of the Hamiltonian ($g\mu_B \hat{\mathrm{S}}_z \mathrm{B}_0$ and $g_N \mu_N \hat{\mathrm{I}}_z \mathrm{B}_0$, respectively) represent the Zeeman interactions of both the electron and nuclear spins with a static field B_0. The third component of the Hamiltonian ($\sum_i \mathrm{A}\hat{\mathrm{S}}_i \hat{\mathrm{I}}_i$) describes the non-Coulombic (specifically magnetic) interaction between the electron, s, and the spin active nucleus, I, and is measured in terms of hyperfine coupling (hfc),[7]

$$\widehat{\mathcal{H}}_{hf} = \mathrm{A}\hat{\mathrm{S}} \cdot \hat{\mathrm{I}} \quad [1.10c]$$

Here, A is termed the dipolar hyperfine coupling tensor and possesses contributions of both isotropic (Fermi contact) and anisotropic (dipole-dipole) origin. The dominant coupling is intimately linked to the matrix in which the radical resides.

The classical model of coupling states that the current originating from the electron's spinning motion, covers a radius comparable to that of the nucleus, and is responsible for generating the nuclear magnetic moment. In regions far from the nucleus, it is assumed that the field from this current is interchangeable with that of a point dipole.[2]

1.3.1.1 Anisotropic Coupling (Dipolar Interaction)

Assuming the interaction of a spin active nucleus and an electron in a radical species can be approximated by the dipole-dipole relationship described in Section **1.3.1**, the interaction energy, E, between the two magnetic moments μ_e and μ_I, separated by a distance r, becomes,[13]

$$\mathrm{E} = \frac{\mu_e \mu_I}{r^3} - \frac{3(\mu_e \cdot r)(\mu_I \cdot r)}{r^5} \quad [1.11]$$

This energy is dependent on the orientations of the dipoles with respect to an applied field, as well as the magnitude of the field itself. The dipolar interaction is usually insignificant in solution and only becomes influential when radicals experience restricted movement, such as is encountered in micelles and highly viscous solvents. In a liquid as the radical rapidly tumbles, r, the distance between the dipoles will adopt an array of values, as will their angle of alignment to the field. Given that these point charges (whose behaviour can be considered as analogous to tiny bar magnets), are oriented in the direction of a strong field, rapid Brownian motion averages the sum of any created fields to zero. However, in a weak field, the magnets are mutually coupled, since they orient about their magnetic dipole axis, not the applied field, so again the anisotropic interaction is zero. But in the weak field the zero result occurs irrespective of tumbling.

Amendments to the energy expression to account for Equations [1.1] and [1.2] yields the corresponding Hamiltonian, which can be summarised to include the traceless and symmetrical hyperfine tensor A^0,

$$\widehat{\mathcal{H}}_{dipolar} = A^0\hat{S}\cdot\hat{I} = -g\mu_B g_N \mu_N \left\{\frac{\hat{S}\cdot\hat{I}}{r^3} - \frac{(\hat{S}\cdot r)(\hat{I}\cdot r)}{r^5}\right\} \quad [1.12]$$

1.3.1.2 Isotropic Coupling (Fermi Interaction)

When the electron is in close proximity to the nucleus, the point dipole approximation fails, as there is a non-zero probability of finding the electron at the nuclear centre, $|\psi_{r=0}|^2 \neq 0$. The magnetic interaction at this distance between this non-dipolar field and the electron's magnetic moment is described by the *Fermi contact mechanism*. The prerequisite for very close approach and finite probability density at the nucleus means it is only present for electrons occupying s-orbitals (it vanishes when $l > 0$, since $|\psi_{r=0}|^2 = 0$), and those possessing *s*-character.

$$\widehat{\mathcal{H}}_{fermi} = a\hat{S}\cdot\hat{I} = \frac{8\pi}{3} g\mu_B g_N \mu_N |\psi_{r=0}|^2 \hat{S}\cdot\hat{I} \quad [1.13]$$

The field model for the nucleus in this case is a current loop and interactions between the magnetic moment of the nucleus and the s-orbital electron occur independently of the external field. The coupling constant, a, is proportional to the

square of the electronic wavefunction at the nucleus (see Equation [1.13]) and the outcome of this contact mechanism is the energetically more favourable antiparallel arrangement of electron and nuclear spins.

The Fermi contact mechanism cannot account for the hyperfine structure in radical species where the unpaired electron occupies a π type orbital. For such radicals, the direct isotropic interaction is zero, since the nucleus is located in a nodal plane. The origin of this hyperfine interaction is explained through spin *Polarisation*.

Consider, a basic example involving the C-H bond of a $R_2HC^{\bullet}$ radical, for which the unpaired electron inhabits a p-orbital.[14] The magnetic interactions between the nuclei and the electrons increase the probability of finding an electron, nearby to the nuclei in the σ-bond (see Figure 1.3). The unpaired electron in the p-orbital influences the orientation of the electron adjacent to the carbon and slightly favours a configuration with the greatest number of unpaired electrons, obeying Hund's rule of maximum multiplicity.[2] As a consequence, the electron close to the hydrogen nucleus will prefer an antiparallel arrangement of spins due to the Pauli exclusion principle.[15] The innate hybridisation of the σ-orbital close to the carbon, and its 1s appearance near to the hydrogen, supports some spin density in the 1s orbital. Hence this gives rise to isotropic coupling *via* the discussed Fermi contact mechanism.

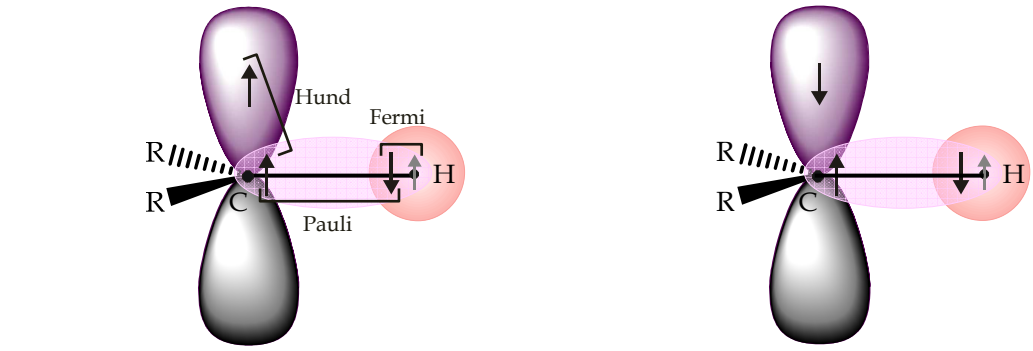

(a) (b)

Figure 1.3 The polarisation mechanism for an unpaired electron in a pure 2p (π) orbital. (a) Is the low energy and (b) Is the high energy arrangement and both of these illustrate how transferring spin polarisation through a bond can lead to a hyperfine interaction.[2, 14] The preferred antiparallel spins are shown near the nucleus (Fermi) and through the C-H bond (Pauli). The low energy arrangement displays the favoured parallel spins (Hund).

For the scope of this work isotropic and anisotropic couplings are both relevant, however the significance of anisotropic effects in the solution phase work are negligible, whereas the anisotropy in solid samples can often dominate over the isotropic coupling.[16]

When electrons are paired within orbitals, contrary to the examples given so far, the spin angular momenta sum to zero, as do the net magnetic moments. It is not surprisingly then, that only species with one or more unpaired electrons have a resultant spin moment, and exhibit interactions with a magnetic field. This behaviour is exploited in recording techniques such as *Electron Paramagnetic Spectroscopy* (EPR), which to date remains the most widely used analytical technique for the study of paramagnetic species.[10]

1.3.2 Electron Paramagnetic Spectroscopy

Transitions between the electron Zeeman levels depicted in Figure 1.1, can be induced once the resonance condition in Equation [1.9] is met. Continuous wave EPR (CW EPR) spectroscopy uses a fixed magnetic field (B_1) from a microwave source and sweeps an applied magnetic field (B_0) to vary the electron level separation. Once the resonance separation in energy is achieved, the microwave radiation is absorbed by the electrons, causing reorientation of the electron spins. This corresponds to the EPR signal and requires a population difference to show a net effect. The resulting EPR spectrum yields information on the effective field at the unpaired electron through the aforementioned g-value, which appears at the central field position. The spectra also reveal hyperfine structure, which arises from the presence of nearby spin active nuclei and can be identified as splitting in the EPR spectral peaks.[6] The process of collecting data and the appearance of the resulting spectra are discussed further in Chapter **2**.

1.4 Radical Pairs

From Table 1.1, it is apparent that radicals are usually created in pairs from diamagnetic precursors and for this reason they are referred to as *radical pairs* (RPs). Upon bond cleavage, the two resulting radicals will each possess an unpaired electron. Consequently the RPs may be divided into two groups depending on the relative alignment of their spins. An *uncorrelated* pair has a random orientation of electron spins and occurs for radicals that encounter in the bulk solution. A *correlated* RP is

generated from a common precursor. For such RPs the total SAM, S, is preserved and the two spins will have the same orientation as that of their precursor.[17]

When considering that an electron can adopt one of two spin-states, the spin correlated radical pair (SCRP) may have four possible permutations of its spin. On conserving S, where $S = s_1 + s_2$, (which is a combination of the spin angular momenta on $R_1^{\bullet}$ and $R_2^{\bullet}$), the spins may sum or counteract one another, giving S as 1 or 0 respectively. If the spins are antiparallel, $S = 0$, and the state obtained is referred to as a singlet (S) state. The number of allowed sub-levels is again given by $2S + 1$, which for the S state equals 1. If the spins are parallel the SCRP is in a triplet (T) state, of which there are 3.

When two radicals encounter in bulk solution, one may expect they instantly react to form a covalent bond. Since a requirement for this to occur is that the electron spins be paired, to satisfy the Pauli principle,[15] recombination is not always guaranteed. Therefore based on the orientation of the spins alone, RPs with parallel electron spins should not couple to produce a non-radical product. However, interactions of the RP with an applied magnetic field have been shown to alter the spin-state from a triplet to a singlet and vice versa.[18] The evolution between the S and T coupled states arises through different mechanisms that are dependent on the magnitude of the applied field. The following section details the experimental conditions that promote spin-state mixing and how altering the reactivity can affect the kinetics of the RP.

1.4.1 The Radical Pair Mechanism

Statistically, when a RP is generated, ¾ of the initial pairs should be in the triplet state, and the remaining ¼ in the singlet. Accordingly only the latter proportion of interactions between singlet RPs should result in bond formation. Results obtained from a number of NMR studies opposed this, and revealed enhanced intensities (now known as *Chemically Induced Nuclear Polarisation*, CIDNP) that could not be rationalised by the statistical prediction.[7] To explain the results, an alternative mechanism was required in which alterations in the radical kinetics could give rise to the witnessed line intensities. This was proposed by the *Radical Pair Mechanism* (RPM).[19, 20] The RPM is depicted by the overall scheme given in Figure 1.4, and offers an explanation for altered reaction and product yields obtained for RPs when under the influence of magnetic fields.

For the discussion in this section the singlet RPs are assumed to be reactive while triplet are unreactive. It should however be noted that this is not explicitly the case.

Triplet correlated RPs with sufficient energy can also recombine to yield an excited state, though this is not relevant to the current work and is therefore considered no further. Under the proposed condition, it is apparent that for triplet correlated pairs, no encounter leading to bond formation will ever arise unless there is the prospect for the spin to flip and generate the compulsory singlet correlated electron spins. For RPs that remain in close proximity, this scenario may develop. Two methods that allow such an event, occur at different stages of RP separation, consequently the distinction between a close pair and a separated pair (as shown in Figure 1.4) becomes pivotal. The RPM diagram proceeds from the formation of the RP, where the medium in which the pair is born influences both its lifetime and subsequent reaction route.

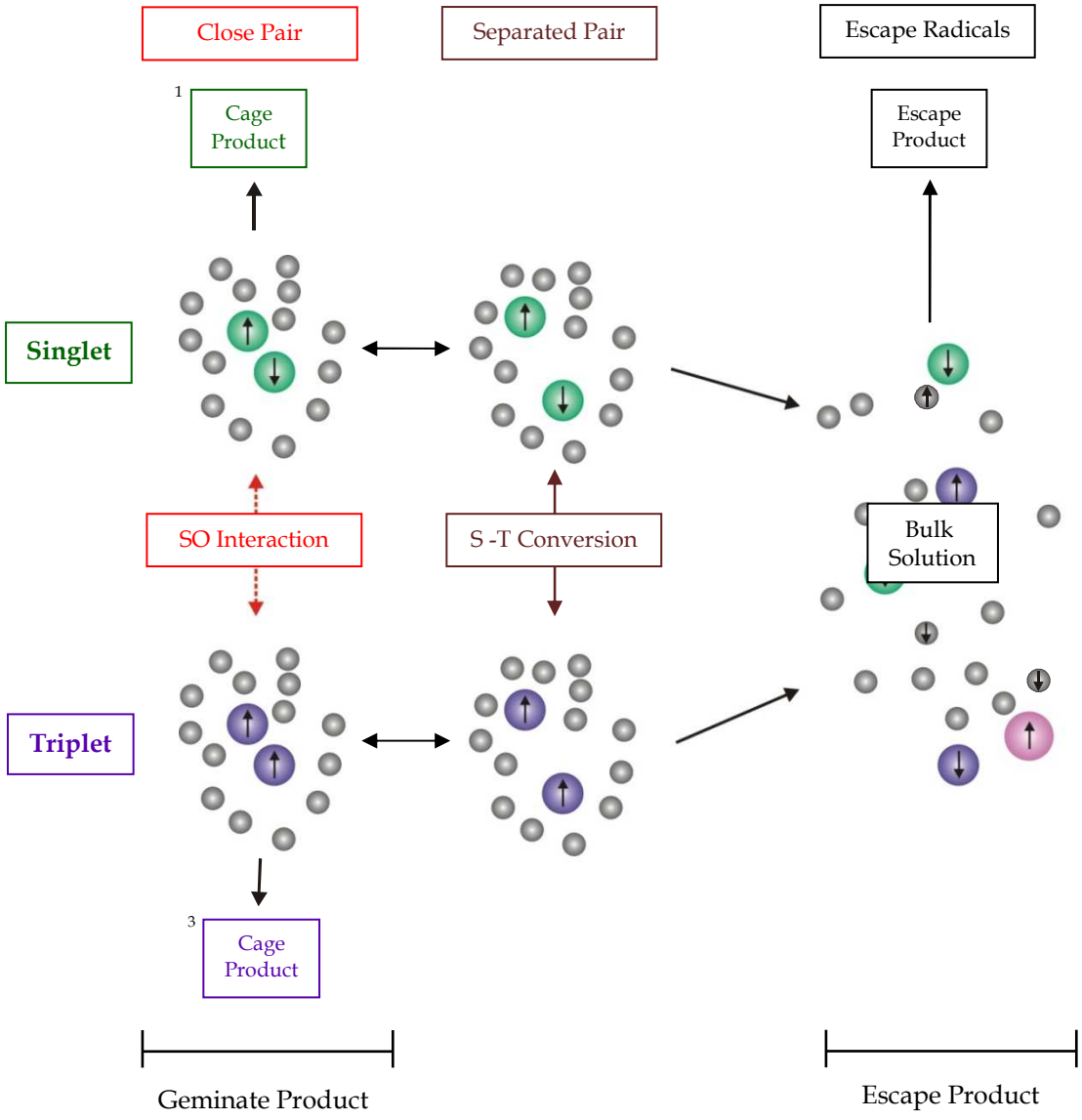

Figure 1.4 Reaction scheme depicting the subsequent encounters of singlet and triplet correlated RPs following their formation.

1.4.2 Radical Pair Diffusion and Recombination

Since radicals are generated in pairs, they are in close proximity after formation. In solution, their separation is prevented by the surrounding solvent molecules, commonly referred to as the solvent cage. The energy barrier for migrating past these neighbouring molecules is typically ~ 10-15 kJ mol^{-1} and confinement of the pair means they remain together for a few thousand collisions, continuously separating and re-encountering, before either combining or escaping into the bulk solution. This phenomenon is the cage effect and occurs to some extent for all RPs in solution.

RPs formed in this manner are often called geminate pairs or g-pairs. As discussed, recombination through the singlet state for these is allowed, while through the triplet state it is forbidden. In theory, for g-pairs in the singlet state, recombination should be immediate following their formation. In reality, the excess energy from bond cleavage tends to separate the radicals and thus the produced radicals are not close enough to allow such instantaneous recombination. Nevertheless the RP may recombine rapidly on a timescale that is governed by the dimensions of the solvent cage.

The remaining unpartnered radicals continue to diffuse through the cage and become separated pairs. Under this condition, weak field interactions such as those from Zeeman and hyperfine effects become significant and can initiate S-T conversion. Interestingly, upon generation, certain close pairs are also able to undergo S-T conversion *via* SO coupling. However, this only manifests in heavier radical centres, predominantly those of transition metals. SO coupling is negligible for lighter atom centred radicals, such as those of carbon and phosphorus that are encountered in this work, and so this phenomenon is not discussed further. The probability of recombination for the triplet correlated RPs within the solvent cage, is higher than that recorded without these field induced developments. Proving a direct correlation between the period of time spent in the cage and an increase in the geminate product.[7]

Radicals that escape the cage and travel randomly through solution to encounter other radicals are known as freely diffusing pairs (f-pairs) or escape pairs. The result of this escape route is a much slower reaction, with its timescale dictated by the rate of migration, and hence it is referred to as a diffusion controlled reaction. RPs retain spin correlation with their original partners, but for f-pairs (uncorrelated pairs), the spin orientation is random. Provided there is correct orbital overlap with the encountered radical (be it from the solvent itself or an alternative f-pair) in bulk solution, recombination will occur. This yields a random a spin-state correlation upon encounter,

which is accordingly reflected in the escape product and adheres to the statistical distribution of S and T coupled states.

The first mechanism for spin exchange is through SO coupling, which only arises in close pairs. Whereas the second is *via* mixing of the singlet and triplet states and is reliant on a separation of $>$ 1 nm,[11] which in turn defines the distance between separated pairs. To determine how an applied magnetic field can induce spin-state mixing it is firstly necessary to consider the four coupled states in the presence of an applied field.

1.4.3 Coupled Spin-States in a Magnetic Field

In a magnetic field the singlet and triplet RPs are labelled in terms of their resulting magnetic quantum numbers. Given that the ground state antiparallel arrangement produces $S = 0$, the consequent magnetic quantum number is also 0. While for when $S = 1$, there are three magnetic quantum numbers, 1, 0, and -1, corresponding to the T_+, T_0, and T_- coupled states respectively.

When in solution, the two radicals possess very weak coupling, and only momentarily on formation does the RP exist in a pure spin-state. Thereafter, the combined spin is neither wholly triplet nor singlet but rather the overall state may be described as a mixed intermediate of the two.[11] A linear combination of the four coupled electron wavefunctions gives an accurate description of the true singlet and triplet states. These resulting electron spin wavefunctions may be written as follows,[21]

$$\left.\begin{aligned} |S_0\rangle &= 2^{-½}(\alpha\beta - \beta\alpha) \\ |T_+\rangle &= \alpha\alpha \\ |T_0\rangle &= 2^{-½}(\alpha\beta + \beta\alpha) \\ |T_-\rangle &= \beta\beta \end{aligned}\right\} \quad [1.14]$$

This outcome is analogous to that obtained when considering the behaviour of both spin and spatial wavefunctions during the approach of two hydrogen atoms, prior to bond formation.[21] The corresponding spin Hamiltonian for a RP ($R_1^{\bullet}$, $R_2^{\bullet}$) in solution can be described by,[7]

$$\hat{\mathcal{H}}_{RP} = \hat{\mathcal{H}}_{ex} + \hat{\mathcal{H}}_{mag} \quad [1.15]$$

The components of the Hamiltonian are a combination of the exchange (discussed later in this section) and magnetic interactions of the unpaired electrons in the RP,

$$\hat{\mathcal{H}}_{ex} = -\mathrm{J}\left(2\hat{\mathrm{S}}_1\hat{\mathrm{S}}_2 + ½\right) \quad [1.15a]$$

$$\hat{\mathcal{H}}_{mag} = \left(g_{\mathrm{R}_1}\mu_B\hat{\mathrm{S}}_{1z}\mathrm{B}_0 + \sum_i^{\mathrm{R}_1} a_i\hat{\mathrm{S}}_1\hat{\mathrm{I}}_i\right) + \left(g_{\mathrm{R}_2}\mu_B\hat{\mathrm{S}}_{2z}\mathrm{B}_0 + \sum_k^{\mathrm{R}_2} a_k\hat{\mathrm{S}}_2\hat{\mathrm{I}}_k\right) \quad [1.15b]$$

The magnetic interaction is the sum of the individual contributions from both the radicals in the pair (refer to Equation [1.10b]). a_i and a_k are the two isotropic hyperfine coupling constants (hfccs) with nuclear spins I_i and I_k, in radicals $\mathrm{R}_1^{\bullet}$, and $\mathrm{R}_2^{\bullet}$, respectively. The nuclear Zeeman terms are omitted from Equation [1.15b], and the electron-electron magnetic interactions average to zero in solution.

There is no simple manner of physically interpreting these paired spin-states, though commonly the classical high field model is used owing to its compliance with quantum principles.[11] Therefore, in an analogous manner to that for a single electron, Figure 1.5 depicts the two vector spins, s_1 and s_2, precessing around the z-axis at a rate defined by their individual Larmor frequencies, as described by Equation [1.7].

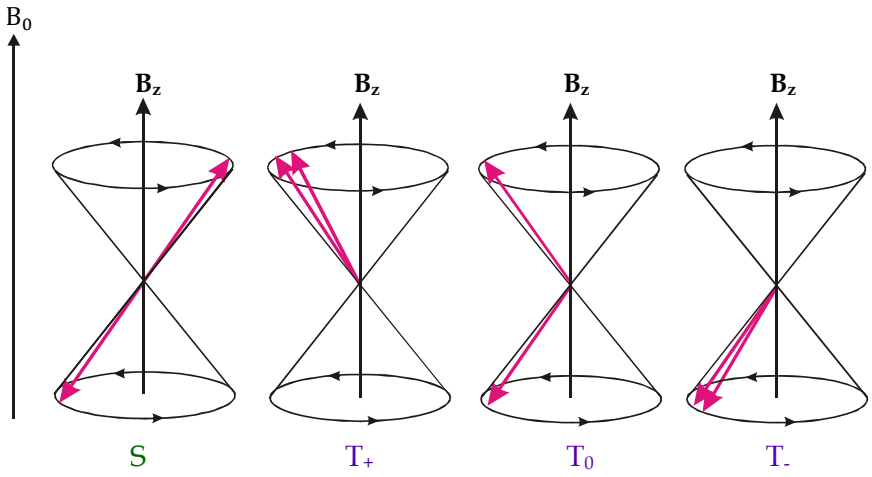

Figure 1.5 The high field vectorial representations of the electron (arrow) spins ($m_s = +½$ upwards, and $m_s = -½$ downward) in the four RP spin-states. The separate radical spins are drawn cycling a cone shape, each at their individual Larmor frequencies.

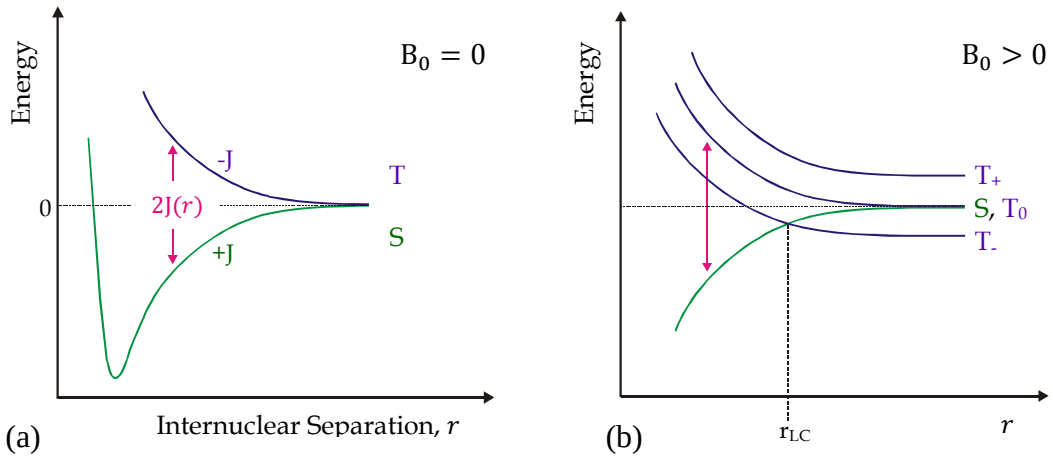

Figure 1.6 The variation in energy of the T and S coupled states as a function of RP separation, r, in the (a) absence, and (b) presence, of an applied magnetic field. 2J is the electron exchange interaction. Note the near degenerate nature of the S and T states at large r when $B_0 = 0$, this remains for the S and T_0 states when $B_0 > 0$. r_{LC} indicates the distance required for the spin-state mixing *via* the level crossing mechanism (Section **1.4.4.1.1**).[7]

The S state is non-magnetic. This is immediately obvious from the vector diagram. Notice how the two spin angular moment vectors remain completely out of phase with respect to all axes. The same is not true for T_0. The total magnetic moment for T_0 is orthogonal to the applied field and consequently this coupled form is independent of changes in the field. The $T_\pm$ states exhibit an overall magnetisation in the direction of the applied field, thus their energies are directly proportional to the strength of the applied magnetic field.

To predict the possibility of recombination of the triplet born pairs, it is necessary to consider the respective energies involved. The energy difference between the S and T coupled states (Figure 1.6, $B_0 = 0$), at any instance is described by, $2J(r)$, the electron exchange interaction. J is a quantum mechanical term and its origin is rooted in electrostatic interactions between the electrons in the pair. It is the energy required to align the two spins of the RP with one another and is given approximately by,

$$J(r) = J_0 e^{-\frac{r}{r_J}} \quad [1.16]$$

Here, J_0 is a scaling parameter, which typically equals 10^{17} rad s^{-1},[18, 22] and is negative for neutral pairs. r is the separation between the RPs, while r_J is the fall off distance and has a value of approximately 49 pm for isotropic solution.[22]

1.4.4 Spin-State Mixing

Clearly, the magnitude of the exchange interaction inhibits spin-state interconversion at small RP distances, (refer to Figure 1.6). As the RP diffuses apart, the electron exchange interaction reduces. When the energetic separation of the singlet and triplet states becomes negligible (typically at 1-1.5 nm)[22] the spin-states of the pair may evolve under the influence of the spin Hamiltonian.[11]

Strictly, at any period following RP creation, (bar immediately) the pair possesses both singlet and triplet character and the recombination probability is linked to the amount of singlet character of the RP. For modelling purposes the distinction of the S and T states is useful. After adequate separation between the pairs and spin evolution, J is able to freeze the mixing so a portion of the RPs can exist in a prolonged pure state. In the case of the recently evolved singlet pairs, this allows recombination. As a result, an initially T born pair, given time and multiple encounters, can recombine to yield a neutral ground state molecule. A greater proportion of RPs will therefore encounter in a singlet state and thereby increase the yield of geminate product, thus altering the predicted statistics. Spin-state mixing directly modifies the ratio of the cage to escape product, while the underlying chemistry remains unchanged. This effect can be observed in an experiment for two reasons; firstly the f-pair product may be different to the original molecule (assuming the medium to be reactive) and secondly this diffusive reaction will occur on a much longer timescale.

The solvent cage becomes highly influential at this stage and governs whether or not the spin-state mixing can occur. An ideal cage will both prevent the radicals diffusing into the bulk solution and simultaneously allow sufficient separation between the RP. This is a much sought after trait, with numerous studies dedicated to the encapsulation of RPs alone (Section **1.5.1**).[18, 23-25]

1.4.4.1 Mechanisms for Coherent Spin-State Mixing

In zero field the three triplet sub-states are indistinguishable (Figure 1.6 (a)) and theoretically, provided there is an appropriate mechanism, spin-state mixing should evolve readily between the triplet state and the singlet (assuming a large r). Spin-state mixing is primarily driven by local hyperfine interactions and therefore also occurs in the absence of an applied magnetic field, the model for this is described later in Section **1.4.4.1.3**. Having previously considered the effect on a single electron, it is useful at this

stage to discuss the influence of an applied magnetic field on all four coupled RP states, before discussing the underlying mechanisms for spin-state mixing.

In Figure 1.7, as a magnetic field increases the Zeeman interaction energetically removes the $T_{\pm}$ levels, to a condition where no coherent spin-state mixing between the S and T_{+}, or T_{-} states can arise. This isolation requires the separation of the T_{+} and T_{-} states to far exceed the value of the average hyperfine coupling in the RP. The T_0 and S states, however, due their non-magnetism in the z-direction, remain a distance of the exchange energy apart regardless of the field strength. At such a distance where $J = 0$, the T_0 and S would be degenerate, this would allow interconversion between these two coupled spin-states.

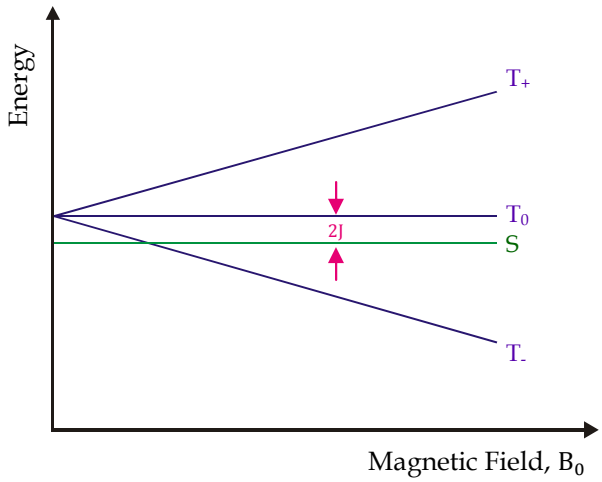

Figure 1.7 The Zeeman effect on the four coupled spin-states of a RP, in an increasing magnetic field, at a fixed inter-radical separation.

There are three coherent spin mixing mechanisms to consider and the relevance of each is governed by the strength of the field and proximity of the RP members.

1.4.4.1.1 Level Crossing Mechanism

Notice (Figures 1.6 (b) and 1.7) how the increase in magnetic field causes an intersection between the S and T_{-} levels (for positive values of J). This occurs at an instant when $r = r_{LC}$ and leads to a temporary degeneracy, which is revealed at low magnetic field strengths. This, the so called J-resonance should have a negligible influence on the overall spin-state mixing in a *normal* solution. This is since only fleeting periods of time will be spent in this briefly encountered energy state that exists during diffusion. Its effects become more pronounced when RP diffusion is restricted,

and pairs that spend significant time at the appropriate r separation will exhibit an enhanced T_- to S mixing rate (and vice versa). Such examples are encountered in micelles or more efficiently in biradical systems, where the level crossing may unlock substantial spin-state mixing.[26] Therefore the effect of this mechanism for mixing is considered insignificant in the majority of solution phase work. While viscous solutions as well as micelles are actively investigated here, the contribution to spin-state interconversion during the temporary level crossing should be negligible in comparison to the other coherent spin-state mixing mechanisms occurring at low fields.

1.4.4.1.2 Δg Mechanism (Zeeman Mechanism)

From the discussions presented earlier (see Section **1.3**), it is clear that a change in the local field of an unpaired electron due to hyperfine interactions and SO coupling, will alter its g-value. Accordingly this will also change its Larmor frequency, given by Equation [1.7]. If both radicals in a RP have unique g-values, they will precess around the magnetic field axis at different rates. For a fixed field strength, the difference in their Larmor frequencies, $\Delta\omega$, will directly depend on the difference in their g-values,

$$\Delta\omega = \frac{\Delta g \mu_B B_0}{\hbar} \quad [1.17]$$

Given sufficient time, the variation between these frequencies, $\Delta\omega$, will cause the phase difference between the states to fluctuate, as described by the high field model in Figure 1.8. This leads to an oscillation between S and T_0 states as the relative spins of the electrons alternate in and out of phase during the RP's lifetime. The rate of interconversion depends on both the field B_0, and the RP's respective electron g-values. The variation in phase is exaggerated by increasing the external magnetic field, which increases $\Delta\omega$, and the rate of S-T_0 conversion accordingly.

When the radicals in the pair experience the same local field, their spin-state mixing rate develops as a function of their relative g-values. This is encountered in larger fields (of $>$ 100mT), where the value of the resultant field, B_{eff}, is increasingly governed by the external field, B_0, and not by the hyperfine coupling (refer to **1.4.4.1.3** of this Section). The Δg mechanism at such a field strength is the principal method of spin-state interconversion, and the proportion of total spins that can recombine in the singlet state will tend toward a maximum of ½, whilst the other ½ (from $T_\pm$ removal),

remain unreactive. If, however, the radicals are identical with respect to both chemical structure and their hyperfine environment, then by virtue of their constant phase relationship, S-T_0 mixing will be prevented. The radicals in the pair will continue to retain their relative coherence for the duration of the RP lifetime or until other processes interfere.

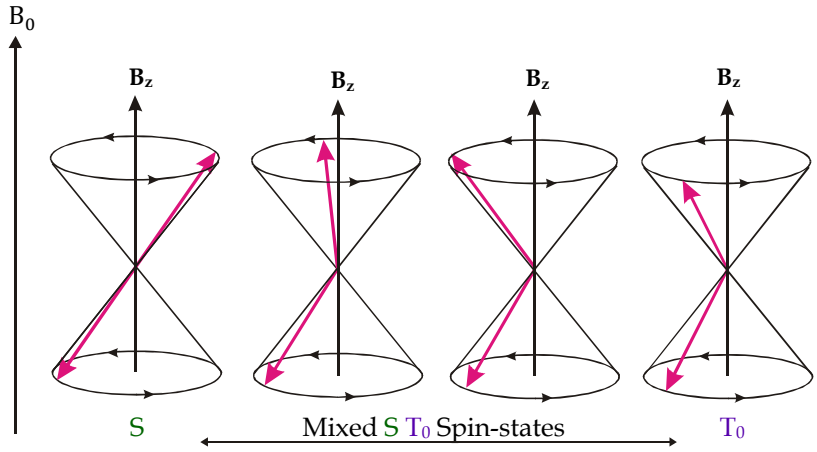

Figure 1.8 The high field representation of the altering electron phase relationships in the T_0 and S RP coupled states. Each electron precesses at its own Larmor frequency, which depends on the local field contributions to the g-value. This difference in the Larmor frequency is given by Equation [1.17]. The conversion of T to S and vice versa over time is illustrated and the intermediate stages comprise of mixed S and T character. A larger Δg, or local field, B_{eff}, promotes faster S-T_0 interconversion.[11]

The Δg mechanism is not the only manner by which alterations in the Larmor frequency can trigger spin-state mixing, as is considered in the next section.

1.4.4.1.3 The Hyperfine Coupling Mechanism

The Hyperfine Coupling Mechanism (HFM) reveals how hyperfine coupling (Section **1.3.1**) from interactions with neighbouring magnetically active nuclei (such as ^{31}P and ^{1}H), can alter the precession rates of the electrons in a RP, in an applied or zero magnetic field. A different model is used to describe the interaction between the electron and the nuclei in each case, and the appropriate model is determined by the strength of the applied field.

The High Field Model

Consider the strong field case, where the quantisation axis is in the field direction. A radical pair ($R_1^{\bullet}, R_2^{\bullet}$), resides in the strong field and consists of a single electron, s_1, interacting with a spin ½ nucleus, I, whilst the second electron, s_2, is not coupled to a nuclear spin. Referring back to Equation [1.8], which describes the contribution from both Zeeman and hyperfine induced fields, it is again anticipated that evolution of the phase relationship ($\Delta\omega$) will occur, driven on this occasion by hyperfine interactions. For the given example, s_2 precesses at the usual Larmor frequency (ω_2), while s_1 is altered by an amount equal to $\Delta\omega = g\mu_B a_1/2\hbar$, by virtue of the additional spin ½ hyperfine contribution to the B_{eff} (Equation [1.18]).

$$B_{eff} = B_0 + am_I \quad [1.18]$$

Therefore in a similar manner to the Δg mechanism, S↔T_0 conversion is permitted through changes in the respective Larmor precession rates. Again, no conversion with the $T_{\pm}$ will ever develop at fields of this magnitude or beyond.

The Low Field Model

Based on Equation [1.18] it is apparent that applied fields comparable to, or less than the hyperfine coupling, $g\mu_B B_0 \leq a$ (the definition of a weak field), can vary the primary axes for rotation of the electron. This allows the precession of the electron to be ever more dominated by the sum of the induced hyperfine fields, i.e. when $B_{eff} \cong am_I$. This scenario is contrary to that of the high field case, where a comparatively large external field is used and the hyperfine interactions are negligible ($B_{eff} \cong B_0$).

For the defined RP, a simple illustration may be envisaged (Figure 1.9). In the first radical ($R_1^{\bullet}$), the spin angular momentum vectors of the proton (I) and electron (s_1) couple to generate a resultant angular moment, J_1. Both the spins rotate around J_1 with identical angular momenta, as well as simultaneously behaving under the influence of the applied field. This process of circling the resultant moment, J_n, occurs independently for non-interacting radicals in solution. When the radicals, $R_1^{\bullet}$ and $R_2^{\bullet}$ are created as a singlet pair (refer to Figure 1.9), they initially exhibit no resultant electron spin, since they reside perfectly antiparallel in all axes. Given time, as s_1 and s_2 precess around their respective J_n moments, the pair will continuously lose and reform this

antiparallel relationship, which is again triggered *via* their differing hyperfine couplings. This net direction is no longer coincident with the external field and so introduces a variable electron spin projection in the applied field axis. This projection in the field direction exhibits the characteristics of $S \leftrightarrow T_{n(n=+,0,-)}$ mixing.[27] The more pronounced the difference in their hyperfine states, the greater the rate of the S-T mixing will be and typically a time period of nanoseconds is observed for spin-state mixing in organic radicals.[11]

Chemical reactions often occur on a timescale more rapid than spin-state mixing, and therefore efforts have focussed on systems where the reaction has intentionally been retarded. Additionally, in weak fields the time taken for S-T evolution may be significantly longer than that required at higher fields, imposing two challenges to recording such effects.

When the two electron spins in the RP both possess varying hyperfine interactions, originating from coupling with multiple neighbouring nuclei, and inter-radical effects (which in reality is often true), the depiction becomes much more complex. The simplified illustration given in Figure 1.9 is no longer valid for this case, since it assumes a stationary frame of reference (s_2).

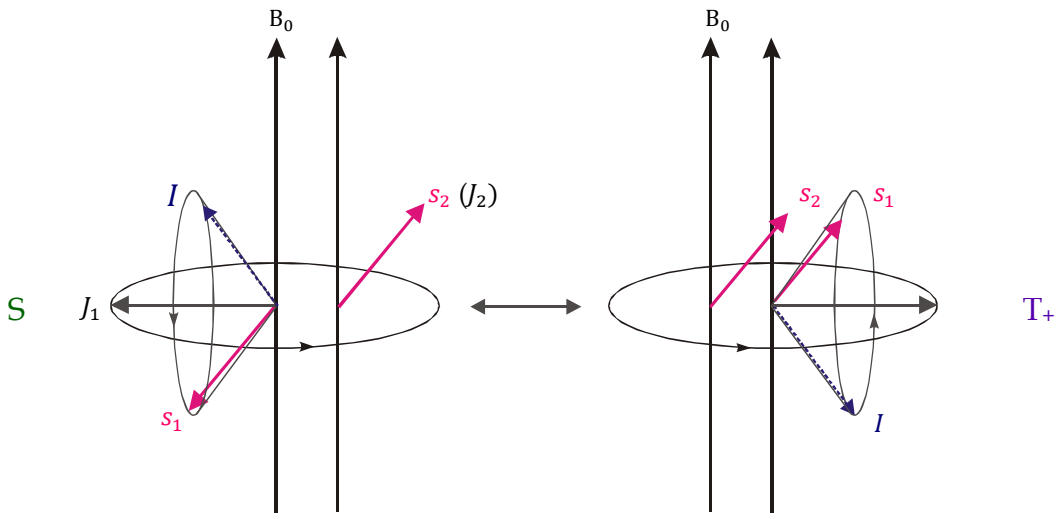

Figure 1.9 Precession of a coupled magnetic nucleus (I) and electron spin (s_1) around their net angular momentum, J_1. The second radical (s_2) in the pair has no hyperfine coupling, so remains static with respect to the applied field, and defines the frame of reference.[21] Rotation around two sets of magnetic axes demonstrates $S \leftrightarrow T_{n(n=+,0,-)}$ interconversion in a low ($g\mu_B B_0 \leq a$) magnetic field. Note that the angular momenta of the electron and nucleus are identical, despite their different magnetic moments.

The Zero Field Model

The HFM also describes the method by which spin-state interconversion is achievable in zero fields. In the absence of an applied field, spin selection rules are integral to the potential for spin-state mixing and the total angular momentum (J_{total}) of the nuclei and electrons, $J_{\text{total}} = J_1 + J_2$, and their projection onto an arbitrary axis, J_z, must both be conserved.[27] This enforces an alteration in the projection of one of the electrons or nuclei to be accompanied by a concurrent change in the other. Abiding by these conditions still allows the electron and nuclear angular momenta to rotate at a rate controlled by their hyperfine couplings, and hence permits S-T_0 mixing to occur. However, these spin selection rules do restrict the extent of zero field oscillations and no $T_{\pm}$ exchange can arise unless a flip in spins of both the electron and nucleus occur simultaneously (see Figure 1.10). This may be triggered by a change in the hyperfine coupling as a result of other magnetically active nuclei. So while $S \leftrightarrow T_{n(n=+,0,-)}$ does occur in zero fields, the $S \leftrightarrow T_{\pm}$ is restricted, and can only occur for a spin coupled to a spin active nucleus.

When the RP is in an applied magnetic field, the selection rules ease. This allows spin interconversion between all available states of T with the S. The spin exchange in an applied field becomes a function of the projection of the total angular momentum (J_z) only and J_z in this case is defined as the direction of the applied field axis.

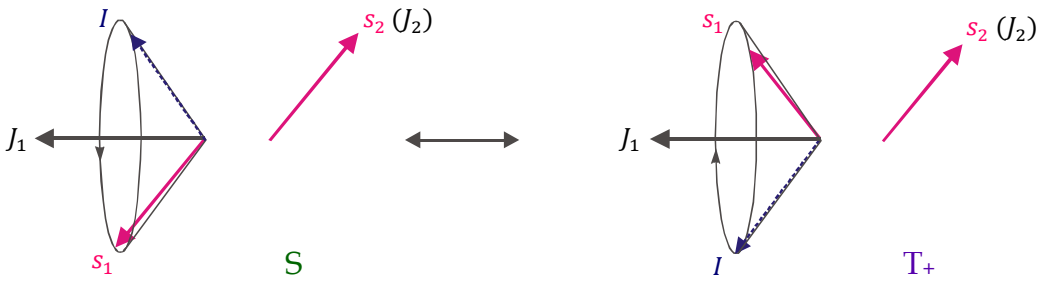

Figure 1.10 The zero field representation of an electron (s_1) coupled to a single spin ½ nucleus (I), whilst residing near a second electron (s_2) that exhibits no hyperfine interaction.[11] Rotation of s_1 at the hfc frequency shows how S-T_+ mixing can develop. The total and J_z angular momentum must both be conserved; hence the extent of spin conversion is limited since complete spin reversal of s_1 with respect to s_2 cannot occur (*cf.* Figure 1.9).

1.4.4.2 Mechanisms for Incoherent Spin-State Mixing

Owing to the conservation of spin angular momentum on formation of a RP, all of the electron spins in the total number of pairs, in solution, will initially have identical orientations. This phenomenon is referred to as *polarisation* and it does not conform to thermal equilibrium as described by the Boltzmann distribution.

The individual spins in solution experience various magnetic interactions during their course of rotational and translational motion. Therefore an unsystematic array of field values with oscillating components of all frequencies will be present. As a consequence of the fluctuating magnetic fields near the RP, two specific types of mechanism may be instigated; these are referred to as spin-lattice and spin-spin relaxation. Both of these mechanisms occur due to anisotropies in g and the dipolar coupling; hyperfine and electron-electron (minor). The effect of these incoherent spin-state mixing processes is illustrated in Figure 1.11, and both the spin-lattice and spin-spin relaxation mechanisms work to establish thermal equilibrium in the spin alignment of the RPs.

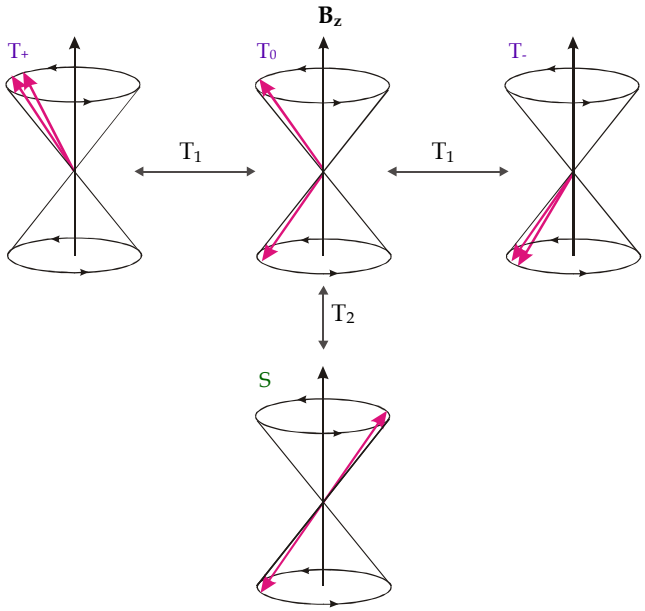

Figure 1.11 A high field vectorial diagram to demonstrate the incoherent spin-state mixing mechanisms present to correct a non-thermally equilibrated system. Both occur as a consequence of a continuously fluctuating local field arising due to radical motion, and cause spin flips or rephasing on timescales labelled as T_1 and T_2 respectively.

Spin-Lattice Relaxation

The spin-lattice relaxation mechanism accounts for the exchange of the electron's energy with its surroundings, the *lattice*. The local field of the electron has associated oscillating frequency components that are proportional to the energy of the electromagnetic wave. When a RP tumbles in solution, one spin may encounter the correct orientation and magnitude to allow transitions between the electron Zeeman levels, among this range of frequencies. At this specific energy the lattice induces spontaneous flipping of one electron spin in the coupled spin-states, allowing S and T_0 to solely exchange with $T_{\pm}$ (and vice versa), as can be seen in Figure 1.11. Interconversion proceeds within the high field limit over the time period defined as T_1, the spin-lattice relaxation time.

Spin-Spin Relaxation

A SCRP has a fixed alignment of spins with respect to the magnetic field axis, B_z. Over time, thermal equilibrium will be achieved by the local field destroying the phase coherence between the spins in the RP, leaving a uniform spin distribution. This development is driven by the static components in the local field as the radical tumbles, and occurs due to the continuously altering Larmor rates of the two spins. Dephasing of $S \leftrightarrow T_0$ states occurs on a timescale labelled T_2, the spin-spin relaxation time, as illustrated in Figure 1.11.

Clearly both spin-lattice and spin-spin effects contribute to incoherent spin-state mixing. The weak coupling of the electron spins with the thermal bath means the period of these incoherent processes is slow (typically microseconds) compared to the RP geminate lifetime and the aforementioned HFM, or Δg mechanisms. Consequently, for the majority of RPs encountered in solution, random spin exchange of this origin is negligible. This, however, is not true for the $^{\bullet}$OH radical in solution, where the adjustments in the solvent hydrogen bonding network alter the orbital contribution to the anisotropic g-value. This generates a fast relaxation time of < 1 ns, thus the spin mixing contributions from the spin-spin and spin-lattice mechanisms dominate. Therefore observing magnetic field effects for such a species is unfeasible given its short lifetime.[28] When the lifetime of the radicals is approximately microseconds, as is the case for the RPs investigated within this work, both coherent and incoherent spin relaxation will unavoidably influence the time evolution of the RP.

1.5 Magnetic Field Effects

The illustration in Figure 1.12 details the effect of both principal coherent spin-state mixing mechanisms on the escape yield of an initially triplet born RP in solution. Inversion of this plot reveals the associated triplet born product in the geminate cage. The area dominated by each mechanism is labelled and both occur at different field strengths. As well as these mechanisms, there is a field region where neither is encountered.

Long after the energetic separation of the $T_{\pm}$ levels from the S (and T_0) and occurring at fields of $>$ 1 T, the escape yield is gradually reduced. Here, the spin interconversion between the T_0 and S states is sufficiently field enhanced through the differences in the g-values of the pair, to increase the proportion of triplet recombination reactions (occurring through the singlet channel) in the geminate cage, over that of the zero field case. This enables more photochemically created T_0 states to evolve into an S state. This is identified as the Δg region in Figure 1.12. Additionally, S-T_0 mixing can also occur through the HFM; however, the effect is much weaker than that from the variation in g at these field strengths.

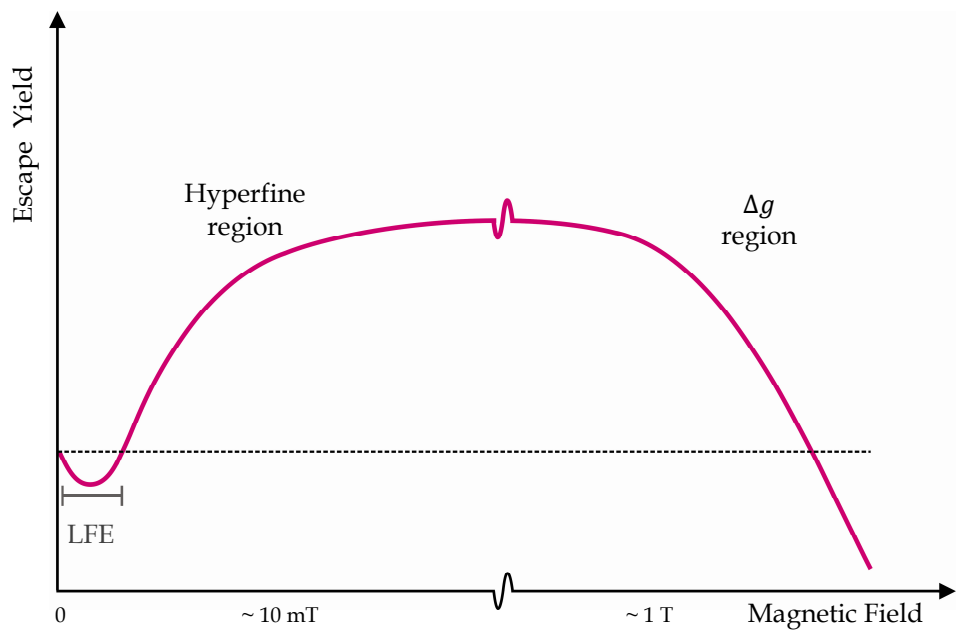

Figure 1.12 The variation in the dominant spin-state mixing mechanisms of a triplet born RP, with increasing field strength. The reaction yield represents the overall escape recombination product. In the low field region the HFM allows spin-state mixing between $S \leftrightarrow T_{n(n=+,0,-)}$ and thus demonstrates a LFE, while an increase in the field $>$ 1 T, alters the dominant spin-state mixing mechanism to become Δg.

The lifetime of the RP is among the spin-state mixing limitations for the Δg mechanism. When Δg is relatively small, the rate of S-T_0 mixing will be longer than the average lifetime (~ nanoseconds) of the RP in the solvent cage. Therefore the spins will not exchange states and thus will not impact the g- and f-pair product ratios. An appropriate example of this involves organic radicals, where the g-values typically vary by 10^{-3}. Realistically at low fields, no spin evolution triggered by Δg can ever develop for the RP, thereby revealing why Δg is not influential to spin-state mixing at low fields.

The plateau area in Figure 1.12 shows a reduction in the spin mixing processes in the geminate cage. This arises after the applied field exceeds the average hyperfine coupling in the pair and after the complete Zeeman separation of $T_{\pm}$ from the S and T_0 levels. During this period the contribution from Δg is usually insignificant and therefore negligible changes in the field effect are normally observed. Consequently, the escape recombination product peaks in this region.

At weaker fields still, in the range of approximately 3 to 10 mT is an area dominated by the HFM. Here, the escape yield gradually rises due to a reduction in the rate of T to S mixing. This stems from lower geminate recombination occurring in the solvent cage as the $T_{\pm}$ levels become increasingly separated in energy form the remaining two states, and thus defines the *normal* MFE.

Based on this theory alone it was originally anticipated that a comparatively low field would not interfere with the S-T interconversion beyond that of the aforementioned MFE. However, predictions to the contrary were made by Brocklehurst in 1976,[29] where an effect was proposed to occur *via* a mechanism opposite in phase to the conventional MFE. It has since been experimentally proven[17, 23, 24, 30-32] and arises at very low magnetic fields (< 3 mT), which are comparable in magnitude to the average hyperfine coupling between radicals in the pair. The manifestation of this type of field effect is labelled as the low field effect (LFE) and is identified accordingly in Figure 1.12.

Application of a weak field causes minor perturbations to a RP system and will,

I. Energetically separate the $T_{\pm}$ states from the S and T_0, *via* the Zeeman Effect. This decreases S-T mixing and gives rise to a normal MFE, which results in an increase in the escape product.

II. Alter the spin angular momentum rules to allow spin-state mixing between the S and all three triplet sub-states, as they all are no longer bound by the selection rules that exist in zero field conditions (refer to Section **1.4.4.1.3**). This reflects as a dip in the escape product as more geminate recombination occurs.

The generated effect, MFE or LFE, at these low fields therefore depends on the competition between the two processes in I and II. A continued increase in the field beyond that of the average hyperfine coupling alters the axis for rotation to become the external field, this dampens the mixing, due to the increased isolation of $T_{\pm}$ levels. A reduction in the recombination yield at the geminate stage is noted along with an increase in the number of f-pairs, in line with a conventional MFE.

While the earlier mentioned low field model describes this interaction, an accurate explanation for a LFE can only be achieved through explicit solutions to the Schrödinger wave equations. These equations calculate the energies of the individual states and from this describe the S-T mixing as oscillations in the quantum coherences of the zero field state, which are unlocked by the application of a weak field.

1.5.1 The Study of Magnetic Field Effects

The ability of large magnetic fields to develop a MFE in laboratory based reactions of RP intermediates, have been rigorously explored.[18, 27, 28] Regularly fields of between 10 mT and 10 T have been observed to be capable of altering the products ratios of many RP systems by more than 10 %, from those recorded in the absence of a field.[18, 23, 33] Far less focus has been directed to investigating the influence of much smaller fields, comparable or less than the average hyperfine coupling interactions (1-10 mT). Furthermore studies conducted on RPs in the geomagnetic field (~ 50 μT) are rare.[34]

Direct epidemiological studies in these low fields and magnetic field links with the onset of disease in humans are often explored.[35] No conclusive trends have yet been defined from biological studies alone; however, the influence of low fields on SCRPs created artificially *in vitro* may provide some insight. An example of the importance of laboratory based investigations is the implementation of the RPM in modelling the origins of avian navigation,[36] which was originally discovered through chemical investigations conducted at much higher field strengths.

Altered RP kinetics have been revealed from fields as low as ~ 0.1 mT, achievable through careful manipulation of the RP lifetimes involved.[28] A more recent publication

has even detailed the first direct effect of a ≤ 50 μT field and shed further light onto the mechanism by which species may navigate in response the earth's magnetic field.[34] Studies have also been conducted in all phases, although the solid and gas phases are less relevant to biological systems, since the spin dynamics in solution are entirely different. Therefore, numerous investigations have been dedicated to liquid phase experiments alone.[17, 18]

On occasions where the S-T mixing from the Larmor precessions is slow in comparison to the lifetimes of the species involved, no discernable field effect can be measured. Many investigations are therefore focused on extending the reaction times, of the RPs, by retarding the rate of recombination. Some of the experimental methods explored in detail include the use of ion-pairs[32] which are joined *via* their mutual coulombic attraction, and to a lesser extent the incorporation of viscous solvents,[37] and the study of biradical systems.[38] While all field effects can be maximised in a RP with a long lifetime, the generation of LFEs is particularly sensitive to this. The hyperfine driven spin-state mixing at low fields is slow and is optimised when $\tau^{-1} \ll a$, where τ is the lifetime of the RP and a is the average hyperfine coupling.[27] The field effects occurring at low fields ($<$ 35 mT) are particularly pertinent to this work; hence the subsequent section solely considers those studies that have observed a LFE.

1.5.1.1 The Low Field Effect

There are two mechanisms that may contribute to a LFE; the level crossing between S and T$_-$ states and the HFM. The latter is the more relevant spin-state mixing mechanism in the solution phase systems used here.

To facilitate sufficient spin-state evolution and in order to generate a large LFE, the RP's lifetime must be enhanced to a minimum of a few hundred nanoseconds. This effect is best demonstrated in situations where the radicals in pair are prevented in their escape from the cage, and has led much attention to the study of such pairs in micellar aggregates.[11, 18, 23, 24] Micelles are desirable for two reasons; primarily RP confinement, since a typical micelle can be manipulated to possess a size in the order of 2-3 nm, which allows the potential for repeated short term diffusion and reencounter.[28] Secondly, RPs in micelles are believed to loosely model the behaviour of biological systems, thus enabling realistic conditions to be re-created *in vitro*.

While multiple studies have been performed in micelles, few probe for a LFE in otherwise neutral radicals, examples are limited and given herein. Shkrob *et al*[24]

photolysed deoxybenzoin derivatives in SDS (Sodium Doceyl Sulphate) micellar solution. This generated a LFE for smaller radicals, which was absent in larger ones, the difference was attributed to the differing hyperfine couplings of the RPs. Tarasov *et al*,[30] similarly used deoxybenzoin, but varied the chains in the alkyl sulphate micelles to investigate their relation to the observed LFE. This revealed a shift in the position of the LFE with the surfactant used. Eveson *et al*[23] studied a range of alkyl sulphate and sulphonate micelles by encapsulating benzophenone. Here, the internal viscosity of the micelle was found to decrease with increasing size, an outcome often supported in both micelles and reverse micelles (see Chapter **5**). This in turn affected the RP dynamics in the micelle and the magnitude of the LFE, as did other parameters such as the temperature of the solution. More recently however, a LFE was demonstrated for (2,4,6-trimethylbenzoyl)diphenylphoshine oxide, MAPO (also commonly known as TMDPO), in detergent solutions of SDS and dodecyltrimethyammonium chloride (DTAC).[25] The LFE originated from the expected coherent spin-state mixing as with all of the aforementioned examples, combined with influences from spin relaxation. This study is particularity interesting owing to the generation of a broad LFE, which is a consequence of the larger average hyperfine coupling in the pair. For such a pair, considerable spin evolution can develop during the lifetime of the RP and over that occurring in the absence of the field. The MAPO precursor is an ideal candidate to probe the experimental conditions that influence the generation of a LFE, and for this reason it was also used in the current work, detailed in Chapter **4**.

Additionally, studies have focused on radical ion-pairs in solution, which by virtue of their electrostatic attraction cause the geminate RP to remain together for prolonged periods of time and can likewise lead to a significant LFE. An example study of this type, by Batchelor *et al*,[32] involved the standard system of pyrene (Py) and 1,3-dicyanobenzene (DCB) radical ions in solution, and was recorded *via* the fluorescence intensity of the cage recombination exciplex molecule. Radioluminescence techniques are also common and have been used to investigate the varying ion separations, in different species of hydrocarbon cations and hexafluorobenzene anions.[29]

Published work studying neutral RPs in viscous solutions is less common than the micelle and ion-pair examples given. Optically detected EPR and TRIR[39] spectroscopy are the few techniques to record a LFE for the neutral pairs effectively surrounded by a viscous solvent. The work of interest in this thesis includes modifying the environment around the neutral RPs in solution. This is achieved through using solvents of varying viscosity and encapsulating the RP in reverse micelles, to determine the effect on the

resulting LFE and MFE. The systems investigated are presented and discussed in Chapters **4** and **5**.

References

1 W. Gerlach and O. Stern, *Zeitschrift für Physik*, 1922, **9**, 353.
2 P. W. Atkins, *Physical Chemistry*, Sixth Edition, Oxford University Press, 1998.
3 G. E. Uhlenbeck and S. Goudsmit, *Naturwissenschaften*, 1925, **13** (47), 953.
4 T. E. Philips and J. B. Taylor, *Physical Review*, 1927, **29**, 309.
5 P. A. M. Dirac, *Proceedings of the Royal Society of London, Series A*, 1928, **117** (778), 610. & **118** (779), 351.
6 N. M. Atherton, *Principles of Electron Spin Resonance*, Ellis Harwood Ltd, 1993.
7 H. Hayashi, *Introduction to Dynamic Spin Chemistry, Magnetic Field Effects on Chemical and Biochemical Reactions*, World Scientific, 2004.
8 A. F. Parsons, *An Introduction to Free Radical Chemistry*, Blackwell Science, 2000.
9 M. Gomberg, *Journal of the American Chemical Society*, 1900, **22**, 757.
10 J. E. Wertz and J. R. Bolton, *Electron Paramagnetic Resonance, Elementary Theory and Practical Applications*, Chapman and Hall, 1994.
11 B. M. Brocklehurst and K. A. Mclauchlan, *International Journal of Radiation Biology*, 1996, **69**, 3.
12 M. Brustolon and E. Giamello, *Electron Paramagnetic Resonance: A Practitioners Toolkit*, John Wiley & Sons Ltd, 2009.
13 L. J. Berliner, S. S. Eaton and G. R. Eaton, *Biological Magnetic Resonance: Volume 19: Distance Measurements in Biological Systems by EPR*, Plenum Publishers, 2001.
14 M. C. R. Symons, *Chemical and Biochemical Aspects of Electron Spin Resonance Spectroscopy*, John Wiley and Sons, 1978.
15 W. Pauli, *Zeitschrift für Physik*, 1925, **31**, 765.
16 A. Carrington and A. D. Mclauchlan, *Introduction to Magnetic Resonance, with Applications to Chemistry and Chemical Physics*, Harper & Row, 1979.
17 C. R. Timmel and K. B. Henbest, *Royal Society of London Transactions Series A*, 2004, **362**, 2573, and references therein.
18 U. E. Steiner and T. Ulrich, *Chemical Review*, 1989, **89**, 51.
19 G. L. Closs, *Journal of the American Chemical Society*, 1969, **91**, 4552.
20 R. Kaptein and L. Oosterhoff, *Journal of Chemical Physics Letters*, 1969, **4**, 214.
21 J. R. Woodward, *Progress in Reaction Kinetic and Mechanism*, 2002, **27**, 165.
22 K. A. Mclauchlan and U. E. Steiner, *Molecular Physics*, 1991, **73** (2), 241.
23 R. W. Eveson, C. R. Timmel, B. Brocklehurst, P. J. Hore and K. A. Mclauchlan, *International Journal of Radiation Biology*, 2000, **76** (11), 1509.
24 I. A. Shkrob, V. F. Tarasov and A. L. Buchachenko, *Chemical Physics*, 1991, **153**, 443.
25 K. Maeda, T. Suzuki and T. Arai, *RIKEN Review*, 2002, **44**, 85.
26 U. Werner, W. Kühnle and H. Staerk, *Journal of Physical Chemistry*, 1993, **97**, 9280.
27 C. R. Timmel, U. Till, B. Brocklehurst, K. A. Mclauchlan and P. J. Hore, *Molecular Physics*, 1998, **95** (1), 71.
28 B. Brocklehurst, *Chemical Society Reviews*, 2002, **31**, 301, and references therein.
29 B. Brocklehurst, *Journal of the Chemical Society, Faraday Transactions*, 1976, **72**, 1869.
30 V. F. Tarasov, N. D. Ghatlia, N. I. Avdievich and N. J. Turro, *Zeitschrift für Physikalische Chemie*, 1993, **182**, 227.

31 D. V. Stass, N. N. Lukzen, B. M. Tadjikov and Y. N. Molin, *Chemical Physics Letters*, 1995, **233** (4), 444.
32 S. N. Batchelor, C. W. M. Kay, K. A. McLauchlan and I. A. Shkrob, *Journal of Physical Chemistry*, 1993, **97**, 13250.
33 K. M. Salikhov, Y. N. Molin, R. Z. Sagdeev and A. L. Buchachenko, Elsevier, Amsterdam, 1984.
34 K. Maeda, K. B. Henbest, F. Cintolesi, I. Kuprov, C. T. Rodgers, P. A. Liddell, D. Gust, C. R. Timmel and P. J. Hore, *Nature*, 2008, **453**, 387.
35 A. Lacy-Hulbert, J. C. Metcalfe and R. Hesketh, 1998, **12**, 395, and references therein.
36 T. Ritz, S. Adem and K. Schulten, *Biophysical Journal*, 2000, **78** (2), 707.
37 T. Sengupta, S. Aich and S. Basu, *Journal of Physical Chemistry B*, 1999, **103**, 3784.
38 U. Werner, W. Kuehnle and H. Staerk, *Journal of Physical Chemistry*, 1993, **97** (37), 9280.
39 J. R. Woodward and C. B. Vink, *Physical Chemistry Chemical Physics*, 2007, **9**, 6272.

2. Experimental Techniques and Development

Overview

The first section of this chapter details the practical method by which continuous wave EPR spectroscopy is able to probe paramagnetic systems. For this instrument the limits in detection determine which species may be monitored, i.e. those with relaxation times and lifetimes longer than the order of a hundred microseconds. This technique relies on a permanent concentration of radicals in the cavity and is therefore applicable to a variety of radicals, including those generated on exposure to radiation, stable radicals, spin traps, spin labels, as well as transition metal complexes. CW EPR is widely applied to observe paramagnetic centres in metalloenzymes and proteins, where following their reactions can provide direct insights to the biochemical and biophysical processes occurring.[1, 2] To allow measurement of these systems, low temperatures equalling those of liquid helium or nitrogen have become standard in slowing the progression of competitive relaxation.[2] Temperatures of 77 K are likewise used here, for the studies on metalloproteins transferrin and lactoferrin. The focus in this work is on using CW EPR to observe the binding of high spin ($S = \frac{5}{2}$) iron at the two active sites in both the proteins. The data for this is included and discussed later in Chapter **3**.

In addition to CW EPR, an experimental arrangement for monitoring radicals in solution that typically decay on a timescale more rapid than microseconds is detailed. The requirements of this technique include an improved instrument time resolution, which extends the measurement ability of the existing instrument to a nanosecond time domain by altering the mode of detection. This is achieved by using a pulsed laser as the master trigger. The laser controls radical generation at a defined pulsing rate, and the response in the cavity as a consequence of the radicals prompts recording *via* a transient recorder. The samples of interest are all solution phase, this means that there are negligible anisotropic coupling contributions. Consequently, the EPR signals from the radicals are centred at approximately 333 mT, which corresponds to the free electron g-value for an X-band (typically 9.5 GHz) spectrometer. This represents a very different scenario to that for the solid samples mentioned earlier. The technique is now restricted by the response of microwave cavity and is therefore a reflection on the design of the machine and not the field scanning rate as encountered with CW EPR methods.

All the magnetic field studies were performed on a time resolved IR (TRIR) spectrometer that monitors RP kinetics. This instrument is capable of accessing the sub-

microsecond time domain. However, to generate a significant LFE and monitor f-pair recombination kinetics, the RP must inhabit an environment that extends its lifetime from hundreds of nanoseconds to microseconds (refer to Section **1.5.1.1**). In this instrument, the IR probe laser has a tunability of around 100 cm^{-1}, centred close to 1800 cm^{-1}, which corresponds to the carbonyl absorption of benzoyl radicals and thus confines the study of RPs to specific carbonyl compounds. The evolution of this setup is described, as well as the introduction of a step scan time resolved IR method to allow magnetic field studies to be conducted over a wider range of IR wavelengths. Finally the advantage of *ab initio* and semi-empirical methods, as complimentary to experimental data, is discussed. This is in addition to a brief background and an account of the procedures used to estimate hyperfine coupling constants (hfccs) for the data included in Chapter **4**.

2.1 Electron Paramagnetic Resonance Spectrometers

This section describes the continuous wave and time resolved EPR methods for acquiring data exemplified by the two different X-band EPR spectrometers used in this work; a JEOL RE-1X EPR spectrometer, controlled by National Instruments LabVIEW[3] software on a windows based PC and a Bruker ELEXSYS E500 CW EPR spectrometer controlled by Xepr software on a UNIX system. The latter was also used in conjunction with a custom built low temperature attachment manufactured by Oxford Instruments, ER 4112HV, which was inserted in the cavity and capable of maintaining a stable temperature of 10 K.

2.1.1 Principles of Continuous Wave EPR Spectroscopy

The elements of a conventional CW EPR spectrometer are illustrated in Figure 2.1.[4] In this instrument a stable supply of microwave radiation is generated by a klystron and reflected off the internal walls of rectangular hollow pipes called waveguides. The amount of microwaves travelling through the spectrometer may be regulated by an attenuator to avoid instances of saturation. As the microwaves are directed through the circulator, *via* waveguides, the radiation meets an opening in the cavity called the iris, its dimensions are such that the microwaves resonate in the cavity to produce a standing wave. This resonance condition confines the dimensions of the cavity to match the wavelength of microwave radiation employed.

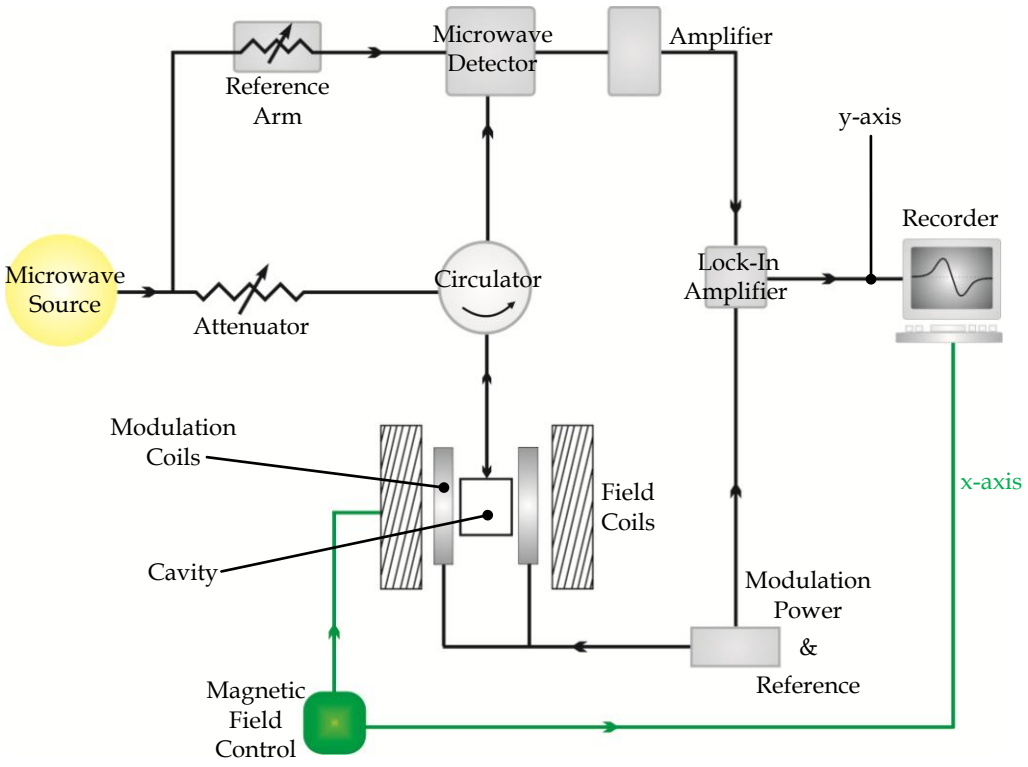

Figure 2.1 The basic components of a CW EPR spectrometer. This setup generates a spectrum by sweeping the magnetic field at a constant mw frequency, and applying a modulation method for detection, to increase the sensitivity. The reference arm insures the mw detector operates within the linear range by supplying additional mw power (bias) that travels through a separate attenuator to adjust its intensity.

In this setup, any back reflection of the microwaves is minimised and they remain in the cavity before eventually dissipating as heat energy through continual contact with the walls. Deliberately, the circulator prevents direct access of the microwaves from the source to the detector, and only back reflected radiation is permitted access through, giving the desired spectrum.

During tuning, an adjustable screw adjacent to the iris allows fine power (amplitude) control of the radiation in and out of the cavity to compensate for any loss that occurs as a result of the sample (in the cavity), thereby providing optimum coupling and sensitivity. The standing wave also serves to increase the pathlength of the radiation through the sample, thus amplifying the signal (see Section **2.1.3** for discussion of the Q factor).

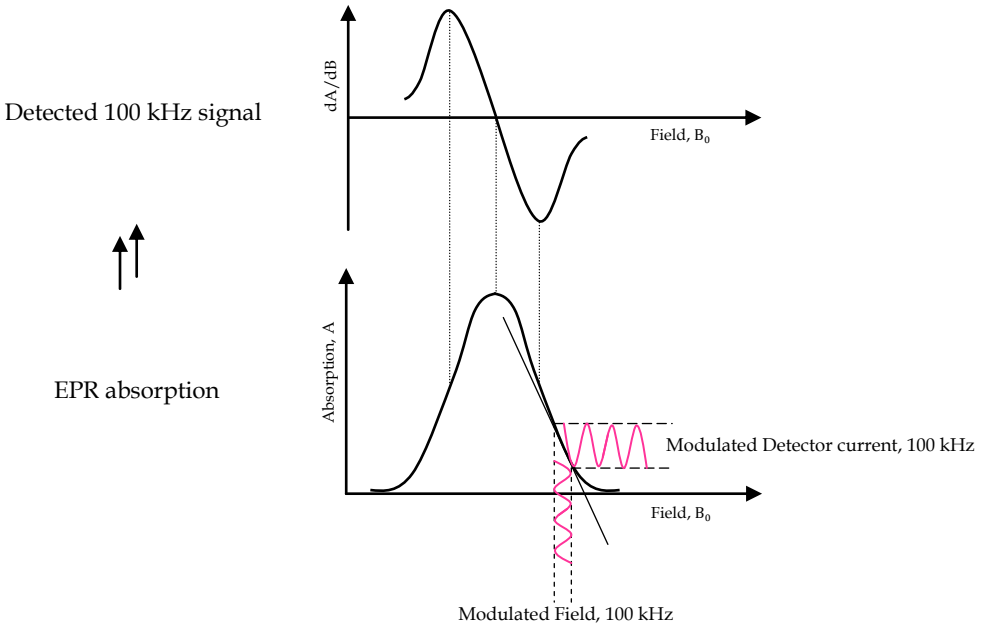

Figure 2.2 An illustration of the effect of an applied 100 kHz modulation field on the crystal detector output current (below), and the corresponding first derivative spectrum from processing the modulated detector current.[5]

The cavity is located between a set of modulation coils and the poles of an electromagnet to apply the variable field to the sample. Once the standing wave is established and the cavity tuned, the magnetic field is swept through the various resonances in the sample. At a magnetic field point where the resonance condition is met the energy of mw radiation equals the energy level separation of the electron states, so triggers absorption of the microwaves by the sample leading to transitions. An alteration in the standing waves as a consequence of absorption leaves the cavity and microwaves uncoupled, and these waves are reflected *via* the circulator to the detector. This radiation corresponds to the EPR signal. For the duration of a scan it is important for the klystron output to remain coupled to the resonating frequency of the cavity. Therefore to avoid drift in the frequency, due to power loss on absorption of the mw energy, an automatic frequency control (AFC) is used. This keeps the source frequency locked to the centre frequency of the resonator, and is achieved using an electronic feedback loop.

A microwave detector crystal converts this radiation into a direct current (DC) signal, though for increased sensitivity a modification to the outlined data collection process is normally used; phase sensitive detection. To the additional modulation coils mounted outside the cavity a small alternating current is applied at a fixed modulation

frequency (see Figure 2.2). This superimposes an oscillating component on the magnetic field applied by the electromagnet during a sweep.

The modulation frequency controls the current applied to the small coils and has a typical value of 100 kHz for most commercial spectrometers.[5] Therefore at any point on the absorption curve, the EPR signal will feature an associated oscillating component whose amplitude will be proportional to the slope of the absorption line (see Figure 2.2). This oscillating component is amplified to give the final EPR signal. The use of a lock-in amplifier can enhance the sensitivity further by monitoring the signal at the detector crystal for alterations solely at this frequency. This filters noise outside this 100 kHz ± 1 Hz range, principally removing the lower frequencies associated with electrical interference.

The phase of the new signal relative to the original modulation signal determines whether the EPR absorption has a positive or negative slope. The result of this mode of data collection is the generation of a first derivative trace of the absorption spectrum, similar to that shown in Figure 2.2.

Phase sensitive detection is particularly useful for;

- Broad line spectra, to reveal details otherwise masked during conventional absorption detection.
- An enhanced sensitivity as already discussed.
- Eliminating baseline instabilities.

While it has many benefits, its parameters must be chosen wisely as the following can distort spectral lineshapes;

- A modulation frequency larger than the linewidth of the EPR signal will cause the signal to broaden (since the signal $\propto$ the slope only when the linewidth $\gg$ modulation frequency)
- A modulation amplitude of greater than the hyperfine couplings will conceal their splitting.

2.1.2 Data Collection Using the Continuous Wave EPR Spectrometer(s)

The collection of data using both spectrometers proceeds as illustrated in Figure 2.1. The sample, contained in a quartz finger dewar or EPR cell (refer to Section **2.3.1** for the specifics) is placed in the cavity and the cavity is then tuned to critically couple to the mw source. The two sets of software, custom written LabVIEW or Xepr, allow the

parameters (Section **2.3.1**) for the scan to be controlled and the latter also enables the spectrometer to be tuned using only the software. The desired field width is swept at a rate defined by the software. The signal from the cavity per field point is sent to the detector to be amplified, and passed to the PC *via* a lock-in amplifier. The software displays this signal as an intensity vs. magnetic field trace, revealing the EPR signal for the entire field sweep, as already discussed.

The internal components in both the CW JEOL and Bruker spectrometers are analogous to those given in Figure 2.1, however additional apparatus were required for the Bruker spectrometer to facilitate the low temperature work. The external components of the Bruker spectrometer are pictured in Figure 2.3. The apparatus common to both CW spectrometers are indicated in black and these include the cavity, the iris (screw), the microwave head and bridge, the electromagnets, the magnetic field control and the console. The function of these has already been covered. Any additional apparatus required solely for the Bruker spectrometer are labelled in red. Specifically these consist of the rotary and turbo pumps, which create a vacuum in the cavity to maintain a steady liquid helium temperature (4 K). A transfer line that is connected to a helium dewar, through this, the liquid helium travels to the cavity; both of these latter features are not pictured to allow a full view of the spectrometer.

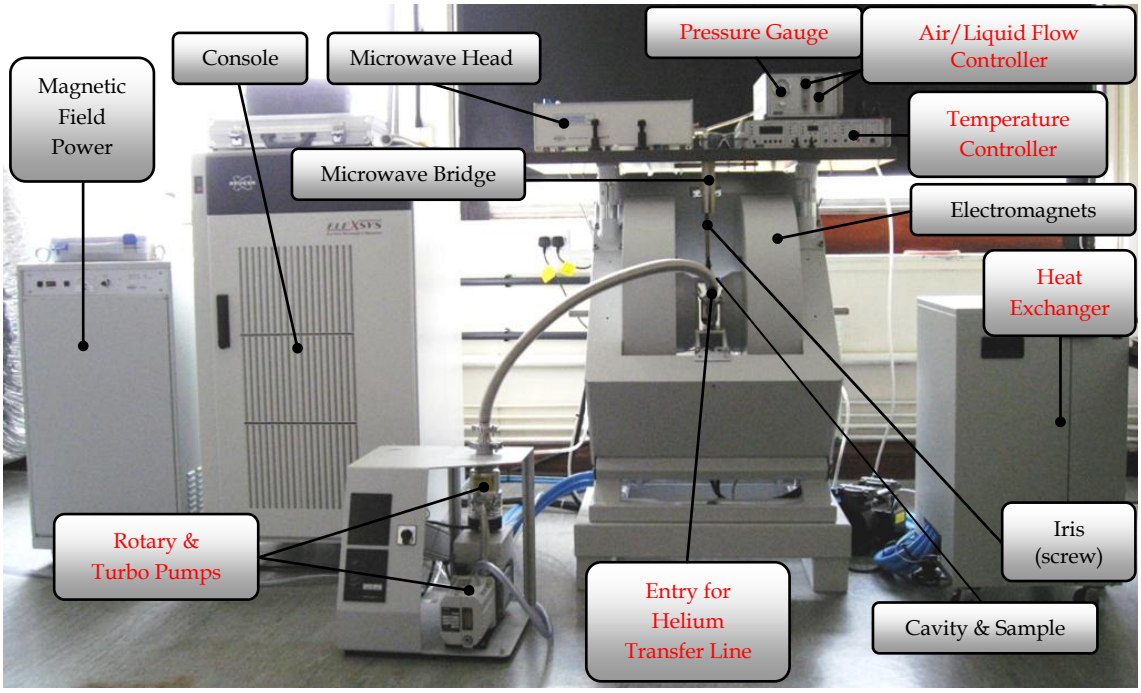

Figure 2.3 The components of the Bruker EPR spectrometer. A few additional pieces of apparatus, compared to the JEOL, are required for low temperature measurements. A transfer line connected to both the helium vessel and the spectrometer would normally be attached at the entry point as labelled.

A temperature control unit which is used in conjunction with a needle valve located on the transfer line to regulate the temperature of the cavity. The desired temperature is set on the control unit that triggers a heating coil when the cavity is overly cool, though the need for this can be eliminated by an appropriately set needle valve. As well as these, there is a pressure gauge to monitor the flow of helium, a heat exchanger, and a water cooler (not shown) for the electromagnets.

2.1.3 Comparison of the Continuous Wave EPR Spectrometers

An obvious variation between the two instruments lies in their respective cavities and consequent quality factors, Q. The sensitivity of a given cavity can be defined by its Q. This is a measure of the how efficiently it stores energy. It therefore depends on factors such as the material of the inner surfaces and extensions of the cavity wall, since both of these can prevent microwave loss. A higher Q value implies a more sensitive cavity. The value can be measured from the resonance signal of the cavity, since $Q = \frac{\nu_{res}}{\Delta\nu}$, where ν_{res} is the resonance frequency, and $\Delta\nu$, the bandwidth. For a fixed frequency the volume of the cavity will also govern the number of modes present, a larger volume allows more modes, and thus increases the Q.[4, 5]

The Bruker instrument features a Super-High-Q ER 4122SHQE cavity with a Q of 8300 when loaded (no sample), and the JEOL spectrometer contains a TE011 cavity with a lower Q of approximately 2000. The Bruker cavity is rectangular, while the JEOL is cylindrical in shape. The maximum sample diameter that can be placed in the JEOL is approximately 11.5 mm, compared with 10.5 mm for the Bruker, and since the sample heights are similar the volume of sample contained in the JEOL cavity is larger. Clearly the Bruker spectrometer has a superior Q factor. This high Q cavity enabled the low iron content in the transferrin of blood serum to be detected, while the signal was absent when recorded on the JEOL spectrometer, thus indicating its additional sensitivity. The results for the transferrin data are included in Chapter **3**.

For CW methods a high Q is preferred for greater sensitivity. However, due to the increased bandwidth, higher Q cavities often create additional issues with *ringing* in signals recorded using pulsed techniques or transient responses. This limits the detection time. Therefore, Q factors of 1000 or lower are advantageous for TREPR techniques to allow responses of tens of nanoseconds to be recorded, though this additionally depends on the operating frequency and the response of the transient instrumentation.[6]

2.1.4 Principles of Time Resolved EPR Spectroscopy and the Modification of the JEOL RE-1X EPR Spectrometer

This method of recording is used to reveal kinetic information on radical species as a function of time, by decoupling the transient event from the magnetic field sweep. The radicals typically decay on a nanosecond to microsecond timescale and are continuously regenerated by an external radiation source, most commonly a pulsed laser.

A Nd:YAG laser is suited to time resolved spectroscopy, primarily due to its pulsed output, providing both a stable and reproducible amount of monochromatic radiation. It can also be used as the master trigger and features a low internal jitter between the firing of the flashlamp and Q-switch. Additionally, the removable harmonic generators enable an easy exchange between wavelengths. While four output wavelengths are accessible, 1064, 532, 355, 266 nm, by using the fundamental, 2^{nd} 3^{rd} and 4^{th} harmonics, most organic chromophores only absorb at the latter two. Another useful feature of this type of laser is the ability to delay the Q-switch, which allows alteration of the peak power without any change in the flashlamp intensity.

The faster detection requirements for the time resolved EPR data collection deem the modulation speed of 100 kHz unsuitable, as this equates to a spectrometer response of only 10 μs. Therefore a more direct mode of detection is normally provided by a low noise detector crystal and the modulation function of the spectrometer is disabled. Furthermore to access a sub-microsecond time resolution the receiver bandwidth must be increased to capture the transient signals. A CW spectrometer will have a narrow receiver bandwidth of approximately 10-100 kHz, which for time resolved studies should be extended to cover 10-200 MHz.[6, 7]

By disabling the modulation, the sensitivity of the technique is compromised resulting in a decrease in the signal to noise ratio (S/N), however this is normally compensated for by use of the sampling method. The sampling method strictly records the output using the transient recorder post laser flash for a defined period to produce a decay curve; these times typically range between 100 ns and several microseconds. Recording over a small time window such as this, improves the scan quality by enabling the temporal separation of the signal from any associated noise. This signal is subsequently stored and integrated by a boxcar averager, which feeds the resulting data to a chart that additionally receives the associated field change. This allows construction of the entire spectrum directly. An alternative to the boxcar, is to record the response as an output voltage on digital oscilloscope, and this is the method used in this work.

2.1.4.1 Data Collection Using the JEOL RE-1X TREPR Spectrometer

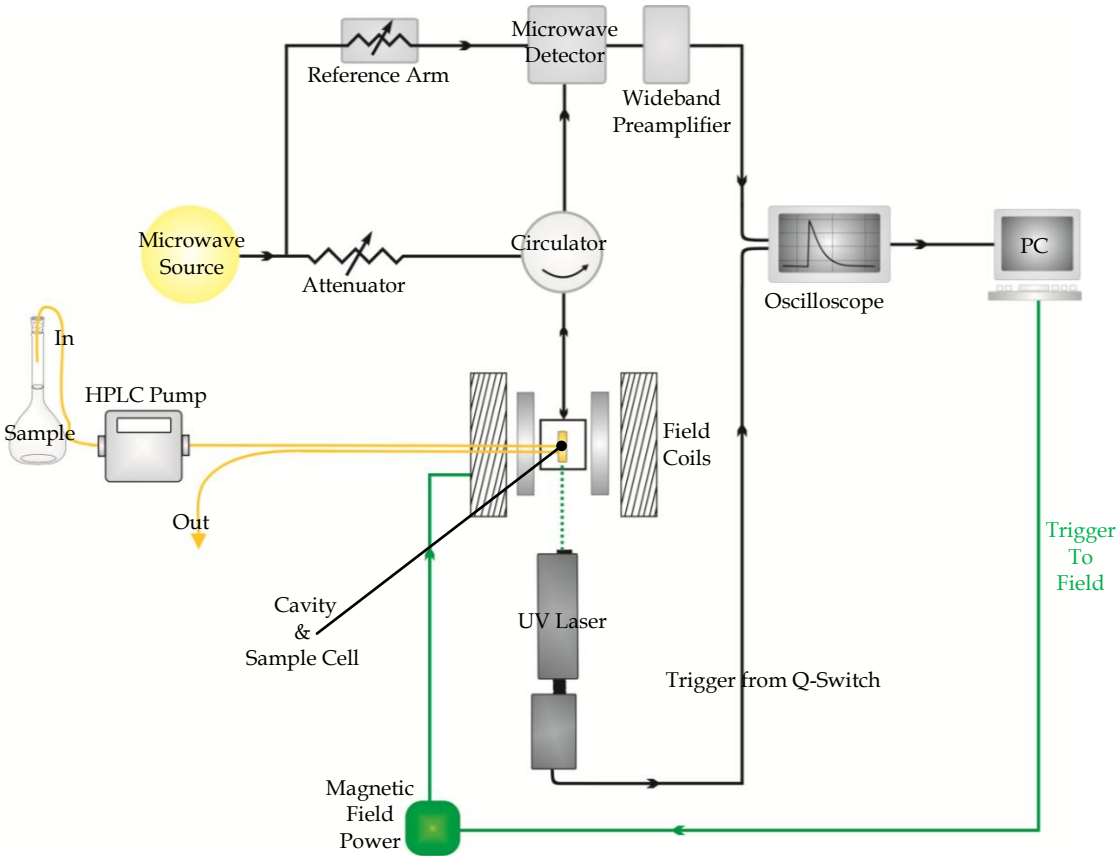

Figure 2.4 The components of the JEOL RE-1X ESR spectrometer used for the time resolved recording of EPR spectra. Modifications from the CW method include triggering radical production using a pulsed laser (15 Hz), measuring using a transient amplifier and disabling the modulation coils; refer to Figure 2.1 for comparison.

The collection of a TREPR spectrum proceeds as illustrated in Figure 2.4. The master trigger for the experiment originates from the Q-switch of the Surelite Continuum I Nd:YAG laser. The RPs are continuously re-generated by the 266 nm (Ultraviolet, UV) laser pulse, at a rate of 15 Hz. A Shimadzu LC-6A Liquid Chromatograph pumps the precursor solution through a flat quartz flow cell (to minimise dielectric loss) situated in the TE011 cavity, at a rate to ensure that fresh solution is photolysed with each consecutive flash of the laser (typically between 1-2.0 ml min^{-1}). In response to the laser flash and radical generation, the cavity sends a signal to the microwave detector. This signal is captured and passed on by the wide band preamplifier (model JEOL ES-WBPA2), to the 100 MHz, 1 GS/s Tektronix TDS220 Two Channel Digital Real Time

Oscilloscope set with a vertical range of 2 V. At this point the signal is sampled and sent to the windows PC.

The oscilloscope is triggered along with the laser flash. The oscilloscope averages 16 laser shots and then transfers the data in real time to a windows PC using custom written LabVIEW[3] software, where integration of the signal can later be performed. The signal at any one field point is recorded the predefined number of times, before continuing to the next field point where the process is repeated. This proceeds until the chosen magnetic field sweep width has been covered. The resulting data are stored as intensity vs. time sets by the LabVIEW control software and there are two basic modes for analysing the data.

Mode 1 displays the original signal from the cavity at each field point specified, and reveals the lifetime of any radicals generated by the laser, while providing a baseline correction when in the absence of any radicals (see Figure 2.5). An off resonance subtraction is necessary to get an accurate mode 1 decay signal, and this is performed prior to analysing the data, again, using LabVIEW. These data for each field point may be compiled into a 3D plot to map the entire time-history of the radicals in the sample, showing both the time and magnetic field dependence. Mode 2, essentially traditional EPR spectra, are intensity vs. magnetic field traces and are extracted by integrating mode 1 data over selected time windows. Unlike in CW EPR spectra, these are direct observations of the signal from the cavity, so the concentration of the radicals is proportional to the integration of the decay curve (relaxation may also contribute).

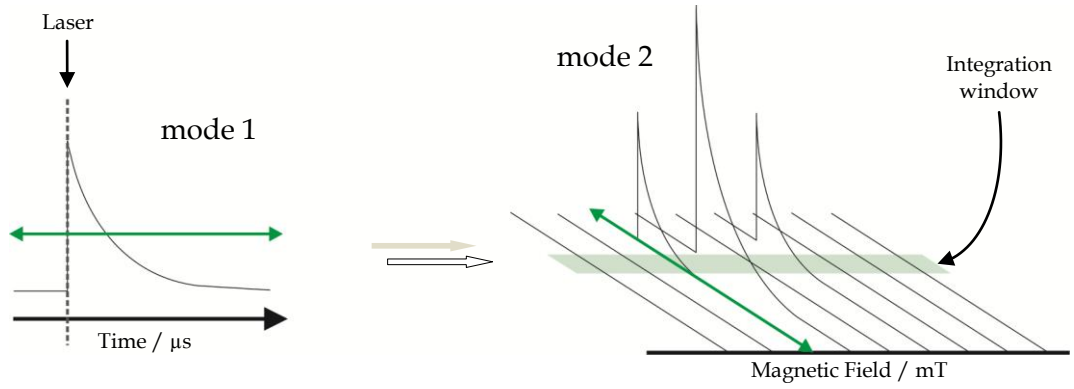

Figure 2.5 Modes for analysing the TREPR data. Mode 1 is the decay curve obtained for a single field point and shows the decay of the cavity response with time. Composite mode 1 spectra for each field point of the magnetic sweep show the data in 3D, mode 2. Mode 2 spectra can be extracted from specified time windows as highlighted by the shaded integration region.

2.1.4.2 Chemically Induced Dynamic Electron Polarisation

TREPR spectra often reveal enhanced emission or absorption lines, which are indicative of a non-Boltzmann distribution of electron spins among the accessible spin-states. This phenomenon is referred to as *Chemically Induced Dynamic Electron Polarisation* (CIDEP).[4] It arises either during the generation of the paramagnetic species, through the conservation of spin angular momentum of its precursor, or *via* the subsequent encounters of the radicals. Two main types of mechanism can be identified from the spectra. First is the RPM, where a combination of emissive (E) and absorptive (A) peaks appear simultaneously, and second is the triplet mechanism (TM), where either enhanced emission or absorption with the usual statistical pattern is observed.

The RPM occurs from the incidence of both triplet and singlet correlated spins among the RPs and develops through coherent spin-state mixing, *via* the HFM or Δg mechanism, as detailed in Section **1.4.4**. This generates a hyperfine dependent polarisation. The TM involves the selective population of triplet sub-levels that are available to a molecule during intersystem crossing from a singlet excited state (Figure 4.2). This occurs before the creation of the RP and therefore manifests in the spectrum as complete electron spin polarisation. The enhanced intensities of the CIDEP lines partially compensates for the loss in sensitivity from disabling the phase sensitive detection.

An EPR spectrum, from both CW and TREPR methods, should allow the accurate determination of g-values as well as hyperfine structure, by way of well separated sharp peaks. This, in addition to the ability to resolve electron spins from low radical concentrations (~ 0.1 μM), makes EPR the most popular technique for the study of paramagnetic species.[1, 8] Nevertheless, the method has limitations and is, for example, relatively insensitive when compared to other forms of spectroscopy. This is since the signal derives from the energy difference between the electron spin-states and furthermore it cannot be applied to study the effects of low magnetic fields on the reaction kinetics of RPs.

2.2 Time Resolved Infrared Spectroscopy Instruments

The focus of the current work resides in a section of the mid infrared (mid-IR) region, which spans 400-4000 cm^{-1}. This area has benefited from continued development in the fast time resolution of its instruments since the 1980s, and is widely applied to study transient species in chemical systems.[9] However, TRIR spectrometers of the type used here, and described in Section **2.2.1** are not commercially available and are therefore built in house with construction primarily requiring a stable source of IR. The most common of sources of IR are continuous wave CO lasers, operating in the region of 2200-1600 cm^{-1}. These are mainly used to probe organometallic compounds, by detecting intermediates *via* their characteristic ν_{C-O} stretches.[10] Alternatively, as is the case in this work, tuneable IR diode lasers may be used. These require cryogenic temperatures and can be tuned over a maximum range of approximately 100 cm^{-1} using a combination of temperature and electrical current controls. As a consequence of the multimodes present, incorporation of a monochromator with the IR diode lasers has become routine, though it is often unnecessary when the additional modes are non-resonant with any sample absorptions. This was the condition when studying transient free radicals here, thus the monochromator was omitted with a concomitant increase in the S/N ratio.

The design of the TRIR spectrometer is based on a previous study by Neville *et al*,[11] and permits the direct observation of transient radical kinetics *via* the distinct benzoyl stretching mode of one of the radicals in the pair. The absorbing chromophore is monitored on a microsecond timescale for the duration of its *in situ* generation and decay, where for the majority of this work, only very low radical concentrations were probed. While the scope of some IR laser based instruments has extended to detecting intermediates beyond the picosecond time resolution,[9] the spin effects of interest, specifically for the low applied fields, manifest on slower nanosecond timescales. Therefore this increased resolution would offer no advantage in the current work. The microsecond to nanosecond range would prove most beneficial in deciphering the difference between f-pair and g-pair recombination kinetics, whereas now the g-pair (approximately 100 ns) is most likely too rapid to detect in homogeneous isotropic solutions.

On radical generation, the current setup measures a small decrease in the overall absorbance of IR at the detector. This signal is rapidly reduced at a rate corresponding to the disappearance of the free radicals and the initial IR absorbance is recovered when

the reaction is complete. With the application of a magnetic field, the effect of the field can be determined from the difference between the two curves, produced from field on and off. Such effects, however, are normally very weak (1 % LFE, 3% MFE), and achieving sufficient S/N ratios can be challenging and involves extensive averaging. A novel single wavelength approach to data collection by modifying the design to incorporate an interferometer could, in principle, enhance spectral sensitivity. By removing the large IR background signal reaching the detector, noise can be substantially reduced, and the small difference in signal, due to the radical absorbance, measured more sensitively.

There are a number of limitations with the current TRIR instrument. As mentioned, the IR probe beam confines the species that can be studied, to those containing a distinct $\nu_{C=O}$ absorption. It is also a single wavelength technique. Consequently, it can only provide insight into the reaction/recombination of the carbonyl containing moiety. It is therefore suited to studying species with known photochemistry, and if alternative mechanisms do occur, it may identify their existence. However, complimentary techniques are required to reveal the underlying processes occurring. Problems can also arise from the multimodes of the IR diode laser when identifying the wavelength of small spectral shifts. While this can be reduced with a monochromator, the variation in the wavenumber of the absorbance can still be 0.5 cm^{-1}, which accordingly defines the maximum wavenumber resolution of this instrument.

Step scan time resolved FTIR spectroscopy (S^2TRS) appears to be a logical advancement of the laser based TRIR system for studying a variety of RPs. This broad recording technique features an increased spectral bandwidth covering the entire mid-IR region. This method would allow multiple different stretching modes to be monitored simultaneously, and can expand on the magnetic field studies of the $\nu_{C=O}$ radicals alone (Section **2.24** for FTIR spectroscopy). This would enable more complex systems to be investigated, for example, it could be applied to probe the photochemistry occurring in proteins or biological species. Interferometric methods for spectral encoding (as described in Section **2.2.2**) also make it superior to most laser based techniques, in determining exact wavelengths. Step scan FTIR spectrometers come self-contained, and are isolated from external vibrations, as well as temperature fluctuations, which should result in fewer baseline instabilities. Atmospheric water absorption may also be eliminated in the instrument, since it incorporates a purge system, whereas in the current TRIR design the presence of water is unavoidable. Additionally, the automatic optimisation and alignment of the signal in the FTIR would improve its accuracy.

Moreover, the two techniques could be complimentary and the step scan instrument would prove useful in isolating the wavelength of active carbonyl stretches in RPs, for use with the TRIR spectrometer.

As with all recording methods, there are still limitations with S^2TRS, most notably in the intensity of the globar source, which can affect the sensitivity of detection. Also the setup of each instrument requires personalising to suit the transient event of interest, and can often be quite challenging.

All three of the spectrometer arrangements are discussed in this section, beginning with the original time resolved infrared system.

2.2.1 Time Resolved Infrared Spectrometer

It is important when using this spectrometer, to eliminate any species that may interfere with the g- or f-pair recombination in the RP, since this would obscure the recorded kinetics. This is achieved by using unreactive solvents and precursors that do not undergo multiple-cleavages at the selected irradiation wavelength. The precursor molecules chosen specifically for this reason, along with their photochemistry, are discussed in Chapter **4**. This next section outlines the components of the TRIR spectrometer, and the procedure for data acquisition.

2.2.1.1 Data Collection Using the TRIR Spectrometer

Figure 2.6 is a schematic diagram of the TRIR spectrometer. The components of the spectrometer are mounted on a Melles Griot laser table to dampen the effects of local vibrations. Central to the build is the cell, which is similar in design to the steel based Specac Omni cell.[12] The ferromagnetic nature of steel makes the original cell unsuitable for use here. Consequently the cell outer was assembled from non-magnetic materials, specifically Delrin. The cell features minor modifications, such as screw-in entrance and exit holes, and a thick back section to compensate for a reduction in strength of the material. 0.1 mm Teflon spacers that enable the pathlength of the solution to be adjusted (minimum spacer, 0.05 mm) are encased between the calcium fluoride (CaF_2) windows of the cell. These windows transmit both IR and UV radiation. A solution of the precursor material in an isotropic solvent is continuously flowed through this cell, with rate of flow regulated by a gear pump (ISMATEC, Digital REGLO-Z). The rate is typically set to 2.0 ml min^{-1} and corresponds to the optimum value.

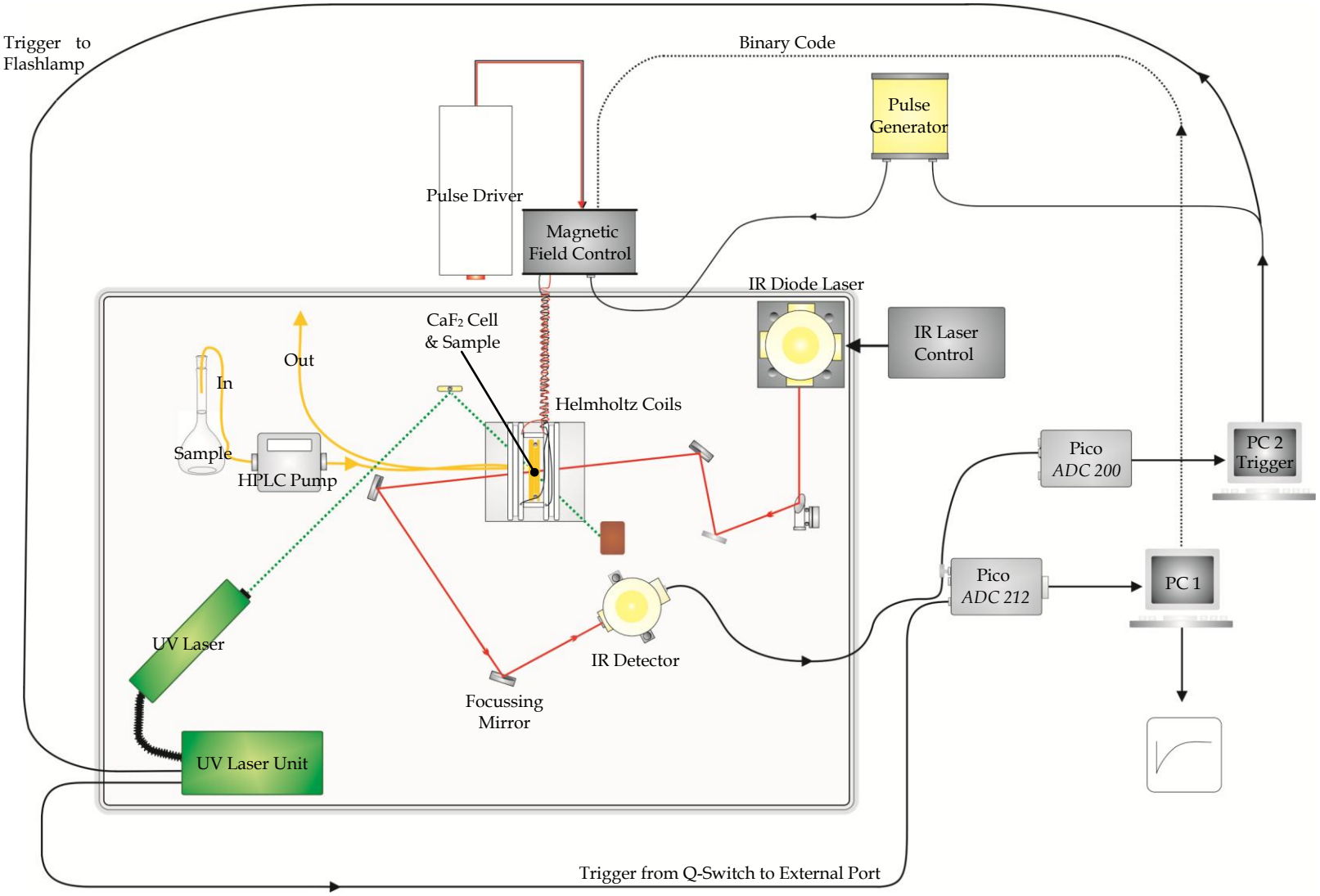

Figure 2.6 A schematic diagram of the TRIR spectrometer setup.

A lead salt diode laser (Laser Components model-L5736-11), as mentioned, provides a continuous source of IR in the range 1780-1880 cm^{-1} through the CaF_2 cell. This probe beam is initially directed *via* a parabolic mirror and is subsequently met by a flat then focussing mirror, with a focal point of approximately 3 mm aimed at the centre of the cell. Following passage through the solution filled cell, this IR beam is optically directed again by successive focussing mirrors into the mercury cadmium telluride (MCT) detector. At this stage the signal is amplified by a 20 MHz low-noise preamplifier and sampled using a 12-bit digitiser (Picoscope ADC-212). This generates a signal which is viewable as a 2D dataset of voltage vs. time, using a custom built LabVIEW[3] program running on PC 1 (see Figure 2.6). On a given millisecond timescale, the output from the IR laser fluctuates, generating peaks and troughs in its intensity. Therefore a second oscilloscope (Picoscope ADC-200) is necessary to solely monitor this output, and act as the master trigger to initiate scans, only at these intermittent periods of peak, stable, IR.

The 4^{th} harmonic of a Nd:YAG Continuum Minilite series II (approximately 1.8 mJ, 266 nm) laser is fired at the cell in pulses (15 Hz). The UV strikes the sample cell in a direction approximately collinear to the IR beam and on crossing these two beams must overlap perfectly to ensure optimum recording conditions. This UV radiation causes photocleavage of the precursor molecule to yield a RP. The IR laser is accordingly tweaked to match the frequency of the $\nu_{C=O}$ absorption in the benzoyl radical of the pair. Once the UV beam passes through the solution, it is prevented from travelling further by a beam dump placed behind the cell and at numerous other positions to prevent interference from reflections. As with the aforementioned Surelite Continuum I laser, the wavelength of the UV beam can be adjusted to the 3^{rd} or 4^{th} harmonic, generating 355 & 266 nm respectively. The chosen wavelength depends on the UV-vis absorption profile of the precursor molecule being studied. The laser power can also be adjusted by altering the Q-switch timing, although this was not necessary as the maximum output power was always used.

The sample is located at the centre of a pair of Helmholtz coils, through which the current flows in the same direction, to produce a resultant field. These coils are responsible for supplying a uniform, homogeneous, pulsed field and the Helmholtz relationship confines their distance apart to be identical to their radius. The amount of current flowing is altered incrementally through binary controls by the LabVIEW program, to allow field effects to be recorded at any field strength less than the

maximum field. The magnitude at any one point may be described by the following equation,

$$B = \frac{8\mu_0 NI}{5^{3/2} r} \quad [2.1]$$

where, B is the Magnetic Flux density in Tesla, and μ_0 the Permeability of free space. The variables are the number of turns per coil (N), the coil current in amperes (I), and the radius of the coil in meters (r), though for a given set of coils only the current may be altered. The coils used have N = 186, and r = 0.043, which corresponds to a field of 31.6 mT for the incremental increase required. The coils are situated on a Mumetal base to prevent the magnetic field from interacting with the other instruments present. In addition to the applied field, all the investigations were conducted in the presence of the earth's own magnetic field.

The pulsed magnetic field is controlled through a pulse generator (Thurlby Thandar Instruments TGP110), which is initially triggered simultaneously with the flashlamp of the UV laser, and both are managed *via* PC 2. The standard delay in the Q-switch firing, in combination with an intentional delay on the pulse generator, causes the pulse of the field to activate on alternate laser shots. This ensures that the maximum field coincides with the flashing of the laser and holds (~ 2 ms) for the duration of the recorded signal. The field off and field on kinetic decays are recorded consecutively, typically with 2000 averages performed per field point to reduce the noise level.

In this work, the results are displayed in two forms. The first is a kinetic trace, which reveals the RP lifetime and is the direct voltage response with time. All the traces of this type are shown for a zero magnetic field. The second form is the MAgnetic effect on Reaction Yield (MARY) mode, which gives a % MFE, and is determined from the relationship in Equation [2.2] for each field point in the scan. This is plotted as the % MFE vs. magnetic field point and typically covers the range 0-31.6 mT.

$$\%\,\mathrm{MFE} = \frac{\int \text{field on} - \int \text{field off}}{\int \text{field off}} \times 100 \quad [2.2]$$

The occurrence of further oscillations in the temporal output of the IR laser made it increasingly difficult to obtain a steady baseline. Therefore no integrations were

performed 6 μs onwards following the laser flash, since by this point the signals were sufficiently small to make the resulting % MFEs too noisy for useful interpretation.

2.2.2 A Basic Interferometer Setup and Fourier Transform

The first successful build of an interferometer, by Michelson,[13] was implemented in the earliest predictions of the speed of light. A small scale variant of this is given in Figure 2.7 to demonstrate the principle of interferometry. Collimated visible light strikes a half silvered semitransparent mirror, called a beamsplitter, at 45 °. The material of this is governed by the source output. For example, for visible light the beamsplitter would be quartz. This divides the amplitude of the light beam in half, with one beam travelling to mirror 1 (M_1) and the other to mirror 2 (M_2). These two beams then follow their individual paths, reflect off their respective mirrors and recombine at the beamsplitter. This signal is then directed to the detector to be digitised.

If the distances of the two mirrors from the beamsplitter are identical, the waves should interfere constructively. If, however, the two waves remain incoherent, it is often due to the additional dispersion of one of the beams. This occurs as one of the beams travels through the quartz pane twice. Under these conditions, a compensating plate is suitably positioned in the setup to correct the amplitude mismatch.

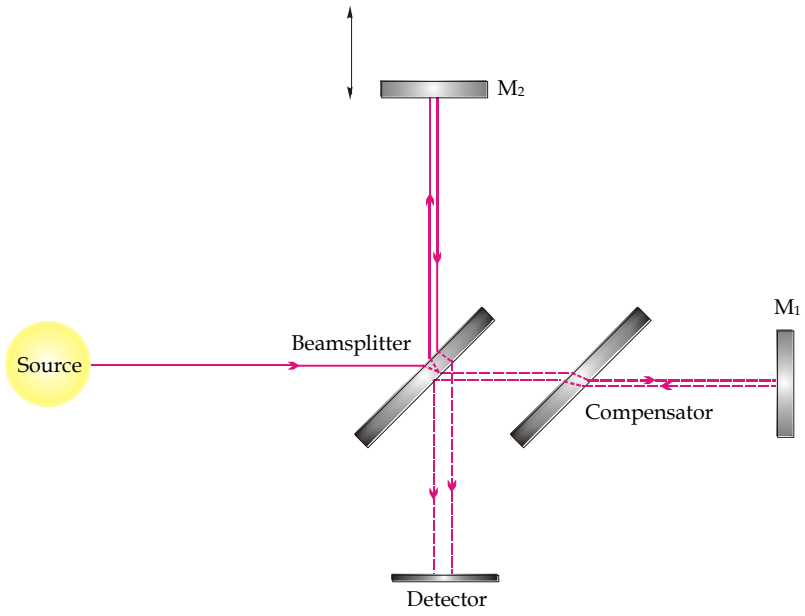

Figure 2.7 The principle components of a Michelson interferometer. The reflections are represented with different paths to distinguish between the beams; in reality all the beams would follow identical paths. The compensator plate corrects for refraction.

For a Fourier Transform IR interferometer, one of the mirrors is fixed whilst the other is mobile. This latter mirror is placed on a smooth mechanical slide to minimise disturbance of the signal during the movement of the mirror. A path difference, δ, is introduced and the signal at the detector oscillates while the two component waves alternate in and out of phase, according to the motion of M_2 along the interferometer arm. To obtain an interferogram, the intensity signal at the detector, I, is recorded as a function of mirror distance (retardation). For monochromatic radiation, the variation of the signal at the detector appears as a sinusoidal wave, and can be described by,

$$I(\delta) = I(\bar{\nu}) \cos(2\pi\bar{\nu}\delta)\, d\bar{\nu} \quad [2.3]$$

$I(\delta)$ is the amplitude of the signal recorded as a function of distance, and $I(\bar{\nu})$ is the intensity of the corresponding wavenumber.

For a polychromatic light source, the signal at the detector appears as a superposition of all the sinusoidal waves at their respective wavenumbers. When the pathlength difference between the mirrors is zero, the waves sum constructively and a peak centreburst is observed on the digitised interferogram. The interferogram for a polychromatic source can be written as the sum of all the individual waves,

$$I(\delta) = \int_0^\infty I(\bar{\nu}) \cos(2\pi\bar{\nu}\delta)\, d\bar{\nu} \overset{\text{FT}}{\rightarrow} I(\bar{\nu}) = \int_0^\infty I(\delta) \cos(2\pi\bar{\nu}\delta)\, d\delta \quad [2.4]$$

Fourier transform (FT) enables conversion between the distance domain, $I(\delta)$, and wavenumber (or frequency) domain, $I(\bar{\nu})$, for each of the constituent waves in a radiation source. For monochromatic radiation the FT will extract a single wavenumber spectrum at its associated intensity. The same procedure, when applied to the intensity of a polychromatic source, will yield the range of wavenumbers present. Due to the complex assortment of wavenumbers in spectral recordings, this function is routinely performed using computers. The resulting wavenumber lines also feature signs of spectral broadening, as a result of the lifetime of the species involved.[13]

As discussed earlier, the current TRIR setup measures a reduction in the absorbance of the IR signal at the detector when the RP is created. This is recovered when the radicals recombine. A rearrangement of the optics on the laser table shown in Figure 2.6, to match those in the Michelson interferometer (Figure 2.7) would allow

destructive interference of the IR beams to occur on recombination at the beamsplitter. This would give an essentially zero background signal against which to record the RP kinetics, while the remainder of the recording procedure would be unchanged. It was anticipated that this would improve the quality of data obtained, and consequently reduce the amount of averaging necessary per scan. A modification of the optics to match that illustrated in Figure 2.7 was attempted for the TRIR design, and the process of doing this is described in the following section.

2.2.3 TRIR Spectrometer Development

The IR signal at the detector in the current TRIR spectrometer is large at ~ 10 V, in comparison to the actual decay curve from the irradiated sample, which is typically 20-40 mV. Given the magnitude of the original signal an accompanying amount of noise is observed, for both the background radiation and the minor signal of interest arising from the recombination of the RP. This associated noise can, however, be reduced if the radical decay could somehow be acquired as an emission type spectrum using a monochromated IR source against a negligible amount of background radiation. This will prevent any direct IR from the source interfering with the detector, and ought to generate a proportionally lower amount of noise, thereby increasing the overall S/N ratio and inherently the sensitivity.

2.2.3.1 Modifying the Optics of the TRIR Spectrometer

The interferometer plan in Figure 2.8 was contained in a transparent Perspex box, and was again constructed on the original laser table. The area within the box was supplied with a continuous flow of nitrogen *via* a corked vent, to dry the environment around the moisture sensitive potassium bromide (KBr) beamsplitter. Silica gel crystals were also positioned near the beamsplitter to absorb any traces of water present. To allow the IR beam from the diode laser into the unit, holes of approximately 1 cm diameter were drilled for entry and exit to the detector, as well as for the sample flow, which were temporarily sealed.

After initial construction, the aim was that sample cells be placed in front of both mirrors (the fixed mirror, M_1 and movable mirror M_2), allowing solution to flow from one to the other. The first sample cell C_1, would provide a background of the absorption by the molecules in the solvent for comparison, whilst the second, C_2, would be photolysed with UV radiation. Suppose the mirrors were located at such a distance to

introduce destructive interference of the IR beams before photolysis, then the absorption of the IR by the radical possessing the characteristic $\nu_{C=O}$ band would result in the appearance of a signal at the detector upon RP formation. When incorporating the monochromator into this setup the optics would need readjusting to minimise the signal at the detector, though this would be minor in comparison to the original build. In this design the overall signal attained would be directly proportional to the absolute absorption of the sample.

Initially a helium-neon (He-Ne, 632.8 nm) red laser was situated in front of the parabolic mirror to align the optics and direct the beam through the interferometer. The signal at the detector was monitored using the original LabVIEW[3] program, generating a voltage vs. time trace. The He-Ne laser served to crudely arrange the positioning of the mirrors and was thereafter replaced with the IR beam.

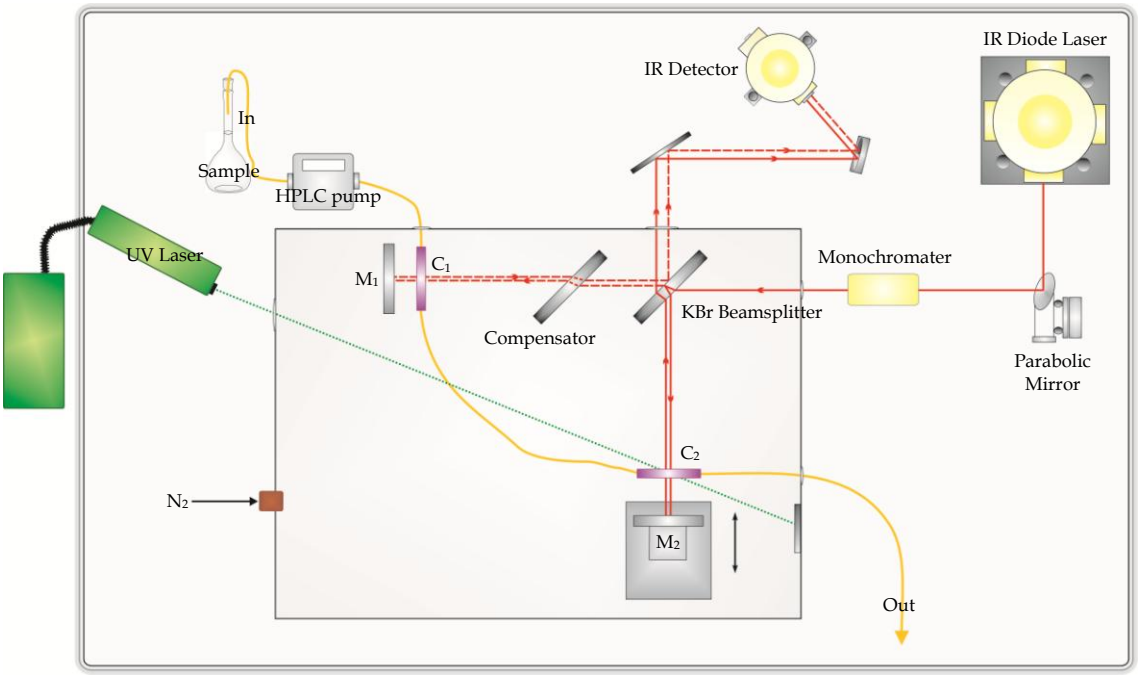

Figure 2.8 The intended setup for the interferometer based TRIR experiment, which is encased in a nitrogen purged Perspex unit to minimise water damage to the beamsplitter and remove interference from water vapour in the recorded signal.

The invisibility of the IR radiation, unavoidably, caused a few problems. Particularly since the intensity of the beam was low and therefore undetectable using infrared sensor cards. A minor adjustment of the optics often resulted in a total loss of signal at the detector; consequently the mirrors regularly required correcting to recover the initial or lost signal. The IR beam also travelled *via* holes into the purged unit and in some instances only a partially reflected beam continued through to the detector. This was due to dispersion occurring at some point in the mirror iteration process and the IR beam was lost inside the unit. A further issue arose from hitting the beamsplitter at 45 °. This split the IR beam unequally to each of the mirrors, and on return to the beamsplitter the beams would be slightly off-axis and unable to interfere constructively to maximise the voltage signal. The optics were adjusted accordingly to correct for this, however, this also meant that in the final setup the mirrors were not visually at 90 ° to the beam, even with the inclusion of a compensator plate. Additionally, over the period of a day the IR beam would drift, causing the intensity at the detector to drop considerably. This intensity could not be recovered without repeated iterations of the optics through the setup.

Once the optics were optimised, and an acceptable voltage signal, compared to that in the TRIR spectrometer was reaching the detector, the monochromator was incorporated. Again, the He-Ne laser was used to initially tweak and position the mirrors. The preliminary steps for constructing the interferometer had been completed and the signal, using the single wavelength IR, had been maximised to ~ 10 V. Upon constructive interference of the two beams, blocking each of the two mirrors independently resulted in nearly half the amount of IR reaching the detector, ~ 6 V. The anti-phase relationship caused the signal to reduce to 2 V, making the total signal approximately 8 V. The detector reading in the absence of any radiation from the diode laser (background signal) was found to be 0.85 V.

A cosine wave could be viewed on the display as M_2 was rapidly moved through multiple retardation positions. This displayed the anticipated maxima and minima for the single wavelength of IR. Undesirably at this stage, there appeared to be large oscillations in the recorded spectra. These were originally proposed to be from vibrations in the nearby environment, since interferometry would naturally increase the sensitivity of the spectrometer. This was, however, clearly not the case, as the vibrations in the signal were greatly reduced when there was no interference of the beams and only one travelled through to the detector. For confirmation, deliberate vibrations were

created and it was concluded that noise was not responsible for the oscillations in the signal. While interferometry is a sensitive technique, the laser table should be equipped to provide adequate damping from external vibrations. It is feasible that irregular environmental noise may still have contributed to the vibration issues, though this was evidently not the main cause in the work described.

Despite the two IR beams successfully interfering in this new design, the noise level in the signal was far too high for any useful spectral measurements of the samples. Further development by incorporating the cells was therefore not undertaken and no additional work was pursued on this setup. The original TRIR spectrometer was reconstructed to match the schematic given in Figure 2.6, with the optics varying from that in the original build.[14]

2.2.4 Fourier Transform Infrared Spectroscopy

The complementary techniques of Fourier transform and interferometry with IR were first commercialised in the late 1960s, in the form of FTIR spectrometers. However, the application of fast time resolution in these instruments was only available from the 1980s onward.[9, 15] Through continued development, their scope has now extended to include the study of dynamic systems, such as short-lived species in reaction kinetics, and the characterisation of protein binding. With the universal appeal of infrared, increased bandwidth, desirable resolution and sensitivity, this technique is superior to most conventional laser based methods. It lacks only in its inability to access the sub-picosecond time domain; an area where laser based techniques currently dominate.

A clear benefit of FTIR lies in the simultaneous recording of all the frequencies, often referred to as the multiplex (or Fellgett) advantage. This enables a complete spectrum to be collected and averaged in the period taken for a single scan on a traditional spectrometer.[13] The instrument also features the throughput (Jaquinot) advantage, where the routinely used narrow slit entrances to the prism or grating element in some spectrometers are replaced by a circular aperture, to allow more of the total radiation through to disperse. It is worth noting that many laser based instruments, such as the one described earlier, operate at a single wavelength so the aforementioned advantage does not apply in this case. The registration (Connes) advantage means that calibration is performed with a He-Ne laser. This generates more accurate and reproducible measured frequencies, and eliminates the potential for human error.

In continuous scan interferometers the mirror moves at a steady velocity, while the associated signal at the detector is measured at regular time intervals. Consequently, the interferogram becomes a function of the time taken for a scan. This method of recording is limited by the total length of time a particular scan takes. It is therefore suited to recording relatively slow kinetic processes, typically of the order of seconds to milliseconds, or static spectra.[9] Rapid scan FTIR is an enhancement of the continuous scanning mode. The mirror speed is adjusted so the duration of a scan averages one order of magnitude less than the lifetime of the species being studied. This enables successive scans to produce instantaneous interferograms with respect to the temporal evolution of the dynamic event. Hence, the entire spectrum can be recorded at once, and FT can be applied to decouple the interferograms to generate the desired frequency spectrum.

The mirror in this instrument requires time to reverse its direction following each scan completion, and therein lays the first limit of continuous velocity scanning. Furthermore, its reliance on a CW globar source defines the dynamic event to be a function of sample response and therefore a function of time. The former of these issues is tackled in more advanced setups, such as ultrarapid scanning. By substituting the usual translational mirror for a rotational one,[16] species with lifetimes of a few hundred milliseconds can be monitored. The rare stroboscopic sampling technique is capable of measuring in the sub-millisecond region, though differs in its manner of data collection. The entire interferogram is collected on multiple sweeps and requires a moving trigger delay, making analysis of the data more complex.

Albeit more expensive than the continuous wave methods discussed so far, the acquisition of data using S^2TRS is most favourable for probing species in this sub-millisecond time domain.

2.2.5 Step Scan Time Resolved FTIR Spectroscopy

Originally this technique was also introduced in the 1960s, and received far less attention than its continuous scan rival until the 1990s, when the limitations of CW spectroscopy were fully realised.[15]

The novelty of step scan stems from its ability to decouple the time dependent IR measurement, from the dynamic event. Here, the moving mirror holds steady at a particular retardation position, where it settles, then sends a pulse to trigger the rapidly decaying process. The change in the spectral intensity at the detector in volts (AC) is

measured at defined points during the relaxation of the timed event and averaged for the desired S/N. The S/N ratio from step scanning is, per single sweep, inferior to that from rapid scanning. However, as mentioned, multiple co-additions can recover this at the expense of a longer timeframe for a complete scan. The mirror then travels to its next position and the process is repeated for all the retardation points. The data files are compiled into individual interferograms to yield a 3D profile, and with the aid of FT these interferograms can generate the corresponding 3D frequency spectrum.

In theory, the resolution of step scan bears no limits in itself, but rather is governed by the capabilities (speed and sensitivity) of the detector and transient digitisers, and not by the scanning speed or globar source. This manner of recording is ideal for obtaining kinetic information on rapid and highly repeatable chemical reactions, occurring on a timescale ranging from microseconds to nanoseconds.

2.2.6 The Varian Step Scan Time Resolved FTIR Spectrometer

The purchased S^2TRS (7000 Series) instrument functions similarly to that described in the earlier section. A notable difference is that the recording technique for this spectrometer involves the movement of both the movable and fixed mirrors during the period of optical retardation. M_2 gradually moves along the axis of the interferometer arm, whilst the *fixed mirror* M_1 oscillates back and forth regularly. The combination of both the mirror actions produces the stepping mechanism. This design allows access to an increased range of scan speeds, from 0.004 Hz (250 s) to 800 Hz (125 ms). The next section outlines the various steps in testing the ability of the spectrometer for studying dynamic events, as well as discussing the associated difficulties in using the instrument.

2.2.6.1 Testing the Spectrometer

A schematic of the final spectrometer arrangement can be viewed in Figure 2.9. The first stage of development of the S^2TRS instrument required installing the various components for the intended solution phase studies of RPs. This included,

- Constructing a cell base to accommodate the height of the IR beam, and a set of magnetic field coils, which would be added lastly to the setup.
- Focussing the probe IR beam and UV excitation beams on to the cell *via* the appropriate optics.
- Arranging the triggering and recording of the transient event.

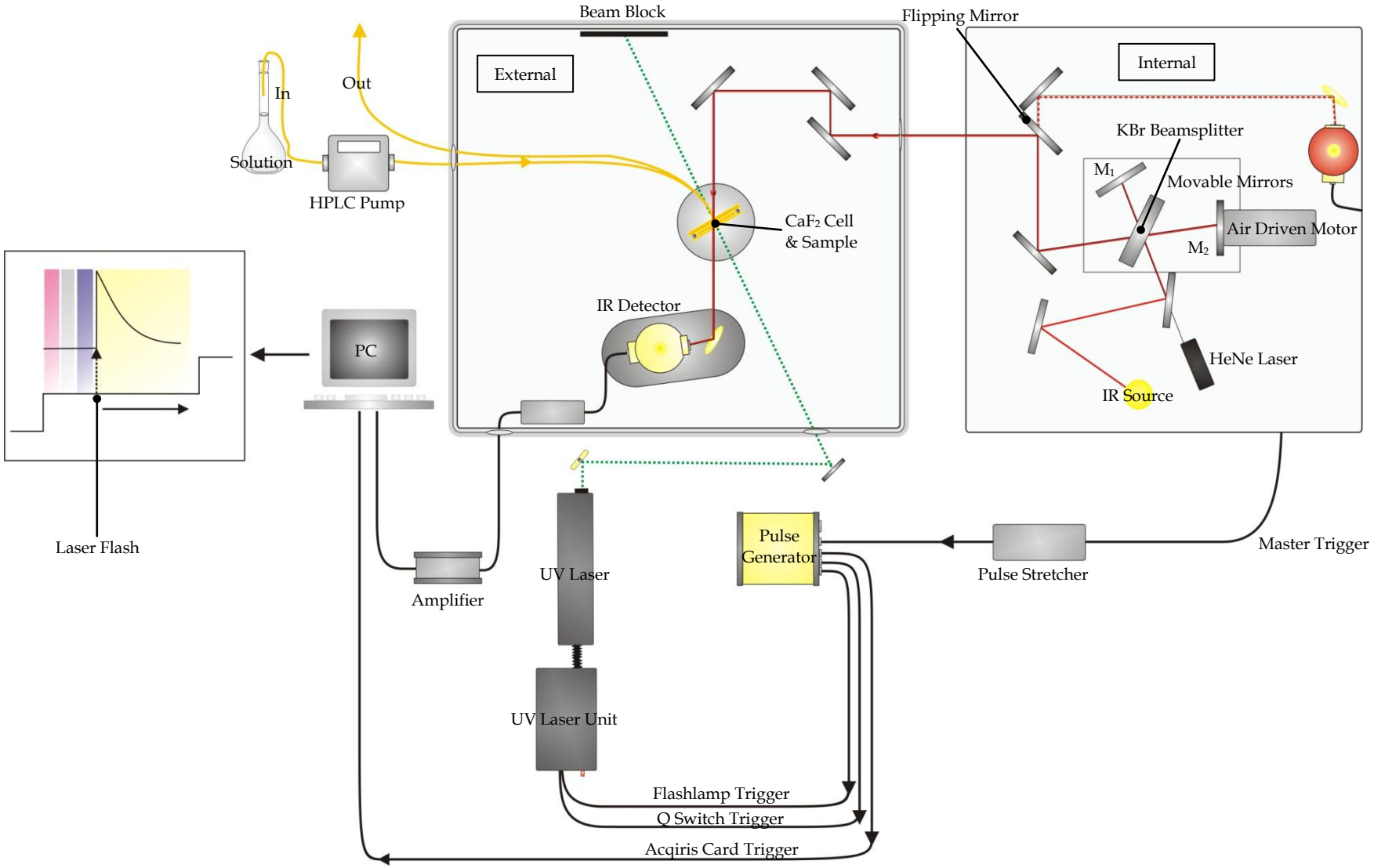

Figure 2.9 A schematic of the step scan spectrometer setup.

A similar cell holder to that used for the TRIR spectrometer was positioned in the external unit of the step scan instrument as shown in Figure 2.9. Alternative cells were also researched, though for ease of cleaning, adjustable pathlength, as well as considering the extent of absorption from the solvent for larger pathlengths, the current cell was the most suitable choice.

The master trigger for the system originated from the back of the FTIR unit. Therefore, it was necessary to build a pulse stretcher to control the pulsing of the Nd:YAG Continuum Minilite I laser. Initially, the triggering sequence was such that the recording of the transient event and triggering of the flashlamp occurred simultaneously, as advised by the manufacturers. Accordingly, the resulting spectra from S^2TRS included a period of delay associated with the Q-switch firing, after which the signal corresponded to the transient event of interest.

Prior to recording any step scan spectra, it was important to determine the strength of the absorption of the precursor molecules, using the CW scanning mode.

2.2.6.1.1 FTIR Studies

The initial tests on the instrument involved acquiring static FTIR spectra. This would give an indication of the concentrations required for the later solution phase work. The (2,4,6-trimethylbenzoyl)diphenylphoshine oxide (MAPO) and bis(2,4,6-trimethylbenzoyl)phenylphosphine oxide (BAPO) molecules (both were investigated in a separate study and the results are discussed in Chapter **4**-their structures can be found in Figure 4.3), were recorded first. These molecules had prior to this been studied on the TRIR spectrometer and were known to have strong carbonyl absorption in the benzoyl radical, from only 20 mM of the precursor in solution. These molecules were prepared in different solvents (cyclohexanol, acetonitrile, ethanol, and propan-2-ol) at varying concentrations in the range 20-300 mM. This was to determine the extent of absorption of the precursor and the commonly used solvents.

For the 20 mM precursor rapid scan, the absorbance signal was from the solvent alone, and there was no evidence of the molecules in these spectra. Therefore, incrementally higher concentrations were used. Concentrations of 100 mM in solution were needed to confidently assign the signals to the phosphorus oxide precursors. All these scans were performed using sodium chloride plates, using the internal compartment of the FTIR spectrometer as labelled in Figure 2.9. At this point the external compartment was still under development to hold the CaF_2 flow cell. Later,

when analogous tests were performed in the external compartment, it was discovered that 150 mM of MAPO and BAPO were necessary for a similar sized signal from the molecules. This indicated that the alignment of the external optics did not steer the IR radiation appropriately out of the spectrometer, since only one mirror (labelled in Figure 2.9) was responsible for directing the radiation outside the unit. The optics were therefore adjusted to improve the intensity of the IR signal level achievable outside the spectrometer.

2.2.6.1.2 Step Scan FTIR Studies

Once the components were in place, the UV photolysis and IR beams were overlapping, and the triggering was setup, the initial time resolved experiments were undertaken. These primarily used 2-hydroxy-4-(2-hydroxyethoxy)-2-methyl propiophenone (αhp) in propan-2-ol. The structure of αhp along with the generated RP is included in Chapter **5**, Figure 5.1, for reference. The intense radical absorption signal in the TRIR system from only 2 mM αhp in solution, as well as knowledge of both the wavenumber of the carbonyl stretch in the benzoyl radical and the lifetime of the RP, made this a suitable choice of precursor for both aligning and preliminary tests on the step scan instrument. After carrying out similar concentration analyses to those detailed in Section **2.2.6.1.1**, for a closed CaF_2 cell (non-flowing) a concentration of 50 mM or higher was decided upon, to achieve a relatively strong αhp peak in the static FTIR spectra. Accordingly, it was anticipated that the benzoyl radical should too be evident in the resulting S^2TRS spectra, after multiple co-additions to improve the S/N.

A lifetime of several microseconds for αhp in propan-2-ol should, from the instrument specifications, be easily probed using the step scan instrument. Yet no appropriate signal was observed. This led to a number of concerns:

I. The potentially poor overlap of the probe IR and UV photolysis beams.

To investigate this, quencher studies of 50 mM αhp with 70 mM trichlorobromo-methane (CCl_3Br) were performed using the rapid scan on the FTIR. The inclusion of this quencher should preferentially form a benzoylbromide adduct (within 2 μs) at ~ 1772 cm^{-1}, rather than regenerating the αhp.[11] This peak occurs as a result of bromine atom abstraction by the transient benzoyl radical. The peak was evident in the spectrum, and increased in absorption with increasing periods of irradiation (see Figure 2.10).

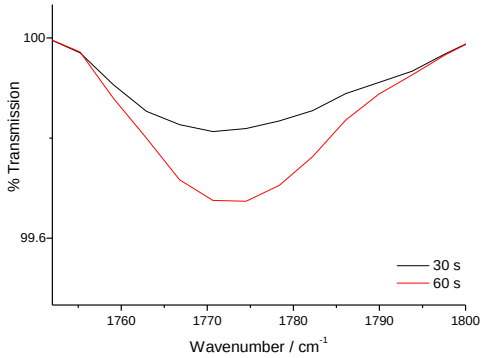

Figure 2.10 The increasing irradiation of 50 mM αhp with 70 mM CCl_3Br. The peak at 1772 cm^{-1} grows with time.

An accompanying decrease in the original precursor carbonyl stretch was noted at 1663 cm^{-1}, though this was repeatedly obscured by a nearby absorption and for this reason is not shown. This additional absorption could possibly have been associated with polymer build up on the cell, occurring after continued irradiation. The observed modification of the precursor and growth of the adduct peaks supported some overlap of the IR and UV beams and the formation of the expected radical intermediates. But still, at this stage, the radical signal was still absent from the S^2TRS data.

αhp with an excess of quencher was found to be appropriate for aligning the IR and UV beams. This was done by probing for maximum product formation at different irradiation points on the cell. At the point of maximum overlap, a notable difference in the intensity of the product peak occurred for these high concentrations of αhp and CCl_3Br, after irradiating for 30 s or more.

While the overall power of the broadband IR source is greater than that of the IR diode laser (in the TRIR spectrometer), the corresponding amount of power per wavelength of the broadband source, is significantly lower. It is therefore reasonable to conclude that a higher concentration of the precursor molecule would be necessary when monitoring the same species using S^2TRS. However, the 25 or 50 fold increase, as used, should have proved sufficient to observe the transient signal, considering the precursor in solution was clearly visible. The absence of the intermediate was no longer considered to be from an inadequate amount of precursor, but more conceivably, from the laser power. This idea was supported by the fact that only prolonged irradiation significantly reduced the absorption of the precursor carbonyl peak and gave rise to a strong signal for the benzylbromide product.

II. The laser power

The original Minilite I was efficient at cleaving 2-20 mM of precursor using 1.8 mJ per 266 nm pulse (measured using the exit beam). A higher concentration of 50 mM may require more energy per pulse and this was initially supplied by a Minilite II. The Minilite II was capable of firing 3.5 mJ per pulse when optimised and focussed using an appropriate lens on to the CaF_2 cell. Given that the concentration of αhp was often increased up to 100 mM, ideally, the pulse power needed to be adjustable. Therefore, the Surelite I was used to control the power output, over a wider range, by altering the delay between the flashlamp and Q-switch. This laser was kept in the final setup and the timing was altered as appropriate for the concentration. Additionally, focussing lenses were used to tightly focus the UV beam to match the size of the IR beam (approximately 3 mm), thus providing maximum overlap. Again, on running the S^2TRS experiment no intermediate signals were noted.

At this point the pathlength in the cell was also investigated up to a maximum of 0.4 mm, after which solvent absorption saturated the detector. To hinder saturation effects (non-linear response), filters were situated in front of the detector to cut down the spectral bandwidth and limit the amount of absorption by the solvent outside the region of interest. For the work with αhp, this covered a range of 650-2200 cm^{-1}. However, the lower limit was governed by the transmission of the CaF_2 windows which began to tail off below 1000 cm^{-1}.

III. The lifetime of the species

In combination with the high concentrations of αhp (50-100 mM), a range of solvents were also used to alter the RP lifetimes. This was performed to determine if the detection issue was associated with the decay time (~ 7 μs) of the RP in the propan-2-ol solution. These studies were conducted in the presence and absence of CCl_3Br, for solutions of increasing viscosity, up to a maximum viscosity of 59 cP (cyclohexanol). None of the resulting S^2TRS spectra showed any evidence of the transient species. The longer scan times did, however, reveal an oscillation in the IR output occurring at 32 μs intervals (62.5 μs, 16 kHz, for a full cycle), which was associated with mirror dither. The amplitude of this transient signal was much larger than that expected from the radical intermediates. This limited the recording timeframes to approximately 5 μs before a reduction in the IR intensity was observed, and the signal of interest removed. Therefore further tests were performed solely within this 5 μs period.

Neither the amount of αhp nor the laser power should be hindering radical detection; as both were increased, accompanying changes in the precursor and product peaks were recorded. The investigation into the RP lifetime similarly confirmed the absence of any signals that could be assigned to the transient species. At this stage, attention shifted to altering the timing sequence of triggering the event and recording. This was particularly important given that the mirror dither would interfere with signals recorded after periods of $>$ 20 μs, and may account for the missing signals.

IV. The timing sequence

After monitoring the sources of potential fluctuations in the timing sequence, it was discovered that the jitter (~ 1.2 μs) in the rise time of the Q-switch caused the largest variation. This led to an uncertainty in the start point of the dynamic event when interpreting the recorded S^2TRS data. The jitter could be reduced (to ~ 10 ns), by controlling both the flashlamp and Q-switch externally using a pulse generator. The trigger arrangement was also modified to capture the data (Acqiris card) simultaneously with the Q-switch firing; here the delay between the shutter for the laser flash and Q-switch signal was also accounted for (10 ns). This final spectrometer setup is illustrated in Figure 2.9. Further details can be found in Section **2.2.6.2**, where the data collection process is outlined.

V. The chemical process

The lack of any signal from the transient radicals following all the modifications to the spectrometer and repeating with the new triggering arrangement, naturally led to testing alternative chemical species. These exhibited kinetics on a much slower timescale, and could be excited without using the pulsed laser source. The chosen chemical alterations also occurred without the solution flowing though the cell and so eliminated as many variables as possible.

This was first performed in a CaF_2 closed cell with a pathlength of 0.4 mm, using 4-anilino-4-nitroazobenzene in propan-2-ol. This system when flashed (visible light) is excited to its cis-state and undergoes a cis→trans relaxation to the ground state. The cis-state was expected to have a distinguishable IR resonance structure to that of the trans-state, likewise this difference should have been evident on comparison of the acquired FTIR data. The kinetics are slow and proceed over 4 s, as confirmed using UV-vis

spectroscopy. This allowed the process to be recorded using the conventional rapid scan method, which records kinetic information independently of the dither. The solution was initially tested with the UV-vis spectrometer using both, a relatively large pathlength of 10 mm, and the smaller 0.4 mm cell, to confirm that isomerism was also observable at the low volumes of solution. Using the pathlength of 0.4 mm during the rapid scan, gave a strong solvent absorption, thus the pathlength of the cell was reduced and the scan repeated. Neither showed signs relating to a change in the conformation of the molecular structure.

Additionally, among other systems, a solution of methyl iodide was investigated. Methyl iodide is reported to efficiently produce radicals, and other recombination products on exposure to visible light.[17] Accordingly, an evolution of the spectrum was expected to occur following an appropriate flash of light, or after ongoing exposure to visible light. The solution was contained in a closed cell in a similar manner to that detailed earlier. The resulting rapid scan spectra revealed some alterations. However, evaporation occurred readily making it difficult to reproduce the results. The solution was neat methyl iodide, so was used at a much higher concentration than any of the samples tested thus far. This suggests that it may have been the magnitude of the transient signal following irradiation which was hindering the observation of the kinetic events.

VI. The intensity of the transient signal

An external lock-in amplifier was used to capture and magnify the signal received by the MCT IR detector. In the setup, it was positioned prior to transferring the response to the windows PC. The signal of the transient change was initially optimised to 10 mV, without the amplifier, through careful alignment and focussing of the IR and UV beams. The amplifier then allowed control of this signal, up to a voltage of 100 mV. Conveniently, this method also enabled the overlap of the probe and UV beams to be directly optimised using an oscilloscope. A transient signal of 100 mV should, in theory, have been sufficient to reveal a change in the resulting spectra, though again, no appropriate intermediate signal was recorded.

Regardless of the various modifications sought, the FTIR instrument has to date, been unable to confidently reveal the presence of any short-lived species in the resulting spectra, using either the rapid scanning or step scan modes. The primary concern when using a S^2TRS instrument for recording transient events is the power of the globar

source. This problem should be overcome following adequate amplification of the transient signal and by the various amendments made, though clearly, this still required further attention.

The relatively high concentrations of precursor molecule employed here, additionally raises questions on the suitability of the technique for recording magnetic field studies, with the intended low fields. At these concentrations, the RPs may be eliminated rapidly and selectively from solution, perhaps making it more difficult to observe the effect of a magnetic field on the RPs. One potential way to investigate this would have been to monitor the product ratios using a fixed magnetic field and continued irradiation of the αhp and CCl_3Br sample. This was, however, not attempted.

Numerous failures in the Parker Balston gas generator responsible for controlling the piston for the moving mirrors, complications with the software, the speed of the mirrors, failures in the water cooler for the source and difficulty in reproducing the spectra has further inhibited the evolution of the experiment. No magnetic field studies, RP studies or simple photochemistry were ever successfully completed using this instrument. In view of all the system modifications, it is suggested that perhaps, the signal processing may be responsible for the absence of any intermediate radical species in the resulting S^2TRS spectra.

The next section outlines how a spectrum is collected using the final spectrometer arrangement, following the various amendments described in this section.

2.2.6.2 Data Collection Using the Final Setup of the S^2TRS Instrument

Mirror M_2 steps to a position, as indicated by point 1 in Figure 2.11, where it holds stationary and stabilises (point 2). Here, a static interferogram is recorded from the DC output of the detector preamplifier, in an identical manner to that in the continuous wave process (point 3). This signal is then averaged and used as the background.

The master TTL trigger (0.5 μs, 5 V) for the experiment originates from the FTIR (point 4), at a rate governed by the Win-IR pro software and is set to coincide with the pulsing rate of the YAG laser; see Figure 2.9 for the scheme. The signal travels *via* an external pulse stretcher (approximately 50 μs) and a delay generator (Berkeley Nucleonics Corporation, model 555) to trigger both the flashlamp and Q-switch of a Surelite I Nd:YAG laser, while incorporating an appropriate delay (point 5) to control the power output.

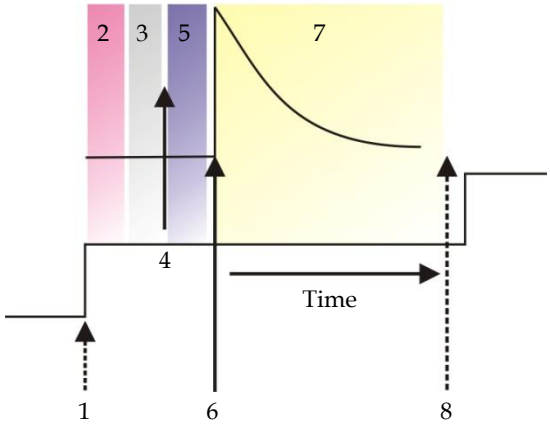

Figure 2.11 The timing sequence for data collection using the S^2TRS instrument. The points, 1-8, occur for each step, as indicated by the Win-IR pro software. 1. The mirror step, 2. The settling time, 3. The background collection, 4. The trigger from the FTIR, 5. The delay in the laser flash, 6. The laser flash 7. The decay of the dynamic event, and 8. The repeat/co-add.

Simultaneous with the Q-switch, a second trigger, from the pulse generator initiates data capture using the Acqiris card located in the PC. The laser flash initiates the photochemistry (point 6), which is monitored in an identical cell to that used in the TRIR system. The dynamic (AC) output from the preamplifier of the detector *via* a external lock-in amplifier (Precision AC Amplifier 9452), measures the change in spectral intensity and the Acqiris card collects interferograms over a period of time set by the software (point 7). This data is subsequently averaged a defined number of times for this particular mirror step to improve the S/N. For the work described, a UDR 8 filter ranging from 650-2200 cm^{-1}, was situated in front of the detector to eliminate spectral interference from stray laser light and reduce the spectral bandwidth. The movable mirror (M_2) then advances to the following position (point 8) and the entire process is repeated. FT of the data gives the dynamic single beam array. The difference in absorbance can be obtained by normalising the dynamic spectra over the reference spectrum.

Currently a time resolution of between 1 ns (limited by the digitiser board) and 250 ms is available on the instrument. In practice the maximum time resolution is defined by the response of the photovoltaic TRS MCT detector, which for this spectrometer is limited to 10 ns. In any case, this resolution should have been more than sufficient to monitor the dynamic events of interest.

The primary aim of this research was to construct a MFE spectrometer based on a commercial step scan instrument. Countless months were dedicated to doing this, and still, the basic requirement of detecting transient species, or indeed confidently assigning any low concentration samples has not been feasible. Further to this, the instrument had many functioning errors and over the period of a year, months were spent awaiting or arranging the exchange of the components, or for replacement parts. This, in addition to the multiple issues addressed earlier, significantly hindered progress. Ultimately and very disappointingly, it was the instrument that was found incapable of the measurements the manufacturers had claimed.

2.3 Materials, Sample Preparation and Procedures

2.3.1 Biological Samples for Chapter 3

Reagents and materials Human serum (HS), transferrin (Tf), ferric nitrate, lactoferrin (Lf), 3-(2-pyridyl)-5,6-bis(4-phenylsulfonic acid)-1,2,4-triazine (ferrozine, Fz), the catecholamines; norepinephrine (NE), epinephrine (Epi), dopamine (Dop), and dobutamine (Dob), and catechin were all purchased from Sigma Chemical Co. Ammonium ferrous sulphate was obtained from BDH chemicals, the liquid nitrogen originated from BOC and the liquid helium from BOC and Air Products.

Preparation of transferrin/lactoferrin catecholamine frozen samples and EPR analysis The Tf (or Lf) catecholamine samples for EPR analysis were prepared by mixing 6 mg ml^{-1}, 75 μM, (Lf, 5 mg ml^{-1}, 63 μM) of iron saturated Tf/Lf (holo-Tf/Lf) and 10 mM tris(hydroxymethyl)aminomethane (Tris)-HCl buffer of pH 7.5 with (or without, in the case of the control sample) the specified concentrations of catecholamines as included in the individual experiments. Lower concentrations were used for the serum (mammalian; bovine and human) samples and these amounts are indicated in the text. The Tf/Lf catecholamine and serum catecholamine mixtures were analysed immediately unless otherwise stated, where alternatively they were either incubated at - 20 ^{o}C or 37 ^{o}C for the time periods indicated in the text.

Samples were prepared and frozen in liquid nitrogen as pellets of, 0.3 or 0.40 ml volume using the custom built device shown in Figure 2.12. 0.1 ml of mixed solution was retained in non-pellet form for each sample. The samples were located in a finger dewar, and surrounded by liquid nitrogen, with a glass or wooden insert to minimise disturbance whilst recording. The spectra were obtained on an X-band JEOL-RE1X CW

EPR spectrometer with the following analysis parameters; centre field: 150 mT, sweep width: 80 mT, field modulation: 1.0 mT, microwave power: 10 mW.

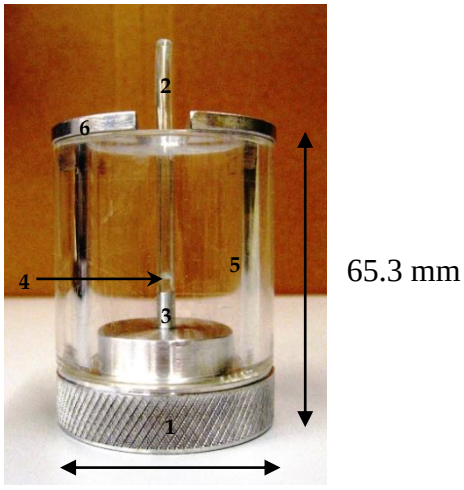

Figure 2.12 The aluminium pellet making device with labelled features, 1. The base made of aluminium with indented edges for easy grip when frozen, 2. PTFE flexible tubing to fit the required sample size, 3. Pellet base to hold PTFE tubing, 4. Route for sample injection using a micropipette to eliminate air pockets, 5. Plastic casing to fit perfectly on the base and hold $N_{2(Liq)}$ to freeze the pellet, 6. Aluminum sliding lid for the pellet maker, to hold the tubing in place and ensure a straight pellet is made. The device is assembled, and 5 & 6 are removed to allow injection. 5 is replaced and filled with $N_{2(Liq)}$, then covered with 6. The pellet was kept encased for 30 seconds before removing 2 and releasing the pellet using a wooden implement into a dish containing $N_{2(Liq)}$ for a further 30 s. Note that different bases were constructed for varying pellet sizes, which were dependent on the spectrometer and dewar/EPR tube size. Pictured is the base for a 2.7 mm diameter sample for use with the standard EPR tube.

Alternatively spectra were recorded on an X-band Bruker ELEXSYS E500 CW EPR spectrometer, again using a finger Dewar, or an ultra low temperature helium attachment from Oxford Instruments (ER 4112HV) inserted directly in to the cavity to provide a stream of helium over the sample contained in a conventional EPR tube. The parameters for this instrument were comparable with those listed for the JEOL spectrometer and adjusted accordingly for the slight shift in centre field positions

between the two spectrometers. All spectra were acquired at a temperature of 77 K, where for the Bruker instrument this temperature was maintained by liquid helium using the defined attachment. Both spectrometers incorporated a flow of nitrogen (gas) into the cavity whilst recording to inhibit condensation on the dewar/EPR tube.

2.3.2 Solutions for the TREPR and TRIR Investigations in Chapter 4

Reagents and Solution Preparation (2,4,6-trimethylbenzoyl)diphenylphoshine oxide (MAPO) and bis(2,4,6-trimethylbenzoyl)phenylphosphine oxide (BAPO), were both obtained in powdered form from Ciba Speciality Chemicals. Reagent grade acetonitrile, *t*-butanol, ethane-1,2-diol, propan-2-ol, trifluoroethanol solvents were purchased from Fisher Scientific Ltd, and cyclohexanol from Sigma Aldrich Co. All chemicals were used as supplied, and prepared in 20 mM (MFE), or 10 mM (TREPR), concentrations under nitrogen flow combined with ultrasonication to ensure complete dissolution during preparation.

EPR Analysis The spectra were obtained on an X-band JEOL-RE1X TREPR spectrometer with the following analysis parameters; centre field: 333 mT, sweep width: 60 mT, microwave power: 1 mW.

2.3.3 Solutions for Chapter 5

2.3.3.1 Reverse Micelle Solutions

Reagents 2-hydroxy-4-(2-hydroxyethoxy)-2-methylpropiophenone (αhp) and 2-hydroxyethoxy-2-methylpropiophenone (mhp) were obtained in powdered and liquid form respectively, from Ciba Speciality Chemicals. 2,2,4-trimethylpentane (isooctane), and sodium bis(2-ethylhexyl) sulfosuccinate (AOT) were purchased from Sigma Aldrich Co.

Solution Preparation 0.7 mM of αhp or up to 20 mM mhp were dissolved in the amount of water for the required water pool size and ultrasonicated. AOT was dissolved in isooctane and mixed by hand. The water was then injected into the AOT solutions to fully disperse the water, this was vigorously shaken and sonicated while degassing for the TRIR measurements. Further details of the sample preparation for the TRIR and DLS measurements can be found in Chapter **5**.

2.3.3.2 Varying Viscosity Solutions

Reagents and Solution Preparation 2-hydroxy-4-(2-hydroxyethoxy)-2-methylpropio phenone (αhp) was obtained in powdered form from Ciba Speciality Chemicals. The reagent grade solvents; acetonitrile, butan-1-ol, butan-2-ol, dichloromethane, ethanol, propan-1-ol, and propan-2-ol were purchased from Fisher Scientific Ltd, and cyclohexanol from Sigma Aldrich Co. 2 mM of αhp was dissolved in the solvents as indicated in the text and prepared under nitrogen flow combined with ultrasonication to ensure complete dissolution during preparation. Where a ratio of solvents is given, this indicates the amount by volume.

2.4 Theoretical Approach and Computational Details

Increasingly, theoretical and experimental data are being combined to gain insights into the structural and thermodynamic feasibility of certain species; this synergistic approach can often aid the interpretation of recorded spectroscopic behaviour. *Ab initio* calculations have long been used to model molecular systems and yield important information, such as equilibrium geometries or vibrational structures. More recently, methods such as density functional theory (DFT) have gained credibility in doing likewise, and have proved valuable in predicting the hfccs of various radicals, including those of phosphorus.[18, 19] DFT is similarly used in this work to assist in unravelling the mechanism of the recorded photochemistry in Chapter **4**, by comparing calculated hfccs with experimentally observed values.

As discussed in Section **1.3.1.2**, the hyperfine interactions between an unpaired electron and magnetic nuclei can be described by the hyperfine tensor, A, which contains information on both the isotropic and anisotropic components (see Equation [1.10c]). As a consequence of the anisotropic interactions being rapidly averaged by tumbling, in solution the observed coupling arises due to the isotropic component alone and this may be estimated from the Fermi contact mechanism. This mechanism can be considered a local property dependent on the spin density, $|\psi_r|^2$, present at the nucleus in question, which in this case is phosphorus. The hyperfine interaction is linked with the *s*-character of the singly occupied molecular orbital (SOMO), thus for the realistic prediction of hfccs it is imperative that both the geometry around the radical centre and the wavefunction are correctly described. This requires firstly, a solution to the Schrödinger wave equation in order to estimate the energy of the system.

The route for approximating the many electron wavefunction of the Schrödinger equation, *via* the Hartree-Fock (HF) method, is detailed briefly in the following section. While this was used primarily on the radical structures, work thereafter applied DFT to locate the optimum molecular structure corresponding to a low energy equilibrium state, as well as to predict the hfccs.

2.4.1 Solving the Schrödinger Equation and the Hartree-Fock Method

The introduction of the Schrödinger wave equation (Equation [2.5]) dates back to 1926.[20] It is a very powerful tool that is able to describe, in detail, most aspects of atomic and molecular structure. However, due to the complexity of the original form of the equation, it is near impossible to solve for all but the simplest one electron systems, i.e. the H_2^+ ion.

$$\hat{\mathcal{H}}\psi = \mathrm{E}\psi \quad [2.5]$$

Here, the Hamiltonian operator may be written as,

$$\hat{\mathcal{H}} = \hat{\mathrm{T}} + \hat{\mathrm{V}} = \frac{-\hbar}{2m}\left[\frac{\partial^2}{\partial x^2} + \frac{\partial^2}{\partial y^2} + \frac{\partial^2}{\partial z^2}\right] + \mathrm{V}(x, y, z) \quad [2.6]$$

The Hamiltonian consists of the kinetic energy, $\hat{\mathrm{T}}$, and potential energy, $\hat{\mathrm{V}}$, terms; including the nuclear-nuclear, electron-electron repulsions and electron-nuclear attraction, of a molecular system.[21] The Hamiltonian operates on the wavefunction ψ, which embodies the information of all of the particles in the system, and yields the energy of the system, E, along with the reproduced wavefunction. Due to the Heisenberg uncertainty principle, the exact positions of all the constituent particles of a molecular system can never be known simultaneously, but rather, the probability density $|\psi_r|^2$ of finding the system at some particle configuration, r, may be calculated.

To simplify the task of solving the Schrödinger equation, many approximations are applied, the first of which is the well known Born-Oppenheimer approximation.[22] The Born-Oppenheimer approximation assumes at one instant whilst an electron is mobile, the nuclei will remain effectively stationary, and thus it decouples the movement of electrons from that of the nuclei. This allows the variables in the

Schrödinger equation to be separated and removes the kinetic energy term for the nuclei (now forming the nuclear Schrödinger equation) whilst making the nuclear-nuclear repulsion term a constant. The Hamiltonian operator reduces to that given in Equation [2.7] to produce a purely electronic equation.

$$\hat{\mathcal{H}}_e = \hat{\mathrm{T}}_e + \hat{\mathrm{V}}_{en} + \hat{\mathrm{V}}_{ee} \quad [2.7]$$

For a molecular system, by fixing the molecule at a certain geometry, the total electronic wavefunction and energy of the molecule can be calculated by solving the electronic Schrödinger equation. If this methodology is repeated for multiple values of r, the resulting information may be compiled to produce a potential energy surface, thus exemplifying the process of determining equilibrium geometries using *ab initio* calculations and work thereafter. At this stage, the electron-electron interactions that exist for a many electron system require further attention.

The Hartree-Fock[23, 24] method estimates wavefunctions *via* the molecular orbital approximation, by separating the Schrödinger equation into solvable one-electron equations. It suggests that a many electron wavefunction, ψ, is the product of single electron functions, i.e. $\psi = \phi_1(1)\,\phi_2(2) \ldots\ldots \phi_n(n)$, where ϕ_n represents the one-electron molecular orbital (MO). Since MOs are composed of atomic orbitals (AOs) and each AO contains one electron that maps out the probability density of finding an electron in that space, the MO allows the total space potentially occupied by the electrons to be calculated. For this method, all nearby electrons and nuclei are treated as a time averaged electric field, called the Hartree-Potential.

While many wavefunctions with different energy conformations can satisfy the Schrödinger wave equation for a system, only the lowest energy conformation will correspond to the ground state. The variational principle states that this minimum energy can be attained by iteratively altering a set of parameters, which in this case are the expansion coefficients required to combine the AOs. The ground state energy, E_0, is associated with a guess or trial (normalised) wavefunction, ψ, by the following relationship,[25]

$$\int \psi^* \hat{\mathcal{H}}\, \psi \; d\tau \geq E_0 \quad [2.8]$$

A realistic trial wavefunction, as used in the HF approximation, should also correct for spin (Fermion antisymmetry),[26] i.e. for when two electrons occupy a orbital. This introduces a second type of potential influencing the electrons; the exchange potential. The exchange potential accounts for the difference in the electrostatic energies of the orbitals in the system, due to the spin of the electrons (as discussed in Chapter **1**). Based on these approximations the one-electron Schrödinger equations can be derived for each HF orbital and these equations have the form,

$$\hat{\mathrm{F}}\phi_i = \varepsilon_i \phi_i \quad [2.9]$$

where, the Fock operator, $\hat{\mathrm{F}}$, represents both the kinetic energy and the mean field potential for an electron in a given spin-orbital. This is shown for the ith spin-orbital, ϕ_i, in Equation [2.9]. Once the ground state wavefunction and energy have been identified using the variational principle, and the corresponding Fock operators are known, the HF one-electron equations can be solved in an iterative manner. This process will continue until the values (wavefunction and spin-orbitals) obtained converge to what is known as a self consistent field (SCF).

2.4.2 Basis Sets

For computational use, HF spin-orbitals, ϕ_i, (or MOs) are composed of a linear combination of basis functions, χ_i (or AOs), and are expressed as the form given in Equation [2.10]. These basis functions are mathematical functions used to describe the spatial part of the orbitals.

$$\phi_i = \sum_{i=1}^{n} c_i \chi_i \quad [2.10]$$

Calculations are performed using a finite number of basis functions, n,[27] and using the coefficients, c_i, that are determined from iterations in the SCF. An exact description of a molecular orbital is possible if an infinite number of basis functions are used, this by definition, is the complete basis set limit. In reality, however, much less freedom is allowed, as the basis set size interlinks with the period of time a calculation will require for completion. Choosing an appropriate basis set therefore entails both an

understanding of the finite number of basis functions allocated to describe an AO, and some knowledge of the chemical structure of the species under investigation.

Routinely, standardised basis sets are used for the calculations. These are complied from two categories of atomic orbital type basis functions; Slater type orbitals (STOs) and Gaussian type orbitals (GTOs). A minimum basis set consists of the fewest number of basis functions required to describe every atomic orbital in the atom, and the simplest of these is the STO. While STOs provide an accurate approximation for atomic one-electron orbitals, as the number of electrons increases, evaluating the resulting integrals become increasingly complex. Thus, for use with software programs such as Gaussian[28] specifically tailored basis functions have been developed, to model the STOs. A linear combination of the GTOs is essential to improve the description of the atomic orbitals, and achieve a level of accuracy comparable to that using the STOs.

The most basic of the linear combinations, adopts the form STO-nG, where n is the number of primitive Gaussian functions (G) forming a single basis function. These are also referred to as single-*zeta* (ζ) basis sets and for the most part they generate crude results. This limits their application to preliminarily molecular calculations, to reduce the computational expense.

Flexibility is added to a basis set by allocating more basis functions per atomic orbital present. Such basis sets are called split valence basis sets, labelled as double-ζ, triple-ζ and so on, depending on how many GTOs are used. They have the form A-BCg, where the first term is the number of Gaussian functions used to describe the core atomic orbital and the hyphen indicates that the basis set is split. The latter two numbers, labelled B and C, show the valence Gaussian basis functions.

Additions are often made to basis sets. Denoted by an asterisk (*), polarisation functions add angular momentum to the atomic orbitals, allowing, for example, a hydrogen to consist of a p-function, as well as the original 1s atomic orbital. A double asterisk (**) indicates that light atoms also feature a polarisation function, and some more computationally expensive correlation consistent basis sets have polarisation inbuilt. This, for instance, is indicated by the p in ccp-VXZ, where X is D for double-ζ, and T for triple-ζ basis sets etc. Broadly, the larger the basis set the greater the flexibility and the closer the result is to that from the infinite basis set.[21]

2.4.3 Post Hartree-Fock Methodologies

While the HF method is loosely accurate, it remains flawed due to the adopted mean field approach, often rendering the probability of finding an electron in close proximity to another, as inaccurate. Therefore methods in addition to the HF, collectively referred to as post-HF, are executed to account for electron correlation (since spin using the HF method is only partially accounted for). These include both *ab initio* and semi-empirical methods. While the former is strictly quantum mechanical, the latter fits calculated results to experimental values and uses tailored mathematical functions to describe molecular properties. Predominantly semi-empirical methods, by way of DFT are applied in the current work, and for this reason only DFT is discussed in the following section.

2.4.3.1 Density Functional Theory

The objective of density functional theory is to replace the many-body electronic wavefunction with electronic density. This is achieved by mapping the ground state electron density, ρ, with the ground state wavefunction and therein reducing the complexity of the Schrödinger equation. Since, the many body wavefunction of an n-electron system (dependent on $3n$ interacting electrons), may be replaced by the electron density (which is expressed as a function of the three spatial coordinates, x, y, and z), the electronic structure calculations are simplified.[21]

This idea of electron density as a functional originated in 1927 from the Thomas-Fermi model,[29] which was used to calculate the energy of an atom by representing its kinetic energy as a function of the electron density. The result was largely inaccurate and remained so, on addition of the exchange energy functional in 1928 by Dirac,[30] due to misrepresentations of the kinetic and the exchange energies, as well as having no appreciation of the electron correlation.

In 1964, Hohenberg and Kohn (HK) unveiled two pivotal theorems.[31] The first was an existence theorem, stating that for a fixed molecular geometry, the ground state wavefunction is a functional of the ground state electron density. The second theory suggested that the ground state electron density distribution minimises the total electronic energy of the system and could be determined *via* a variational method i.e. it is self consistent.

In theory, by constructing an electronic Hamiltonian with electron density as the function, the energy or indeed any ground state property of a molecular system could be

attained, in an equivalent manner to that from explicit solutions of the Schrödinger wave equation. The energy evaluated, in terms of electron density, has the form given by Equation [2.11]. It includes contributions from the kinetic energy, T, nuclear-electron attraction, V_{en}, and electron-electron interaction potentials, which are conveniently split into two parts: the coulomb (exchange) potential, J, and the exchange-correlation potential, V_{xc}.

$$E(\rho) = T(\rho) + V_{en}(\rho) + J(\rho) + V_{xc}(\rho) \quad [2.11]$$

The possibility of such a Hamiltonian was very appealing to theoreticians; however, the design of accurate mathematical functionals for the kinetic energy and exchange correlation proved problematic, therefore an alternative approach was sought.

Today the DFT is most commonly implemented through the Kohn-Sham (KS), method,[32] which was introduced in 1965 as an amendment of the HK model. Here, the many body problem of interacting electrons in a static external potential is reduced to non-interacting electrons moving in an arbitrary effective potential. By using a reference system the kinetic energy may be identified exactly from KS orbitals. The resulting KS-DFT equation is analogous in form to the time-independent Schrödinger, with the exception being that the potential experienced by the electrons is expressed as a function of the electron density.

Modelling the electron exchange interaction part of the density functional has remained the main challenge of the KS-DFT method, and was initially accounted for by the local density approximation (LDA).[32] The LDA considers the electron density at the coordinate where the functional is being measured, and correlates this with the exact exchange energy for a uniform non-interacting electron gas. This method has since been adapted to include spin *via* the local spin density approximation (LSDA). Overall, the application of both of these functionals is somewhat limited, as the electron density of molecular systems often deviates significantly from that approximated by the ideal electron gas.[33]

Further improvements to the LDA (or LSDA) include the use of electron density gradients at each coordinate in the system, which account for a non-uniform electron density distribution in the molecular structure.[34] These, in addition to the LDA, and correlations based on alternative gases have led to the generation of many novel functionals, most influentially the BLYP functional. The BLYP was discovered to be

capable of accurately predicting molecular geometries and ground state energies to a level unparalleled by the earlier local density based calculations. But by far the most applied functional for DFT is the Becke three parameter Lee, Yang, Parr hybrid exchange functional, (B3LYP),[35, 36] which is an amendment to the BLYP to include a gradient corrected correlation. This hybrid functional (which incorporates aspects of *ab initio* HF methods) has contributed greatly to the widespread use of DFT, and is shown to calculate energies analogous to those attained using higher post-HF (MP2[‡]) methods, in only a portion of the computing time.[33]

Possessing the exact exchange-correlation potential is vital for accuracy, for both DFT and post-HF methods alike. While comparisons are often made with MP2, DFT by treating the particles in the system collectively is at present lacking in its ability to describe weaker physical properties, such as hydrogen bonding. It is unclear how to logically develop these exchange functionals to extend the application of DFT further; however the model for DFT remains the most convenient for the treatment of larger molecules of the type investigated in this work.

2.4.4 Procedure for Estimating hfccs Using Density Functional Theory

The size of the molecule for which the hfccs are calculated is essential to deciding upon the chosen method of calculation. While post-HF is preferred when dealing with systems containing a few atoms (i.e. $N_{atom} \leq$ 1-5), when the system exceeds 5 atoms DFT is normally recommended.[34] The main reasons are that DFT avoids the expense of the more traditional post-HF methods, by deriving the energy directly from the electron probability density, rather than the molecular wavefunction. Thus, the dimensionality of the problem is drastically reduced, and DFT calculations can be performed faster than post-HF methods. This difference in speed is heightened by the fact that multiple determinant calculations require very large basis sets with high momentum basis functions. Whereas DFT can produce accurate results with relatively small basis sets which are, in principle exact, the post-HF method remains intrinsically approximate.[34]

Within this work all computations were performed using Gaussian 03.[28] The geometry optimisations were first performed using HF approximations to find the optimum molecular structure in a low energy equilibrium state. Thereafter DFT calculations were employed using the B3LYP method combined with 6-31g* basis set, and were executed to the very tight convergence criteria, with an ultrafine grid

[‡] Second order Møller-Plesset Perturbation theory.

specified. Single point calculations undertaken to estimate hfccs were performed from the geometry optimised structures using the B3LYP functional in all instances, combined with the triple-ζ basis set (TZVP),[37] for low computational cost, as well as with the Dunning polarised correlation consistent triple-ζ cc-pVTZ and/quadruple-ζ cc-pVQZ[38, 39] basis sets for further confirmation of the hfccs achieved using a higher level of theory. GaussView[40] visualisation software was used to illustrate all the structures obtained. Further details of the procedures used here can be found in Chapter **4**.

References

1 W. R. Hagen, *Biomolecular EPR Spectroscopy* CRC Press, 2009.

2 L. J. Berliner, S. S. Eaton and G. R. Eaton, *Biological Magnetic Resonance: Volume 19: Distance Measurements in Biological Systems by EPR*, Plenum Publishers, 2001.

3 LabVIEW, 6ii (ed), National Instruments, 2001.

4 N. M. Atherton, *Principles of Electron Spin Resonance*, Ellis Harwood Ltd, 1993.

5 J. E. Wertz and J. R. Bolton, *Electron Paramagnetic Resonance, Elementary Theory and Practical Applications*, Chapman and Hall, 1994.

6 M. Brustolon and E. Giamello, *Electron Paramagnetic Resonance: A Practitioners Toolkit*, John Wiley & Sons Ltd, 2009.

7 J. A. Weil, J. R. Bolton and J. E. Wertz, *Electron Paramagnetic Resonance: Elementary Theory and Practical Applications*, Wiley-Interscience, 1994.

8 A. F. Parsons, *An Introduction to Free Radical Chemistry*, Blackwell Science, 2000.

9 G. D. Smith and R. A. Palmer, *Handbook of Vibrational Spectroscopy, volume 1, Theory and Instrumentation*, John Wiley & Sons Ltd, 2002, and references therein.

10 M. W. George, M. Poliakoff and J. J. Turner, *Analyst*, 1994, **119**, 551.

11 A. G. Neville, C. E. Brown, D. M. Rayner, J. Lusztyk and K. U. Ingold, *Journal of the American Chemical Society*, 1991, **113**, 1869.

12 Specac, http://www.specac.com/shop/transmission/complete-omni-cell-for-liquids.

13 J. M. Hollas, *Modern spectroscopy*, 2004.

14 B. C. Vink, *Time Resolved Infrared Studies of Weak Magnetic Field Effects on Radical Pair Reactions*, University of Leicester, Thesis, 2007.

15 T. J. Johnson, A. Simon, J. M. Weil and G. W. Harris, *Applied Spectroscopy*, 1993, **47** (9), 1297.

16 P. R. Griffiths, B. L. Hirsche and C. J. Manning, *Vibrational Spectroscopy*, 1999, **19**, 165.

17 G. M. Harris and J. E. Willard, *Journal of the American Chemical Society*, 1954, **76** (18), 4678.

18 L. Hermosilla, P. Calle, J. M. García de la Vega and C. Sieiro, *Journal of Physical Chemistry A*, 2005, **109**, 1114.

19 M. T. Nguyen, S. Creve and L. G. Vanquickenborne, *Journal of Physical Chemistry A*, 1997, **101** (17), 3174 and references therein.

20 E. Schrödinger, *Physical Review*, 1926, **28** (6), 1049.

21 C. J. Cramer, *Essentials of computational chemistry: theories and models*, John Wiley & Sons Ltd, 2004.

22 M. Born and J. R. Oppenheimer, *Annals of Physics*, 1927, **79**, 361.

23 D. R. Hartree, *Proceedings of the Cambridge Philosophical Society*, 1928, **24**, 328.

24 V. A. Fock, *Zeitschrift für Physik*, 1930, **61**, 126.

25 P. W. Atkins, *Physical Chemistry*, Sixth Edition, Oxford University Press, 1998.

26 W. Pauli, *Zeitschrift für Physik*, 1925, **31**, 765.

27 C. C. J. Roothaan, *Reviews of Modern Physics*, 1951, **23**, 69.

28 M. J. Frisch, G. W. Trucks, H. B. Schlegel, G. E. Scuseria, M. A. Robb, J. R. Cheeseman, J. A. Montgomery, T. Vreven, K. N. Kudin, J. C. Burant, J. M. Millam, S. S. Iyengar, J. Tomasi, V. Barone, B. Mennucci, M. Cossi, G. Scalmani, N. Rega, G. A. Petersson, H. Nakatsuji, M. Hada, M. Ehara, K. Toyota, R. Fukuda, J. Hasegawa, M. Ishida, T. Nakajima, Y. Honda, O. Kitao, H. Nakai, M. Klene, X. Li, J. E. Knox, H. P. Hratchian, J. B. Cross, V. Bakken, C. Adamo, J. Jaramillo, R. Gomperts, R. E.

Stratmann, O. Yazyev, A. J. Austin, R. Cammi, C. Pomelli, J. W. Ochterski, P. Y. Ayala, K. Morokuma, G. A. Voth, P. Salvador, J. J. Dannenberg, V. G. Zakrzewski, S. Dapprich, A. D. Daniels, M. C. Strain, O. Farkas, D. K. Malick, A. D. Rabuck, K. Raghavachari, J. B. Foresman, J. V. Ortiz, Q. Cui, A. G. Baboul, S. Clifford, J. Cioslowski, B. B. Stefanov, G. Liu, A. Liashenko, P. Piskorz, I. Komaromi, R. L. Martin, D. J. Fox, T. Keith, M. A. Al-Laham, C. Y. Peng, A. Nanayakkara, M. Challacombe, P. M. W. Gill, B. Johnson, W. Chen, M. W. Wong, C. Gonzalez and J. A. Pople, *Gaussian 94, revision D.01* 2004, Wallingford CT.

29 L. H. Thomas, *Proceedings of the Cambridge Philosophical Society*, 1927, **23** (5), 542.

30 P. A. M. Dirac, *Proceedings of the Cambridge Philosophical Society*, 1930, **26**, 376.

31 P. Hohenberg and W. Kohn, *Physical Review*, 1964, **136**, B864.

32 W. Kohn and L. J. Sham, *Physical Review*, 1965, **140**, A1133.

33 M. Head-Gordon, *Journal of Physical Chemistry*, 1996, **100**, 13213, and references therein.

34 W. Kohn, A. D. Becke and R. G. Parr, *Journal of Physical Chemistry*, 1996, **100**, 12974.

35 A. D. Becke, *Journal of Chemical Physics*, 1993, **98**, 5648.

36 C. Lee, W. Yang and R. G. Parr, *Physical Review B*, 1998, **37**, 785.

37 N. Godbout, D. R. Salahub, J. Andzelm and E. Wimmer, *Canadian Journal of Chemistry*, 1992, **70**, 560.

38 K. A. Peterson, R. A. Kendall and T. H. Dunning, *Journal of Chemical Physics*, 1993, **99**, 9790.

39 K. A. Peterson, R. A. Kendall and T. H. Dunning, *Journal of Chemical Physics*, 1993, **99**, 1930.

40 R. Dennington, II., T. Keith, J. Millam, K. Eppinnett, W. L. Hovell and R. Gilliland, *GaussView*, version 3.09; Semichem: Shawnee Mission, KS. 2003.

3. Catecholamine Mediated Iron Liberation from Immune Defence Proteins Transferrin and Lactoferrin

Microbial endocrinology, a term conceived in the early nineties is a newly recognised interdisciplinary approach to probing the development of infectious disease. The objective of this field is to rationalise the pathway(s) by which microbes can utilise host hormones and related chemicals, to initiate the growth of pathogenic processes. This can thereby suppress the innate immune system and can often lead to infection in the host. Interest in this area focuses on catecholamines (along with their derivatives), specifically norepinephrine, epinephrine, and dopamine, where the former are referred to as *fight or flight* hormones due to their incidence in the body in response to stress. The first documented enhancement of Gram-negative bacteria cultures by stress hormones arose in 1992.[1] Further work has since detailed that microorganisms have evolved specific methods of detecting these hormones, which they seem to regard as environmental cues to trigger the production of proteins that are required for pathogenic processes.

Iron as the key nutritional element essential for bacterial growth in all humans, mammals and bacteria alike, forms part of the underlying mechanism. As do the catecholamines, which have been shown to enhance bacterial growth through provision of normally inaccessible host iron (bound by transferrin and lactoferrin).[2] Host defence mechanisms in the body naturally withhold iron to retain bacteriostasis and it is this bound iron which pathogens must sequester to mediate bacterial growth.

This chapter is concerned with determining the role of catecholamines in enabling the capture of sequestered iron and the potential clinical applications of EPR. The first is addressed by recording the EPR spectra of the high spin iron(III) at the transferrin (or lactoferrin) binding sites. The binding site (either the N- or C-terminal) with and without iron is pictured in Figure 3.1 for reference. This is followed by monitoring the modifications in the characteristic transferrin (or lactoferrin) di-peak EPR spectrum on addition of the chosen catecholamines. The aim, by investigating the binding status of transferrin, is to predict or support a mechanism by which iron removal from transferrin may occur. The studies into the clinical applications of EPR are similar to those already mentioned; however for this, lower physiologically relevant concentrations of the catecholamines are used and whole blood serum is used as the source of transferrin.

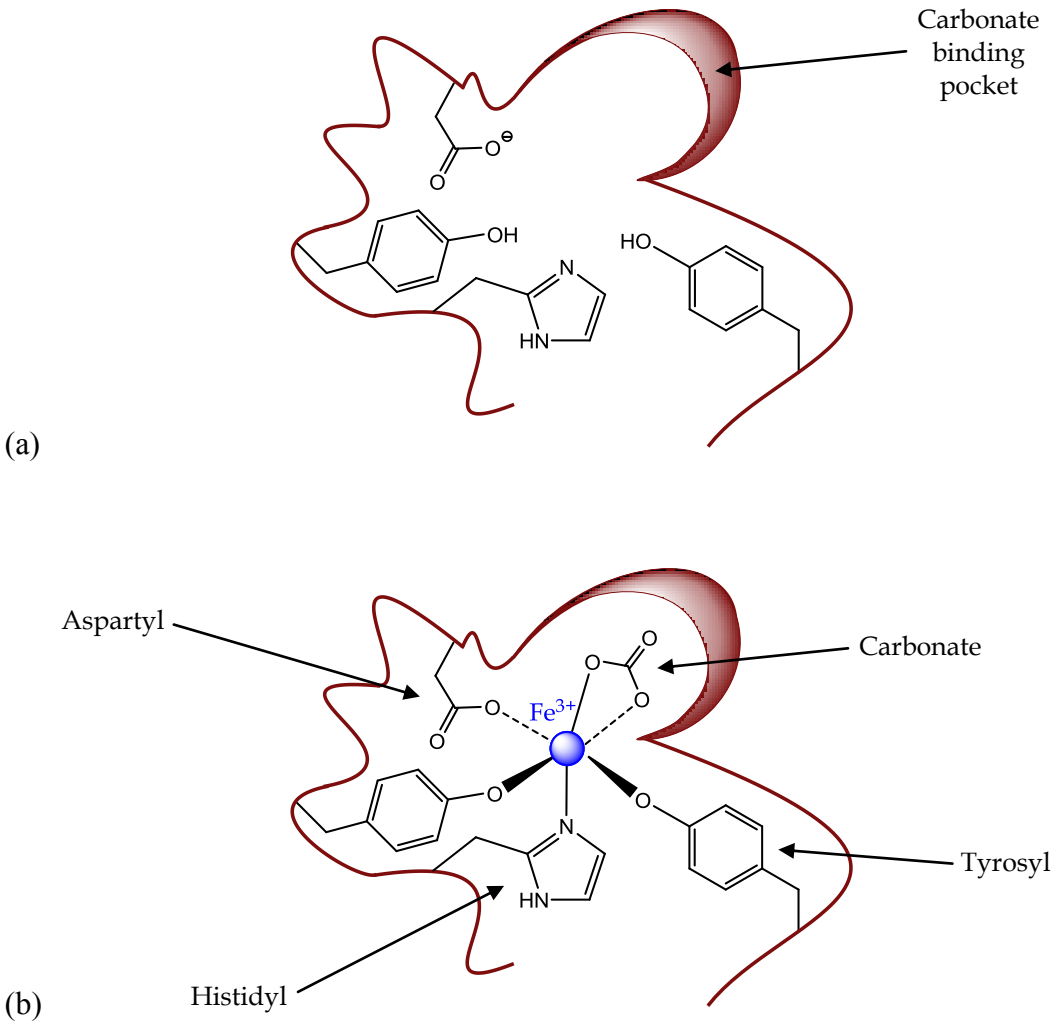

Figure 3.1 Transferrin binding site. (a) Is without and (b) Is with iron(III). The iron(III) is bound as a six-coordinate structure, by two tyrosyl, one histidyl, one aspartyl and a carbonate ligand. All three forms of transferrin bind 2 ferric irons and 2 counter ions (CO_3^{2-}) per protein.

3.1 Iron Transport and Iron in Infection

Transferrin (Tf) is a glycoprotein present in mammals. Its physiological role in serum is to complex with iron(III) and release it to iron (Fe) dependent cells. In the body, Tf may adopt three forms, serum Tf (or serotransferrin) as described, lactoferrin (Lf) from mucosal secretions and ovotransferrin (ovo-Tf), from the albumin of eggs. The concern addressed in this work, resides with the two aforementioned iron proteins, though it is reasonable to predict the outcome would be similar for ovo-Tf.

Tf owns one of the highest metal binding affinities recorded, revealing an affinity of 10^{-23} M for ferric iron. It is able to specifically yet reversibly bind with Fe(III) at two

separate locations, labelled the N-terminal and C-terminal. Strictly, since Tf can bind two ferric ions it may exist in up to four iron binding states, iron-free (apo), iron-replete (di-ferric/holo) and mono-ferric; where a single iron is bound to either the N- or C-terminus. The concentration of serum Tf is typically 35 μM and approximately 70 % of this exists in the non-iron bound apo form.[3]

Both Tf and Lf are structurally similar; however, the binding affinity of Lf is 300 times higher than that of Tf, making it well adapted to the secretions in which it is found. Considering the partially iron saturated state of Tf and Lf, a modest 10^{-16} M concentration of free iron circulates in serum (or in host tissues), and infectious bacteria normally require at least 10^{-6} M to grow *in vivo*.[4, 5]

Upon infection, the primary mammalian defence mechanism is to utilise the surplus binding capacity of Tf (apo form) by seizing any remaining free iron, further removing the potential nutrient sources from serum. This intentionally low concentration of iron available in serum should render pathogens unable to grow. Nevertheless, bacteria do multiply *in vivo*, indicating the evolution of specific mechanisms that disturb the homoeostasis by removing the Tf bound iron. Two types of iron capture are known. Bespoke Tf-binding proteins (Tbps) may specifically bind to the Tf of their host, reduce and lift the iron directly. Studies that support this noted that deliberate inactivation of the Tbps, in several species, resulted in a significant decrease in virulence, thereby exemplifying the importance of bacterial access to Tf (and Lf) in the growth of infectious disease.[4] Alternatively, bacteria may synthesise a species with a superior Fe(III) binding affinity to capture the complexed iron from the host proteins. This occurs for Tf and other forms of bound iron, such as ferritin (iron storage protein), alike. Upon the cusp of iron deficiency such structures, known as siderophores; typically catecholate or hydroxamate molecules of low molecular weight (MW), are synthesised. Once Fe(III) is freed the role of the siderophore is to assist iron internalisation into the bacterial wall. This proceeds *via* specific *tonB* receptor proteins located at the outer (bacterial) cell membrane. Due to the strength of the ferric binding in siderophores, ferric reductases within the bacteria are necessary to reduce and remove the bound iron. This model also supports the siderophores to be recyclable, so only a limited concentration need be produced. Importantly, not all microorganisms rely on siderophores; however, the implication of a reduction mechanism for removing iron is common. In, for example, *Clostridium perfringens*, iron capture is facilitated by reduction of the Tf bound Fe(III) to Fe(II), by creating a microanaerobic environment.[4]

Often, in the presence of Fe-Tf (iron bound transferrin) and Fe-Lf alone, certain siderophores prove ineffective at iron capture and require the aid of catecholamines (CAs) to mediate removal.[2] Moreover catecholamine induced bacterial growth among certain species of Gram-negative bacteria have also been reported in the absence of either Tf or Lf, thus indicating a second type of mechanism may also simultaneously occur.[6, 7]

3.2 Catecholamine Production in Mammals

Derived from tyrosine, catecholamines are a family of stress hormones which form part of the sympathetic nervous system (SNS). Leading to the point of catecholamine secretion by the adrenal medulla in response to stress (both physiological stress and physical trauma), the SNS operates only at a basal level. The catechol (3,4-dihydoxybenzoyl) group as shown in Figure 3.3 forms the foundation of all the accordingly named catecholamines. To this substituted ortho-hydroxy benzene ring structure, primary or secondary amine chains are attached (see Figure 3.2).

The mammalian pathway for catecholamine production originates from L-dihydroxyphenylalanine (L-dopa) sourced from food as phenylalanine, or directly from dietary protein containing tyrosine. Dopamine (Dop) is generated first, then is sequentially converted to norepinephrine (NE) and finally epinephrine (Epi), *via* the mechanistic route given in Figure 3.2.

3.3 The Therapeutic Use of Catecholamines

As well as naturally in the body, catecholamines also have significant clinical applications as positive inotropes (heart stimulants). They are administered in up to half of all intensive care units (ICUs) for their hemodynamic and renal effects.[8] The most widely used catecholamines are Dop and NE and often, both of these are infused together.

Dop can be infused at rates in excess of 10 $\mu g\ kg^{-1}\ min^{-1}$, to selectively stimulate α-adrenergic receptors. Since NE also acts through the α-adrenergic receptors some of this response may be attributed to NE, produced from the metabolism of Dop *via* the scheme in Figure 3.2. Lower doses, 3-10 $\mu g\ kg^{-1}\ min^{-1}$ trigger β-adrenergic receptors, while dopaminergic receptors require only 0.5-3 $\mu g\ kg^{-1}\ min^{-1}$.

Catecholamines

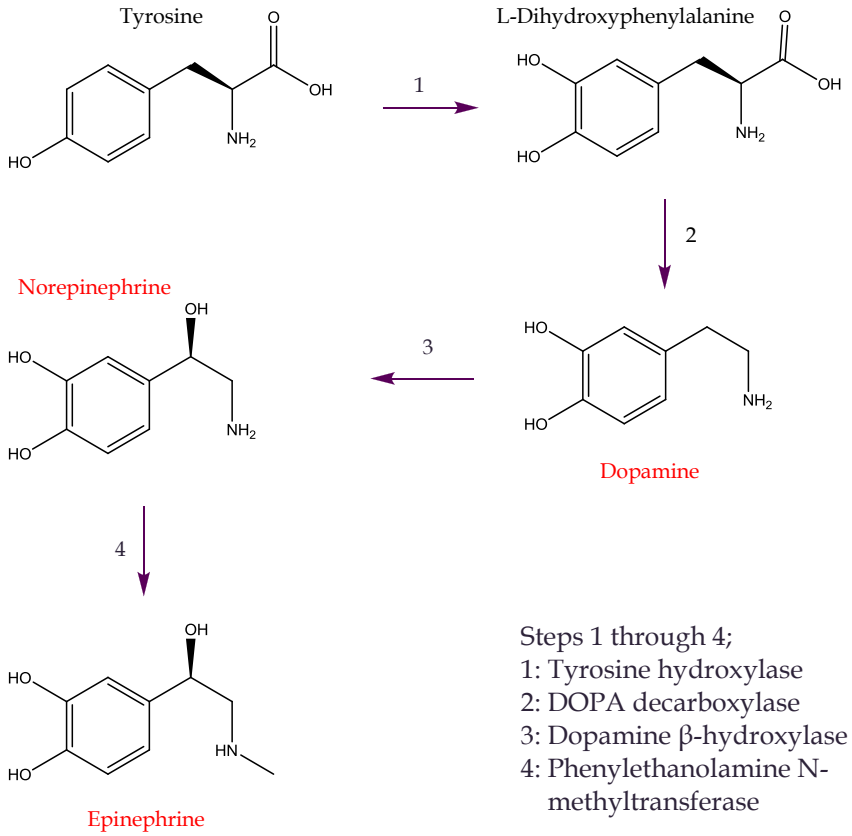

Figure 3.2 Catecholamine Biosynthesis illustrates the pathway for catecholamine production in the body, originating from non-catecholamine tyrosine. This forms L-dihydroxyphenylalanine (L-dopa), dopamine (Dop), norepinephrine (NE), and epinephrine (Epi) *via* the steps indicated. Common abbreviations are indicated in brackets and the structures familiar to the present work are highlighted in red. The enzymes for conversion are indicated by numbers 1-4, and step 1 is rate limiting.

Catechol Moiety

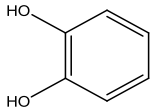

Inotropes

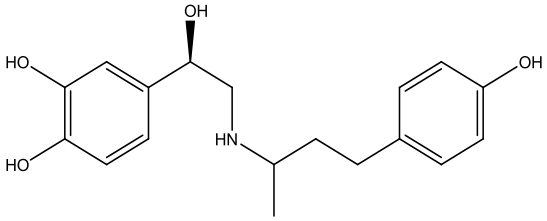

Dobutamine

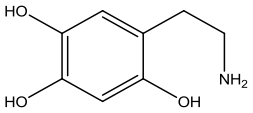

6-Hydroxydopamine

Other Catechol Species

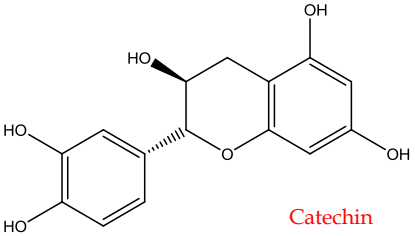

Catechin

Anion Structure

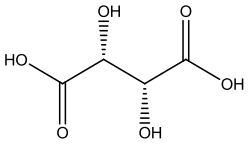

Bitartrate

Figure 3.3 Catechol containing species shows the structures for the catechol moiety along with inotropes dobutamine (Dob) and 6-hydroxydopamine (6-OHDA). While catecholamines are naturally occurring throughout the mammalian body, the inotropes shown are synthetic. Other structures referred to in the main text are catechin and the bitartrate anion. All species highlighted in red are relevant to the current work and abbreviations are given in brackets.

The chosen dose of inotrope depends on the required function and routinely for renal treatment, low doses are used. Measurements of the resulting plasma concentrations of Dop are revealed to be dependent on the dose as indicated earlier, in addition to the category of patient receiving it.[9]

The serum levels of the exogenous drugs are governed by the interplay of two key processes, pharmacokinetics and pharmacodynamics, which consider both the influence of the body on the drug and the drug on the body. In healthy individuals the drugs are rapidly metabolised and removed (typically within 2-2.5 minutes). However, patients with renal dysfunction are shown to have considerably lower Dop clearance levels, thus allowing an accumulation of the catecholamines in serum.[10] In either case, the interpatient variation in plasma Dop levels are often unpredictable from the infusion rates and those with septic shock and head trauma reveal elevated levels of Dop in their blood serum. A noteworthy study of septic critically ill patients, measured the levels of Dop in serum after infusion with low dose 2 $\mu g\ kg^{-1}\ min^{-1}$. This revealed a 1.4 µM concentration after 60 minutes and a further increase to 3.5 µM for higher doses of 6 $\mu g\ kg^{-1}\ min^{-1}$, both of these confirm significant enhancements over the baseline amount of 0.04 µM.[9] Clinical investigations of NE also show variable plasma concentrations in response to infusion. From these studies it was proposed that high doses may saturate the natural metabolic pathway and could therefore rationalise the often observed non-linear pharmacokinetics.

Since Dop and NE are both administered on infusion their effects should be additive. Furthermore, catecholamine metabolism in the body may affect the levels of the other (not directly infused) catecholamines in serum. For example, the breakdown of the hormone Dop, produces both NE and Epi *via* the route given in Figure 3.2, and this is just one of the many pathways available to covert these hormones into other catecholamine derivatives. Clearly, the potential for a high catecholamine concentration in serum exists and is more prevalent for the ill (due to stress), who are further supplemented with catecholamines for organ support. For these patients the implication of catecholamines in iron theft from Tf could alter the bacteriostatic nature of their blood. This may allow their serum to become an accessible source of iron, thus enabling bacteria to breed in the body, whilst in a particularly vulnerable state.

3.4 Catecholamines, Inotropes and Iron Acquisition by Bacteria

The correlation between trauma associated sepsis, and septic shock mortality with heightened levels of one or more catecholamines in mammals, have been studied in considerable depth. It is now well accepted that the body is more prone to illness during episodes of stress.[2, 6, 11] A curious outcome given that earlier stress models of exposure to catecholamines had consistently demonstrated an increase in the capacity of macrophages (of the innate immune systems) to eliminate invading pathogens. Though evidently, catecholamine exposure renders the host more susceptible to infection.[12] The direct role of bacteria in response to the released neurochemicals were first examined by Lyte and Ernst.[1]

The study by Lyte and Ernst[1], who pioneered this area of microbial endocrinology research, involved *in vitro* work monitoring a minimal salt-serum-supplemented medium (serum-SAPI), incubated with NE, Epi, Dop, Dopa and varying levels of selected Gram-negative bacteria; *Escherichia coli* (*E.coli*, enteric pathogen), *Yersinia enterocolitica* (enteric pathogen) and *Pseudomonas aeruginosa* (opportunistic pathogen). An increase in the levels of bacteria after defined incubation periods was revealed. This highlighted changes in the growth of the strain of Gram-negative bacteria in response to the stress hormone used, and NE was found to be most potent to all strains. Many *in vitro* studies since have shown a similar outcome when using the catecholamines and their pharmacologically inactive metabolites. Recorded data on the enhanced growth of enteric pathogens *E.coli*[11, 13] and *Salmonella*[14] is in particular quite extensive.

NE is documented as being the most effective growth stimulator of the catecholamines. The magnitude of the growth in serum or blood is recorded to be up to 10^5 higher than in its absence, for the same 24 hour period.[6, 11, 15] Similar effects of catecholamines are demonstrated for bacteria common amongst humans and frogs,[16] as well as in other species such as non-vertebrates, specifically oysters.[17] Yet, the most frequently tested of strains remain the Gram-negative bacteria of the human gut; an area controlled by the enteric nervous system (ENS). It is inundated with NE and Dop sympathetic nerve terminals and here, catecholamines exist in secretions even under normal conditions. The gut is also home to approximately 10^{12} microorganisms and so elevated levels of catecholamines should have the greatest impact in this area of the body. The localised production of catecholamines occurs due to heightened levels of tyrosine hydroxylase, which is triggered through acute stress. This enzyme catalyses the

rate limiting step in the Dop/NE synthesis pathway, see Figure 3.2.[18] Naturally, to counteract the excessive presence of catecholamines, mammals have evolved mechanisms to regulate levels in the gut *via* appropriately located catecholamine degrading enzymes, for example, phenol sulfotransferase, which are common along the gastrointenstinal (GI) tract.

Numerous examples of a sustained increase in catechol and related stress hormones have been reported over the duration of, or following infection. Examples include cortisol (Glucocorticoid), Epi, and NE, which are found in saliva during stress and coincide with the onset of periodontal disease.[19] As well as increases in the norepinephrine and epinephrine levels of plasma in patients suffering septic shock.[20] Moreover, catecholamine initiated growth is not isolated to one region or bacterial species, since these hormones are widespread throughout the human body.

Catecholamines also enhance bacterial virulence. In the case of respiratory pathogens such as *B. bronchiseptica*, triggered exposure with catecholamines evokes the production of *BfeA* siderophore receptors,[21] which are essential for bacterial uptake of iron in the mucosal secretions. The ensemble of data available has also highlighted the importance of a certain catechol moiety present among the range of molecules: catecholamines (norepinephrine, epinephrine, and dopamine), inotropes (isoprenaline, dobutamine and their metabolites) as well as plant extracts (catechin, caffeic acid, chlorogenic acid and tannic acid), which are all capable of mediating bacterial growth.[15-17,21,22] Likewise this catechol group is also in siderophores such as *enterobactin*.[11, 23-25] The catechol moiety is proposed to form a complex with the Tf/Lf bound ferric iron, and *via* an unknown manner is able to reduce the iron binding affinity of Tf/Lf for the iron, thus rendering the proteins susceptible to theft. In the case of siderophores, it is understood that capture occurs directly and that they enable transfer of the ferric iron into the bacterial cell for growth. The mechanism by which stress hormones liberate the Tf/Lf iron remains to be determined, though various studies, as reviewed in the following passage, suggest that complex formation does occur.

Insight into the mechanism of catecholamine mediated iron removal was provided by denaturing urea-polyacrymide gel electrophoresis (urea-PAGE), which allowed separation of the four possible binding states of Tf.[15] The incubations of purified holo-Tf with NE, or Dop and bacteria resulted in a loss of the Tf bound iron from the gel data, with the release being catecholamine concentration dependent and the amount liberated in agreement with that required for bacterial growth.[11, 23, 26] Furthermore radio

labelling the iron (^{55}Fe) in combination with passage through non-denaturing (sephadex) gels, implied a stable complex was formed between the NE and ^{55}Fe-Tf. This was interpreted from the identical elution results obtained with and without the addition of catecholamine. This work also concluded that iron loss only occurred under denaturing conditions. Notably, by virtue of NE, it was discovered that iron could also be shuttled from holo-Tf across a protein barrier to apo-Tf.[15] Again this supported the idea of complex formation, though on this occasion between ^{55}Fe-NE, which would enable iron transport and potentially deliver iron directly to the bacteria. Similar patterns were documented for Lf and the addition of excess iron to the incubation mixtures prevented iron loss from Tf or Lf developing.

This concept of an intermediate structure between the catecholamine and Fe, which enables iron transport into bacteria, is further strengthened by studies by Gérard *et al.*[27] Who demonstrate that a complex does indeed form between Fe(III) sourced from inorganic salts and NE. At this stage it is necessary to point out that catecholamines have also enhanced growth for Gram-negative bacteria in the absence of either Tf or Lf, implying the existence of a second route for growth increase. The production of a non-LuxS dependent autoinducer (AI), whose structure is as yet unknown, has been revealed for particular enteric bacteria. It has been shown to promote growth to a level equalling that achievable in the presence of Tf or Lf and the catecholamines. Moreover, the induction of NE-AI requires only 4-6 hours of exposure to NE,[6] following which it maintains its own synthesis, suggesting more long term effects of the localised increases in catecholamines are a possibility.

3.5 The Reduction of Fe(III) to Fe(II) - A Potential Iron Capture Mechanism

Regulation of non-bound iron in the mammalian body is, as discussed, imperative. Not only for reasons concerning bacterial growth, but also its precipitation as insoluble $Fe(OH)_2^+$. This, is able to catalyse the generation of reactive oxygen species (ROS), such as hydroxyl ($^{\bullet}OH$) and superoxide ($O_2^{\bullet-}$) radicals, when in an aerobic environment (see Figure 3.4). The association of ROS with degenerative diseases like Parkinson's have long been established.[28] Consequently, the role of catecholamines in iron removal from the species of ferritin and Tf in plasma is considered pivotal in hindering its progression and the effects of catecholamines have been studied in detail outside the

field of microbial endocrinology. Such studies have offered additional insight to the possible route of catecholamine triggered iron theft from Tf or Lf.[29]

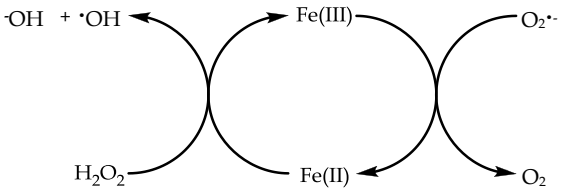

$$O_2^{\bullet-} + H_2O_2 \longrightarrow {}^{\bullet}OH + {}^{-}OH + O_2$$

Scheme 3.4 The production of reactive oxygen species *via* the Fenton/Haber Weiss processes.

The application of optical absorption spectroscopy to an iron(III)-catecholamine complex, in combination with gel filtration studies has revealed that catecholamines possess the ability to reduce iron(III)-bleomycin to a ferrous state. Iron loss ensued *via* the initial complexation of Fe(III) to the catecholamine, which was identified by a signature purple colour. The complex was monitored by absorption during the time course of reduction while the purple colour was gradually removed. This study also agreed that NE had the fastest rate of reduction among the catecholamines and is therefore in agreement with its discussed influence on bacteria.[30]

A mechanism for the catecholamine mediated reduction was proposed by El-Ayaan *et al*,[31] who incubated NE with iron(III) hydroxide. Internal electron transfer in the Fe(III)-NE complex forced the iron to be reduced to a ferrous state and subsequently removed. Thereafter, the catecholamine produced a quinone *via* an intermediate semi quinone. For NE mediated transfer of iron, a minor contribution from outer sphere electron transfer was also recorded. This resulted in the direct formation of the semiquinone and no complex. Whereas for L-dopa, dopamine and epinephrine, monitored in separate studies, catecholate complexes were explicitly formed.[32] Conversely, 6-hydroxydopamine (6-OHDA), a dopamine analogue used for treatment of patients with neuroblastoma, was discovered to react exclusively through outer shell electron transfer and no intermediate complex was detected.[33] While El-Ayaan *et al* did

verify the existence of a NE intermediate complex, able to reduce ferric iron, arguably the medium for the tests were acidic (pH $<$ 3.5) and much lower than the pH 7.5 balance in the body (bar the stomach, where Lf resides), so the mechanism is not necessarily applicable to physiological conditions. Furthermore, this mechanism is only supported for low pH, while at higher pH the formation of bis- or tris-Fe(III) complexes are favoured and these are considered relatively stable toward internal electron transfer.[32] This however, does not eliminate the possibility that binding to a protein, such as Tf in serum, may alter the nature of the iron binding and influence the processes occurring.

A ferric iron reduction mechanism is often implicated as the pathway to iron acquisition from biological proteins such as ferritin. Many *in vitro* models to investigate the mechanistic route use inorganic salts as the source of iron and are therefore equally relevant to Tf/Lf. Moreover, the evolution of pathogenic methods to acquire the tightly bound iron also shares the common theme of iron reduction in some part of the mechanistic route for capture. This indicates that reduction too may be involved when the catecholamine accesses the Tf/Lf bound iron.

Borisenko *et al*[34] examined the interactions of the catecholamine 6-OHDA (4 mM) with Tf (20 µM) in Tris-HCl buffer (10 mM, pH 7.4) using EPR spectroscopy. The incubations were monitored over time and the characteristic di-peak Fe(III) high spin signal was gradually transformed, alluding to a loss of Fe from the Tf for physiological levels of iron saturation. The detailed report considered the various contributions from the presence of oxygen, and competitive redox cycling processes. Three routes for iron release were suggested; reduction of Fe(III) by 6-OHDA, reduction by $O_2^{\bullet-}$, or release as a result of protein damage by $^{\bullet}OH$. Speculation over protein damage arose from the similarity of the new single peak to that anticipated from the tyrosine mutant in the N-lobe of Tf. However, on treatment with cut-off filters of 30 kDa (Tf 80 kDa) the signal was removed, suggesting no Tf protein damage had occurred. Evidence for the first mechanism arose from tests with ferrozine (Fz), a well known iron(II) chelator, added to the Fe-Tf and 6-OHDA mix and performed in the absence of oxygen to eliminate $O_2^{\bullet-}$. No alteration in the shape of the original EPR signal developed, though the amplitude was reduced by 20-40 % in a 2 hour period.

Often, the difficulty in interpreting biological results in an aerobic environment is the complex role of iron and oxygen. Aerobic conditions more relevant to the body should encourage the release of iron from the proteins. This would further propagate

oxidation of 6-OHDA, the production of $O_2^{\bullet-}$, peroxide, and $^{\bullet}OH$ radicals (see Scheme 3.1), thus accelerating the release of iron from Tf. This situation would be complicated further still *in vivo* where the activities of ferroxidase (assists in Fe(III) re-uptake) may affect the availability of iron sourced from Tf.

EPR as demonstrated by Borisenko *et al*[34] offers a powerful tool for probing the direct catecholamine initiated modifications in Tf iron binding. The simultaneous loss from Tf /Lf and subsequent gain by species can be monitored *in situ*, rather than relying on complimentary techniques alone. 6-OHDA due to its toxicity and redox potency has been extensively studied and it is often shown to behave differently to catecholamines.[35] For this reason, it is possible the EPR data on this dopamine analogue may have revealed a unique effect. The present study aims to clarify the binding status of a range of catecholamines to predict or support a mechanism by which iron removal from Tf may occur. The ultimate goal here is to use EPR to monitor alterations in the Tf binding status when exposed to clinical concentration of catecholamines, as are administered widely to ICU patients typically over several days and therein give reason to endorse EPR as a potential diagnostic tool.

3.6 Results and Discussion

The primary aim of this study was to ascertain whether the interaction of catecholamines with the iron in Tf occurred at physiological pH, as well as to determine if the proposed intermediate complex was observable by EPR. Here the pH was maintained using a tris(hydroxymethyl)aminomethane (Tris)-HCl buffer, at pH 7.5. All initial tests were performed on NE and repeated for the other catecholamines or inotropes. Prior to, and subsequent to EPR acquisition, all the Tf catecholamine pellets were immediately retained for further bacterial growth analyses, to determine any increased virulence after catecholamine exposure. The control samples in all the figures are indicated in black and unless shown otherwise, underwent no, or very negligible change in their EPR characteristics over the same period of incubation. In instances where Fe appears without a defined oxidation state it infers Fe(III), i.e. Fe-Tf, and in the absence of an indicated recording time the spectra were gathered within 10 minutes of mixing and the spectra obtained at a temperature of 77 K.

3.6.1 The Interactions of Norepinephrine, Epinephrine and Dopamine with Transferrin at Physiological pH

The signature X-band EPR spectrum of high spin ($S = \frac{5}{2}$) holo-Tf (di-ferric) can be viewed in Figure 3.5 (a). In Tf the Fe(III) occupies a low symmetry site, which is rhombic with some axial character. This gives the EPR spectrum of Tf three g-values; a well defined double peak at a g-value of 4.3, and broader lines at g = 9, and $g < 2$. However, only the former of these peaks is studied for changes in the transferrin iron binding status.

Following an 18 mM addition of catecholamine NE to the holo-Tf buffer mix, the spectrum rapidly modifies to replace the di-peak profile with a new more conventional looking EPR signal. This alteration in the iron-replete Tf signal is indicative of a shift in the Fe-Tf binding characteristics. Consequently, to capture a more gradual transformation of the iron-replete Tf, lower concentrations of NE were necessary.

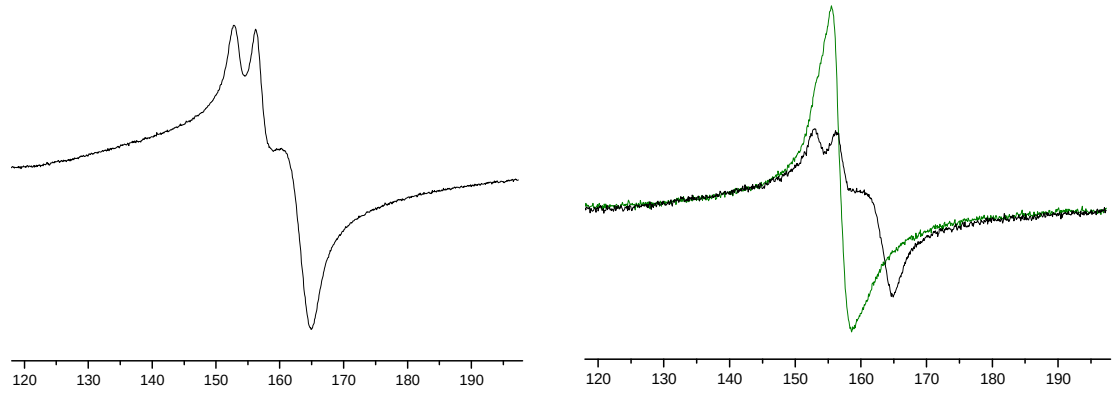

(a) (b)

Figure 3.5 Both EPR spectra exhibit 75 µM (6 mg ml^{-1}) holo-Tf and 10 mM Tris-HCl buffer. (a) Shows the di-ferric Tf EPR spectrum at a g-value of 4.3 and reveals a double peak motif. (b) Shows the overlapped results from identical mixtures to (a) with (green) and without the addition of 18 mM NE; notice the new peak is more intense. Both sets of spectra were acquired using the Bruker EPR spectrometer with a low temperature attachment, as described in Sections **2.1.2** & **2.3.1**. Spectrum (a) was recorded at 10 K while (b) was at the usual 77 K. The clarity of the features of the Tf peak are similar at both temperatures.

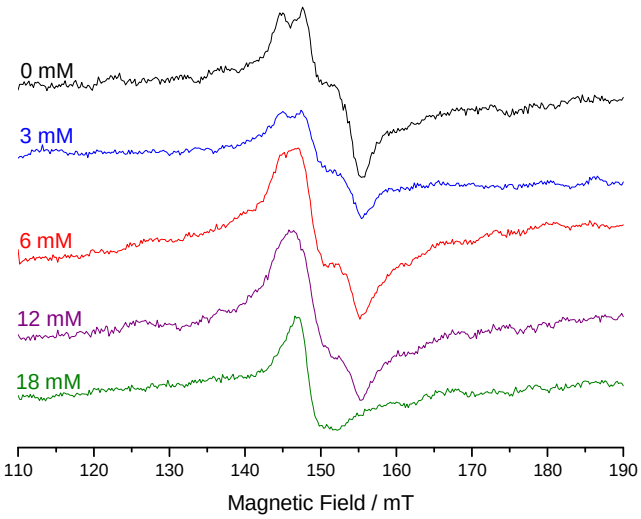

Figure 3.6 The EPR spectra of 75 µM holo-Tf and 10 mM Tris-HCl buffer, with and without various concentrations of NE in the range 0-18 mM. All spectra were recorded using the JEOL EPR spectrometer and a finger dewar. Notably 18 mM NE is required for a complete change of the Tf di-peak spectrum.

The EPR spectra in Figure 3.6 support the change to the 75 µM holo-Tf signal in the presence of NE to be concentration dependant. Here, the spectra for increasing concentrations of catecholamine are displayed in descending order. The two extremes exhibit this evolution of the spectrum most clearly (as included in Figure 3.5 (b)), with 18 mM NE required for a complete transformation of the Fe-Tf signal. Importantly these spectra feature an intermediate transitional stage where the superposition of both the peaks may be deciphered. Although a range of concentrations were originally tested to capture this transition, a selection of the lower concentrations have been omitted due to their similarity with the iron-replete Fe-Tf spectrum alone (data not shown).

Borisenko *et al*[34] offered three possibilities for the cause of a parallel change in 6-OHDA treated Tf. Iron release from Tf, a shift in the valency of the bound iron or protein modification. Simultaneously performed denaturing urea-PAGE containing 6 M urea[36] reveals the removal of iron from Tf as potentially responsible for the EPR transformation recorded (see Figure 3.7).

The gel data confirms the source of iron from holo-Tf to be fully saturated and over time reveals its conversion to mono-ferric and apo forms. Evidently, the complete removal of iron does not occur within the maximum 1440 minutes incubation period and iron loss develops for the N-terminal earlier than the C, which is in agreement with

stronger iron binding at the C-terminal. This trend of selective iron assimilation from the two lobes is common to all the catecholamines, though there is a variation in the iron removal rates between them.[37] The increasing concentrations of NE in the EPR spectra reflect this gradual loss of iron by a steady removal of the double peak. This is accompanied by the emergence of the new signal, proposed to be from the iron now binding to the catecholamine and is most consistent with a Fe(III)-catecholamine complex, due to the g-value centred at ~ 4.3.

The effects of the NE concentrations used in Figure 3.6 are immediate and the transformations seen occur within the 10 minutes required for sample preparation, freezing (refer to Section **2.3.1**) and recording. Predictably, this timescale differs from that of the urea-PAGE analysis, which concludes that NE mediated removal of iron from transferrin evolves on a timeframe of hours, not minutes. This occurrence is also supported in the literature.[15] The concentrations of NE and Tf used for the urea gel data here (4 mM NE) and in literature (≥ 250 µM NE) are both far lower than that in the EPR study. By allocating a parallel incubation period at these lower concentrations one could envisage an equivalent result to be attained using EPR (lower concentrations are considered later). NE concentration dependent iron removal from Tf has previously been highlighted by denaturing urea-PAGE,[15] where in a similar manner to here, the complete removal of iron was never achieved. It has however, been documented for other catechol containing compounds such as dihydroxybenzoic acid (DHBA), three of which are present in siderophore enterobactin.[38]

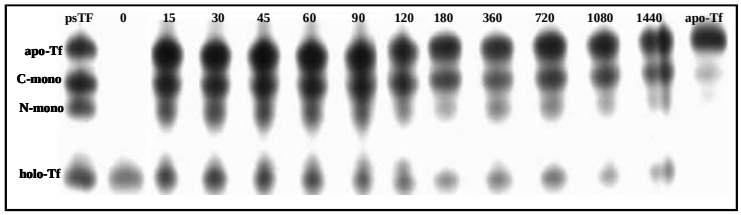

Figure 3.7 Urea gel data of 20 µM holo-Tf, with Tris-HCl buffer and 4 mM NE, after loading 40 µg of Tf per stack. The markers reveal the timescale for iron removal quoted in minutes and abbreviations include; psTf as partially saturated transferrin, C-mono and N-mono indicate the mono-ferric forms of transferrin and apo-Tf is transferrin in the absence of bound iron.[36]

The sensitivity of the EPR instrument used is influential to interpreting the data correctly. Due to the larger margin for error and the associated difficulty in tuning when using a dewar on the JEOL system, often the signal magnitudes of the Tf samples could not accurately be compared as the intensity was found to vary for the same sample on successive runs, regardless of the spectrometer settings. Data from the JEOL spectrometer will therefore, on occasion, provide a purely shape based analysis. For example, compare Figure 3.6, with identical spectra in Figure 3.5 (b). The latter was recorded on the Bruker EPR spectrometer, which incorporates a low temp unit to supply a continuous stream of helium. This caused minimum disruption of the system and demonstrated a repeatable increase in the magnitude of the new peak, which was not evident from the data in Figure 3.6. This increase in magnitude is unusual, since the intensity of the EPR signal is proportional to the paramagnetic ion content of the sample (calculated by double integration) and here the iron concentration remains constant. An increase would imply a greater availability of iron following addition of the catecholamine, which could only be rationalised by the uptake of free iron present in the holo-Tf sample to maintain its saturation.

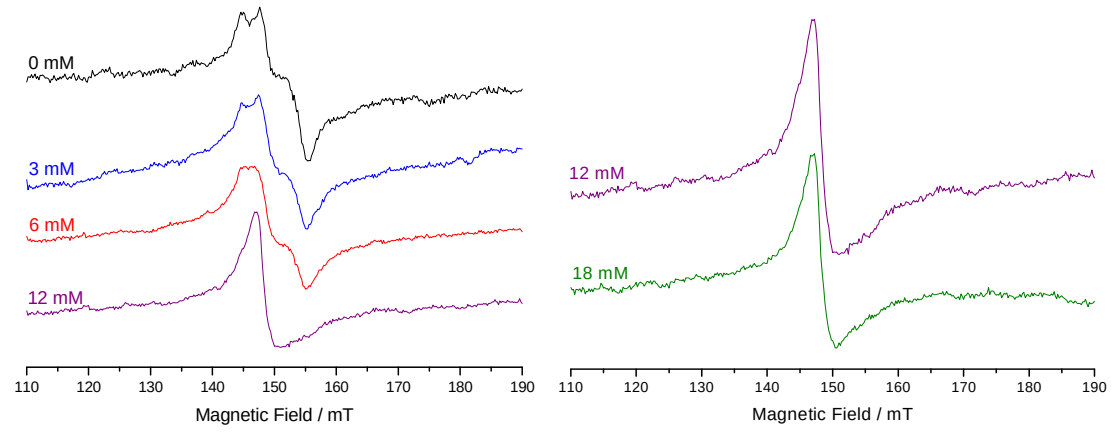

(a) (b)

Figure 3.8 (a) Displays the EPR spectra of 75 µM holo-Tf and 10 mM Tris-HCl buffer, with and without select concentrations of Epi in the range 0-12 mM. Notice that 12 mM Epi is required for the complete removal of iron bound to Tf, a lower concentration than that required for NE. (b) Shows the EPR spectrum from an 18 mM Epi addition to the mixture compared with the 12 mM Epi given in (a). The immediate signal reduces. All spectra were recorded using the JEOL EPR spectrometer.

Referring back to Figure 3.6, one would predict an initial decrease in the intensity of the iron-replete Tf signal given that the removal of iron is occurring. This would thereafter be overshadowed by the emergence of the new peak. Both these events are borne out in the data shown, though the 18 mM NE concentration result counteracts the prediction, thereby highlighting the possibility of error when comparing intensities for the JEOL instrument.

A parallel trend to that seen for NE is noted for Epi, where the steady removal of iron accompanies EPI's increasing addition (see Figure 3.7 (a)). Curiously, however, the complete removal of iron from Tf occurs for a lesser 12 mM concentration of Epi, compared with the 18 mM required for NE. NE would typically be expected as faster, given the evidence of increased bacterial responsiveness that was discussed in Section **3.4**. Further additions of Epi, totalling 18 mM, served to consistently reduce the signal intensity of the Tf containing Fe-Epi signal, thus implying that some iron may have been freed from the resulting Fe-Epi complex into solution (Figure 3.8 (b)). Alternatively some of the Fe(III) may have been reduced by the catecholamine, which would be in agreement with the proposed mechanism. On longer incubation, a more extensive removal of iron was also noted for the lower concentrations of NE and Epi used in this work and required up to a few hours dependent on the concentration of catecholamine (data not shown). Therefore the modification of the Fe-Tf spectrum is both time and concentration dependant.

The urea-PAGE supplementary experiments of Tf incubated with Epi, support the Fe removal from holo-Tf to a mono-ferric or apo form to be faster than for NE, though overall a very similar removal and component profile is obtained for Epi (the data is viewable in the reference).[36]

Identical holo-Tf, Tris-HCl buffer and catecholamine concentration mixes to the aforementioned were monitored for Dop (see Figure 3.9). This revealed a notable yet smaller change in the Tf iron binding status, with the spectra still heavily featuring a double peak well after the addition of 18 mM Dop. Recall that an 18mM concentration previously provided immediate and total NE facilitated removal of iron (Figure 3.6).

A selection of the Tf Dop EPR spectra is included in Figure 3.9, where a characteristic drop in the shoulder of the Tf peak signifies iron removal is occurring. This prompted the testing of higher Dop concentrations, which showed that for an immediate transformation of the di-peak Tf signal a comparatively large concentration of Dop was necessary.

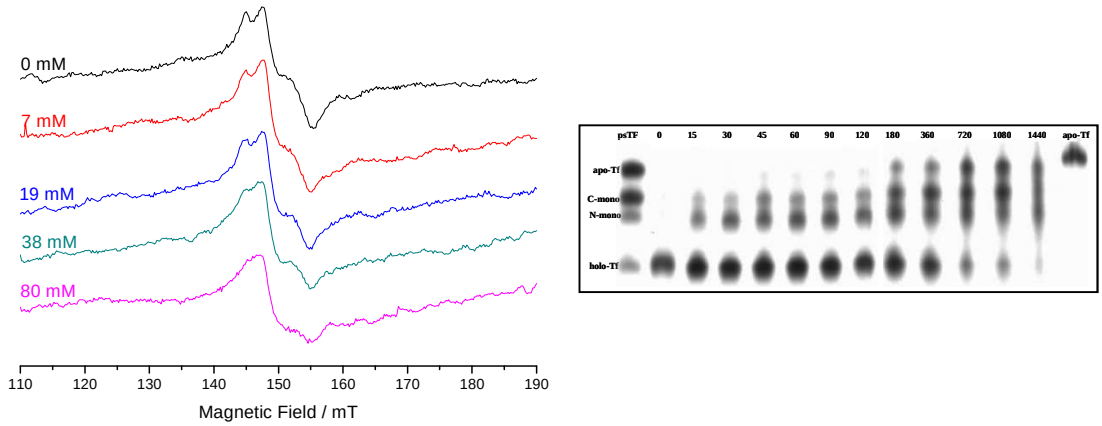

(a) (b)

Figure 3.9 (a) Shows the EPR spectra of 75 µM holo-Tf and 10 mM Tris-HCl buffer, with increasing concentrations of Dop, recorded using the JEOL EPR spectrometer. Notice, the Tf incubated with the highest concentration of Dop (80 mM) still exhibits some bound Fe-Tf character. (b) Shows the urea-PAGE data for 20 µM holo-Tf, with Tris-HCl buffer and 4 mM Dop incubated with over different time periods. Both datasets prove that Dop initiated Tf iron loss is much slower than for the other catecholamines; NE and Epi. For a list of the abbreviations used in the urea-PAGE, consult Figure 3.7.

The di-ferric peak did eventually disappear at a concentration of 80 mM Dop, however, the Tf bound iron was still distinguishable in the spectrum and clearly the complete removal had not developed. Further concentration increases were not pursued.

Urea-PAGE established a steady reduction in the iron saturation of holo-Tf arising from the Dop initiated loss of iron. Unusually, at early incubation periods, selective release of iron occurred from the C-terminal faster than the N. With time, these rates were interchanged, see Figure 3.9 (b).[36] Focusing on the 1440 minutes track, an equal distribution of the mono-ferric components of Tf and apo-Tf are revealed, with all the markers being narrower and less intense than for the other two catecholamines. This differing result suggests some mechanism, unknown at present, may be interfering with the progression of iron loss for the Dop treated Tf samples.

In view of the more gradual release rate of iron from transferrin that occurs in the presence of Dop, 12 mM Dop was incubated at - 20 °C with holo-Tf and Tris buffer. The resulting EPR spectra were collected using the Bruker EPR spectrometer pictured in Section **2.1.2**, as are all the spectra included from this point onward. Up to 24 hours was required for complete removal of iron from Tf and repeated exposure to air by

reanalysing the pellets significantly hindered iron loss, as is demonstrated by the spectra in Figure 3.10 (b). The spectra in Figure 3.10 (a) show the signal from a Tf treated Dop pellet, which after initial recording was kept in a sealed vessel and frozen, with minimal exposure to air. Figure 3.10 (b) displays spectra for an identical Tf Dop sample whose exposure to oxygen was recurring, at the intervals specified, where following 43 hours of incubation the complete removal of iron had not yet developed.

The clear variation in the iron removal times of Dop and NE or Epi could, on initial inspection, be due to some structural dissimilarity. This is unlikely, given that the only functional group variation between the neurochemicals is the absence of one hydroxyl group in Dop, which may influence its affinity for iron binding, though one would predict not so dramatically (see Figure 3.2 for the structures).

The more feasible explanation arises from the nature of the anion; NE and Epi were purchased as bitartrate salts, whereas Dop exists solely in the form of a hydrochloride. Fortunately, both NE and Epi may be purchased in bitartrate and hydrochloride forms, allowing identical urea gel and EPR analyses, to be performed for both sets of catecholamines. The results obtained for NE and Epi sourced from the hydrochloride salts yielded similar trends to those for Dop. This concludes that it is the chloride ions, which had such a marked effect on the iron removal rates.

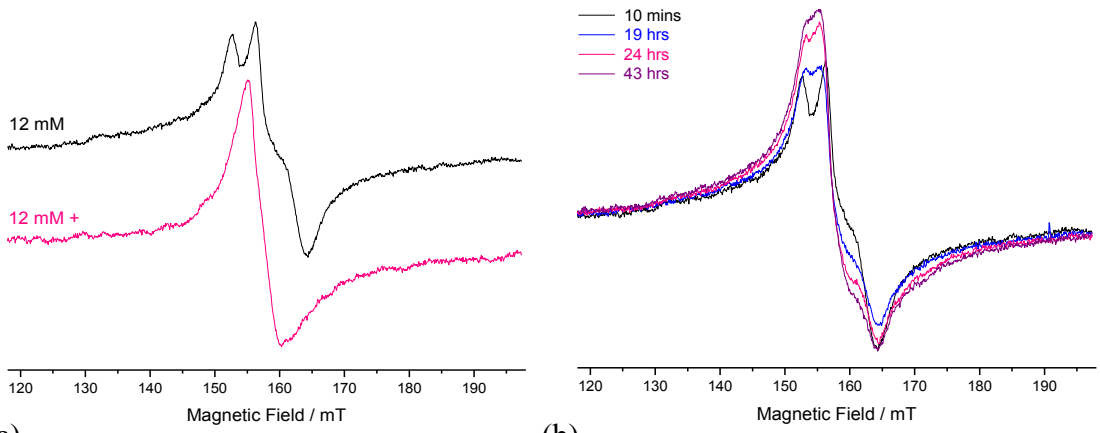

(a) (b)

Figure 3.10 (a) Shows the EPR spectra of 75 µM holo-Tf, 10 mM Tris-HCl buffer and 12mM Dop, with '+' and without a 24 hour incubation period at - 20 °C. (b) Demonstrates the influence of repeated exposure to air over 43 hours for an identical Tf treated 12 mM Dop sample; the iron removal is slower. Both spectra sets were recorded using the Bruker EPR spectrometer, with a continuous flow of helium operating at 77 K.

The incidence of chloride ions in the samples poses an additional binding opportunity for ferric iron and indeed ferrous ions. Consequently, competitive binding could occur and thus reduce the iron pool, which may affect both the catecholamine and indirectly the Tf. Once a ferrous ion exists in a bound state it will not immediately be reoxidised for potential re-uptake by Tf. Though iron theft from the catecholamine by a temporal iron(II) sink, such as a chloride ion, may sequester the Fe(II) and enable easier oxidation whilst bound to the chloride, allowing Tf to once again capture the ferric iron, inevitably prolonging its release. This is offered as one possibility. An array of processes may however, be occurring simultaneously, including those which are oxygen dependent and therefore are not easily detangled from the EPR and urea-PAGE data alone.

Previous studies have highlighted that the distribution of Fe(III) between the N- and C-terminals of Tf can alter in the presence of chloride ions. These ions are documented to accelerate the removal of iron from the C-terminal with respect to the N-terminal.[39] Similar trends were shown in this work, for the urea-PAGE analysis of the Dop treated Tf samples, given in Figure 3.9 (b). An EPR difference spectroscopy investigation to show the effect of chloride ions on the Tf binding status, has revealed only a weak alteration in the intensity of the Fe-Tf di-ferric peak and no significant alterations in the shape, following the addition of up to 429 mM sodium chloride.[40] This latter study indicates that while chloride ions may influence the iron binding in the present work, it is the catecholamines that predominantly enable their access to the Tf bound Fe. Conversely, at low pH the chloride concentration is shown to be proportional to rate of Fe-NE complex formation, however, the reverse process (decomplexation) is favoured with increasing pH, but remains unstudied for a pH $>$ 3.5.[31] A combination of all these factors may explain the slower release of iron from the Dop containing Tf samples, as earlier observed using EPR. From this work and the literature, two points are certain. One that the presence of chloride ions does retard iron removal from Tf and two, that their presence bears significance to processes which may compete with iron capture naturally in the mammalian body. That said, typically, the endogenous concentration of the chloride anions is much lower than the amounts used here. As a therapeutic agent, Dop is administered in its hydrochloride form and later the influence of the chloride ions on clinical concentrations of Tf is assessed.

Concerns may also be raised over the bitartrate anion structure interfering with iron binding, since it too contains adjacent OH groups, which are theoretically capable of binding ferric iron in an analogous manner to the catecholamines (Figure 3.3). These

reservations are easily alleviated when considering the extensive testing on the catecholate metabolites, which are available as bitartrate salts yet have no effect on bacterial growth, over that of the control. The collection of data can now confidently assign iron removal from Tf as due to the involvement of catecholamines and other catechol containing moieties.[11, 15, 23] Still, for confirmation using EPR, an alternative catechol compound is tested and discussed in Section **3.6.4**.

To summarise the key points of this section,

- The iron binding status of the characteristic Fe-Tf EPR signal is altered on addition of NE, Epi, and Dop, and is shown to be both concentration and time dependant.
- The new EPR signal is proposed to be from the catecholamine binding to the Fe(III) from Tf.
- The urea-PAGE data also confirms that loss of iron from Tf occurs with time.
- The chloride ions in the Dop hydrochloride appear to affect the rate and extent of iron removal from Tf.

3.6.2 The Interactions of Dobutamine with Transferrin and the Influence of an Iron (II) Sink

Further to the EPR studies involving the naturally occurring catecholamines it was decided to do the same analyses for an example synthetic catechol containing compound, since these too are well documented to promote bacterial growth.[11, 41] The chosen candidate was dobutamine (Dob), which is a widely used inotropic agent. In an analogous manner to that previously described for norepinephrine, epinephrine and dopamine, dobutamine concentrations were prepared and the corresponding EPR signals in the presence of Tf recorded. The spectra yielded no discernable change in the immediate Tf EPR signal at Dob concentrations of up to 24 mM, implying that Dob was unable to initiate the immediate release of iron from Tf irrespective of concentration. This was unsurprising for two reasons; its form as dobutamine hydrochloride and its clear structural dissimilarity to the catecholamines tested so far (refer to Figure 3.3 for the dobutamine structure).

The Tf treated Dob samples were therefore incubated and over a period of 24 hours only a minor reduction in the Tf bound iron signal was noted, see Figure 3.11. This verified some loss of iron had occurred from Tf, though no transformation in the shape of the EPR spectrum arose. In view of this small drop in signal intensity and the

comparatively high concentration of Dob used to achieve this change, iron removal was confirmed as being extremely slow, certainly beyond that expected due to the interference by chloride ions alone (*cf.* Dop data; Figure 3.10).

If indeed a mechanism of iron(III) reduction is supported as the route of iron theft from Tf, the introduction of an iron(II) chelator such as ferrozine (Fz) should encourage further iron capture. The dye would complex with any reduced Fe(II) ions present, this includes scavenging them directly from Dob. At physiological pH Fe(II) would rapidly be oxidised to insoluble Fe(III) if unbound in the sample, allowing immediate re-uptake by Tf. This would support the maintenance of a redox cycle between the loss and gain of iron by Tf and the catecholamine, hence prevent net loss of iron ever occurring, if the rate of iron removal is slow. A situation of this manner can be inhibited if the Fe(II) is complexed, by an appropriate iron(II) sink with a high affinity for Fe(II) and here the spectra should reflect the true loss of iron from Tf. To verify the role of Fz, 12 mM Dob was incubated with Tf, buffer and varying concentrations of Fz, see Figure 3.12 (all the components were added to the incubation mix in the written order).

It is worthwhile noting that a switch from a faint peach colouring from Tf, to magenta, accompanied the addition of Fz to the Tf Dob solutions. This is a clear indication of Fe(II)-Fz complex formation and therefore catecholamine mediated iron reduction, since no alteration in Tf spectrum occurred without the catecholamine, or on addition of Fz to the Tf solution alone.

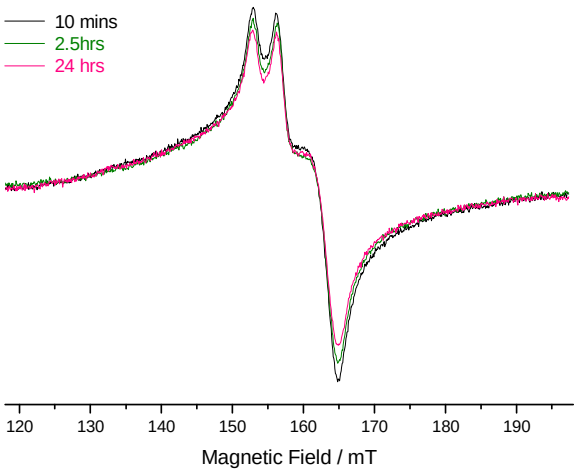

Figure 3.11 The EPR spectra of 75 µM holo-Tf, 10 mM Tris-HCl buffer and 12 mM Dob, monitored at the indicated times over a 24 hour period. Only a small amount of iron is released from Tf. Note; separate and identical incubation mixtures were used for each recording and that the Tf standard has been omitted due to its perfect overlap with the 10 minute result.

Regardless of the amount of added Fz or length of incubation, the iron was never fully removed from Tf. Using an iron(II) sink did, however, enhance the speed of iron loss. Compare the results from Figure 3.12 (b) with the same 24 hour time period indicated in Figure 3.11, which was recorded in the absence of Fz. From consideration of the collected data featured in Figures 3.11-12, it is evident that a reduction in intensity of the iron-replete Tf EPR signal is initially observed, followed by an increase due to the presence of the Dob bound iron alongside the remaining Fe-Tf. This is in accordance with that occurring for the former catecholamines (for examples see Figures 3.8 & 3.10).

For the 12 mM Dob Tf sample in the absence of Fz (Figure 3.11) solely a decrease in the intensity of the Tf bound iron is observed, with no evidence of the Fe-Dob complex. Given a longer incubation the EPR spectrum may have revealed an analogous change to that displayed in Figure 3.12 (a) considering a continued decrease in the Fe-Tf peak was observed. Subsequent to the 5 days incubation for the 0.4 mM Fz sample, it retains some of its double peak character, whilst for the addition of 1.6 mM Fz the double peak is clearly more distorted even after 24 hours. To reiterate, the complete removal of iron bound to Tf has not been recorded in any of the incubation mixtures tested and only a selection of the data is included here.

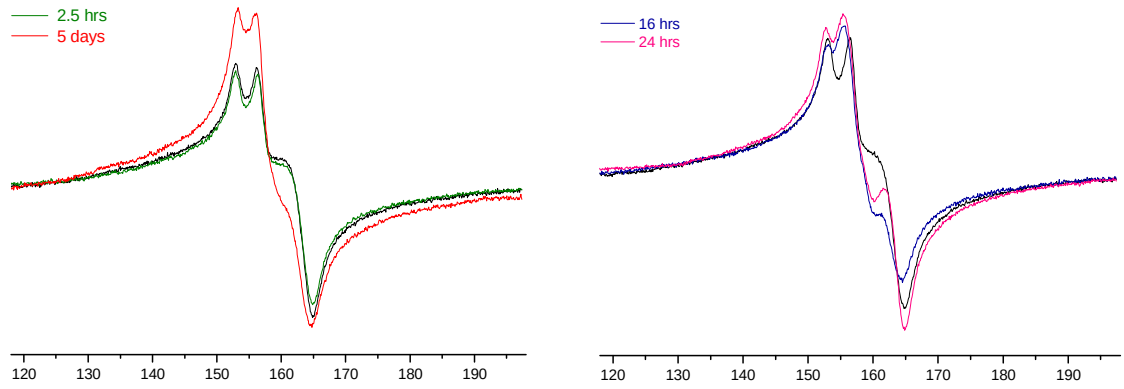

Figure 3.12 The EPR spectra of 75 µM holo-Tf, 10 mM Tris-HCl buffer, 12 mM Dob and different concentrations of Fz, monitored over different incubation periods. Note that the different components were added to the pellet mix in written order. (a) Shows the EPR spectra with 0.4 mM Fz incubated for up to 5 days, while (b) Shows the addition of 1.6 mM of Fz incubated over 24 hours. The data reveals that a larger concentration of Fz aids faster iron removal from Tf. In both datasets the signal for the holo-Tf control is indicated in black.

It is also appropriate to mention that three Fz molecules are required to bind an iron(II) centre. So the 1.6 mM Fz concentration used here should have the potential to scavenge all the Fe(II) reduced from Tf, since only 0.45 mM of Fz is required to bind the 150 µM of iron available from Tf.[42] Higher concentrations of Dob tested up to 24 mM incubated with Fz only negligibly enhanced the rate of iron removal, as did higher concentrations of Fz (data not shown). The final EPR spectra, after an adequate incubation period, were for the tested samples very similar; indicating a limit in the extent of iron removal had been reached.

This striking variation in iron removal times when compared with the other catecholamines is, as mentioned, most likely structural. On binding ferric iron, the Tf undergoes conformational changes in the areas surrounding the two iron binding terminals. Topological studies have identified that access to the C-terminal is more restricted than that in the nearby N-terminal, a finding that is also in agreement with the differing iron removal rates from the two lobes.[37, 43] This may offer an explanation into the behaviour of Dob, given that the additional chain on Dob (*cf.* NE, Epi, and Dop) may obstruct access to the C-terminal. This would lead to inefficiency at removing the iron and may also account for the encountered limit in iron removal, for the higher concentrations of Fz. This combined with competitive binding from the chloride ions results in a much retarded iron removal process.

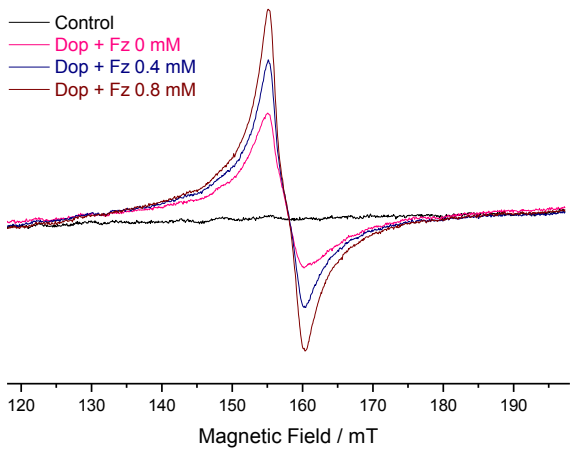

Figure 3.13 The EPR spectra of 75 µM holo-Tf, 10 mM Tris-HCl buffer, 12 mM Dop and increasing amounts of Fz, monitored over a 24 hour incubation period at - 20 °C. The Fe-Dop peak increases with increased Fz concentration. Note that both Dop and Fz are EPR silent and the latter is indicated by the control line.

To further highlight the mechanistic role of Fz in catecholamine mediated iron removal from Tf, samples of 12 mM Dop incubated with increasing amounts of Fz were recorded after a 24 hour incubation period (see Figure 3.13). The strength of the new signal increased with increasing Fz concentrations. This trend is opposite to that recorded for analogous NE, and Epi mixtures, which both revealed a reduction in intensity of the Fe-CA peak. Importantly, the NE and Epi results were recorded on the JEOL spectrometer, so accordingly had a greater associated error compared to that of the Dop data. Assuming the alterations in the intensities to be correct, the Dop result may be rationalised by the faster and more complete binding of Fe(III) from Tf, for a given time period, while the decrease in NE and Epi is most likely due to Fe(III) reduction. However, the influence of the chloride ions, like before, cannot be dismissed and may interfere with the acquired Dop spectra, thus giving rise to the opposite trend. In any case, the effects of Fz and the chloride ions require further attention and this is performed in the next section.

It should also be noted that upon Fz addition to all the catecholamine treated Tf samples the solutions turned a vivid magenta colour, confirming the presence of iron(II).[42]

3.6.3 Investigation of Catecholamine Inorganic Salt Complexes

Previously Gérard *et al*[27] and El-Ayaan *et al*[31] independently established (using UV-vis spectroscopy) that catecholamines could bind iron(III) inorganic salts. On this premise, the same was attempted in the current study using EPR, for both ferric nitrate (Fe^{3+}) and ammonium ferrous sulphate (Fe^{2+}) salts, each used at a concentration of 150 µM, to equal the amount of iron bound in Tf (75 µM). This study was intended to demonstrate that catecholamines could bind both Fe(III) and Fe(II) species and in doing so could confirm a route of reduction for iron removal from Tf, as well as confirm the identity of the new peak. Additionally, investigations with iron salts were performed to provide further insight into the role of Fz and the chloride ions on the Tf iron EPR spectra.

The Fe^{3+} and Fe^{2+} solutions with buffer and without the addition of catecholamine were, as anticipated, EPR silent, as were the catecholamines alone (refer to Figure 3.13). The addition of NE to the iron salts generated a detectable signal with both Fe^{3+} and Fe^{2+}, indicating a complex must have formed between the catecholamine and the iron species. Curiously, both the EPR signals feature an identical g-value. This value

was also coincident with that from the previous iron catecholamine complexes recorded in Tf solution (refer to Figures 3.5 (b), 3.8).

A similar trend to that observed with NE, was noted for Epi additions to ferric (Fe^{3+}) and ferrous (Fe^{2+}) solutions. While, for Dop the variation between the two iron signals was much less pronounced, the overall signal intensity was also lower and the spectra appeared slightly different in shape. This is again most likely a consequence of the chloride ions present and is examined in more detail later in this section.

Given the different spin-states of Fe(II) and Fe(III) as $S = 2$ and $S = \frac{5}{2}$, respectively, there is no precedent for them to have identical g-values, or for the Fe^{2+} sourced spectrum in Figure 3.14 to correspond to an Fe(II)-NE complex when a g-value of approximately 4.3 arises due to an Fe(III) species. Moreover, the absence of any additional EPR signals could indicate that the paramagnetic Fe(II)-NE complex may in fact be EPR silent, an occurrence which is commonly noted for iron(II) species due to the short spin-lattice relaxation times of ferrous iron.[44] Additionally a bimodal cavity may be required due to the nature of the zero field splittings (non-Kramer's pairs), which are caused by the integer number of unpaired electrons. This gives rise to EPR transitions triggered by mw radiation with its magnetic component parallel to the z-axis and so cannot be monitored using the perpendicular mode cavity used in this work.

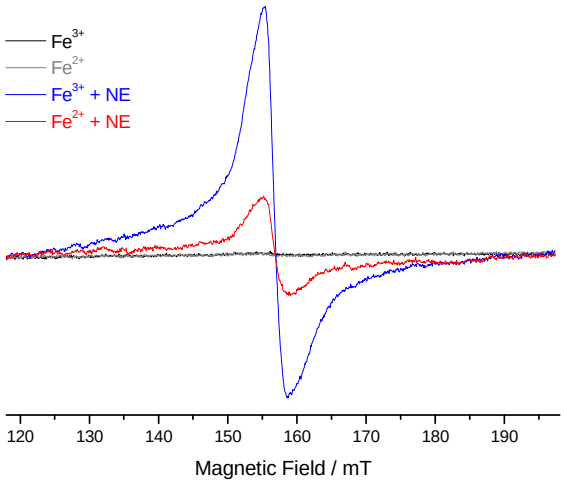

Figure 3.14 The EPR spectra of 10 mM Tris-HCl buffer, 150 µM ferric nitrate (Fe^{3+}) or ammonium ferrous sulphate (Fe^{2+}) solutions, with and without the addition of 12 mM NE. Note, no signal occurs for solutions without NE and the Fe^{3+}-NE has a greater intensity than Fe^{2+}-NE.

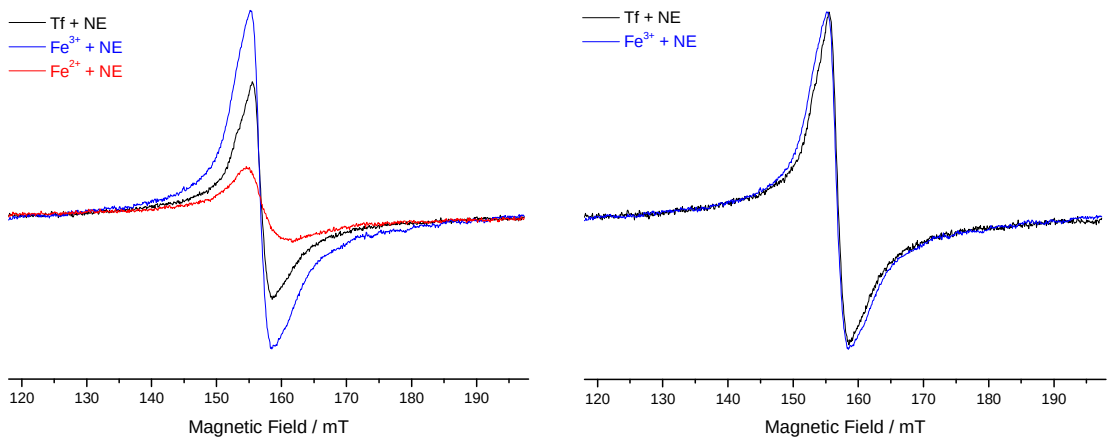

(a) (b)

Figure 3.15 (a) The EPR spectra of 18 mM NE, and 10 mM Tris-HCl buffer, containing 150 µM ammonium ferrous sulphate (Fe^{2+}), or 150 µM ferric nitrate (Fe^{3+}) or Tf 75 µM as the source of iron. (b) Is the normalised (Fe^{2+} data excluded) spectra from (a).

Therefore, all the recorded iron salts spectra are assumed to solely explore the binding status of the Fe(III) ion. This is certainly feasible as an amount of iron(III) is naturally present in the ferrous sulphate solutions and would predictably give rise to a much reduced signal intensity for the Fe^{2+} sourced solution (see Figure 3.14).

The iron-NE signals using iron from Fe^{2+} and Fe^{3+} are compared to that from an analogous NE treated Tf solution in Figure 3.15 (a). Clearly, the spectra overlap well (Figure 3.15 (b)) and have identical g-values. This implies all that all three iron signals do arise from the same oxidation state of iron, Fe(III).

It is apparent that the peak from the Fe^{3+}-NE complex is more intense than that recorded for the Fe-NE in Tf solution. This suggests that access to the iron for binding in Tf is more difficult for NE, than in an iron salt and under this condition the peak (Fe-Tf) would be expected to grow over time as more NE is complexed to the Tf iron. Another possibility is that iron has been reduced by the NE and the peak should decrease with time, at least until an equilibrium between the Fe(II) and Fe(III) states is achieved. Alternatively, both of these may simultaneously occur. The use of inorganic salts as the source of iron should remove the factor of access to the iron and highlight the effects of catecholamine mediated reduction alone, over time. Importantly, work from several researchers has shown that after the reduction of Fe(III) to Fe(II) for a system of ferritin with 6-OHDA, the Fe(II) was not easily released from the

catecholamine and required an external chelator, such as bacteria, to facilitate iron removal.[35] One would therefore predict a point where only negligible changes in the spectra are observed if iron(II) is not easily removed from the catecholamine. On this basis, the EPR signals of the catecholamines with iron were monitored at regular intervals over a period of two hours and at 24 hours to determine if any alterations in the catecholamine bound iron signals arose. Efforts were also made to minimise the effect of oxygen in all of the samples in this section.

Little variation was noted among the EPR signals for a two hour period, for any of the catecholamines. The chosen spectra in Figure 3.16 reveal the largest change observed of all the catecholamine solutions and this occurred for Epi added to the iron salts. A decrease in the ferric iron signal over 24 hours indicates the ongoing conversion of Fe(III) to Fe(II). The intensity of the ferrous iron signal also decreases to a small degree and is likewise attributed to the reduction of Fe(III). Both spectra therefore suggest that some release of Fe(II) into solution may have occurred.

Another possibility is that the majority of the Fe(III) reduction occurred within the preparation time, since unlike Tf, there would be no iron accessibility constraints. This could justify the similarity in the intensities of the different iron catecholamine solutions, over the initial two hour recording period. Furthermore, in all the data acquired so far the immediate change in the spectra has been the most noticeable, thus implying that an alternative method was required for investigating Fe(II) production.

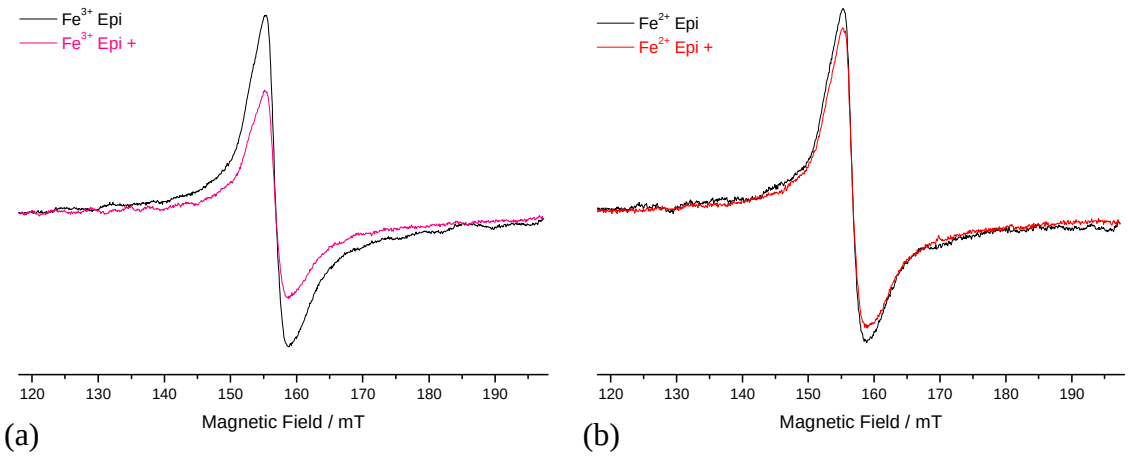

Figure 3.16 The EPR spectra of (a) 150 µM ferric nitrate (Fe^{3+}), or (b) 150 µM ammonium ferrous sulphate (Fe^{2+}), to 10 mM Tris-HCl buffer and 12 mM Epi monitored before and after '+' 24 hrs incubation at - 20 °C. A small reduction in intensity is noted for both ferric and ferrous iron solutions, indicating the reduction of Fe(III) to Fe(II).

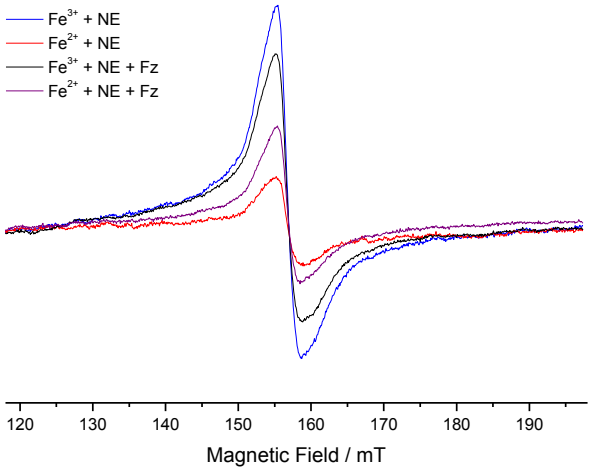

Figure 3.17 The EPR spectra of 150 µM ferric nitrate (Fe^{3+}), or ammonium ferrous sulphate (Fe^{2+}), with 10 mM Tris-HCl buffer, 12 mM NE and 0.45 mM Fz. There is a reduction in the signal intensity after the addition of Fz to the Fe^{3+} NE solution.

Since the Fe(II)-catecholamine complexes were unobservable, it was appropriate to probe for the presence of Fe(II), using incubations of the catecholamine and iron salts with Fz. As discussed, any non-complexed Fe(II) released is reoxidised to Fe(III), which in the case of Tf would allow re-uptake into vacant sites and may prevent the complete removal of iron from Tf. With the presence of an iron(II) sink, iron(II) would be removed from the pool of re-bindable iron and a net loss of Fe from Tf would be observed in the EPR spectrum. In the Tf sourced spectrum this appears as a reduction of the Fe-catecholamine signal, as earlier noted for the NE and Epi Fz samples. Therefore to support this and confirm reduction, a decrease in both the Fe(III)-catecholamine peaks would be anticipated here, when iron(II) is removed from solution.

In Figure 3.17 it is evident that the Fe^{3+}-NE peak is less intense following the addition of 0.45 mM Fz and is therefore in agreement with an increased rate of reduction of Fe(III), by NE. Unexpectedly, the Fe^{2+}-NE signal increases after adding the Fz, which would suggest more Fe(III) is present than prior to Fz addition. While the samples were degassed to eliminate the exposure to oxygen, it is possible that some oxygen remained and caused the increase in intensity of the Fe^{2+}-NE signal. The trend for Epi, however, follows the anticipated result, where both the iron peaks are reduced in intensity.

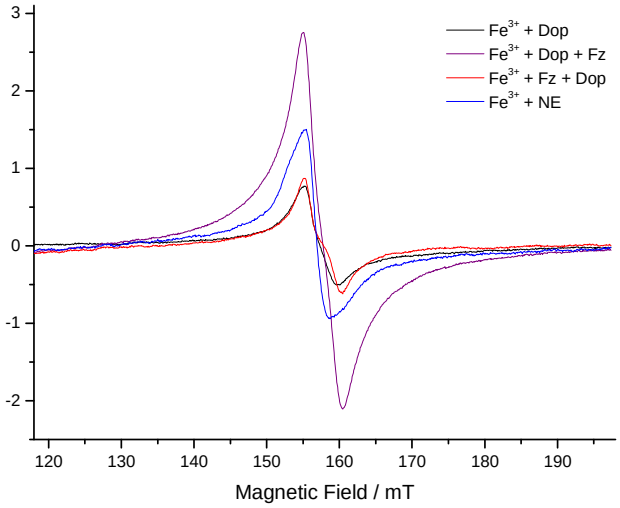

Figure 3.18 The EPR spectra of 150 µM ferric nitrate (Fe^{3+}), 10 mM Tris-HCl buffer, and 12 mM Dop. Compared with spectra for 0.45 mM Fz added before and after the Dop, and the NE treated Fe^{3+}solution. A large peak occurs for Fz added lastly to the Dop inorganic iron solutions. This has a different g-value to the Fe^{3+}-NE signal, indicating it is not from a Dop bound iron.

The EPR spectra for the addition of Fz to Dop can be viewed in Figure 3.18. A considerable increase in the magnitude of the signal occurs after the addition of Fz and it is far greater in intensity than any of the signals recorded so far. This large peak also features an altered g-value, which suggests it does not arise from the expected catecholamine bound iron and may tentatively be assigned to ferric chloride ($FeCl_3$), with perhaps some overlap from the Fe-Dop. The chloride ions demonstrate a greater affinity for the ferric ion, than does Dop. This recorded result therefore offers an explanation for the long timeframe required for iron capture in the Tf treated Dop samples. Additionally, it suggests that the earlier EPR spectra for Fz added to Dop, (Figure 3.13), almost certainly show a significant contribution from $FeCl_3$. Notice the similarity of the peaks, to the Dop with Fz large signal given in Figure 3.19. Given that the spectra in Figure 3.13 overlap perfectly, it is also proposed that the new signal following iron removal from Tf, in all the Dop treated spectra is predominantly that of $FeCl_3$.

Furthermore, the colour of the pellet for this sample exhibited a more intense magenta than has been witnessed previously, indicating the presence of more Fe(II) in this solution. This is in accordance with the lower intensity EPR signals (for Dop) observed in the absence of Fz, as the majority of iron may have been in ferrous form.

Also in Figure 3.18 is the EPR spectrum for Fz added prior to the Dop. The shape of this spectrum reveals a shoulder unseen in the other salt data, a trait that is mirrored for the Fe^{2+} salt Dop data with Fz added first. This again is most likely from the influence of $FeCl_3$ in addition to the anticipated Fe-Dop.

Given that multiple redox processes including those of oxygen (despite degassing) may be contributing to the changes in the EPR signal, it is difficult to decipher the recorded spectra fully and the iron salts data results remain, at times, speculative.

To summarise the key points of this and the previous section,

- Fz aids the removal of iron from Tf in all the catecholamine and inotrope samples tested.
- The inorganic iron salt data reveals the definite existence of a catecholamine bound iron signal, for NE and Epi.
- The Fe-CA salt signals yield an identical g-value to that from the Fe-CA in Tf.
- The presence of chloride anions compete with the catecholamine(s) for ferric iron binding in Tf, and have indicated a stronger binding affinity for Fe(III) than Dop (from dopamine hydrochloride).
- The salt data for Dop suggests the new peak in the Tf treated Dop samples, is from $FeCl_3$ and not the anticipated Fe-Dop.

3.6.4 Interactions of Catechin with Transferrin

Concerns over the extent of anion involvement in the evolution of the di-ferric Tf EPR spectra, naturally led to the study of a non-anion based catechol compound, specifically catechin. Catechins are plant extracts, commonly found in teas, so are ingested rather than produced by the body and in that respect differs from the former catecholamines. Previous investigations into common dietary catechols, established catechin could facilitate the growth of enteric bacterial pathogens, such as *E.coli*, to a level of 10^4 over that of the non-supplemented controls.[22] This demonstrated potency made catechin an appropriate choice to confirm that iron loss from Tf proceeds irrespective of the presence of the bitartrate or chloride anions. The current study should therefore prove that the anions do not themselves complex the iron to trigger its removal.

Clearly, the catechin is bulkier than the previously studied catecholamines (excluding inotrope dobutamine). This implies access to the C-terminal of Tf may again be hindered. Refer to Figure 3.3 for the structure of catechin.

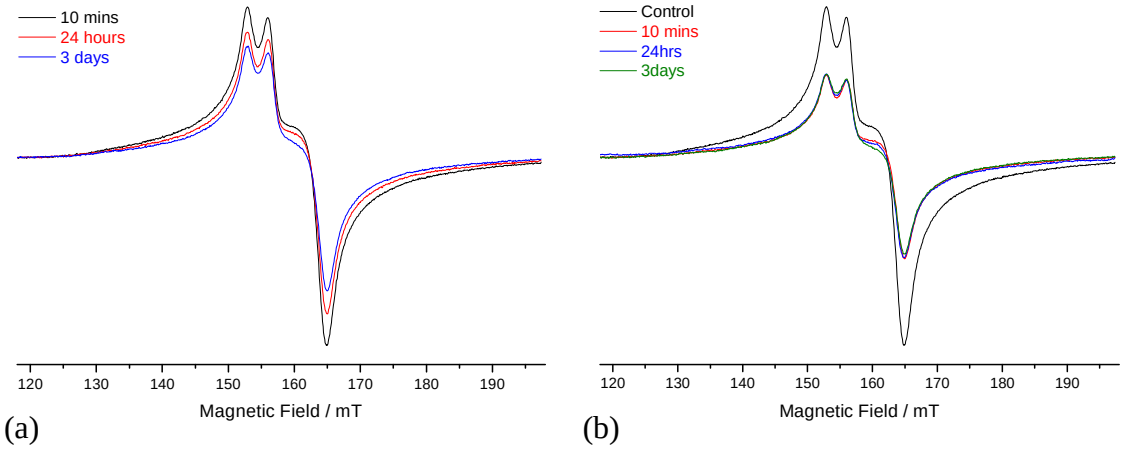

Figure 3.19 (a) The EPR spectra of 75 µM Tf, 10 mM Tris-HCl buffer and 2 mM catechin monitored over an incubation period of 3 days, and kept at 5 °C in accordance with catechin storage guidelines. (b) Shows the EPR spectra for the inclusion of 0.4 mM Fz in addition to the components in (a). Both sets of data reveal a decrease in intensity, with little/no accompanying alteration in the shape of the signal.

Immediately upon addition of the catechin to the solution mix as indicated in Figure 3.19 (a), and for the subsequent 3 hours no difference in the Tf EPR spectrum was noted (the 3 hour and immediate data is not shown as the spectra overlapped with the 10 minute result perfectly). Incubations over a 24 hour and 3 day period yielded the reductions in intensity as displayed in Figure 3.19 (a). Among the initial signs of an alteration in the Tf binding status is a characteristic drop in the shoulder of the Fe-Tf peak. This is not evident in the spectra, where the change in the shoulder is a consequence of a reduction in the intensity only. Upon the addition of 0.4 mM Fz the signal intensity was immediately reduced (Figure 3.19 (b)) and for these spectra an alteration in the shoulder is visible. Although slow to appear, this alteration reveals the onset of the Tf signal shape transformation. One may suspect this slow change, as previously considered for Dob, is due to an insufficient amount of Fz. However, for higher concentrations of up to 1 mM Fz, where the Fz is far in excess of the iron from Tf, the effects are similar. Therefore, the collection of spectra supports the limit in iron capture to be its accessibility and perhaps the rate of iron removal. On comparison with the NE and Epi solutions the evolution of the catechin spectrum is significantly slower; refer to Figures 3.6 and 3.8. For the inclusion of 3 mM or indeed 2 mM (data not shown) NE or Epi to Tf, an immediate reduction in the intensity was recorded.

The results in this section suggest that the removal of iron from Tf by catechin occurs in the absence of any anion species. The rate as predicted is slow, most likely due to the inefficiency of catechin at accessing the bound iron, in combination with the lower concentrations used (necessary to maintain solubility of the catechin). This test was performed for proof of principle and not to capture the complete removal of iron, which according to the data shown in Figure 3.19 may take a number of days. Ultimately, the magnitude of catechin mediated bacterial iron uptake, in *E.coli*, is documented to be similar to that achieved by the catecholamines. Though for efficient iron uptake by the bacterial acquisition mutants, catechin is shown to require double the concentration of the catecholamines.[22]

3.6.5 Norepinephrine Mediated Iron Removal from Lactoferrin

Given the extensive investigation of Tf iron binding in the presence of a number of catecholamine and related species *via* EPR, it was necessary to do likewise for Lf. Lf, as discussed, resides in an area alongside catecholamines where bacteria actively thrive, the gut.[2] The ability of NE and other catecholamines to facilitate the removal of iron from Lf has often been demonstrated, implying the proposed mechanism of iron reduction applied to Tf may also be pertinent here.[15]

Lf was initially tested to establish the minimum concentration for an appropriately intense signal, whilst maintaining complete dissolution of the protein. A Lf concentration of 62.5 µM (5 mg ml^{-1}) was decided upon and the corresponding datasets for the NE Lf incubations are displayed in Figure 3.20. The overriding difference between the NE treated Lf EPR spectra and those of the NE with Tf, are the timescales of iron acquisition. For the solutions of Lf, the concentration dependence is more subtle, with a gradual reduction in the Fe-Lf signal along with a drop in the shoulder becoming increasingly clear for concentrations of up to 36 mM NE. Further increases beyond 36 mM were not sought given the retarded iron removal rate from this protein (see Figure 3.20 (a)).

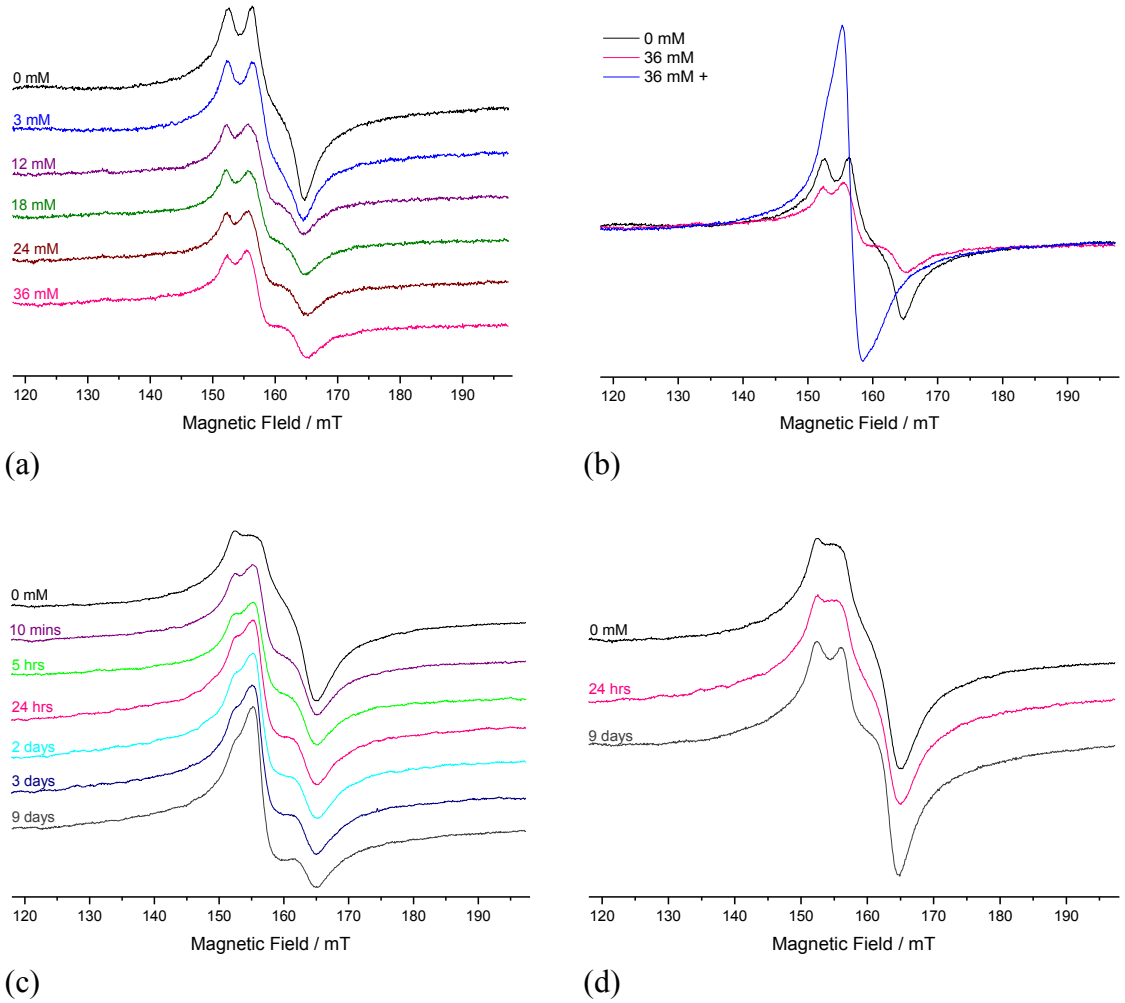

Figure 3.20 The EPR spectra for Lf incubated under different conditions. (a) Features 62.5 µM (5 mg ml^{-1}) Lf, 10 mM Tris-HCl buffer and increasing concentrations of NE shown in descending order. Notice that more than 36 mM NE is required for the complete loss of iron from Lf. (b) Shows selected overlapping data from (a), along with the spectrum from incubating the 36 mM sample for more than '+' 5 days. These spectra highlight the intensity and shape evolution occurring for Lf. (c) Is similar to (a), but replaces concentration with time (as labelled), while maintaining a fixed concentration of 12 mM NE. Following a 9 day incubation period with NE, the Lf sample still retains some Fe binding character though the double peak is almost removed. (d) Shows the change in the control sample, over the same 9 day period of incubation. Notice how the di-peak profile gains definition, importantly there is no change in the overall Lf signal intensity for the standard. All incubations were kept at - 20 °C between recordings.

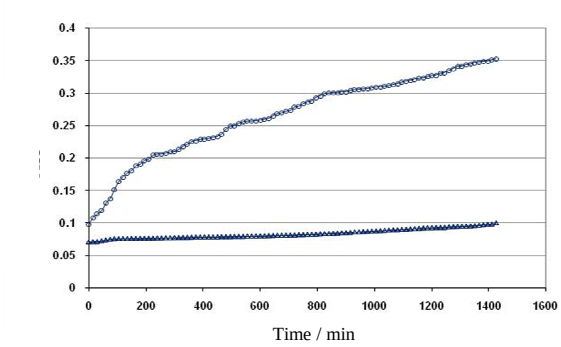

Figure 3.21 The release of Fe(II) over time, from a sample containing 20 µM Lf incubated in buffer with 4 mM NE, in the absence (squares) and presence (circles) of 0.4 mM Fz. Measurements were made using a Varioskan densitometer recording at 560 nm to monitor the formation of an Fe(II)-Fz complex.[36]

Figure 3.20 (b) shows the spectra for the Lf control, along with the highest sample concentration of 36 mM NE and the same 36 mM NE solution incubated for more than 5 days. A total removal of iron from Lf occurs only after the prolonged incubation and yields the anticipated single peak associated with the catecholamine bound iron. This prominent peak also supports some iron(II) to be retained by the catecholamine in the absence of an external chelator, which is in agreement with the catecholamine mediated removal of iron from ferritin.[35] Further to this, solutions of 12 mM NE added to Lf with differing incubation times were monitored (see Figure 3.20 panel (c)). Here, the spectra indicate an incubation time of well beyond 9 days would prove necessary to strip iron from Lf, which for the identical study involving Tf was complete within minutes (*cf.* Figure 3.6). This accordingly highlights the difference in iron retention between the two proteins.

The results given in Figure 3.20 are unsurprising when considering Tf and Lf possess differing affinities for ferric iron and human Lf binds ferric iron up to several hundred times more tightly than either Tf or ovo-Tf.[45] A full structural model suggested this disparity may lie in their inter-lobe linkers. This region is found to be helical in Lf while unstructured in Tf and may account for the easier iron theft from Tf.[37]

The poor resolving power of Lf on urea-PAGE meant the usual complimentary urea gel analysis was impossible to perform for the Lf samples. Alternatively, densitometry was applied to monitor the time course of Fe(II) evolution, *via* the characteristic absorption of the Fe(II)-Fz complex at ~ 560 nm.[42] 20 µM iron saturated

Lf incubated with 4 mM NE in the absence and presence of Fz was recorded. The results can be viewed in Figure 3.21 and confirm an increase in the Fe(II) with time. Curiously, the sample in the absence of Fz also revealed a shallow increase over the same 24 hour time period and may be attributed to the Fe(II)-NE complex, since in the absence of the catecholamine no increase was recorded. The control data showed no complex formed between the Fz and Fe(III), or with Lf, which proves both the specificity of Fz for iron(II) and the catecholamine mediated Fe(III) reduction mechanism.

Figure 3.20 (d) displays the EPR control spectra for the Lf sample over the 9 day period. During this time it retains the same intensity, though interestingly this demonstrates the first significant alteration in the shape of the standard sample. The Lf di-peak gains definition, implying the control may not have possessed full iron(III) saturation on initial recording. This seems unlikely however, given the superior Fe(III) binding strength of Lf over Tf, which has always retained a di-peak motif in the control. The shape adopted ultimately by Lf (following 9 days) is representative of the original sample given in panel (a).

Such a large exposure of catecholamines to Lf, or Tf, is very unlikely to occur *in vivo*, as is the incubation period of more than 9 days that is required to strip iron from Lf. It is more realistic for a patient to be administered catecholamines for up to 5 days, with the concentration of catecholamines in serum resembling values closer to 10 µM and theoretically able to reach 30 µM in the case of Dop infusion. The work up to now has established the interactions between the catecholamines and the iron binding proteins Tf and Lf, for large concentrations of both. It is now beneficial to probe the influence of clinical concentrations of catecholamines to validate the use EPR as a diagnostic tool and confirm if the effects of the lower catecholamine concentrations on Fe-Tf binding in serum are observable by EPR. The use of lower catecholamine concentrations paralleling those encountered in serum are assessed in the following section.

3.6.6 The Interaction of Catecholamines with the Transferrin of Bovine and Human Serum

The initial stage of these investigations involved monitoring the Tf EPR signal of bovine serum in buffered solution. This was performed firstly for appearance and secondly to determine the signal intensity; whether or not alterations could be

deciphered for this low concentration of endogenous Tf. For the work detailed in this section the incubations were maintained at 37 °C, to reflect the temperature in the human body. Typically solutions were incubated over a period of 3 or 5 days, to replicate the maximum possible exposure time to exogenous catecholamines that patients in the ICU may encounter (refer to Section **3.3**).

3.6.6.1 Bovine Serum

The EPR spectrum of bovine serum in Tris-HCl buffer is displayed in Figure 3.22 (a). The appearance of this spectrum clearly differs from that of the holo-Tf dealt with so far. For this the di-peak profile is undefined and is most likely a consequence of the partially iron saturated nature of Tf in the mammalian body.[4] The absence of the di-peak profile for the bovine sera studies requires interpretation of the Tf binding status in this section from alterations in intensity of the signals alone.

To investigate the transformation in the serum Tf binding status, the bovine serum was supplemented with 12 mM NE (see 3.20 (b)). This generates a final EPR signal mirroring those obtained using higher concentrations of holo-Tf and confirms that complete iron removal does ultimately occur. Surprisingly, the rate of iron capture is more gradual from such a low concentration of endogenous Tf. Important evolutionary features of this serum Tf spectrum include, a dip in the shoulder along with the increase in intensity being accompanied by a more symmetrical line shape.

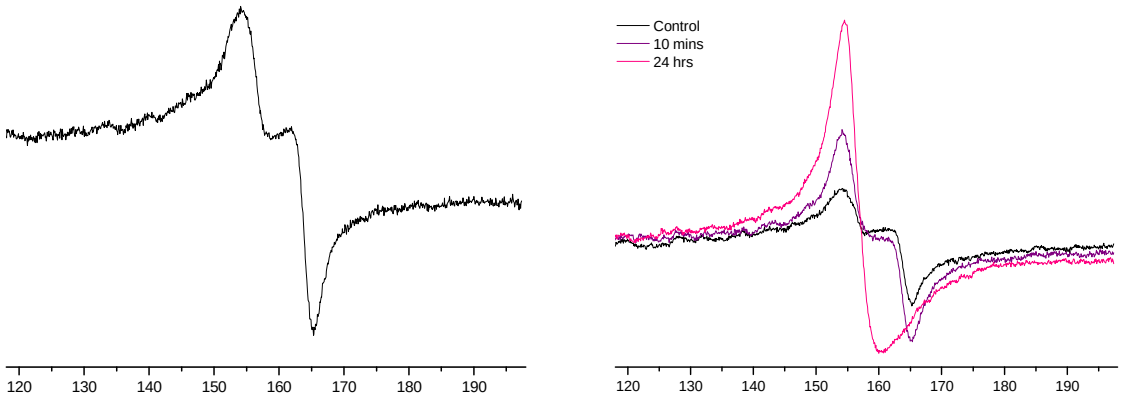

Figure 3.22 (a) The EPR spectrum of bovine serum diluted with 10 mM Tris-HCl buffer. (b) Shows the same as (a) but including 12 mM NE, monitored immediately and after an incubation period of 24 hrs at 37 °C. These samples had access to air.

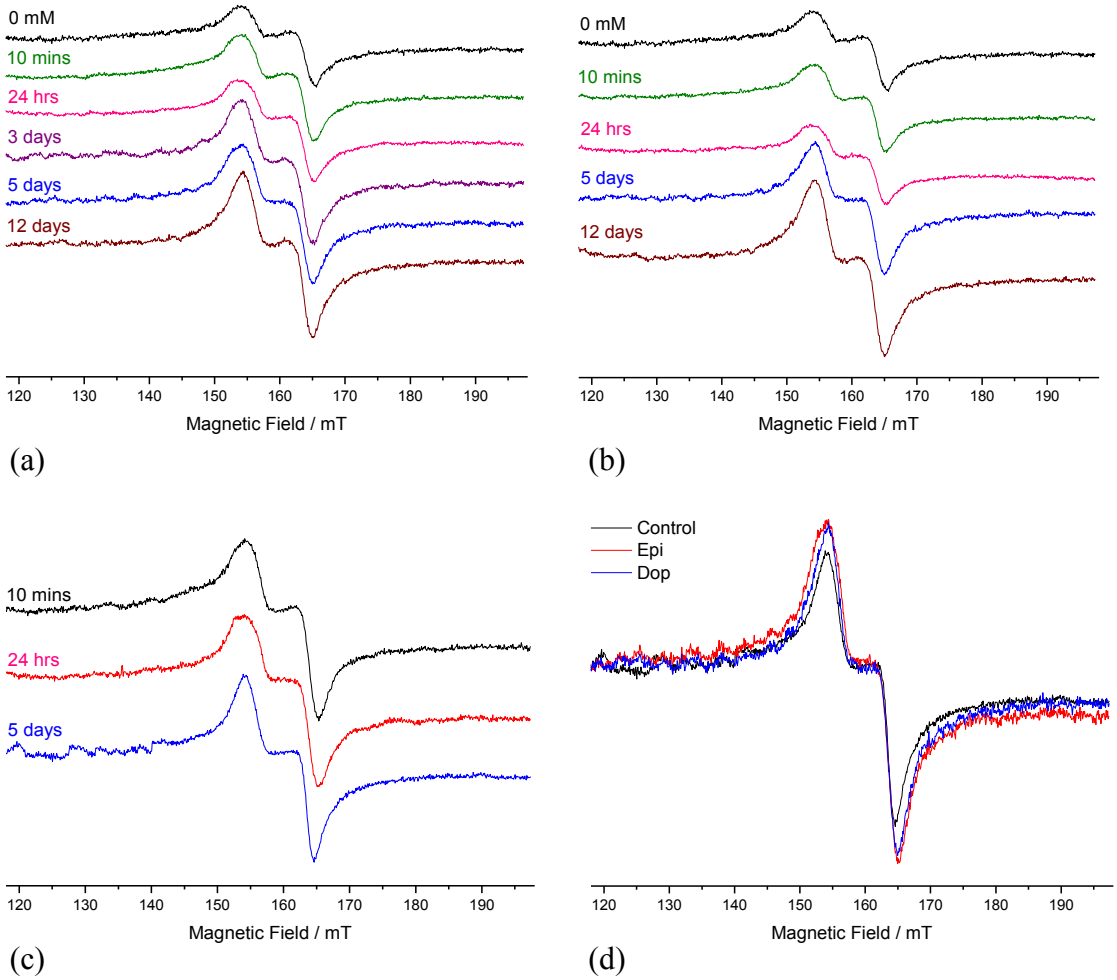

Figure 3.23 The EPR spectra of bovine serum with 10 mM Tris-HCl buffer and (a) 10 µM Epi or (b) 10 µM Dop, monitored over time. (c) Shows the control EPR spectra only, with an equivalent dilution to that from the addition of the catecholamines. (d) Shows a comparison overlay of the data for Epi and Dop following the 5 day incubation. All solutions were monitored after increasing incubation periods as labelled and kept at 37 °C between recordings, under aerobic conditions. Both (a) and (b) have identical intensity scales to highlight the increase in magnitude. Following the 12 day incubation with the catecholamines, the Dop signal is stronger than the Epi. In (c) the EPR signal undergoes negligible intensity change under the same conditions and appears as the standard plot (black) in (a) and (b).

Equivalent solutions containing 10 µM of the catecholamine were prepared and the serum Tf EPR signals recorded (see Figure 3.23). Considering the correlation between concentration and incubation time with the transformation of the Fe-Tf signal, the resulting spectra were not expected to alter dramatically (i.e. not to the extent of the 12 mM NE sample) for the 10 µM catecholamine additions. However, an EPR observable change was still envisaged, at least over the 5 day treatment period. The data in Figure 3.23 (a) and (b) demonstrates the influence of 10 µM Epi and Dop respectively, when added to bovine serum with Tris-HCl buffer.

A gradual signal increase was noted for both Epi and Dop solutions over the 5 days, during which time the control underwent a very negligible change in intensity (see Figure 3.23 (a)-(c)). The data for up to 12 days is included for information and proves that the iron from serum Tf continues to be removed long after initial exposure to the catecholamine. Figure 3.23 (d) exhibits the overlay data for Epi and Dop with that of the standard after 5 days of incubation, both the catecholamine inclusive solutions reveal a similar increase in intensity and both are clearly stronger than the standard.

Aerobic and anaerobic conditions were investigated in this work. The data in Figure 3.23 is a selection from the aerobic samples, which, considering blood plasma contains a supply of oxygen, are more relevant to the body. The anaerobic serum spectra also revealed alterations in the Tf EPR signal intensity. Though, conversely, the signal intensities returned to their original values or lower, following the 5 days and thus supported no/insignificant net loss of iron from the majority of the samples. Notably in literature the ability of catecholamines, for example Epi, to influence the pathogenesis of *Clostridium perfringens* has been directly linked to the extent of oxidation. The more oxidised solutions were found to be less potent, which is surprising considering the trends in iron acquisition found here.[46] The presence of oxygen should perpetuate the release of iron from Tf, by the catalysed production of ROS, however in the chloride containing medium, it was earlier shown to have an inhibitory effect (see Figure 3.9).

From the data in this section it is clear that physiological concentrations of catecholamines, Epi and Dop, have triggered a change in the bovine serum Tf iron binding status. The ability to decipher this change using EPR, for such low concentrations of catecholamines is promising for its future use as a method for testing for increased virulence. For further confirmation of the effect of the catecholamines on the serum Tf EPR signal and its direct effect on human serum, it was necessary to

investigate fresh human serum, isolated from healthy volunteers for the remaining studies. These samples were centrifuged and incubated for analysis within 24 hours of collection.

3.6.6.2 Human Serum and Comparisons with Iron-Replete Transferrin

Figure 3.24 (a) shows the relative EPR signal intensities of fresh whole human sera (HS), in Tris-HCl buffer, compared with a known concentration of 10 µM holo-Tf. This overlay plot allows an estimation of the iron concentrations used in this work. Evidently, the Tf bound iron in serum HS2 is much lower than the approximated 10-20 µM value for blood serum, and HS1 is lower still. Both of these concentrations may retard the rate of iron removal beyond that observed for the bovine serum, if the slower rate of iron acquisition is a consequence of the lower concentrations. Encouraging, however, is the ability to detect the low intensity of HS1 at 77 K. This highlights the sensitivity of the spectrometer and its potential in measuring serum Tf iron binding integrity *in vivo*.

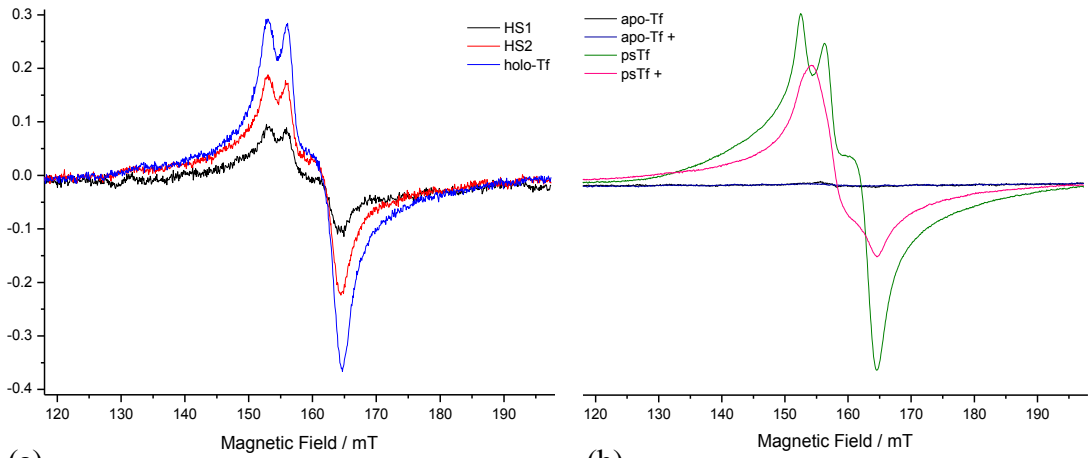

Figure 3.24 (a) The EPR spectra of human serum batches HS1 and HS2 in 10 mM Tris-HCl buffer, compared with an analogous incubation mix of 10 µM holo-Tf. The weakest iron signal occurs for HS1, while HS1 and HS2 are both lower than 10 µM holo-Tf in iron concentration. (b) Shows the spectra for 125 µM apo-Tf and psTf with '+' and without the addition of 6 mM NE. Following the addition of NE to psTf, the intensity of the final EPR signal is far lower than that of the original.

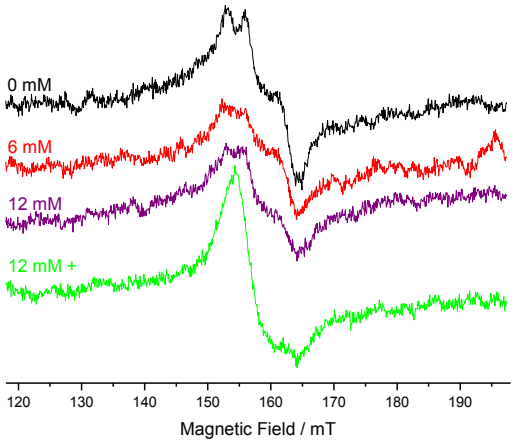

Figure 3.25 The EPR spectra of HS1, 10 mM Tris-HCl buffer with 6 and 12 mM NE, monitored over an incubation period of '+' 5 hours maintained at 37 °C.

The outlines of both the HS1 and HS2 EPR spectra are similar to that in holo-Tf, which is surprising given the partially saturated nature of Tf in mammalian serum and the appearance of the bovine serum spectra.[47] To verify the saturation of the human blood samples it was beneficial to attain the EPR spectrum of partially saturated Tf. The shape of psTf signal (Figure 3.24 (b)) is analogous to the iron-replete Tf and varied only in the asymmetry of the di-peak, a feature which is also subtly present in the human sera samples. Curiously here, the addition of NE to psTf generated an immediate signal less intense than the original psTf signal, an effect unseen in the data so far and possibly due to a slower rate of iron removal (preferential binding at the C-terminal), compared with, for example Figure 3.5.

The primary study, as in shown Figure 3.25 involved HS1. Where as a consequence of the weak iron concentration in the Tf of this serum (*cf.* serum Tf signal in Figure 3.24 (a)), attempts to monitor the modification in the Tf iron binding status with clinical supplements of catecholamine proved impractical. This therefore defines the lower limit for examining the interactions of catecholamines with Tf in clinical samples. Higher concentrations of 6 and 12 mM NE did, however, confirm that iron removal from Tf would inevitably occur for whole human serum. A gradual loss of iron from serum Tf occurred following the addition of 12 mM NE and as demonstrated for the bovine serum, an immediate transformation in the signal was not observed. Over the subsequent 5 hours, the characteristic Fe-NE single peak emerged, with a trace of the Tf bound iron still distinguishable in the spectrum. The retarded Tf iron removal rates encountered for both sets of sera (bovine and human) could imply alternative processes of significance are simultaneously occurring. Given that one would normally predict

faster removal in the presence of such a large excess of catecholamine. This may be due to the involvement of ferroxidase, which should facilitate the re-uptake of iron by Tf. Or from the natural antioxidants present, which would counteract the production of ROS and slow the release of iron from Tf.

Serum HS2 with buffer was likewise incubated with 10 μM NE, Epi, Dop, and 30 μM Dop, as well as alone for a total of 3 days. During this period spectra were recorded immediately following addition, after 24 hours and finally at 3 days. Notice the near perfect overlap of the control spectra after the 3 day period, given in Figure 3.26. This suggests any alterations in the remaining Tf test spectra may be attributed to the interactions of the catecholamines.

An overall reduction in the magnitude of the Tf bound iron signal is common among all the catecholamine treated serum solutions (see Figure 3.27). The largest drop in the signal intensity occurs for Epi. This is therefore in agreement with the most rapid iron removal rates by Epi, from the earlier EPR and urea-PAGE datasets. The addition of 30 μM Dop did not decrease the intensity of the Tf bound iron beyond that noted for the 10 μM Dop sample. In fact it is the only HS test case in which the signal increases following the initial 24 hour incubation period. This unexpected intensity change could reasonably be due to the chloride ions binding aqueous free iron in serum, which would mediate iron uptake by Tf. Equally, however, if this were the case it should, conceivably to a lesser extent, be evident in the lower concentration 10 μM Dop data, which it is not.

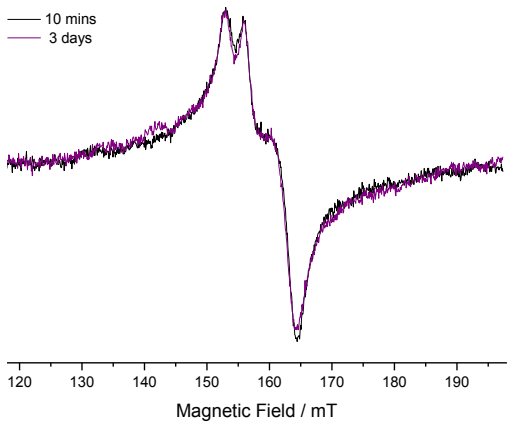

Figure 3.26 The EPR spectra of HS2 and 10 mM Tris-HCl buffer, after an incubation period of 3 days at 37 °C. Notice there is a negligible change in intensity of the two signals.

To reiterate, the weaker Tf signals indicate iron loss has occurred in all the physiological concentration samples. The implication of free iron with respect to bacterial growth is clear, though the method by which catecholamines liberate iron from the host proteins remains one of debate. *In vivo* this freed iron, by virtue of the suggested Fe-CA complex, may gain access to localised bacterial, in a similar manner to the aforementioned siderophores. The possibility of this and the proposed mechanism of iron capture are discussed further in the next chapter.

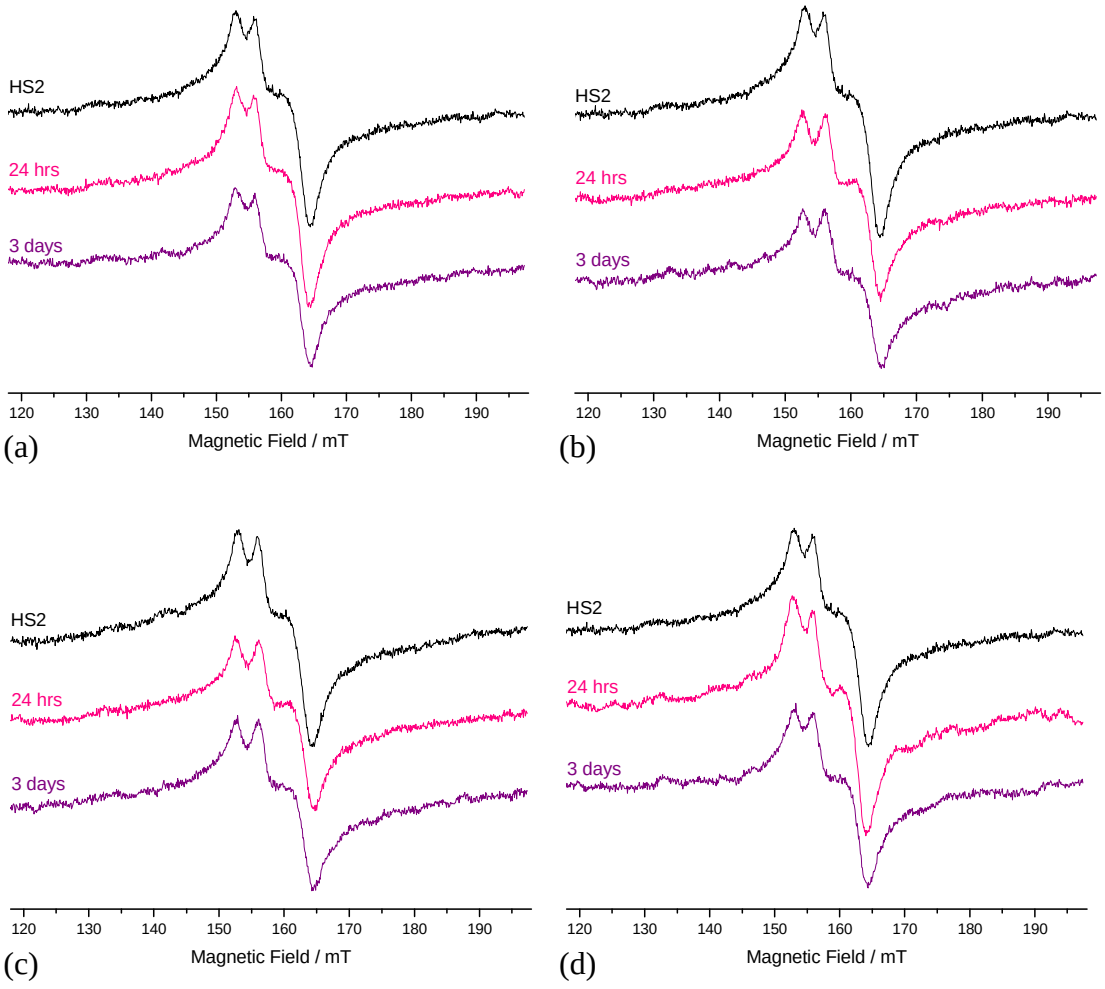

Figure 3.27 The EPR spectra of HS2, 10 mM Tris-HCl buffer, with (a) 10 µM NE, (b) 10 µM Epi, (c) 10 µM Dop and (d) 30 µM Dop. All the samples were monitored at 24 hours and 3 days of incubation. Between recordings they were kept at 37 °C. After 3 days a reduction in the intensity of the Tf signals is noted for all the serum catecholamine solutions. Note that a negligible change occurs in the control data over the same 3 day period, *cf.* with Figure 3.26.

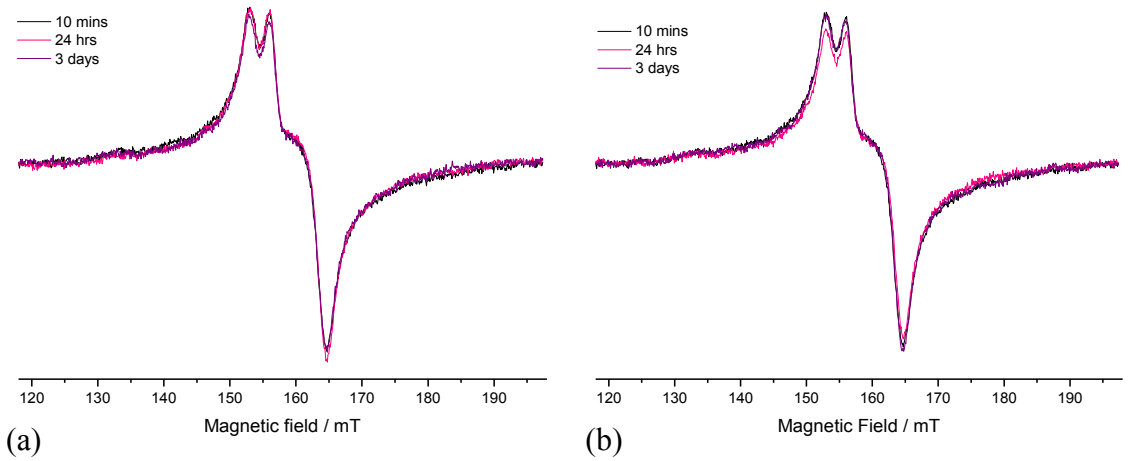

Figure 3.28 (a) Shows the EPR spectra of 10 µM holo-Tf, 10 mM Tris-HCl buffer and 10 µM NE, monitored following 24 hours and 3 days of incubation. (b) Shows the EPR spectra including 20 µM Fz in addition to the components listed in (a). A faster and greater decrease in the intensity of the signal is noted in the presence of Fz, following 24 hours of incubation.

A parallel study to those with endogenous Tf was performed using 10 µM holo-Tf, Tris-HCl buffer and 10 µM NE. This was to examine whether a similar reduction in signal strength was observed for the holo-Tf sourced iron, the results are given in Figure 3.28 (a). Unexpectedly, a slight increase in the holo-Tf signal is noted following 24 hours incubation under identical conditions to the HS2 samples. This may logically be explained by uptake of excess iron, which could be present to maintain the saturation level of Tf. It may also be argued that this should equally occur in serum, since the Tf is well known to be partially saturated.[4] However, for this work, only the 30 µM Dop human serum treatment showed an initial increase in the iron intensity (Figure 3.27 (d)). Referring back to Figure 3.28 (a), following 3 days of incubation, an overall reduction in the signal intensity is noted, yet the change is far smaller than that recorded for the human sera samples.

Analogous treatments were prepared in the presence of Fz, see Figure 3.28 (b). While a clear reduction in the di-peak Tf signal was noted after 24 hours, these spectra revealed no net decrease over the 3 day period. The inclusion of Fz has thus far encouraged the extraction of iron from Tf and the result here is no different. The extent of iron removal appears to reach a limit in this case, after which the re-uptake of iron by Tf seems to be favoured. This usually implies an inadequate supply of Fz i.e. too low a concentration to chelate any further iron(II) and is often feasible given three times as

much Fz is required to bind one Fe(II) ion. This idea, however, is unsupported by the minimal loss of iron in the spectra, which is much less than the amount of Fz available for binding, rendering this outcome difficult to explain.

All the samples of bovine and human sera were retained to assess any increases in the uptake of the freed iron, by bacteria. This was first performed by treating the samples with gut bacteria *E.coli* strain O157:H7 for a maximum of 5 hours and once more examining the EPR spectra for alterations in the shape and intensity of the signal. The results proved unequivocal, due to the limited amount of sera at our disposal and an unavoidably large reduction in sample volume for several of the incubation mixtures, after elimination of the bacteria.

The post incubation human serum was also analysed after 18 hours in the presence of skin bacteria, *Staphylococcus Epidermidis*. The bacterial growth increased by up to sevenfold in the NE treated samples, over that of the control. This proved that clinically relevant doses of catecholamines could alter the iron binding integrity of Tf, and compromise the bacteriostatic nature of blood.[36]

3.7 The Proposed Pathway for Iron Removal

Having demonstrated the direct influence of the catecholamines, norepinephrine, epinephrine, dopamine, and other catechol containing species such as dobutamine, and catechin, on the Tf and Lf iron binding status using EPR, it is now possible to discuss in greater depth the potential mechanism occurring, as well as to review further evidence to support its existence. The proposed pathway for iron capture from Tf and Lf is illustrated in Figure 3.29.

The mechanism details bidentate iron(III) binding occurring primarily from the N-terminal of the protein to the catecholamine. This iron capture process is facilitated by the pH control of the solution (Tris-HCl buffer), which enables ionisation of the two hydroxyl groups and aids the proposed model for binding. The resulting complex as highlighted in purple is observable by EPR and is suggested to undergo internal electron transfer causing reduction of the iron. This iron may subsequently be released from the catecholamine to be sequestered by bacterial ferrous uptake systems. Simultaneous outer electron transfer may also be occurring, however EPR spectroscopy cannot be used to report this since no intermediate structure is created and the semiquinone is produced directly *via* route b. *In vivo*, in the presence of Gram-negative bacteria the

ferric acceptors as indicated in Figure 3.29 will also acquire ferric iron using siderophores, in the manner previously discussed.

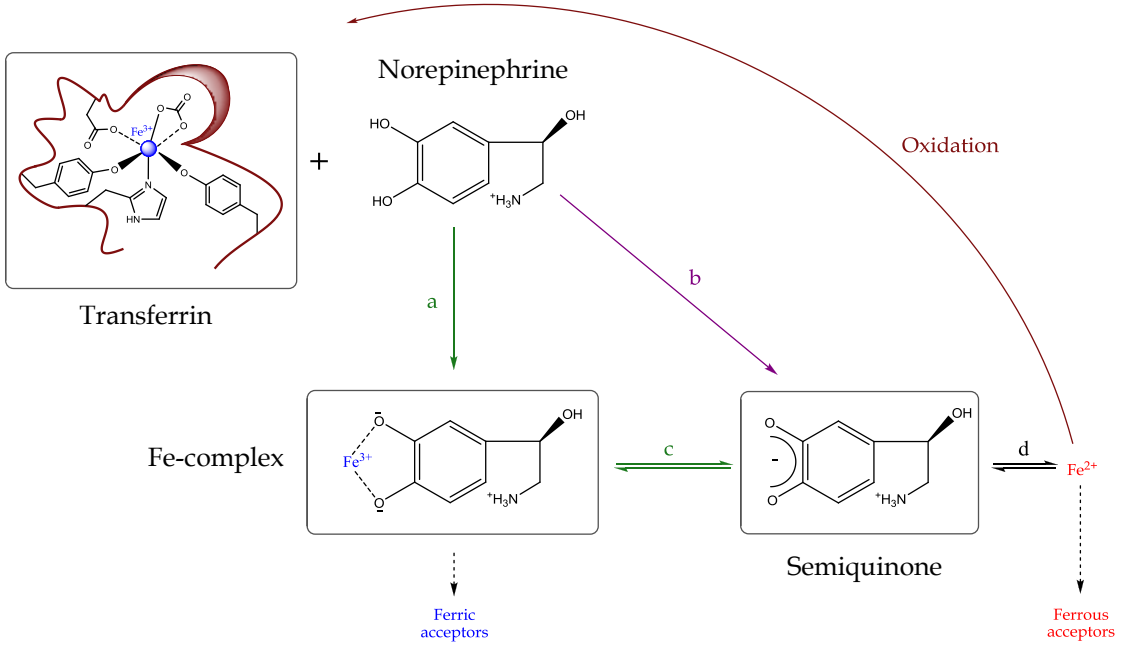

Figure 3.29 The proposed pathway of iron reduction by NE.[31] Inner sphere electron transfer involves the catecholamine entering Tf (or Lf) and binding preferentially to Fe^{3+} at the N-terminal. By oxidation of the catecholamine and simultaneous reduction of Fe^{3+}, the iron may be seized from Tf (or Lf) and at some point released. Outer sphere electron transfer produces no complex and releases Fe^{2+} directly. An Fe(II) sink such as Fz should promote Fe^{2+} production. While an excess of Fe^{2+} in solution, without a chelator should cause the re-uptake of Fe by Tf. The ferric and ferrous acceptors indicate bacterial acquisition mutants and any species able to act as an iron sink. All the EPR detectable species are boxed; these are the Tf, Fe-NE complex, and the semiquinone.

An excess of unbound Fe(II) in solution, if released by the catecholamine, should be able to reverse this scheme, resulting in the oxidation and re-uptake of the ferric iron by Tf. Incubations of Tf/Lf with NE, monitored over prolonged periods revealed negligible changes in the intensity of the new Fe-CA peak, demonstrating firstly that the

bound iron is retained by the CA (not released and re-uptaken by Tf) and secondly that the ferric to ferrous reduction, if occurring in these samples, rapidly reached equilibrium. Competitive binding of the ferric/ferrous irons in the catecholamine complexes may further facilitate iron capture by Tf. This has already been implicated as the reason for slow or incomplete iron removal in the presence of certain catecholamines, compare for example Figures 3.8 (a) with 3.9 (a).

A potent iron(II) scavenger such as Fz should encourage the rapid removal of Fe(II) from solution and should therefore inhibit oxidation occurring. Simultaneously this should enhance the rate of Fe(II) production, thus propagating iron theft. This theory is easily verified by monitoring the evolution of Fe(II) with time, which also inherently clarifies the oxidation state of released iron. While the reduction of ferric iron was hinted at from the alterations in the EPR recordings along with the characteristic colour changes, it remains unconfirmed.

Measurements were made using identical samples to those described in Figure 3.21, with and without supplementing the mixture with 0.4 mM Fz, see Figure 3.30 (a).[36] The figure shows rapid iron(II) release for the NE inclusive sample, a result which is mirrored for Epi (data is viewable in the reference).[36] The absorption level sharply increases and plateaus at approximately 90 mins, indicating the majority of iron from Tf is reduced and removed by this time. Thereafter, only a gradual increase in Fe(II)-Fz is noted with the rate now reflecting that in the absence of Fz.

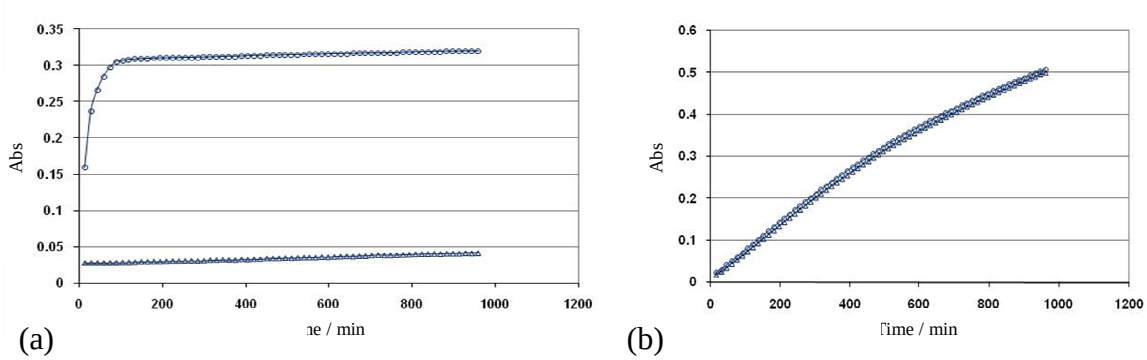

(a) (b)

Figure 3.30 The release of Fe(II) over time, from a sample containing 20 µM Tf incubated in buffer with 4 mM of (a) NE and (b) Dop in the absence (squares) and presence (circles) of 0.4 mM Fz. Measurements were made using a Varioskan densitometer recording at 560 nm to monitor the formation of an Fe(II)-Fz complex. NE shows an increase in the Fe(II)-Fz complex formation with time, while Dop supports little/no variation in the absence and presence of Fz.[36]

Conversely, the Dop data in Figure 3.30 (b), revealed no such increase in iron(II) expression and the presence and absence of Fz showed near identical results. This observation for Dop with Fz may be rationalised by the dominant species in the EPR spectra being from $FeCl_3$ (Figure 3.13) and not the Fe-Dop as anticipated. This would accordingly reveal a slower rate of iron reduction, as comparatively less Dop, than NE or Epi, would be bound to the ferric iron. The lack of change in Fe(II) liberation on addition of Fz, additionally suggests that $FeCl_3$ is the major contributor to the EPR peak in the absence of Fz, as was earlier proposed from the iron salts work. However, some change between the rates of Fe(II) expression would still be expected, and this does not explain the more intense absorption at 560 nm by the samples including Dop (*cf.* with NE in Figure 3.30). Notably, the Dop samples for the Fe(II) densitometry studies gradually turned brown in colour, unlike the EPR samples which were explicitly magenta in colour. This colouring is proposed to be from the by products of Dop oxidation, and may be responsible for the intense absorption in the visible region, occurring at the same wavelength as the Fe(II)-Fz complex, regardless of Fz addition.

Figure 3.30 (b) would suggest that Fz should have no influence on the rate of ferric iron reduction in the aerobic chloride ion containing solutions. This may well be the case, though Fz clearly accentuates the rate at which Dob binds to ferric iron from Tf (see Figure 3.12), and increases the intensity of the new EPR signal with the increasing addition of Fz (see Figure 3.13). This may therefore be interpreted as the chloride ions preferentially binding to the iron, thus negating the effects of the NE with respect to iron reduction.

Further data to explore the effects of 0.4 mM Fz on the NE treated Tf mixtures was also gathered by urea-PAGE and is given in Figure 3.31 (a). On comparison with the urea-PAGE profile in the absence of Fz, it also suggests a more rapid removal of iron from Tf (*cf.* Figure 3.7). Notice, 1440 minutes of incubation for NE with Tf (Figure 3.7), proves inadequate for a complete loss of iron in samples devoid of Fz. In this sample clear traces of C-mono and holo-Tf remained. An equivalent result to this may be attained within 15 minutes with the assistance of a Fe(II) sink (see Figure 3.31 (a)). Furthermore the removal of iron in the final track (1440 mins) is more extensive for the inclusion of Fz, where, ~ 98 % of Tf is in its apo form (Figure 3.31 (a)).

(a)

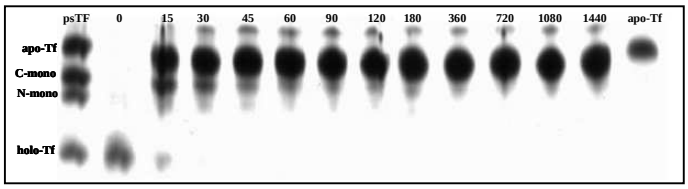

(b)

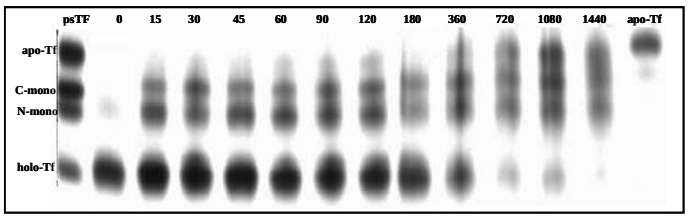

Figure 3.31 Urea gel data of 20 µM holo-Tf, with Tris-HCl buffer, 4 mM (a) NE or (b) Dop, and 0.4 mM Fz. The timeframe of iron removal is significantly reduced in the presence of Fz for NE, *cf.* Figure 3.7. Dop shows only a little change from the addition of Fz and the profile is similar to that in Figure 3.9 (b).[36]

The 90 minute (91 % apo-Tf) marker in Figure 3.31 (a), correlates with the onset of the plateau region in iron(II) expression (Figure 3.30 (a)), after this the rate of iron loss from Tf is far slower than at earlier times. This effect of Fz also agrees with the earlier mentioned decrease in the Fe-NE (or Fe-Epi) binding signal that occurs with increasing additions of Fz and is attributed to faster iron reduction. The urea-PAGE report for Dop with Fz varied only its reduction of iron-replete Tf mark, whilst N-mono and C-mono termini remained iron bound, compare Figure 3.31 (b) with 3.9 (b).

The urea-PAGE data (Fz) and Fe(II)-Fz absorption profiles were alike for both NE and Epi, which is unsurprising given their similar behaviour thus far (data for Epi not shown). Dop, however, showed a negligible effect from the inclusion of Fz with both techniques and only appeared to be influenced by Fz in the evolution of the Tf EPR spectra. The competitive nature of the chloride anions from the Dop solutions makes the results obtained more complicated in terms of rates and extent of iron removal. It is therefore of more limited use in confirming a mechanism of iron reduction. Suffice to conclude it does eventually undergo the familiar transformation in its Tf EPR spectrum, implying a much retarded version of the mechanism may be occurring. Furthermore, the chloride ions do not hinder the overall reduction in the human Tf iron signal as shown in Figure 3.27, or in fact the bovine serum samples (Figure 3.23 (b)), where the spectral changes observed are comparable to those

occurring for NE and Epi. Though importantly the new peak for the sera samples had not yet emerged.

Evidently, the timescale of Fe(II) production from recording the Fe(II)-Fz complex and the removal of iron from Tf using urea-PAGE (Fz) are both in good agreement (for NE and Epi at least). This suggests the catecholamine mediated loss of iron coincides with Fe(II) generation. This combined with the ferric iron binding modifications observed from the EPR signals, all favour a mechanism of reduction to facilitate pathogeneses.

3.8 Conclusions

The current work uses EPR to explore the mechanism by which catecholamines liberate iron, at physiological pH, from the normally inaccessible hosts transferrin and lactoferrin. This removal of iron nurtures the growth of invading pathogenic bacteria in blood or serum, which are well documented to multiply when in the presence of the aforementioned neurochemicals.[15, 20] The pathway for extraction of the strongly bound ferric iron by catecholamines has to date, remained elusive, though the present study provides further insight into the processes occurring. Additionally, this work demonstrates the ability of EPR to detect reductions in the transferrin bound iron signal of human serum, when exposed to therapeutically relevant concentrations of catecholamines. This supports the possibility that EPR may have considerable medical applications in predicting the onset of catecholamine mediated infections.

The characteristic Tf and Lf, iron binding EPR signals evolve over time. This is triggered by the presence of catecholamines; norepinephrine, epinephrine, dopamine and synthetic inotrope dobutamine. A decrease in intensity of the Tf (or Lf) bound ferric iron signal is accompanied by the generation of a second signal. This is proposed to be from the catecholamine now binding to the ferric iron for the protein samples treated with NE and Epi. However, for the solutions inclusive of chloride the new peak is assigned to $FeCl_3$ with overlap from the Fe-CA. A number of factors are shown to affect the rate of catecholamine ferric iron binding. Among these is the structural size of the catechol species, which often hinders access to the host protein, interference from competitive binding, as well as the time period of incubation and the catecholamine concentration.

Given the weaker binding affinity of catecholamines for ferric iron in comparison with Tf or Lf, it is difficult to envisage that direct abstraction from Tf could occur.[3, 4, 27,

[31] Evidence for a pathway of reduction from developments in the EPR spectra in combination with the complimentary techniques of urea-PAGE and ferrozine iron(II) binding, confirm the iron loss from transferrin to coincide with iron(III) to iron(II) reduction.

The proposed route of iron extraction in sequence order may involve the following; entering the protein and complexing to the ferric iron at the two specific binding sites. Urea-PAGE suggests this occurs for the N-terminal prior to the C-terminal. This forms a Fe(III)-catecholamine complex, (in addition to $FeCl_3$ for Dop) as recorded using EPR and confirmed by the study of ferric and ferrous salts. The reduction of iron(III) occurs and is followed by Fe(II)-catecholamine complex removal from the protein. The complex extraction here is achievable given the far lower affinity of Tf for an iron(II) valency. Furthermore since catecholamines likewise possess a higher affinity for ferric over ferrous iron, the possibility that some of the Fe(II) is detached from the catecholamine complex is also considered. The rapid oxidation of any uncomplexed iron(II) species may be prevented by inclusion of an iron(II) sink, ferrozine, which is demonstrated to promote faster and more extensive removal of iron from Tf. Fz may also loosely model the behaviour of ferrous uptake systems *in vivo*, suggesting iron theft should be enhanced in the presence of bacteria. Quite reasonably, the effect of Fz is shown to differ for Dop treated Tf samples, when compared to NE and Epi. The former reveals significant interference in Fe(II) production, which is ascribed to competitive iron binding by the chloride ions present, as earlier discussed. While the presence of chloride ions is relevant to clinically administered catecholamines and processes occurring naturally in the body, it is not shown to interfere with the iron binding ability of the low catecholamine concentrations tested in this work.

It has previously been demonstrated that enterobactin (Figure 3.32 (a)) can both extract Tf bound iron and access the bacterial cell for microbial growth. This has been proven for a number of pathogens, including *E.coli* and *Salmonella.*[15] Investigation of the enterobactin (ferric uptake, *tonB*) mutants for growth indicate ferrous uptake systems in bacteria (*E.coli*), may additionally be involved in the capture of iron released from the catecholamine mediated interaction with Tf. Therefore, it is proposed that ferrous iron bound catecholamines can potentially, behave as pseudo-siderophores. Moreover, this low molecular weight solute is suggested to promote growth of bacteria when separated from the pathogens *via* a dialysis membrane *in vitro*, which mimics the physical conditions of a bacterial wall. A structural representation of the possible binding geometry of norepinephrine and iron is depicted in Figure 3.32 (b). It parallels

the proposed octahedral binding of ferric iron in enterobactin. A comparison of the two structures in Figure 3.32 reveals considerable similarity and supports the pseudo-siderophore model as a possibility.

In addition to behaving similarly to siderophores, with respect binding ferric iron in Tf, catecholamines are revealed in the present work, to reduce Fe(III) to Fe(II). This is an ability of ferric reductases that are necessary to release bound ferric iron from the siderophores, when internalised into the bacterial cell. Accordingly, catecholamines appear to encompass the key features of siderophores and ferric reductases, both of which prove essential to capture and use/store iron. This further strengthens the potential role of catecholamines as pseudo-siderophores.

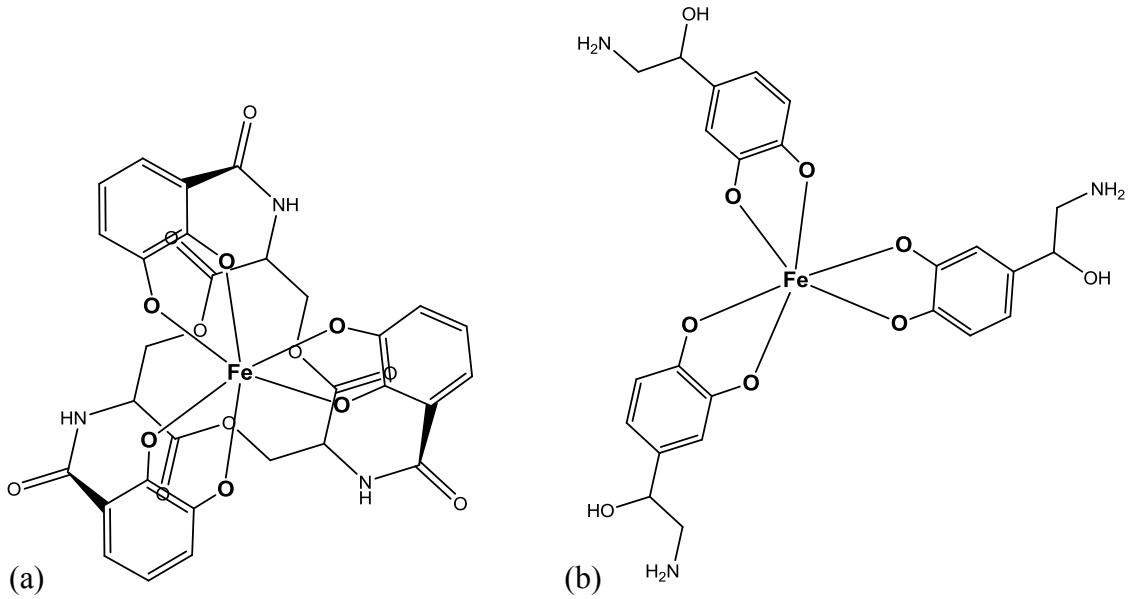

Figure 3.32 Structures of (a) siderophore-enterobactin binding a ferric iron and (b) the potential ferric/ferrous iron binding occurring for catecholamines such as norepinephrine (pseudo-siderophore). While enterobactin can directly source ferric iron, catecholamines like norepinephrine pictured are proposed to reduce the ferric iron to an accessible form to assist the bacterial acquisition.

The ability of pharmacologically administered catecholamine concentrations is also shown to visibly alter the iron binding status of human serum, which has demonstrated links with increased virulence.[36] It is well reported that patients in ICUs are more prone to develop infections through heightened stress levels and more than half receive catecholamine support for renal and cardiac functions.[8, 11, 20] Here the

catecholamines, both generated and administered are likely to reveal an additive effect. Notably, a concentration of 3.5 μM has been measured *in vivo* following infusion with only a low-medium dose of Dop.[9] Consequently, the steady catecholamine mediated removal of iron from such patients suggests their blood could become a more accessible nutritional source for bacteria, thereby supporting pathogenic growth. Moreover, the assessments in this work have only involved a single addition of catecholamine. *In vivo* this would be continuous, along with simultaneous catecholamine removal, though it is the interplay between the two processes that governs the final serum concentration and it is often variable between patients, thus requires extensive testing.

This clinical implication highlights the role of EPR as a potential diagnostic technique. A rapid and suitably sensitive assessment by EPR of the serum from at risk patients could be completed within minutes. This would determine any enhanced vulnerability to infection through compromised iron content in their serum Tf. Furthermore, the ease of sample retention (in pellet form) after recording is non-wasteful and enables further analyses to be performed on the same sample. Additionally, the use of liquid nitrogen temperatures throughout this work, which is widely accessible in hospitals, only adds to its appeal.

The limited supply and strict blood handling regulations deterred any further investigation into human blood samples during the time period permitted. Nevertheless the primary aim of this work has been demonstrated.

3.9 Future Work

Clearly an in depth EPR examination of the effects of physiological catecholamine concentrations on human transferrin is required, in order for this to be a realistic method to probe clinical samples. This, could be achieved through, for example,

- A greater pool of samples; spanning from healthy volunteers to more infection prone ICU patients, to certify that a modification in the EPR signal is observable among all catecholamine inclusive solutions. In addition, this could give insight on the other multiple species in blood, which may also have varying implications on the signal evolution with time.
- Obtaining samples from psychologically stressed individuals, to assess the impact of naturally produced catecholamines, on their Tf serum iron content.

- Blood samples taken before and after inotrope support, to directly probe for an additive effect, from two or more infused catecholamines, or from catecholamine metabolism.
- Assessing the EPR spectra of serum samples exposed to strains of gut born bacteria, as was attempted earlier in this work for *E.coli*. This would identify the extent of iron removal, over that occurring in the absence of the catecholamines.
- Localised investigations of the catecholamine Tf interactions during sepsis.
- Monitoring of the time period for the Tf bound signal to return to the original signal shape/intensity following catecholamine exposure. This could be used to examine any long term effects, since bacterial virulence is known to increase after a much shorter exposure period of only 4-6 hours.[6]
- A parallel study of Lf, since this source of iron resides in an environment of the body where bacteria are abundant and it has access to both NE and Dop as well as an array of bacterial species.

If indeed EPR can consistently reveal an alteration in the binding characteristics of transferrin for low catecholamine concentrations, its role in studying stress levels in patients and susceptibility to infection could be invaluable.

References

1 M. Lyte and S. Ernst, *Life Sciences*, 1991, **50**, 203.

2 P. P. E. Freestone, S. M. Sandrini, R. D. Haigh and M. Lyte, *Trends in Microbiology*, 2008, **16** (2), 55, and references therein.

3 L. Lambert, P. J. Perri, P. J. Halbrooks and A. B. Mason, *Comparative Biochemical and Physiology, Part B: Biochemistry and Molecular Biology*, 2005, **142** (2), 129.

4 C. Ratledge and L. G. Dover, *Annual Review of Microbiology*, 2000, **54**, 881, and references therein.

5 K. G. Wooldridge, J. A. Morrissey and P. H. Williams, *Journal of General Microbiology*, 1992, **138** (3), 597.

6 P. P. E. Freestone, R. D. Haigh, P. H. Williams and M. Lyte, *FEMS, Microbiology Letters*, 1999, **172**, 53.

7 M. Lyte, C. D. Frank and B. T. Green, *FEMS Microbiology Letters*, 1996, **139**, 155.

8 M. A. Smythe, S. Melendy, B. Jahns and C. Dmuchowski, *Critical Care Medicine*, 1993, **21** (9), 1319.

9 A. R. J. Girbes, M. T. Patten, B. V. McCloskey, A. B. J. Groeneveld and K. Hoogenberg, *Intensive Care Medicine*, 2000, **26**, 1685.

10 R. N. Juste, L. Moran, J. Hooper and N. Soni, *Intensive Care Medicine*, **24**, 1217.

11 P. P. E. Freestone, *Shock*, 2002, **18**, 465.

12 P. K. Peterson, C. C. Chao, T. Molitor, M. Murtaugh, F. Strgar and B. M. Sharp, *Reviews of Infectious Diseases*, 1991, **13** (4), 710.

13 M. Lyte and M. T. Bailey, *Journal of Surgical Research*, 1997, **70**, 195.

14 P. H. Williams, W. Rabsch, U. Methner, W. Voigt, H. Tschäpe and R. Reissbrodt, *Vaccine*, 2006, **24** (18), 3840.

15 P. P. E. Freestone, M. Lyte, C. P. Neal, A. F. Maggs, R. D. Haigh and P. H. Williams, *Journal of Bacteriology*, 2000, **182** (21), 6091.

16 K. S. Kinney, C. E. Austin, D. S. Morton and G. Sonnenfeld, *Microbial Pathogenesis*, 1999, **26**, 85.

17 A. Lactose, S. K. Malham, A. Cueff and S. A. Poulet, *Applied and Environmental Microbiology*, 2001, **67**, 2304.

18 G. A. Nieuwenhuijzen and R. J. Goris, *Current Opinion in Clinical Nutrition & Metabolic Care*, 1999, **2**, 399.

19 B. Kennedy, E. Dillon, P. Mills and M. G. Ziegler, *Life Sciences*, 2001, **69**, 87.

20 M. Lyte, *Trends in Microbiology*, 2004, **12** (1), 14, and references therein.

21 M. T. Anderson and S. K. Armstrong, *Journal of Bacteriology*, 2006, **188**, 5731.

22 P. P. E. Freestone, N. J. Walton, R. D. Haigh and M. Lyte, *International Journal of Food Microbiology*, 2007, **119** (3), 159.

23 P. P. E. Freestone, R. D. Haigh, P. H. Williams and M. Lyte, *FEMS, Microbiology Letters*, 2003, **222**, 39.

24 P. P. E. Freestone, R. D. Haigh and M. Lyte, *FEMS Microbiology Letters*, 2007, **269**, 221.

25 A. Roberts, J. B. Matthews, S. S. Socransky, P. P. E. Freestone, P. H. Williams and I. L. C. Chapple, *Oral Microbiology and Immunology*, 2002, **17** (5), 296.

26 C. P. Neal, P. P. E. Freestone, A. F. Maggs, R. D. Haigh, P. H. Williams and M. Lyte, *FEMS Microbiology Letters*, 2001 **194**, 163.

27 C. Gérard, H. Chehhal and M. Aplincourt, *Journal of Chemical Research (S)*, 1999, 90.

28 J. D. Adams (Jr) and I. N. Odunze, *Free Radical Biology & Medicine*, 1991, **10** (2):161, and references therein.

29 H. P. Monteiro and C. C. Winterbourn, *Biochemical Pharmacology*, 1989, **38** (23), 4177.
30 R. A. Løvstad, *The International Journal of Biochemistry*, 1990, **22** (6), 641.
31 U. El-Ayaan, R. F. Jameson and W. Linert, *Journal of the Chemical Society, Dalton Transactions*, 1998, 1315
32 G. N. L. Jameson and W. Linert, *Journal of the Chemical Society, Dalton Transactions 2*, 2001, 569, and references therein.
33 W. Linert, E. Herlinger, R. F. Jameson, E. Kienzl, K. Jellinger and M. B. H. Youdim, *Biochimica et Biophysica Acta - Molecular Basis of Disease*, 1996, **1316** (3), 160.
34 G. G. Borisenko, V. E. Kagan, C. J. Hsia and N. F. Schor, *Biochemistry*, 2000, **39** (12), 3392.
35 G. N. L. Jameson, R. F. Jameson and W. Linert, *Organic & Biomolecular Chemistry*, 2004, **2**, 2346.
36 R. Shergill, S. M. Sandrini, J. Woodward, R. Muralikuttan, R. D. Haigh, M. Lyte and P. P. E. Freestone, *Journal of Bacteriology*, 2010, **192** (12), 587.
37 J. Wally, P. J. Halbrooks, C. Vonrhein, M. A. Rould, S. J. Everse, A. B. Mason and S. K. Buchanan, *Journal of Biological Chemistry*, 2006, **281** (34), 24934.
38 S. Ford, R. A. Cooper, R. W. Evans, R. C. Hider and P. H. Williams, *European Journal of Biochemistry*, 1988, **178**, 477.
39 O. Zak, P. Aisen, J. B. Crawley, C. L. Joannou, K. J. Patel, M. Rafiq and R. W. Evans, *Biochemistry*, 1995, **34** (44), 14428.
40 D. A. Folajtar and N. D. Chasteen, *Journal of the American Chemical Society*, 1982, **104**, 5775.
41 C. P. Neal, P. P. E. Freestone, A. F. Maggs, R. D. Haigh, P. H. Williams and M. Lyte, *FEMS Microbiology Letters*, 2001, **194** (2),163.
42 L. L. Stookey, *Analytical Chemistry*, 1970, **42** (7), 779.
43 S. Bailey, R. W. Evans, R. C. Garratt, Gorinsky B, Hasnain S, Horsburgh C, Jhoti H, P. F. Lindley, A. Mydin, R. Sarra and J. L. Watson, *Biochemistry*, 1988, **27**, 5804.
44 J. E. Wertz and J. R. Bolton, *Electron Paramagnetic Resonance, Elementary Theory and Practical Applications*, Chapman and Hall, 1994.
45 D. Caccavo, N. M. Pellegrino, M. Altamura, A. Rigon, L. Amati, A. Amoroso and E. Jirillo, *Journal of Endotoxin Research*, 2002, **8** (6), 403.
46 W. H. Traub, D. Bauer and U. Wolf, *Chemotherapy*, 1991, **37** (6), 426.
47 J. J. Bullen, H. J. Rogers, P. B. Spalding and C. G. Ward, *Journal of Medical Microbiology*, 2006, **55**, 251.

4. A Novel Bisacylphosphine Oxide Photoreaction

This chapter focuses on uncovering the identities of the previously unobserved radicals that are produced when BAPO (Figure 4.3) is irradiated in alcohol or water containing solutions. This new photochemistry is firstly probed using TREPR spectroscopy, to investigate the route of radical formation and construct plausible reaction mechanisms. This is followed by performing DFT calculations to evaluate the likelihood of formation of these proposed radicals, by estimating their hyperfine coupling constants, which are then compared with the recorded spectroscopic data.

Free radical polymerisation for crosslinking monomers is commonly used in industry to solidify and harden materials, this process is called curing. While conventionally polymerisation was heat initiated, the benefits of increased selectivity, heightened production speeds and quality, combined with less environmental waste has seen photocuring prevail as the most desirable technique for polymerisation. It now replaces the aforementioned thermal curing for the majority of applications in the coatings, inks and adhesives industry, as well as expanding the application further afield to microelectronics, and photoimaging technologies.[1]

The TRIR spectrometer allows the photoreactions of a variety of commercially available photoinitiators to be studied.[2, 3] The common feature among them is the efficient UV initiated generation of a benzoyl radical ($C_6H_5OC^{\bullet}$) or substituted analogue. This absorbs at a distinct carbonyl frequency, $\nu_{c=o}$, that differs significantly (~ 150 cm^{-1}) from that of the precursor molecule. The benzoyl radical by virtue of its absorption in the 1780 cm^{-1} to 1880 cm^{-1} region of the infrared spectrum, absence of competitive processes and easily manipulated lifetime, is an ideal candidate to monitor magnetic field effects using the TRIR spectrometer described in Section **2.2.1**. Two types of precursor molecule were used for the work described in this thesis, the first were organic α-hydroxy ketones. These include αhp (as discussed in Section **2.2.6.1.2**) and to a far lesser extent 2-hydroxyethoxy-2-methylpropiophenone, mhp. Both of these were used to probe reverse micelles and the former used to investigate viscosity effects, in Chapter **5**, their structures are also given therein. The second group of molecules studied are the acyl phosphorous oxides. These are introduced in this chapter and were investigated for their unique spin properties that occur as a result of the large hyperfine coupling in the generated phosphorus radical.

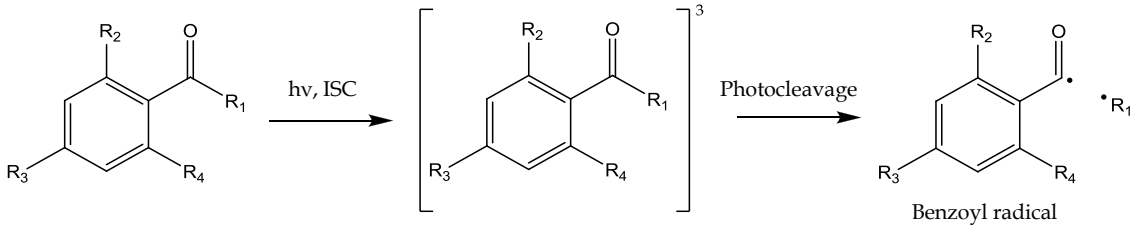

Figure 4.1 The photoexcitation of α-hydroxy ketones occurring *via* classical type I cleavage, to produce a RP. The benzoyl moiety features a $\nu_{c=o}$ absorption at ~ 1820 cm^{-1}, which allows it to be recorded using the TRIR spectrometer.

The photochemistry of α-hydroxy ketones is well understood and follows the general scheme shown in Figure 4.1.[3] When exposed to UV radiation, an electron in the α-hydroxy ketone precursor is promoted to the lowest unoccupied molecular orbital (LUMO), thereby destabilising the molecule. Refer to the Jablonski diagram in Figure 4.2. From the resulting singlet excited state (S_1), the molecule undergoes intersystem crossing (ISC) to the lowest triplet state (T_1), followed by fragmentation of the α-carbon bond.[3-5] This process is called *type I Norrish cleavage*, and all the molecules discussed in this work cleave in this manner. The rate of cleavage is revealed as dependent on the substituents R_3 and R_1 and occurs faster for *para*-unsubstituted mhp than αhp, due to the selective nπ character of the lowest triplet state.[3] The resulting radicals are separately able to initiate polymerisation. The rate of polymerisation among the different benzoyl radicals is again dependent on the nature of the substituent, R_2 to R_4 (on the ring). An increasingly substituted ring structure favours faster addition to unsaturated species, such as thiophenol and *n*-butylacrylates.[6]

Photopolymerisation and photocuring technologies are constantly evolving. This is achieved through the design of novel and specific initiators for specialist applications such as the coating of wood, plastics and inks. For the curing of clear lacquers, specially formulated photoinitiators have been available for years, however, the same is not true for the curing of pigmented lacquers.[7] Pigments determine the colour and opacity of materials and it is this colour that poses many additional obstacles in the formulations for curing pigmented systems. Coloured coatings compete with the photoinitiator for absorption of incident UV light and the remaining amount of near UV-vis radiation (> 300 nm) that passes through the pigmented solutions is not adequately absorbed by the photoinitiators used for clear coatings. The result is a slow or incomplete polymerisation, rendering the same photoinitiators unsuitable for use with pigmented

solutions.[8] Attention has therefore shifted to the development of new photoinitiators, which possess a higher molar absorption in the 300-400 nm range. However, the efficiency of the photocleavage described by the *quantum yield*, Φ, is often compromised when modifying molecules to attain this shifted absorption.[3]

α-aminoacetophenones[9] and thioxanthone[10] derivatives were found to possess this desired quality and a combination of both their functionalities served to increase their efficiency further.[11] This propelled their popularity in commercial applications involving printing inks and electronics. Undesirably, the tendency of these derivatives to impart a considerable yellowing to the finish upon polymerisation of thicker layers deemed them unacceptable for the curing of white pigmented coatings.[12]

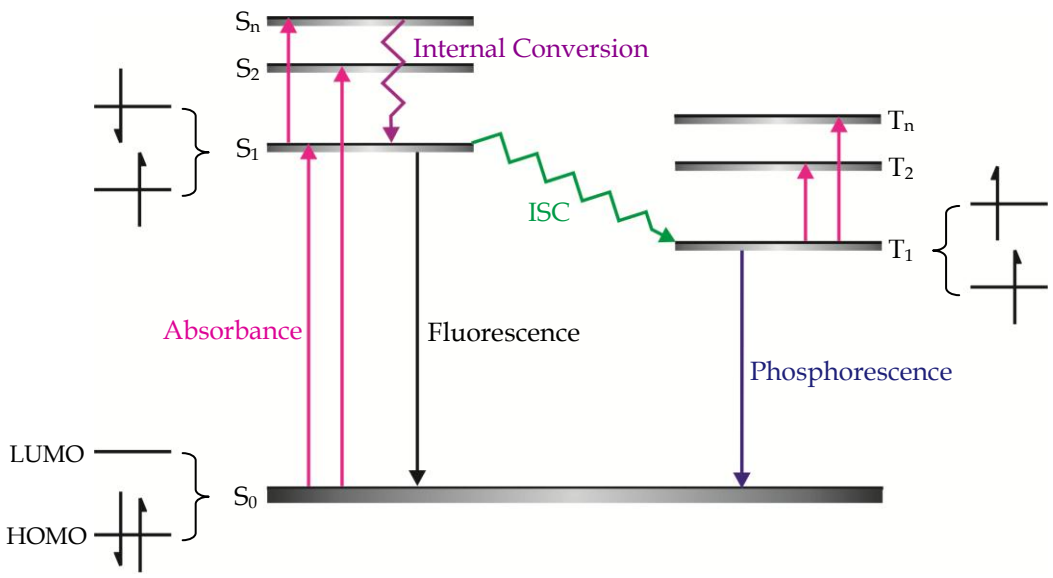

Figure 4.2 The Jablonski diagram to illustrate the possible transitions between the lower electronic states of a photoexcited molecule. The straight arrows indicate radiative processes, and the zigzagged arrows are non-radiative. The example molecule contains an even number of electrons with no orbital degeneracy, and the vibrational levels have been omitted from the diagram for simplicity.

4.1 Mono and Bisacylphosphine Oxides

The breakthrough arose from monoacylphosphine oxides (MAPOs). These have existed for decades in some areas of industry, although, have only recently emerged in radiation curing. Specifically in the manufacture of white furniture coatings, and thick sections.[13]

Among the key properties of MAPOs is the extended absorption into the visible region, which occurs at λ_{max} = 380 nm and can be assigned to the $n \rightarrow \pi^*$ transition. As well as travelling relatively unhindered through pigments, these longer wavelengths (~ 400 nm) allow the curing of deeper layers than achieved by previous methods, with depths up to several centimetres noted in some applications.[12] The peak absorbance centred around 230 nm ($\pi \rightarrow \pi^*$) proves particularly valuable for surface curing processes. The high energy photons associated with this short wavelength increase the rate of radical formation and consequently polymerisation. Moreover, the yellowing of coatings often encountered with other photoinitiators disappears upon curing, along with the long wavelength absorption due to the acyl-phosphinoyl bond. This allows radiation to travel progressively further through the coating.[8]

Monoacylphosphine oxide (MAPO), commercially recognised as Darocur TPO, forms the basis for a new class of photoinitiator which are derived from variations of this molecule.[2] The structure of MAPO is included in Figure 4.3 (a) for reference. These derivatives as well as MAPO are capable of producing a smooth, colourless, transparent finish, however, are limited in the depth of the coating film that may be applied to a given surface. For this reason alternative acylphosphine oxides are necessary to meet the more rigorous demands during polymerisation and are supplied in the form of bisacylphosphine oxides (BAPOs). BAPOs encompass all the benefits of MAPOs plus an increased efficiency driven by the ability to generate up to four highly reactive radicals upon irradiation. Each of these radicals is an effective photoinitiator, serving to increase the overall rate of the radical reaction, over that achievable with MAPOs. This makes these molecules very valuable for use in polymerisation reactions.[13]

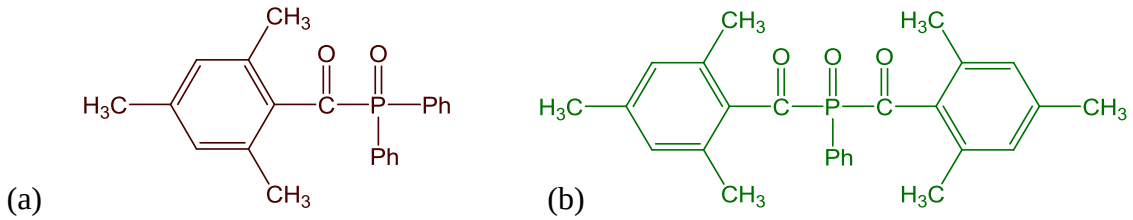

Figure 4.3 Structures of (a) (2,4,6-trimethylbenzoyl)diphenylphoshine oxide (MAPO) and (b) Bis(2,4,6-trimethylbenzoyl)phenylphosphine oxide (BAPO).

The UV-vis absorption profile of BAPO reveals a λ_{max} = 368 nm, a value lower than for the aforementioned MAPOs. Though, it is the bathochromic shift of the $n \rightarrow \pi^*$ transition that gives BAPOs a higher molar absorption at wavelengths of $\geq$ 400 nm, thus allowing the through cure desired, and adding to their widespread appeal. BAPOs like MAPOs photobleach the material after UV exposure and polymerisation, leaving a white appearance as opposed to the off white encountered with other photoinitiators.[8] Although this photoinitiator was developed primarily for manufacturing dental materials, it has since found extensive use in industry.[13]

4.1.1 The Reactivity of Mono and Bisacylphosphine Oxides and Investigation of the LFE

It has been well documented that upon irradiation, both mono and bisacylphosphine oxides undergo rapid α-cleavage, proceeding *via* a short lived triplet state ($\tau_T < 1$ ns), to produce an acyl-phosphinoyl RP with high efficiency (Φ = 0.56).[14-16] The photochemical route parallels that described in Figure 4.1 for the α-hydroxy ketones, though cleavage for these phosphorus molecules is faster and more efficient.[3] Both of the resulting radicals have been extensively studied. In particular, attention has focused on the structure and reactivity of the phosphorus based radical,[8, 14, 17, 18] which is found to be a few orders of magnitude more reactive than the benzoyl radical towards olefins.

The relative reactivities and the polymerisation progress of numerous mono and bisacylphosphine oxides have been studied using a variety of techniques. The most abundant reports feature TREPR and laser flash photolysis (LFP) with the latter used solely for the direct detection of the phosphinoyl radical using near visible light.[17-20] The application of TRIR spectroscopy is far less common. However, has been used to probe the $\nu_{c=o}$ stretch of the resulting 2,4,6-trimethylbenzoyl radical, with an IR diode laser in a manner similar to that described in this work. The study investigated the addition of the resulting carbon based radical to species, such as thiophenol (PhSH) and quencher CCl_3Br (also used in Chapter **2**). These species alter the lifetimes of the transient IR curves and yield information on the addition rates.[21] The corresponding rates for the phosphorus radical were for this study again determined from LFP.

More recently TRIR spectroscopy and S^2TRS have identified combination products from the photolysis of MAPO.[6] The TRIR system was able to detect only the benzoyl[†] radical. Whereas, S^2TRS was used to monitor the deletion of both the $\nu_{C=O}$,

[†] Acyl radical and benzoyl radical are used interchangeably.

and $\nu_{P=O}$ ground state absorptions of MAPO, upon photolysis. Simultaneously, S^2TRS also recorded the generation of the transient radicals, occurring 1.1 μs following the laser flash. The trimethylbenzoyl radical absorbed at the usual 1800 cm^{-1}, and the phosphorus radical at 1160 cm^{-1}. Given that the photolysis of MAPO was performed in acetonitrile, the lifetimes of the radicals were only several microseconds and within 5 μs the dimerised product of a pair of phosphinoyl radicals was detected.

Many similar accounts of the reactivity of the MAPO and BAPO phosphorus radicals as well as their derivatives can be found in the literature.[13, 17, 18, 20] Their relative reactivity can be attributed to the degree of *s*-character in the SOMO, in combination with the localisation of electron spin on the phosphorus atom.[17] Since the SOMO dictates the local geometry around the phosphorus centre, the greater the amount of *s*-character of the SOMO, the more pyramidal the adopted shape will be. An increasingly bent structure, as found in MAPOs, provides easier access to the lone electron for subsequent reactions. This explains the heightened reactivity of the radical, over that encountered with BAPOs and also rationalises their respective hyperfine coupling constants. The hfc for the MAPO phosphorus radical is invariably higher than the BAPO, due to the partial delocalisation of the spin into the phenyl ring for the latter structure. It is this demonstrated high reactivity, which has ensured that phosphorus oxide derived photoinitiators now play a fundamental role in many commercial polymerisation processes.[13]

Previous analogies have been made between acylphosphine oxides and aryl ketones (such as the α-hydroxy ketones); however, the spin properties of acylphosphine oxides differ considerably. Notably the hyperfine couplings between the lone electron and the phosphorus radical centre are typically in the region of 40 mT, in contrast to the carbon based radical centre, which exhibits a typical coupling of ~ 2 mT. This large hyperfine coupling exhibited by the phosphorus centred radical, when partnered with a small coupling makes the RP produced upon photolysis of the acylphosphine oxides an ideal candidate for generating a broad low field effect.[22, 23] The LFE is more pronounced for RPs with large hyperfine couplings (a), and/or longer lifetimes (τ), from the relationship $\tau^{-1} \ll a$, (see Section **1.5.1**). So again, in reference to aryl ketone molecules that generate radicals in a similar environment to the acylphosphine oxides (i.e. both have identical lifetimes), the LFE for the phosphorus RP will inherently be larger. This therefore allows a more detailed exploration into the environmental factors that affect the magnitude of the field effect. The LFE from the

photolysis of MAPO has formerly been observed to extend up to 50 mT in encapsulated spin chemistry studies,[24, 25] though remains unstudied in different RP environments.

In this work, measurements of the magnetic field effects from the MAPO and BAPO (Figure 4.3) derived radicals in viscous homogeneous solution were recorded. An unexpected MARY dependence for BAPO led to a more detailed investigation using time resolved EPR spectroscopy. This combined with theoretical predictions of the hfccs assisted in unravelling the mechanism of the recorded photochemistry.

4.2 Results and Discussion

4.2.1 The Unusual Magnetic Field Effect

20 mM of MAPO and BAPO each prepared in cyclohexanol were flowed through the CaF_2 cell of 0.1 mm pathlength, at a speed of 1.7 ml min^{-1}. The decay curves were recorded for various field points ranging from 0-37 mT, with the magnetic field consecutively off, then on for 2000 averages to obtain the resulting MARY data displayed in Figure 4.4. This data is presented as a % MFE vs. magnetic field strength plot, in accordance with Equation [2.2].

The MAPO photoinitiators exhibit the expected LFE.[25] Since cleavage proceeds through the triplet state, the spin Hamiltonian describing the generated RP possesses a higher triplet character (i.e. the RP is triplet correlated). This ensures that any recombination occurring is as a result of S-T mixing. To reiterate the discussion in Chapter **1**, the effect of a weak field is to enhance the amount of S-T mixing over that occurring in zero field conditions, by removing the spin-state degeneracies present. This supports a higher proportion of singlet recombination arising in the geminate cage, which for isotropic homogeneous solution occurs within 1 μs. This, however, cannot be distinguished from the f-pair phase in the current setup, since both are measured at the same frequency. Therefore the observed field effect most likely arises from both g- and f-pair recombination effects.

The recorded kinetic curves confirm enhanced g-pair combination, by revealing a lower radical yield compared to the zero field condition, thus proving a reduction in the number of f-pairs escaping the cage. By processing the radical decay data using Equation [2.2], the sign of the resulting MARY data differs from a conventional MFE, and gives rise to the witnessed LFE. This result is consistent with the radicals expected from type I α-cleavage, as shown in Figure 4.1. It is the strong hfc in the phosphinoyl

radical combined with the negligible hfc in the benzoyl radical, which has generated such a substantial LFE, an occurrence that is often noted in literature.[22, 23, 26]

There is considerable similarity between the radicals known to be formed from the photocleavage of MAPO and BAPO. They feature identical benzoyl radicals and vary only in their respective counter radicals. Therefore, a comparable field dependence was anticipated for BAPO with perhaps a change in the depth and position of the LFE, due to lower hfc in the phosphorus based radical. Clearly, the observed field dependence for the BAPO derived RP is distinctly different. There is no evidence of a LFE. Indeed this pair appears to demonstrate an opposite phase field effect, in line with a conventional MFE, arising from gradual triplet state ($T_{\pm}$) removal through the Zeeman effect. This limits the spin-state mixing to the S and T_0 states, causing an increase in the number of RPs escaping the cage and manifests as a higher proportion of radicals recorded using the IR beam. To probe for a definite MFE higher magnetic fields than those used here would be necessary, requiring up to 600 mT to observe MFE saturation in the case of the micelle encapsulated MAPO radicals.[25]

This result is difficult to account for if the RP is indeed the expected one. All current evidence would predict rather similar behaviour for both the MAPO and BAPO derived RPs unless their lifetimes were obviously different. This unusual behaviour led to further investigation of the photochemistry of these two reactions in more detail, using time resolved EPR spectroscopy.

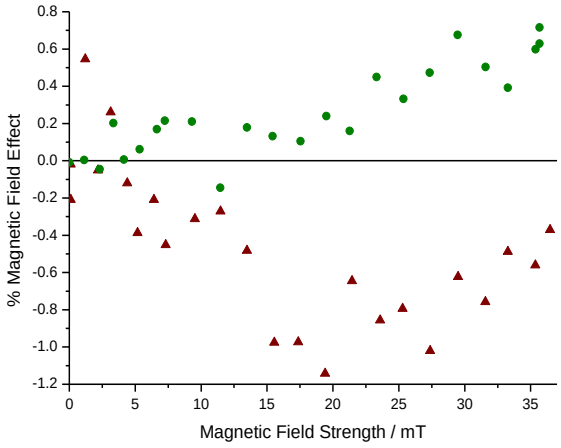

Figure 4.4 The MARY curves recorded for the ▲ MAPO, and ● BAPO derived RPs in cyclohexanol solution, conducted at different magnetic field strengths in the range 0-37 mT, at room temperature.[27] The MAPO radicals display a clear LFE. Whereas the BAPO radicals show no such LFE and immediately show the onset of a typical MFE, with very shallow field dependence.

4.2.2 The Time Resolved EPR Investigation of BAPO

The TREPR spectra obtained from the laser flash photolysis of MAPO and BAPO in acetonitrile are presented in Figure 4.5 (a). Both the MAPO and BAPO spectra clearly exhibit three enhanced absorption peaks and reveal signs of CIDEP. This confirms that the radicals were produced *via* triplet mechanism (TM) polarisation, occurring as a result of a non-Boltzmann population distribution among the electron spin levels, on intersystem crossing to the triplet excited state (Section **2.1.4.2** for CIDEP). The selective population of the energy levels is retained in the generated radicals.

The large doublet originates from a phosphinoyl radical, whilst the inner peak can be assigned to the carbon based benzoyl radical, whose couplings are unresolved at this sweep width. This result is in accordance with the expected photochemistry and previous findings.[18] The two spectra only differ in their respective ^{31}P hfccs, where the value for the BAPO phosphorus radical (26.6mT) is significantly lower than that from the MAPO phosphorus radical (37.2mT). This variation can be rationalised by the frontier orbital approach and the amount of *s*-character in the SOMO, as mentioned earlier (see Section **4.1.1**).[17]

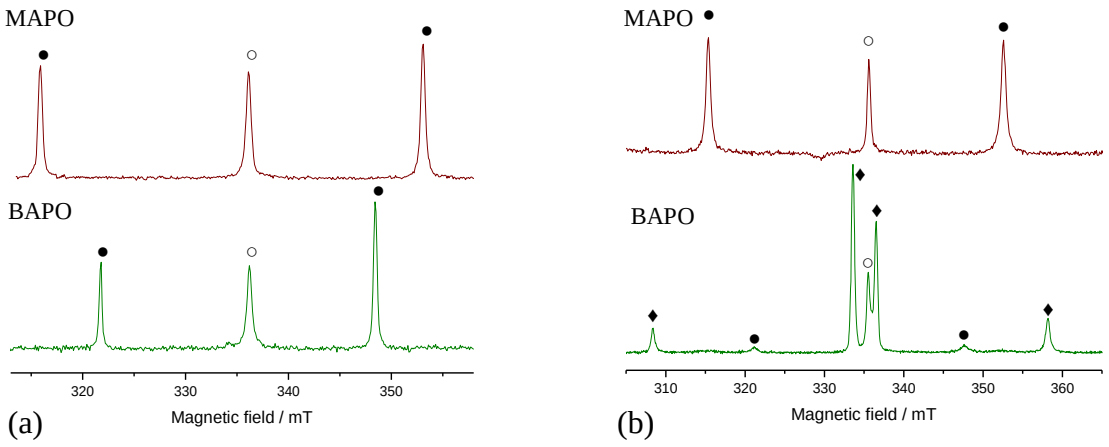

Figure 4.5 The TREPR spectra from the photolysis (266 nm) of 10 mM MAPO and BAPO in nitrogen saturated (a) Acetonitrile, and (b) Cyclohexanol, recorded 500-1000 ns after laser excitation. The peaks are as follows, ○ benzoyl radical, ● phosphorus radical, ♦ unknown radical species. All the spectra are highly spin polarised in enhanced absorption, and reveal only slight distortion of the high and low field lines.

The TREPR spectra for MAPO and BAPO photolysed in cyclohexanol are presented in Figure 4.5 (b). In this solvent the spectrum obtained for MAPO is effectively equivalent to that obtained in acetonitrile and in previous literature studies.[18] It exhibits a hyperfine coupling of 37.2 mT for the phosphorus based radical, alongside the expected central benzoyl peak. The BAPO spectrum, however, is markedly different. The phosphinoyl peaks with a ^{31}P hfc of 26.6 mT, and the central benzoyl peak are still present, but additional strong spectral lines are also observed. These consist of two additional sets of doublets; a small central doublet with a hyperfine coupling of 2.9 mT, and a much larger doublet with a coupling of 49.8 mT. These previously unobserved spectral features indicate that the photochemistry in this system is much more complex than originally anticipated and suggested by the TREPR spectra recorded in acetonitrile. This result can be explained either by a completely different photochemical pathway or by competition between the existing α-cleavage process and an additional reaction. Consequently, further investigations were performed using TREPR experiments to gain insight into the nature of the observed species.

The spectra were recorded for 10 mM BAPO photolysed in acetonitrile with only 5 % cyclohexanol by volume added, where again, the same behaviour was observed. By viewing the relative time decays and evolution of the various radical species, the BAPO TREPR datasets can provide additional insight into the origin of the unknown radicals. Figure 4.6 shows the data from the photolysis of BAPO in the acetonitrile/cyclohexanol mix displayed in two forms, mode 2 and mode 1, respectively, as described in Section **2.1.4.1**. It is important at this stage to remember the decay of a particular spectral line can be influenced both by the removal and relaxation of the radical species involved, so it is not necessarily a definite reflection of the lifetime of the radical generated.

The first dataset (a), is composed of the TREPR spectra collected 100-1000 ns following the laser flash, with integration performed every 100 ns. While (b), displays the lifetimes for the individual radicals formed.

The most striking feature of time decay (b), is the longevity of the radical responsible for the small doublet, which remains prominent long after 4000 ns has elapsed. Both sets of data reveal the original phosphinoyl radical signal to decay most rapidly, closely followed by the benzoyl radical, which dominates the early spectra (~ 100-300 ns) in (a). The signals absent from the acetonitrile spectrum are shown to reach a maximum later in time than either of the previously identified radicals.

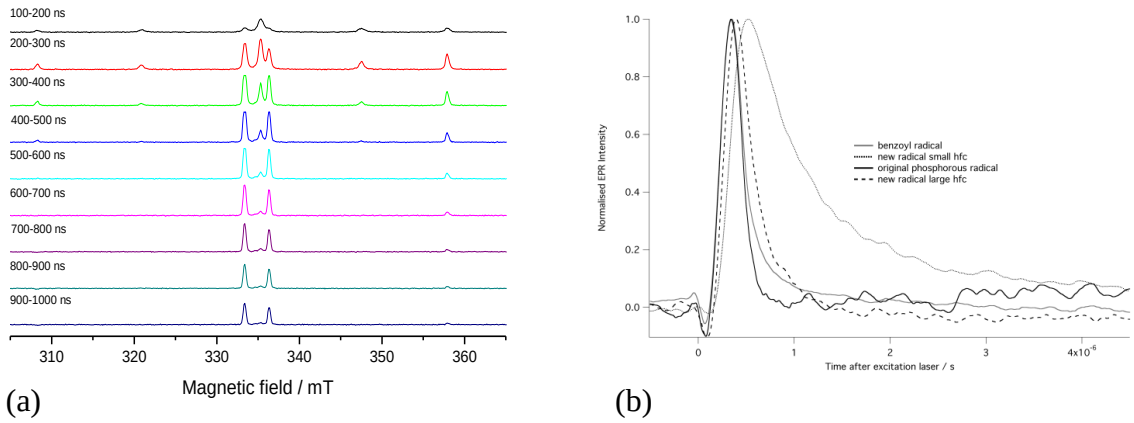

Figure 4.6 (a) The TREPR spectra for 10 mM BAPO photolysed in a nitrogen saturated acetonitrile and cyclohexanol solvent mix. The spectra are shown after integration is performed at 100 ns time intervals. (b) Is the corresponding time dependence for each of the radicals featured in (a).

The first conclusion that can be drawn from this data is that the four unidentified signals absent from the acetonitrile spectrum do not originate from the same radical, but most likely come from at least two different species. It is also feasible that the delay in the appearance of the CIDEP signals, for the two new signals, implies that they are generated from one or both of the original radicals. Though for the radical with the large hfc, the relaxation time looks similar to the original two radicals and thus the change in the rise time of the signal seems best explained by its generation through a secondary process. For the new signal with the small hfc, the relaxation time is much longer, which may also lengthen the rise time. Importantly, there is no evidence to suggest that the traditional phosphinoyl/benzoyl radicals are formed from the new radicals in this system.

Formation of the two new signals in a sequential process is certainly worth consideration based on the delay in their generation. Particularly since BAPO has, in certain polymerisation reactions and spin trap studies, been shown to undergo α-cleavage of both carbonyl moieties after addition to an adduct, or by forming a combination product. However, this often occurs through continued irradiation of the same sample, and may not necessarily be as relevant here.[13, 17] The possibility of a sequential reaction is explored further in Section **4.2.3.2**.

A number of conclusive factors were revealed by the aforementioned sets of data, and collectively these aided to construct the initial photochemical mechanism. These key factors are summarised as the following,

- The photolysis of BAPO in solutions containing cyclohexanol generates at least two radical species not observed in the photolysis of BAPO in pure acetonitrile.
- The signals from the phosphinoyl/benzoyl radicals are stronger than new radical signals at very early times, so it is reasonable but not necessary, to suggest that the new radicals may be formed from the conventional RP.
- The new radical with the 2.9 mT coupling relaxes relatively slowly.

Thus it appears that the presence of cyclohexanol is critical to the formation of the previously unobserved radicals. The most likely event to occur in this system is a nucleophilic attack between the alcohol group of the cyclohexanol and the carbonyl group of the BAPO molecule, to form a hemiketal. Previous studies of acylphosphine oxides[28] have concluded that the presence of the phosphine oxide group can enhance the reactivity of a carbonyl group with respect to hydration and hemiketal formation and such a process is likely to be more effective in BAPO than in MAPO. If hydration were to take place in MAPO, the conjugation of the benzene ring to the carbonyl group would be removed. Therefore the molecule would no longer absorb in the correct region of the UV for flash photolysis, resulting in an absence of radical signal in the mid IR, and TREPR spectra. As a consequence if any pre-reaction does occur for MAPO, it remains silent to the spectroscopic methods used here. Since BAPO contains two benzoyl groups, it is possible for one to be converted to a hemiketal and for the molecule to continue exhibiting benzoyl group photochemistry.

To further test this hypothesis, the photochemistry was observed with a range of solvents possessing a different propensity for hemiketal formation. Propan-2-ol and water were both selected to confirm that it is the reaction with the OH group that is vital for the creation of the additional species. Ethane-1,2-diol was chosen based on the presence of two alcohol groups and therefore the potential to form a cyclic ketal. Two alcohols considered poor at hemiketal formation were also investigated. Trifluoroethanol due to its much lower pKa (reduced nucleophilicity of the OH oxygen) as well as *t*-butanol, which despite having the highest pH, is likely to experience hindrance when forming hemiketals due to steric crowding.

Figure 4.7 shows the TREPR spectra obtained in these five systems, with the results being in good agreement with the earlier predictions. Propan-2-ol and water both clearly display signals from the new radical species. In ethane-1,2-diol, the additional peaks are more dominant and the hyperfine coupling measured between the outermost peaks is significantly larger than for the other alcohols, indicating the solvent molecule

must in some way be attached in this radical. Notably there is also an additional doublet present (barely visible) with a hyperfine coupling of 38.1 mT, the likely origin of this new signal is from the formation of a cyclic ketal. Only a very weak signal is observed in *t*-butanol as expected due to the steric reduction in the OH availability. The hyperfine coupling between the outermost peaks is, in this case, smaller than for propan-2-ol, again indicating the presence of some part of the alcohol molecule in the radical responsible for these peaks.

Encouragingly, the stronger acid, but poorer nucleophile trifluoroethanol, also reveals the anticipated behaviour. It exhibits almost exclusively the photochemistry recorded in acetonitrile and a negligible signal from the new radical species. A final important observation stems from the size of the new small hyperfine coupling constant (2.9 mT in cyclohexanol), which also subtly appears to vary across the different solvents. This suggests the solvent may likewise be attached in the radical causing the smaller doublet. On the basis of these results, hemiketal formation was proposed as the primary reaction step leading to the generation of the new TREPR signals.

Also noteworthy at this stage is that in addition to the TREPR studies, ^{31}P NMR experiments were performed on BAPO dissolved in various alcoholic solvents. However, the results proved unequivocal and DFT calculations were undertaken to better understand the observations from the TREPR results.

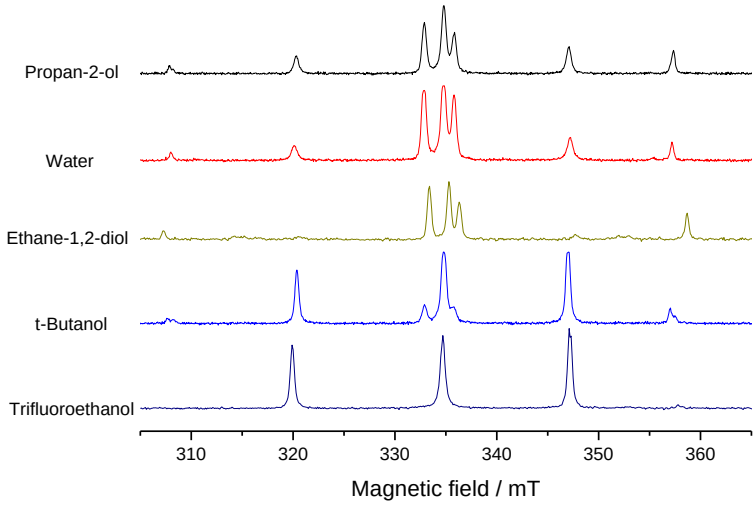

Figure 4.7 BAPO photolysed in acetonitrile with varying alcohols and water added, to determine the influence of the solvent on the produced radicals. The observation time window for these spectra is from 500 to 1000 ns after laser induced photoexcitation.

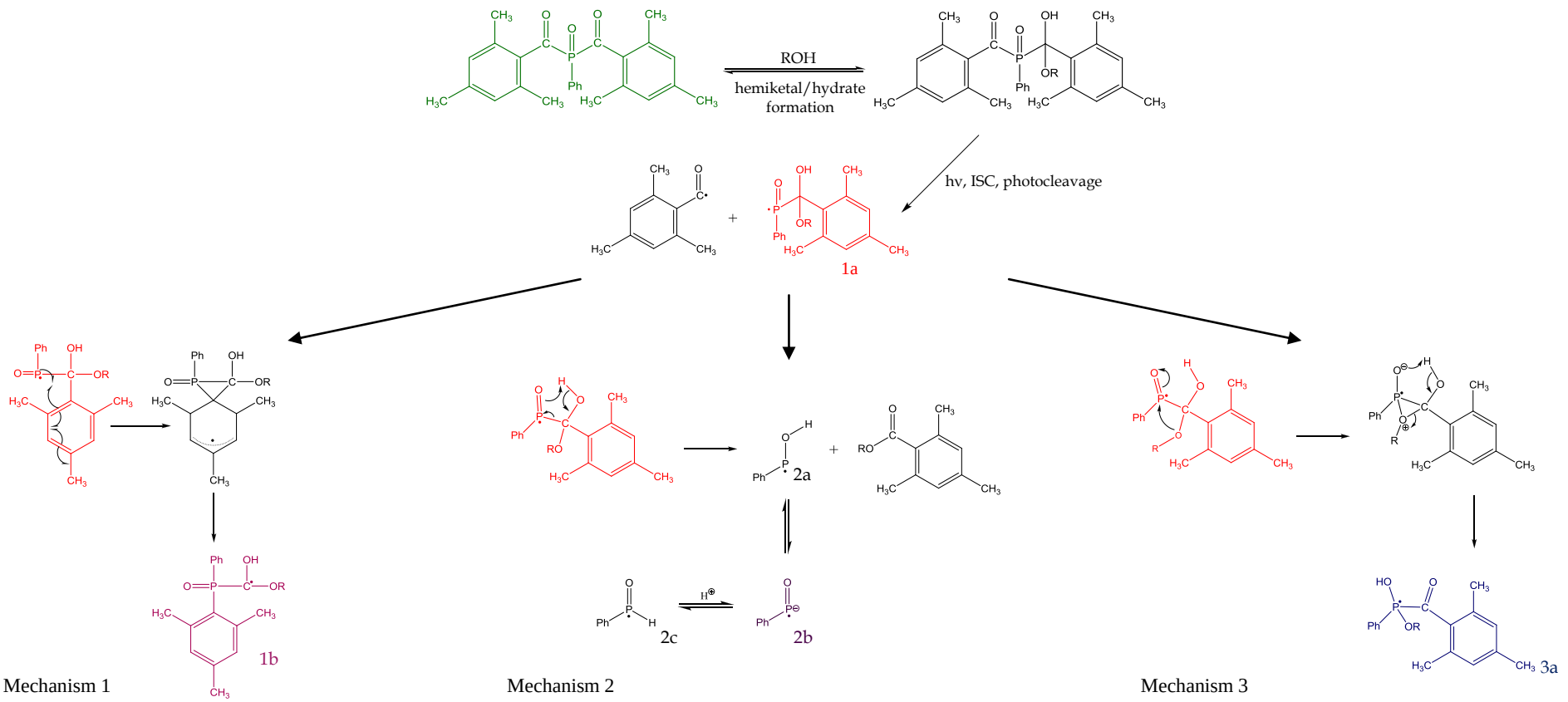

Figure 4.8 The likely photochemical pathways for the production of the unknown radical species from the photolysis of BAPO in alcohol/water containing solutions. In all three mechanisms the initial step is hemiketal formation, followed by photochemical cleavage. Mechanisms 1 and 2 show the radical species capable of generating the small hfcc, whilst Mechanism 3 contains the structure most likely to cause the large unknown coupling. R is dependent on the reaction medium.

4.2.3 Possible Mechanisms Occurring

Suppose, as a result of the nucleophilicity of the solvent (alcohol/water) and prior to photoexcitation, an equilibrium were established between BAPO and its hemiketal/hydrate form. Then, since both forms contain the absorbing chromophore, they would both be capable of undergoing photoexcitation during the laser flash. Clearly the regular form of BAPO would give rise to the photochemistry as observed in acetonitrile, so requires no further attention. The photochemistry of the resulting hemiketal would however, upon photoexcitation and subsequent ISC to the T_1 state, undergo α-cleavage by photolysis, to produce the acyl-phosphinoyl RP, as shown in Figure 4.8.

The phosphinoyl radical produced is a potential candidate for the unassigned EPR doublet featuring the 49.8 mT hfcc in cyclohexanol. Here, considering the group adjacent to the central phosphorus is now a four-coordinated carbon centre, the radical (1a), may adopt a more tetrahedral (Td) structure than the MAPO derived phosphorus radical and accordingly give rise to a larger hfc. This phosphinoyl radical, upon intramolecular rearrangement, may potentially generate a carbon centred radical capable of producing the small hfcc of 2.9 mT (see Mechanism 1 of Figure 4.8). In principle, the hfc in this radical should depend on the nature of the attached alcohol. The EPR data from the various alcoholic solutions given in Figure 4.7, reveal such a change to occur for the small coupling. This effect is best demonstrated by the spectrum recorded in ethane-1,2-diol when compared with the analogous spectrum in water.

Alternatively, after initial hemiketal formation and cleavage of the molecule by photolysis, a cyclic mechanism, *via* a stabilised five-membered ring may dominate. This would produce the three possible structures shown in Mechanism 2 of Figure 4.8. The tautomeric interconversion between the radicals 2a ⇌ 2c is likely to be slower than the timescale of spectral recording. Therefore, as a consequence of the added stability of one these resulting radicals, it alone may be responsible one of the unassigned signals in the TREPR spectrum.

From these mechanisms, five radicals with the potential to generate the additional peaks in the TREPR spectra exist. The next logical step, with the aid of computational chemistry, was to estimate the hfccs for these radical structures to determine their feasibility. To eliminate unnecessary computational time, the solvent in which the reaction occurs was assumed to be water and thus, R = H, where applicable. The details

of the calculations performed are discussed in the following passage, while a brief theoretical background to the calculations can be found in Section **2.4**.

4.2.3.1 Density Functional Theory Calculations on the Potential Radicals

For the perfect correlation of calculated hfccs with experimental data, top level post-HF methods are required. This results in a complex wavefunction and entails the use of large basis sets, both of which are computationally demanding. Consequently, these are unrealistic to perform for larger molecules of the kind discussed here. Efforts have therefore focused on alternative methods, such as DFT, which prove reliable whilst sparing excess computational time. Theoretically DFT, through its account of electron correlation has the ability to generate well correlated spin properties. A number of studies have explored this possibility, though literature specifically on calculating the isotropic hfccs of phosphorus centred radicals is sparse,[29-32] and those using DFT are fewer still.[29, 30, 32]

Different functionals for DFT calculations have been shown to generate very similar optimised structures,[33] and work by Nguyen *et al*[30] suggested that the B3LYP[34, 35] functional yields relativity accurate coupling constants for ^{31}P. The most relevant work from literature was conducted by Hermosilla *et al*,[32, 33] who likewise opted for the B3LYP functional and deduced a protocol for estimating isotropic hyperfine couplings for radicals similar in structure to those in the present study. This proceeds from the B3LYP/6-31g* combination of method and basis set to find the minimum energy. While reserving the more computationally expensive combinations B3LYP/TZVP and B3LYP/cc-pVTZ (or cc-pVQZ for medium sized molecules) solely for the single point (SP) calculations, performed thereafter, to predict the hfccs of the radicals. A comparison of these results with the previous study by Nguyen *et al*,[29] which both share some common radicals, reveals a consistently lower minimum energy configuration from the 6-31g*/B3LYP optimised structure, over analogous calculations performed with MP2. However, the hyperfine couplings estimated from each do not necessarily correlate better for the lower energy structures, and generally MP2 generated structures are recognised to better reflect the experimental geometries.

The same protocol as Hermosilla *et al* was followed for the MAPO and BAPO derived phosphorus radicals, as well as the proposed structures (1a, 1b, 2a, 2b, 2c) indicated in Figure 4.8. Initially the HF energy was evaluated by calculating the partially optimised structure using the minimum basis set STO-3g*. After this DFT

calculations with the B3LYP functional were performed, followed by exchange of the basis set for the moderate 6-31g*, where the calculation was repeated. Finally, full structural optimisations using tight then very tight optimisation constraints were undertaken to determine the final geometry. Single point calculations were performed on the resulting equilibrium structures using the B3LYP/TZVP basis set, while maintaining the same DFT method. To determine the influence of a higher level of theory on the hfccs, by increasing the number of basis functions, the cc-pVTZ set was applied to molecules with atoms greater than 17 and the cc-pVQZ (consisting of more basis functions) for radicals with atoms fewer. This is also in accordance with the literature.[32]

Information regarding the resulting energies, bond angles, and hfccs for the MAPO and BAPO derived phosphorus radicals is located in Table 4.1. The MAPO derived phosphorus radical generates a ^{31}P hfcc of 29.7 mT, which is equal to that calculated for a structure investigated by Hermosilla *et al*.[32] Both also have near identical ground state energies. The literature radical however, appears to feature a P-O bond as opposed to the P=O here. This may therefore be an indication of the length of the P-O bond, or a representation solely showing σ-bonds as the nature of the bond will be revealed in its length, which is not given. The P=O bond length of 1.52 Å in both MAPO and BAPO phosphorus radicals is in agreement with the expected values of 1.519 Å for a molecule of the form RP=O where R is an alkyl, or aryl group.[36]

The starting geometry at the phosphorus centre, from planar and Td, were also recalculated for the MAPO radical to confirm that a consistent minimum energy and associated hfc were attained. When locating the minimum energy structure for the Td arrangement, it was necessary to fix select angles in the two phenyl rings. This was due to the size of the radical and the extent of distortion (of the starting geometry) from the already established near planar equilibrium geometry. This allowed only minimum movement in the rings while the majority of the motion occurred around the spin bearing phosphorus centre. Accordingly, this was also repeated for the planar initial geometry for consistency, these results are both given in Table 4.1. There were two methods used for restraining the motion of certain bonds and angles in the molecular system. The first was by listing the constants, which restricted the movement of the listed angles and bonds, through the bonds, allowing easier location of the minimum energy. However, on instances where this was not sufficient the redundant internal coordinates were fixed. This allowed the chosen bond lengths and angles to be defined, holding atoms in relative position rather than restricting the movement through existing

bonds. This method inherently reduced the associated computational time, by eliminating the need to locate the equilibrium position of the chosen moieties. An example of which are the methyl groups; known to be most stable in their Td arrangement. This method is justified since the chosen bonds/angles involved would not alter significantly during the course of the calculation and could be confirmed by referring to the bonds angles and lengths in the unconstrained molecules. After completing the various steps towards a tight convergence the output was then taken and re-optimised with all the bonds and angles mobile to ensure the minimum was located. All instances fixed, or not, generated exchangeable ^{31}P hfccs and equilibrium energies; however, the original MAPO radical structure remains the most stable. Equivalent calculations were performed on the BAPO phosphorus radical, including the planar and Td starting geometries. Similarly, there was little variation among the energies and ^{31}P hfcs attained. For this radical the methyl groups joined to the phenyl rings were additionally fixed in their relative positions and movement for these structures focused around the phosphorus and carbonyl group. Likewise here, the original structure was not fixed, thus required many additional steps and starting geometries to locate a stable configuration.

Notably, the dihedral angles around the phosphorus for the MAPO and BAPO radicals are in accordance with the anticipated shape based on the *s*-character of the SOMO orbital. The BAPO radical is more planar at 127.3 °, than the MAPO, 124.6 °, though the difference is small and not obvious from the orientations depicted in Table 4.1. The predicted ^{31}P hfccs are underestimated by approximately 6.0-7.5 mT when compared with experimental values of 37.2 and 26.6 mT collected earlier in this chapter (refer to Figure 4.5). The use of the triple-ζ cc-pVTZ basis set combined with the B3LYP functional did improve these predicted values at a considerable cost in computing time. A greater than fourfold increase was required over that for the equivalent TZVP single point calculations, for only a modest gain in accuracy (see Table 4.1).

Given the documented reduction in computed errors (often from cancellation rather than the intrinsic quality of the method) when calculating phosphorus radical geometries using MP2, over analogous calculations with DFT, a single MAPO radical calculation was performed at this level.[31] The calculation was undertaken to firstly determine the improvement in the hfcc and secondly, if this could be matched by SP calculations using a more expensive basis after the initial DFT geometry optimisation. The results for this are located in Table 4.1 in the row labelled MAPO'. There is also an

account of the radical geometry and associated hfcc, which was estimated using the SP calculation described earlier, as well as at the MP2 level with the same basis set (TZVP). Clearly the hfccs from the MP2 geometry are closer to the experimentally determined hyperfine couplings. This is a consequence of the structure around the phosphorus being more bent than that attained from the DFT optimisation, *cf*. dihedral angles of 120.8 ° with 124.6 °. The extent of improvement however, does not validate the more than threefold increase in the total computing time for the geometry optimisation at MP2 level (time not shown). Particularly since the result from the SP cc-pVTZ♦ after DFT optimisation differs by less than 1 mT. Using MP2 for both geometry optimisations and SP calculation further improves the estimated hfcc. A noted concern when using DFT is the tendency to overestimate phosphorus oxide bond lengths,[29] therefore this received particular attention when computing the molecular geometries. The MP2 and DFT predicted lengths differ by only 0.01 Å, and both of the resulting values are within the range expected for this type of radical species.

A selection of the results for phosphorus centred radicals most chemically similar to those included here, were also repeated using both the B3LYP/6-31g*//B3LYP/TZVP and B3LYP/6-31g*//B3LYP/cc-pV(T or Q)Z as appropriate. Reasons for repeating these included confirming the best procedure for the calculations, specifically for the larger molecules. Additionally, this was performed to investigate any changes occurring in the geometries and hfcs as a result of fixing/restraining certain bonds. When considering the smaller radicals (i.e. bearing atoms fewer than 6), the individual steps as highlighted earlier were not necessary due to the fewer degrees of freedom. Consequently, the tight constraints could be performed in the initial calculation with ease. The convergence criteria for these smaller systems required additional manipulation to correlate the outcome better with experimental data. Theoretically, a molecule of this size with a large basis set such as the quadruple-ζ cc-pVQZ should generate the most accurate result among all the radicals tested. The optimised structures suggested for the phosphorus radicals from the literature overall agreed well with the literature hfcs and therefore supported the procedures used in this work. However, one result for the largest molecule tested ($C_{10}H_{16}OP^{\bullet}$), located after numerous starting geometries, including the final near Td arrangement of atoms around the phosphorus, is given in Table 4.2. This revealed a 4.5 mT underestimation in the ^{31}P hfcc predicted when using an identical protocol to the literature. The final structure adopted two equatorial hydrogen atoms with the bulkier groups axial, as opposed to the one equatorial and one axial hydrogen anticipated. The latter structure was only attained

when the initial geometry around the phosphorous centre was almost identical to that found in literature.[32] While the radical with the equatorial hydrogen atoms is lower in energy, the hfccs in the radical structure with one axial and equatorial hydrogen complies with known experimental values hfccs.[37] This again reveals the sensitivity of the predicted hfcc to the equilibrium geometry. All the relevant information is given for information in Table 4.2.

Results from the DFT calculations for all five radicals are located in Tables 4.3-4.4. Clearly from the calculations, the proposed phosphorus radical, 1a, is not responsible for the large doublet in the TREPR spectrum, as the calculated and experimental ^{31}P hfccs are not remotely similar. In fact the hfc value is comparable with the experimental data (26.6 mT) from the traditional phosphinoyl radical produced from direct BAPO photocleavage. Importantly, the calculated hfccs are explicitly underestimated in relation to the experimental values, a trend which is obvious from both the various radicals in this work and those reported in the literature. This eliminates radical 1a as the source of the 26.6 mT coupling when considering the cc-pVTZ only serves to increase its coupling. A lower ^{31}P coupling of 24.9 mT is attained when calculated from an initial Td structure around the phosphorus. This again is unlikely to cause the hfc of 26.6 mT, which is most consistent with direct type I α-cleavage occurring simultaneously. Considering radical 1a adopts a more Td configuration around the phosphorus than the MAPO derived phosphorus radical, the coupling for 1a was expected to be greater (*cf.* dihedral angles of 118.9 ° and 124.6 °). Adversely, the two nearby oxygen atoms may withdraw electron density from the phosphorus causing the reduction in the estimated hfc. This effect is noted as more prevalent when the oxygen groups are directly attached to the phosphorus.[17]

Structure 1b on the other hand has a calculated hfc, which is comparable with the smaller hfc of 2.9 mT observed in the TREPR spectrum. Likewise this predicted value is higher than the observed experimental result, though the correlation with experimental data is unknown for a phosphorus atom adjacent to a spin bearing centre. Whilst the generation of 1b requires the prior production of 1a, the lack of observed signal from 1a does not rule out its fleeting formation and conversion to 1b. Radical 1b therefore remains a potential candidate for generating the new signal with the 2.9 mT coupling constant. Particularly since this radical would be sensitive to the nature of the attached solvent. The corresponding ^{13}C hfcs for the spin bearing carbon are also included for information. The magnitude of these in addition to the low abundance of ^{13}C, eliminates the carbon coupling as the source of the 2.9 mT unassigned signal.

Table 4.1 Results from the B3LYP/6-31g* geometry optimisation followed by SP calculations using B3LYP/TZVP (B3LYP/6-31g*//B3LYP/TZVP), and B3LYP/cc-pVTZ♦ to predict the hfccs of the MAPO and BAPO derived phosphorus radicals, calculated using Gaussian G03. Δ and † indicate the starting geometries at the ^{31}P centre were planar and Td respectively. All ZPE corrections were determined from geometry optimised structures using the B3LYP/6-31g* combination of method and basis set and scaled accordingly to match these. The MAPO' radical data was obtained from geometry optimisations performed using MP2/6-31g* method and included for the SP calculations using B3LYP/TZVP or MP2/TZVP± thereafter. Literature values are from the work by Hermosilla *et al* and experimental refers to the data collected in Section **4.2.2** using TREPR. The dihedral angles are shown for phosphorus as the central point and reveal the MAPO and MAPO' radicals as more Td than the BAPO.

Radical	Geometry	Bond Å	State	Energy Hartrees	a_{iso} Theoretical mT	Computational time hrs - mins - s	a_{iso} Literature mT
MAPO	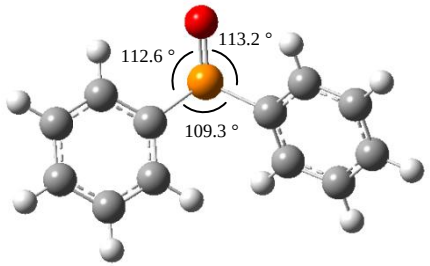 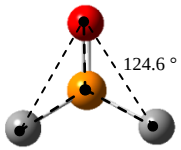	P=O 1.52	^{2}A	-880.0553743 -880.0851461$^{\blacklozenge}$ -880.0553472$^{\Delta}$ -880.0553175† ZPE 0.182823	29.7 31. 3$^{\blacklozenge}$ 29.7$^{\Delta}$ 29.8†	0 - 41 - 30.3 2 - 54 - 43.4$^{\blacklozenge}$	Theoretical 29.7 31.3$^{\blacklozenge}$
MAPO'	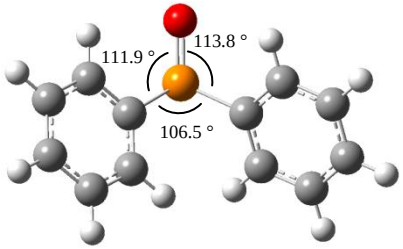 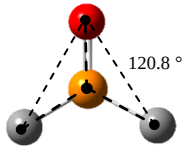	P=O 1.51	^{2}A	-880.0543417 -877.9336118$^{\pm}$ ZPE 0.186130	30.0 32.1$^{\pm}$	0 - 57 – 9.8 4 – 50 - 53.6$^{\pm}$	Experimental 37.2
BAPO	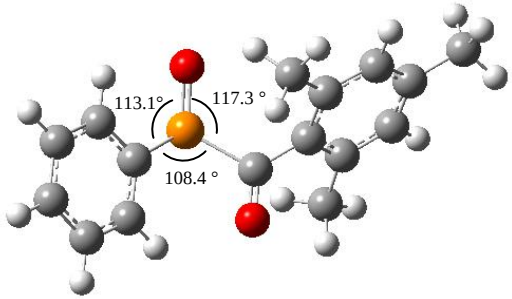 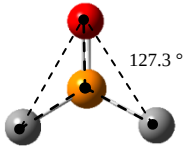	P=O 1.52	^{2}A	-1111.4039768 -1111.436797$^{\blacklozenge}$ -1111.4029764$^{\Delta}$ -1111.4029684† ZPE 0.273366	20.6 21.9$^{\blacklozenge}$ 20.5$^{\Delta}$ 20.5†	1 - 39 - 39.6 6 - 59 - 2.3$^{\blacklozenge}$	Theoretical - Experimental 26.6

Table 4.2 Results from the B3LYP/6-31g*//B3LYP/TZVP, and B3LYP/6-31g*//B3LYP/cc-pVTZ♦ to predict the hfccs in the $C_{10}H_{16}OP^{\bullet}$ radical calculated using Gaussian G03. Literature and Experimental values are from the work by Hermosilla *et al*, and Davies *et al* respectively.

$C_{10}H_{16}OP^{\bullet}$ Radical Geometry	Bond Å	State	Energy Hartrees	a_{iso} Theoretical mT		Computational time hrs - mins - s	a_{iso} Literature mT
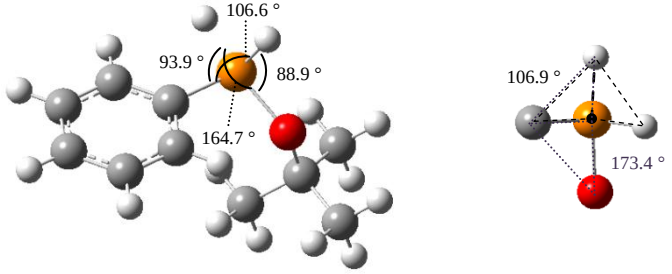	P-O 1.79 P-H_{ax} 1.49 P-H_{eq} 1.41	^{2}A	-807.3998332	^{31}P $^1H_{ax}$ $^1H_{eq}$	50.8 11.9 -1.1	0 - 32 - 49.1	Theoretical ^{31}P 50.9, 53.0♦ $^1H_{ax}$ 12.0, 11.9♦ $^1H_{eq}$ -1.1, -1.1♦
			-807.4238574♦	^{31}P $^1H_{ax}$ $^1H_{eq}$	52.9♦ 11.8♦ -1.1♦	2 - 39 - 52.6♦	
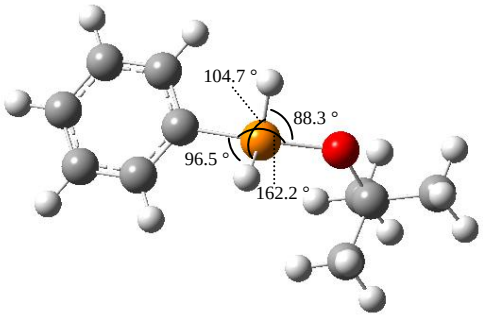 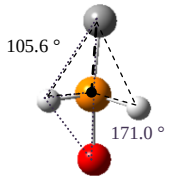	P-O 1.78 P-H_{eq1} 1.40 P-H_{eq2} 1.41	^{2}A	-807.4015929	^{31}P $^1H_{eq1}$ $^1H_{eq2}$	46.4 -1.0 -0.8	0 - 31 - 55.5	Experimental ^{31}P 55.7 $^1H_{ax}$ 12.7 $^1H_{eq}$ 1.0
			-807.4257369♦	^{31}P $^1H_{eq1}$ $^1H_{eq2}$	48.3♦ -1.0♦ -0.8♦	2 - 45 - 45.8♦	

Table 4.3 Results from the B3LYP/6-31g*//B3LYP/TZVP, and B3LYP/6-31g*//B3LYP/cc-pVTZ$^{\blacklozenge}$ to predict the hfccs of 1a and 1b both calculated using Gaussian G03. Δ and † indicate the starting geometries at the ^{31}P centre were planar and Td respectively, no planar geometry was calculated for radical 1b due to the coordination around the ^{31}P. All ZPE corrections were determined from geometry optimised structures using the B3LYP/6-31g* combination of method and basis set and scaled accordingly to match these. Exp refers to the experimental data collected in Section **4.2.2**

No.	Radical Geometry	Bond Å	State	Energy Hartrees	a_{iso} Theoretical mT	Computational time hrs - mins - s	a_{iso} Exp mT
1a	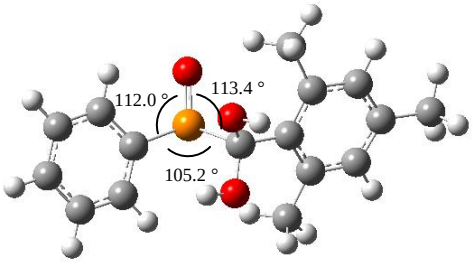 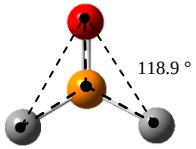	P=O 1.52	^{2}A	-1187.8523504 -1187.8863338$^{\blacklozenge}$ -1187.8507684$^{\Delta}$ -1187.8513389† ZPE 0.300397	27.7 29.0$^{\blacklozenge}$ 27.7$^{\Delta}$ 24.9†	2 - 18 - 12.8 9 - 9 - 36.3$^{\blacklozenge}$	49.8
1b	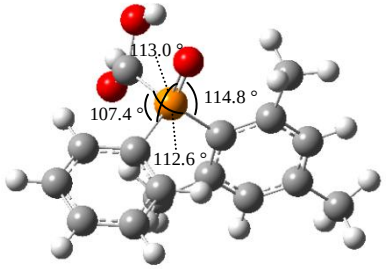 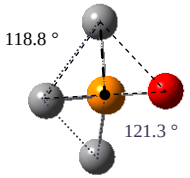	P=O 1.52	^{2}A	-1187.8504749 -1187.8882493$^{\blacklozenge}$ -1187.8492177† ZPE 0.229735	3.9 ^{13}C 7.8 4.1$^{\blacklozenge}$ ^{13}C 6.8$^{\blacklozenge}$ 3.9† ^{13}C 7.8†	2 - 35 - 25.9 9 - 49 - 24.6$^{\blacklozenge}$	2.9

Table 4.4 Results from the B3LYP/6-31g*//B3LYP/TZVP, and B3LYP/6-31g*//B3LYP/cc-pVTZ♦ or B3LYP/6-31g*//B3LYP/cc-pVQZ‡ to predict the hfccs of the radicals 2a, 2b, and 2c produced *via* Mechanism 2, calculated using Gaussian G03. All ZPE corrections were determined from geometry optimised structures using the B3LYP/6-31g* combination of method and basis set and scaled accordingly to match these. Exp refers to the experimental data collected in Section **4.2.2**

No.	Radical Geometry	Bond Å	State	Charge	Energy Hartrees	a_{iso} Theoretical mT	Computational time hrs - mins - s	a_{iso} Exp mT
2a	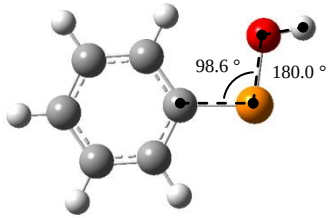	P-O 1.68	^{2}A"	0	-648.9413561 -648.9613568♦ -648.9904297‡ ZPE 0.102952	6.4 7.3♦ 5.9‡	0 - 6 - 39.9 0 - 35 - 1.9♦ 7 - 39 - 17. 5‡	2.9
2b	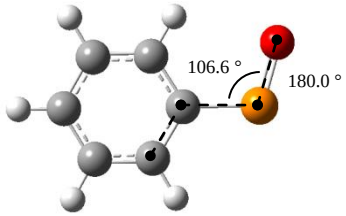	P=O 1.56	^{2}A"	-1	-648.3867456 -648.4052618♦ -648.4393397‡ ZPE 0.091374	2.8 3.1♦ 2.6‡	0 - 6 - 23.9 0 - 33 - 19.5♦ 8 - 29 - 4.8‡	2.9
2c	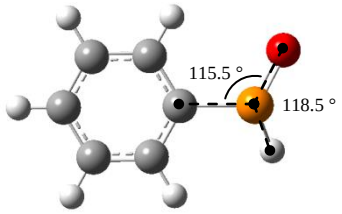	P=O 1.52	^{2}A	0	-648.921957 -648.9463388♦ -648.977881‡ ZPE 0.101330	29.6 31.4♦ 30.9‡	0 - 7 - 25.7 0 - 37 - 48.8♦ 7 - 35 - 20.7‡	49.8

Table 4.5 Results from the B3LYP/6-31g*//B3LYP/TZVP, and B3LYP/6-31g*//B3LYP/cc-pVTZ♦ to predict the hfccs of 3a calculated using Gaussian G03. All ZPE corrections were determined from geometry optimised structures using the B3LYP/6-31g* combination of method and basis set and scaled accordingly to match these. Exp refers to the experimental data collected in Section **4.2.2**

No.	Radical Geometry		Bond Å	State	Energy Hartrees	a_{iso} Theoretical mT	Computational time hrs - mins - s	a_{iso} Exp mT
3a	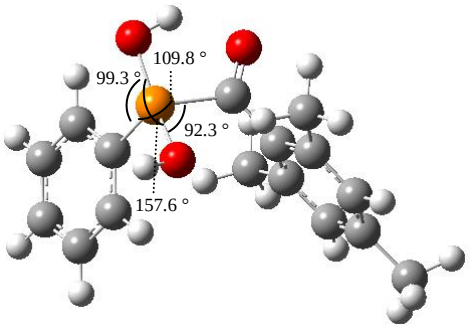	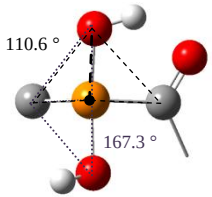	P-O 1.70 1.76	^{2}A	-1187.8579647 -1187.8914843♦ ZPE 0.298509	60.1 63.5♦	2 - 25 - 5.4 9 - 18 - 44.8♦	49.8
3a▲	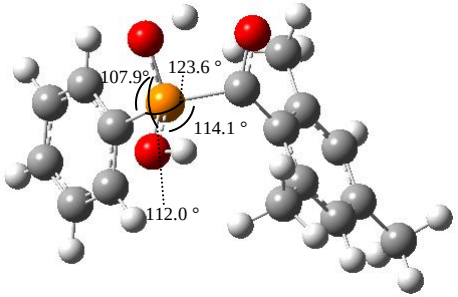	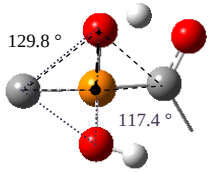	P=O 1.60 1.63	^{2}A	-1187.8779565 -1187.9191717♦ ZPE 0.298238	-1.5 -1.6♦	2 - 17 - 18.3 9 - 9 - 24.5♦	49.8

The hfcc obtained for the phosphorus centred anion 2b is equal to 2.8 mT, which corresponds very well to the 2.9 mT separated doublet observed in the earlier TREPR spectrum (see Table 4.4). A further increase to 3.1 mT is noted when the triple-ζ cc-pVTZ basis set is employed. With the quadruple-ζ cc-pVQZ set, this value drops to 2.6 mT, though this more accurately describes the electron density at the spin centre, and accordingly the hfc. Neither of the tautomers 2a or 2c are of the correct magnitude to cause either unassigned signal in the TREPR spectra. 2a is more stable than 2c by ~ 0.02 Hartrees, (52.51 J mol^{-1}), indicating it may primarily be formed before rapid deprotonation to generate the radical anion 2b.

Whilst on the basis of these calculations the large hfcc remains unaccounted for (see next paragraph), there do however, exist two possibilities for the origins of the small doublet, with one more likely than the other. Species 2b has a calculated hfc closer to the observed one than species 1b, and also has a simpler means of production (by direct cleavage of the P-C bond). All the solvents in which this additional photochemistry was observed are sufficiently polar to make formation of such an anion a thermodynamic possibility.

Previous studies[29, 33] have examined hfcs in a range of phosphorus centred radicals. By reviewing trends in these couplings, it is possible to make reasonable predictions about the identity of the radical with the large hfc. A third potential mechanism may be constructed, and is illustrated in Figure 4.8, Mechanism 3. The size of the hfc between the electron and the phosphorus nucleus depends strongly on the geometry around the phosphorus atom and consequently on the number of groups attached to it. A structure with two groups attached tends to give ^{31}P coupling constants of less than 10 mT, whereas when three groups are attached the couplings are typically around 30 mT. For structures with four groups surrounding the central phosphorus atom, even larger coupling constants of 40 to 50 mT are often recorded.

The arrangement of the atoms adopted by each radical with the same number of substituents is very similar. With the four-coordinate structures being least planar and therefore generating the largest hfcc. This leads to the possibility of a phosphorus radical with four-coordinating groups being the source of the large doublet. Conceivably this may be produced from the intramolecular nucleophilic attack of the phosphorus oxide bond, proceeding *via* a phosphorus epoxide based intermediate structure (see Mechanism 3 of Figure 4.8). This epoxide intermediate was also considered as a potential source of the TREPR signals. However, the initial optimisation

step in all attempts, including in the simplest systems, was the cleavage of the P-O bond forming the epoxide. This revealed the instability of the intermediate radical and suggested that if the structure were formed it would only exist momentarily, hence escape detection. It is for this reason not a feasible candidate for any of the unassigned signals. Similar calculations were performed on carbon based epoxides to probe the validity of the method of calculation for structures of this type and the carbon based epoxides unlike the phosphorus ones were found to be stable (data not shown).

The size of the resulting coupling from the proposed radical 3a should be sensitive to the nature of the attached alcohol/water, as this can strongly influence the geometry at the phosphorus centre. Such a variation is demonstrated by the hfcs in the TREPR spectra, when recorded in different solvents (see Figure 4.7), and therefore supports the formation of the four-coordinated species.

A number of isomers of structure 3a are clearly viable given the tendency for a phosphorus radical of this type to adopt a trigonal bipyramidal (TBP) shape and the two most generated of these energy configurations are detailed in Table 4.5. These arise from the OH groups as more axial, 3a, or equatorial, 3a▲. A ^{31}P hfcc of 60.1 mT was calculated for 3a, a much higher value than the experimental result of 49.8 mT, yet still in reasonable agreement with the large doublet. Whereas for the lower energy conformation 3a▲, the predicted coupling was very weak, at 1.5 mT, indicating the electron is not localised on the phosphorus atom. This, therefore does not follow the trends noted for a four-coordinated structure in the experimental literature or in the estimated hfcs, leaving its existence questionable.

It is clear from examining the structure of radical 3a that a simpler mechanism for the formation of this species would involve initial addition of the alcohol/water to the phosphorus atom generating the phosphorus equivalent of a hemiketal. This could then photocleave to generate structure 3a directly. However, there remain a number of reasons to indicate this does not occur. Firstly, if this route did proceed, it should also occur in the photolysis of MAPO in which no additional signals are observed. Secondly, there is no precedent for such a process to arise in the ground state molecule, since P=O bonds are much less reactive toward addition of alcohols/water than carbonyl groups. If attack did occur it would rapidly reverse back since there is no leaving group to enable the production of a stable species. In the radical the reactivity is altered making attack by the oxygen on an adjacent carbon atom entirely reasonable (as shown in Figure 4.8 Mechanism 3). It is therefore also feasible for the hydroxyl neighbouring group to

attack the susceptible phosphorus radical, resulting in a carbocation phosphorus radical. Though without the potential for proton exchange as in Mechanism 3, the phosphorus radical 1a would reform and the route would proceed as in the mechanism discussed.

Hence, the proposed radicals responsible for the additional EPR signals may arise from three different rearrangements of the phosphorus radical 1a, produced from the photocleavage of the hemiketal, as indicated in Mechanisms 1, 2 and 3. Radical 2b is proposed as the most likely candidate for the doublet with the hfc of approximately 2.9 mT and radical 3a is the only reasonable candidate for the doublet with the very large coupling of 49.2mT. One observation from Figure 4.7, however, still raises doubts as to whether the hyperfine coupling in radical 2b does give rise to the small doublet. Given that the radical responsible for the small doublet also reveals an altered hfc, when in different solvent environments, suggests the solvent should again be attached. This accordingly favours radical 1b to be the species causing the 2.9 mT signal.

For all the data included here, accompanying frequency calculations were performed on the geometry optimised structures to determine the nature of the minima. No imaginary frequencies were obtained, thus confirming a local minimum was found and reattempts from various geometries were also sought to establish a potential global minima. Zero point energies (ZPEs) from these calculations are included for information and include the corrections as appropriate for the 6-31g* basis set and B3LYP method.[38]

4.2.3.2 Formation of the Unknown Radicals from the Traditional Radical Pair

The proposed radicals, 1a, 2b and 3a all agree with the unassigned experimentally acquired hfcs and each radical is formed *via* a feasible reaction pathway, as shown in Figure 4.8. There is however, an alternative route worth consideration, which involves the sequential formation of either or both new radicals from the phosphorus radical of the original RP. Figure 4.9 illustrates the two mechanisms by which both of the most likely radicals indicated in Figure 4.8 may be generated *via* nucleophilic attack on either the phosphorus or the carbonyl group of the phosphorus centred radical. This mechanism assumes no pre-equilibrium of the hemiketal/hydrate in the solution before photolysis.

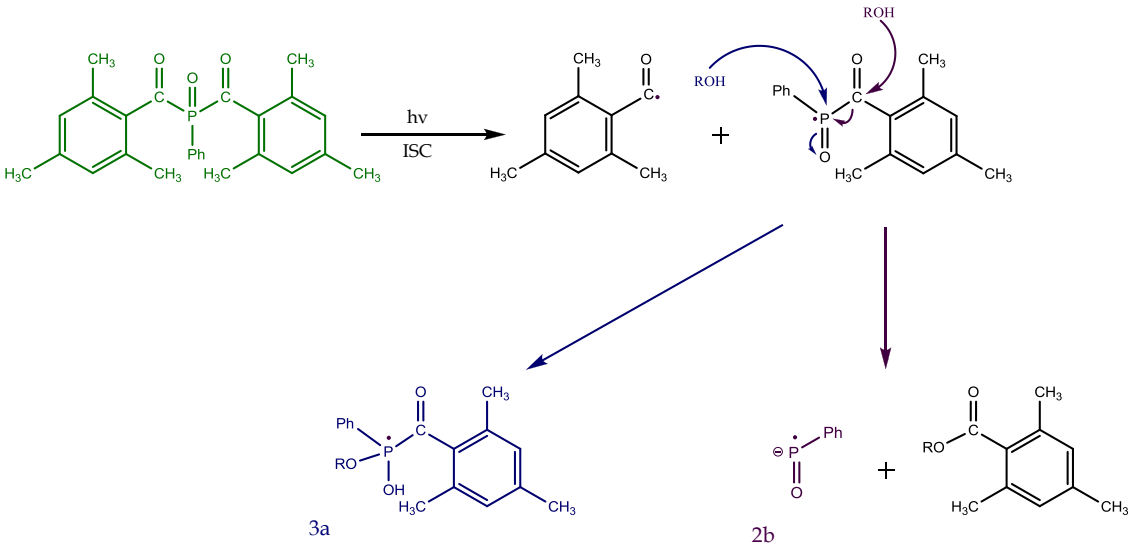

Figure 4.9 An alternative photochemical pathway for the photolysis of BAPO in alcohol/water containing solutions to produce the radicals 2b and 3a from the original acyl-phosphinoyl RP. R is dependent on the reaction medium.

The mechanism for generation of both of these radicals is less complex than that described in Figure 4.8. This coupled with the delay in the time dependence of the CIDEP signals is strongly suggestive that no pre-equilibrium exists and that the original phosphorus containing radical photoproduct is sufficiently reactive due to the presence of the adjacent carbonyl group to undergo the reactions as described by Figure 4.9. This can also explain the absence of signal from an equivalent species of 3a being present in the case of MAPO when photolysed in the same solutions. The carbon based radical 1b therefore has a much more elaborate formation pathway relative to these two species, requiring the initial creation of a hemiketal with subsequent rearrangement, as previously described. This implicates 2a as the most likely radical to cause the small hfc observed.

4.3 Conclusions and Future Work

The work in this chapter revealed differing magnetic field effects for the RPs formed from the photolysis of MAPO and BAPO in cyclohexanol solution. The MAPO photoinitiators demonstrated the expected LFE, consistent with α-cleavage, whilst BAPO showed only a very weak conventional MFE. This unusual photochemistry of BAPO was further probed using TREPR studies, which clearly identified the presence of additional radicals when BAPO was photoexcited in alcohol/water. This gave rise to two additional doublets whose origin was both unknown and contrary to the well understood photochemistry of BAPO occurring in acetonitrile. The mechanism of formation and the nature of these unassigned radicals were investigated. By employing different alcohols and observing the effect on the TREPR spectra alongside DFT calculations to estimate isotropic hfccs, three possible structures were proposed.

It is essential to remember that the DFT calculations can only suggest if a given radical may reasonably be assigned to the observed signal and conclusions beyond this cannot simply be drawn from calculated couplings alone. Experimental evidence is necessary to confidently link the route of formation to the proposed radicals investigated here. Within the scope of this study it is not possible to say unequivocally by which route the radicals are formed, indeed it is possible that multiple pathways occur simultaneously. However, the proposed structures for the radicals 1b, 2b, and 3a, seem probable based on the DFT calculations, the feasibility of the mechanisms, and the known reactivity of similar phosphorus molecules. Further work would entail investigation of the likely pathways and methods to determine the definite identity of the radicals produced.

References

1 S. P. Pappas, *Radiation Curing in Science and Technology*, Plenum, New York, 1992.

2 Ciba Speciality Chemicals, http://cibasc.com.

3 S. Jockusch, M. S. Landis, B. Freiermuth and N. J. Turro, *Macromolecules*, 2001, **34** (6), 1619.

4 J. Eichler, C. P. Herz, I. Naito and W. Schnabel, *Journal of Photochemistry and Photobiology A: Chemistry*, 1980, **91**, 39.

5 J. Eichler, C. P. Herz and W. Schnabel, *Die Angewandte Makromolekulare Chemie*, 1980, **91**, 39.

6 C. S. Colley, D. C. Grills, N. A. Besley, S. Jockusch, P. Matousek, A. W. Parker, M. Towrie, N. J. Turro, P. M. W. Gill and M. W. George, *Journal of the American Chemical Society*, 2002, **124** (50), 14952.

7 R. S. Davidson, *Journal of Photochemistry and Photobiology A: Chemistry*, 1993, **73**, 81.

8 U. Kolczak, G. Rist, K. Dietliker and J. Wirz, *Journal of the American Chemical Society*, 1996, **118**, 6477.

9 K. Meier, M. Rembold, W. Rutsch and F. Sitek, ed. D. R. Randell, Special Publication No. 64, The Royal Society of Chemistry, London, 1987.

10 A. W. Green, A. W. Timms and P. N. Green, *Proceedings of the Conference of Radtech Europe*, 1991, Edinburgh, 636.

11 G. Rist, A. Borer, K. Dietliker, V. Desobry, J. P. Fouassier and D. Ruhlmann, *Macromolecules.*, 1992, **25**, 4182.

12 W. Rutsch, H. Angerer, V. Desobry, K. Dietliker and R. Hüsler, *Proceedings, XVI Conference on Organic Coatings: Science and Technology, Athens*, 1990, 423.

13 W. Rutsch, K. Dietliker, D. Leppard, M. Köhler, L. Misev, U. Kolczak and G. Rist, *Progress in Organic Coatings*, 1996, **27**, 227, and references therein.

14 J. E. Baxter, R. S. Davidson, H. J. Hageman, K. A. Mclauchlan and D. G. Stevens, *Journal of the Chemical Society; Chemical Communications*, 1987, 73.

15 S. Jockusch, I. V. Koptyug, P. F. McGarry, G. W. Sluggett, N. J. Turro and D. M. Watkins, *Journal of the American Chemical Society*, 1997, **119**, 11495.

16 T. N. Makarov, A. N. Savitsky, K. Möbius, D. Beckert and H. Paul, *Journal of Physical Chemistry A*, 2005, **109**, (10), 2255.

17 G. W. Sluggett, P. F. McGarry, I. V. Koptyug and N. J. Turro, *Journal of the American Chemical Society*, 1996, **118**, 7367, and references therein.

18 S. Jockusch and N. J. Turro, *Journal of the American Chemical Society*, 1998, **120**, 11773.

19 R. M. Williams, I. V. Khudyakov, M. B. Purvis, B. J. Overton and N. J. Turro, *Journal of Physical Chemistry B*, 2000, **104**, (44), 10437.

20 A. Kajiwara, Y. Konishi, Y. Morishima, W. Schnabel, K. Kuwata and M. Hamachi, *Macromolecules*, 1993, **26**, 1656.

21 G. W. Sluggett, C. Turro, M. W. George, I. V. Koptyug and N. J. Turro, *Journal of the American Chemical Society*, 1995, **117**, 5148.

22 D. V. Stass, N. N. Lukzen, B. M. Tadjikov and Y. N. Molin, *Chemical Physics Letters*, 1995, **233**, 444.

23 D. V. Stass, B. M. Tadjikov and Y. N. Molin, *Chemical Physics Letters*, 1995, **235**, 511.

24 H. Hayashi, Y. Sakaguchi, M. Kamachi and W. Schnabel, *Journal of Physical Chemistry*, 1987, **91** (15), 3936.

25 K. Maeda, T. Suzuki and T. Arai, *RIKEN Review*, 2002, **44**, 85.

26 J. R. Woodward and C. B. Vink, *Physical Chemistry Chemical Physics*, 2007, **9**, 6272.

27 R. Shergill, M. Haberler, C. B. Vink, H. V. Patten and J. R. Woodward, *Physical Chemistry Chemical Physics*, 2009, **11**, 7248.
28 I. R. Katzhendler, R. Karaman, H. Zaher and E. Breuer, *Journal of the American Chemical Society, Perkin Transactions 2*, 1997, 341.
29 M. T. Nguyen, S. Creve and L. G. Vanquickenborne, *Journal of Physical Chemistry A*, 1997, **101** (17), 3174 and references therein.
30 M. T. Nguyen, S. Creve, L. A. Eriksson and L. G. Vanquickenborne, 1997, **91** (3), 537.
31 C. J. Cramer and M. H. Lim, *Journal of Physical Chemistry*, 1994, **98** (19), 5024.
32 L. Hermosilla, P. Calle, J. M. García de la Vega and C. Sieiro, *Journal of Physical Chemistry A*, 2005, **109**, 7626.
33 L. Hermosilla, P. Calle, J. M. García de la Vega and C. Sieiro, *Journal of Physical Chemistry A*, 2005, **109**, 1114.
34 A. D. Becke, *Journal of Physical Chemistry*, 1993, **98**, 5648.
35 C. Lee, W. Yang and R. G. Parr, *Physical Review B*, 1998, **37**, 785.
36 NIST, http://cccbdb.nist.gov/expbondlengths.
37 A. G. Davies, M. J. Parrot and B. P. Roberts, *Journal of the Chemical Society, Chemical Communications*, 1974, 973.
38 J. B. Foresman, *Exploring Chemistry With Electronic Structure Methods: A Guide to Using Gaussian* Gaussian, 1996.

5. The Effect of the Radical Pair Environment on Recombination and the Magnetic Field Dependence

The solution in which a radical pair is born is influential to its dynamics. The properties of the solvent cage govern the extent of RP diffusion and escape from the cage. The cage can be manipulated to extend the RP lifetime and thereby alter the recombination kinetics. This chapter focuses on changing the environment around the selected RPs and recording the kinetics and magnetic field dependence using the TRIR spectrometer, in the manner described in Section **2.2.1.1**. By using reverse micelles and solutions of increasing viscosity, the RP should experience a greater barrier to diffusion compared to that in a homogeneous solution. This should enhance the degree of S-T mixing and increase the sensitivity of the RPs to an applied magnetic field. Considering, the degree of spin-state mixing is linked to the separation distance of the RP in the micelle, it is also necessary to attain an approximate value for this. The first section of this chapter details the preparation, analysis (using dynamic light scattering) and corresponding field effects for varying sized reverse micelles in solution.

αhp was selected for both sets of studies, due to its high photolysis Φ of radicals, and the hyperfine coupling in the resulting RP. This average hfc has, in low fields, driven efficient S-T mixing of the radicals in the pair and previously given rise to a significant LFE.[1] A second molecule mhp was also chosen for study in the reverse micelles. Mhp has identical hyperfine couplings to αhp, though is structurally different, possessing no *para*-substituent on the benzene ring, (see Figure 5.1). This difference in structure should allow the effects of hydrogen bonding to be explored. It has previously been suggested that hydrogen bonding with the solvent can stabilise the RP leading to an increased lifetime and enhanced magnetic field effects.[2] The additional OH in αhp should further test this theory in the reverse micelles, when compared to mhp. Hydrogen bonding effects were also investigated by using non-hydrogen bonded solutions in the second Section (**5.2**) of this chapter.

Interest in this low field region is, as mentioned in Chapter **1**, associated with modelling the reactions occurring in biological systems. RPs in micelles are therefore of particular importance, since micelles exhibit key characteristics of living cells, for instance, their ability to self organise and incorporate species.[3] For this reason they are often referred to as microreactors. Furthermore, probing the RP conditions that maximise the generated MFEs are fundamental in understanding the mechanisms occurring and their influence on the kinetics of RP recombination.

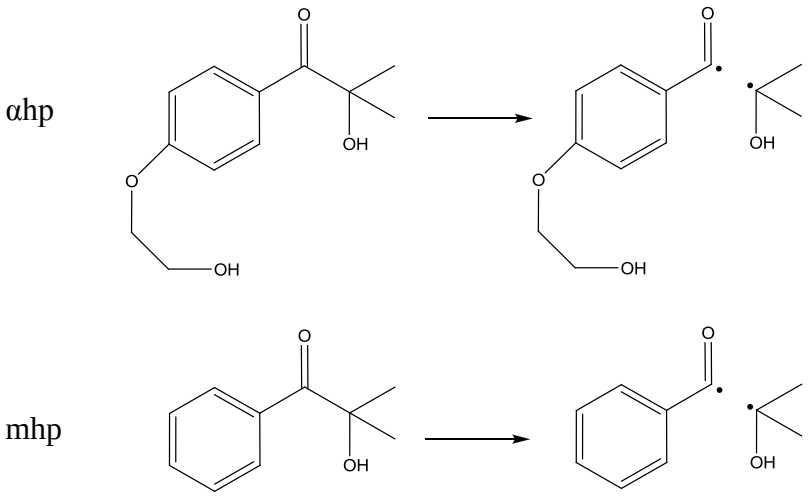

Figure 5.1 Structures of photoinitiators 2-hydroxy-4-(2-hydroxyethoxy)-2-methyl propiophenone (αhp), and 2-hydroxyethoxy-2-methylpropiophenone, **(**mhp), along with the radical pairs created after exposure to 266 nm radiation, in accordance with the photochemistry described in Figure 4.1.

5.1 Micelles

5.1.1 Structure of a Micelle

Micelles are self organised spherical aggregates of amphiphilic molecules. Amphiphiles contain both hydrophobic and hydrophilic domains within the same molecule. The non-polar hydrophobic chain (labelled the tail) resides in the low polarity organic solvent, while the hydrophilic head, (ionic/non-ionic/zwitterionic) remains in contact with water. The assembly of these molecules in an aqueous solution is dependant on the concentration of the surfactant. At low concentrations these amphiphiles congregate at the air-liquid interface forming a monolayer. Addition of further surfactant increases the hydrophobic attraction/electrostatic repulsion between the amphiphiles and the aqueous solution to a point where the formation of micelles is thermodynamically favoured. This is the *critical micelle concentration* (cmc). The cmc is experimentally defined, and its onset is apparent from the discontinuity of properties such as surface tension, conductivity, and viscosity of the solution.[4]

The aggregation number (N_{agg}) reveals the average number of surfactant molecules that form a micelle in solution. Its limits are governed by a balance of thermodynamics and electrostatics. The cmc, as described above, defines the lower limit

for N_{agg}, while ionic repulsion, due to overcrowding of polar heads, controls the upper limit.

The thermodynamic favourability for aggregation is driven by changes in the Gibbs free energy (ΔG). Gibbs free energy is more usefully described in terms of its components, enthalpy (ΔH), and entropy (ΔS), to give $\Delta G = \Delta H - T\Delta S$. At room temperature there are effectively zero contributions from the enthalpy, hence ΔG is dominated by the changes in entropy. The ΔS for the system is positive from a combination of two effects; an increase in the entropy of the solvent and the motility of the hydrocarbon tails. These entopic increases are somewhat offset by a decrease in the entropy from the amphiphiles aggregating, though it remains positive. When hydrophobic molecules (as exemplified by non-polar tails of the surfactant), enter an aqueous solution, there is a breakdown in the hydrogen bonding network in the solution surrounding the non-polar tails. The aqueous solution around the caged hydrocarbon structure maximises its entropy by reducing the surface area of the surfactant molecule, thus favouring a spherically symmetrical aggregate structure (micellisation). For such a system, the ΔG is negative and micelle formation is spontaneous; its origin is called the hydrophobic effect. This outcome also occurs for the introduction of a hydrophilic molecule into a bulk organic solvent, though in this instance it is referred to as the hydrophilic effect.

The term micelle or *reverse micelle* refers to the orientation of the surfactant molecules in solution, and is controlled by the ratio of water to organic solvent. With low water content in organic solutions, the micelles will form with the polar head groups internalising the water. Here, it is the dipole-dipole and ion pair interactions between the amphiphiles that are responsible for aggregation, as opposed to the attraction/repulsion implicated earlier on.[5] The size of *water core* or *pool size* (w) in these reverse micelles is primarily governed by the amount of water, and is described by,

$$w = \frac{[H_2O]}{[\text{Surfactant}]} \quad [5.1]$$

For a fixed w, the micelle size is often shown to remain constant for an increasing concentration of surfactant. This is proposed to influence only the number of micelles without altering their properties.[6,7] However, this assumption becomes obscured at low

and high water pool sizes, where the addition of surfactant has been reported to reduce the water pool dimensions, or alter the shape of the reverse micelle.[5] Therefore, while Equation [5.1] does allow the water content of a reverse micelle to be precisely varied without compromising w and the size or shape, its range is found to be very surfactant dependent.

Sodium bis(2-ethylhexyl)sulfosuccinate (AOT) is a popular anionic surfactant that is used to form stable reverse micelles. Among the appealing features of AOT is its ability to solubilise large volumes of water in an organic phase ($w \leq 60$). The limit of this is dictated by the surrounding medium, the solute and temperature of solution, along with any factor capable of altering the packing.[5] The stability of a reverse micelle is governed by the ratio of water to surfactant rather than total concentrations of each in solution. Accordingly, the reverse micelles formed from relatively high concentrations of up to 500 mM AOT, have previously been characterised.[8]

For the work presented in this chapter the chosen non-polar solution is 2,2,4-trimethylpentane (isooctane). This decision was based on the structurally similar tail of AOT to that of the solvent, a property which is reported to improve reverse micelle stability.[5, 9] Importantly, the elimination of water from this ternary (water/AOT/ isooctane) system is seldom guaranteed. An amount of water is naturally expected in both the non-dried AOT and isooctane, though, the influence on the water pool size should in theory be negligible for a larger w. The contribution of this excess water for when the $w = 0$ is considered later in Section **5.1.4.2**. Consequently micelles will form regardless of the intentional addition of water to the AOT/isooctane mix, provided the concentration of AOT is above the cmc.[10]

The nature of the core water in the reverse micelles has also been extensively studied and its properties are known to be dependent on the volume of the micelle. Production of the so called water in oil *microemulsions*, as opposed to reverse micelles, arises when water is the major component of the amphiphilic aggregates[‡], i.e. for $w > 12$. Minimal amounts, $w < 3$, often reveal partial occupancy of the water pool by the clustering of solvated water molecules. The water in this core is immobilised, through hydrogen bonding with the head groups of the surfactant, and there is no detectable free water in these aggregates. The presence of this *bound* water is identified by the behaviour of these micelles, which cannot be rationalised by equilibrium thermodynamics or by surface tension.[11, 12] Moreover, in these low water pool sizes the

[‡] Aggregate refers to both a reverse micelle or the structures in a microemulsion

AOT molecules are often shown to adopt a staggered arrangement. This decreases the water pool size further and increases the propensity for rigid hydrogen bonding.[9]

By increasing the water content of the system, a defined surfactant monolayer structure in the outer wall is supported. This corresponds to the length of the AOT molecules. While both bound and free water coexist in the larger water pools, they rapidly exchange and the core resembles that of *free water*. Here, bulk water properties of viscosity, hydrogen bonding, and polarity are exhibited.[6] For these micellar aggregates, ΔG can once again be defined by the surface tension of the liquid film.

A third type of water has also been reported to exist at the interface. This water reveals no hydrogen bonding with its surroundings and is effectively isolated from the remaining bound and free water in the core of the micelle. Despite the vast amount of literature available to characterise the reverse micelles/microemulsions using techniques such as dynamic light scattering (DLS), small angle X-ray scattering (SAXS), nuclear magnetic resonance (NMR) and viscometry, a complete physical model of reverse micelles is not yet available.[5]

5.1.2 Distribution of a Substrate

A hydrophilic substrate may be encapsulated in the water pool of these aggregates. This allows a molecule, usually insoluble in the bulk, to be shielded from the organic phase by a film of AOT (refer to Figure 5.2). An ideal condition of encapsulation would involve a single molecule contained per micelle. Following UV initiated RP formation in the micelle, the pair would remain encased and through restricted diffusion exhibit a longer lifetime than that achievable for the same RPs in homogeneous solutions of a higher viscosity. Under the influence of a magnetic field, this lengthened geminate stage should allow greater spin-state mixing to develop in the RP. The altered product ratio, compared to that in the absence of a magnetic field, should be observable in both the LFE and MFE traces.

The polar head groups of the AOT, which build the *Guoy-Chapman layer*, reside partially immersed in water (see Figure 5.2). This region combined with the anionic *Stern layer* is responsible for restricting the diffusion of the trapped substrate, by limiting the entry and exit pathways to the core of the micelle. This interfacial region is known to have a high ionic strength and a heterogeneous micropolarity.[13] The mobility of the AOT tails in the oil medium extends the barrier to diffusion further however, the dynamic behaviour of the micelles means they continuously deform and reform. This

facilitates escape of the RP from the reverse micelle by two routes; single AOT molecule or water pool exchange and both typically occur on a microsecond timescale.[4, 14]. The latter switches the entire water pool and their contents on coalescence of the micelles and is in general slower than single AOT exchange (tens of microseconds).

The minimum water pool size is limited by the amount of water naturally present in the AOT and isooctane. While purification of both the solvent and AOT can reduce this and has occasionally been performed in literature,[11] more often micelles are made directly from the purchased reagents, as is the case here.

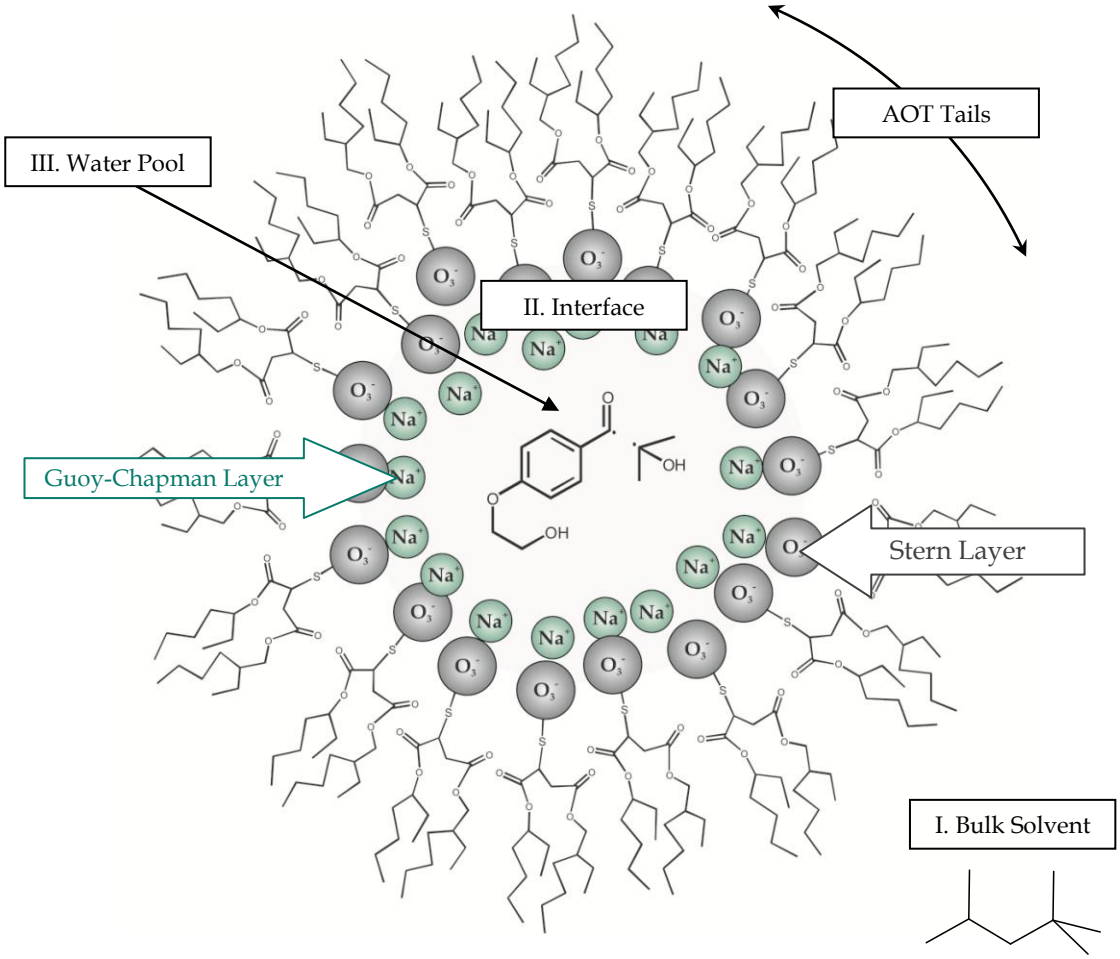

Figure 5.2 A 2D cross sectional view of a water/AOT/isooctane reverse micelle. The structure illustrates the ideal conditions for MARY studies, where the micelle contains a single αhp RP in its water pool. Here, three locations for the substrate exist, though the insolubility of the molecules in bulk solution (pictured inset with an isooctane molecule), concludes only two possibilities, II and III.

Based on the structure of a reverse micelle, there are three domains where molecule may reside (see Figure 5.2).

I. The apolar bulk solvent, isooctane.
II. The micellar interface formed by the surfactant monolayer.
III. The internal water pool.

There should be a negligible probability of finding the substrate molecule (either αhp or mhp) in the bulk solvent, as it is insoluble and polar and therefore would be attracted to the water core/interface. The other two positions are both feasible and determining whether the molecule preferentially resides in site II or III is less simple. In any case, both positions should contribute to the size of the water pool. Therefore, it is initially proposed that the molecule is located in the water pool, and the possibility that it is not is considered later on in this chapter.

Thermodynamic factors are well established to affect the statistical distribution of neutral molecules within the micelles. However, a less complex mathematical treatment for predicting this may alternatively be applied. Under the assumption that the micelles are monodisperse, the entrance and exit of identical molecules to and from the micelles is classed as a random event. The distribution of substrates within the micelles for this model follows a random type Poisson distribution,[15]

$$P_j = \bar{n}^j \frac{e^{-\bar{n}}}{j!} \quad [5.2]$$

where P_j, is the probability of finding j molecules per micelle, and $\bar{n}$ is the mean occupation number per micelle,

$$\bar{n} = \frac{[\text{Solute}]}{[\text{Micelle}]} = \frac{N_{agg}\,[\text{solute}]}{[\text{AOT}]-\text{cmc}} \quad [5.3]$$

Equations [5.2] and [5.3] allow the probability to be calculated for various concentrations of substrate and AOT. The AOT cmc is taken as 5×10^{-4} mol dm^{-3}.[10] Whereas, the N_{agg} values originate from two methods that were used to interpret the data from the dynamic light scattering (DLS) experiments performed in this study.

5.1.3 Sample Preparation

This paragraph details the sample preparation procedure for use with the TRIR system and expands on that given in Section **2.3.3.1**. The appropriate mass of AOT, determined in the same manner as the example calculation in Section **5.1.3.1**, was dissolved in isooctane and shaken by hand. While the substrate molecule, either αhp or mhp, was prepared separately in deionised water, at a concentration of 0.7 mM, or up to 20 mM respectively. For the majority of solutions in this work, the concentration of the precursor molecule controlled the minimum amount of water required and from this the corresponding amount of AOT was calculated. It was impractical to keep the AOT concentration constant, since the small water pools such as $w = 2$, demanded very large amounts. The use of large amounts of AOT may alter the viscosity of the micelle solution and thereby influence the dynamics of the RP; this possibility is also examined in detail later. The substrate solution was sonicated before its addition to the AOT in isooctane, *via* injection, using a syringe to complete the ternary mix. The solution was initially agitated by hand until it became transparent, following which it was sonicated for a further 30 mins under nitrogen flow to remove oxygen.

Tests were conducted to determine the benefits of centrifuging and filtering the samples in addition to the usual sonication process. Large volumes (500 ml) were centrifuged using a DuPont Instruments Sorvall RC-5B refrigerated superspeed centrifuge, running at a speed of 8000 rpm for 1 hour, these conditions are in accordance with those given in the literature.[8] The intention was to improve the monodispersity of the solution and remove any excess particles, such as uncoordinated AOT. This was expected to reduce the scatter from the UV/IR lasers and generate a smoother kinetic decay trace and more importantly, reduce the noise in the resulting magnetic field effect. No such gain was noted in the magnetic field dependence, so it was considered unnecessary to continue centrifuging and filtering the samples for use with the TRIR spectrometer.

The overriding factor in the quality of the IR kinetic signal arose from the volume of water in the samples. Given the high IR absorbance of water in the range of interest, using the minimum amount of water was essential to achieve a workable signal level. This resulted in a limited water pool size. It was unfeasible to study a water pool size greater than $w = 30$, or use a higher concentration of the substrate molecules, as a parallel increase in water would be required. Therefore a compromise between the

water, the concentration of the precursor molecules and the AOT was made in the calculations.

5.1.3.1 Example Calculation

The following is an example calculation for a solution containing micelles for which $w = 15$. The method is derived from the minimum amount of water; 12.50 ml (0.694 mol, $[H_2O]$ = 2.78 M) are required to dissolve αhp (0.70 mM, 175 μmol, 39.20 mg). Referring back to Equation [5.1], where $w = \frac{[H_2O]}{[AOT]}$, this gives the amount of [AOT] = 185.16 mM (46.29 mmol, 2.787 × 10^{22} molecules), which corresponds to 20.58 g of AOT. To estimate the concentration of micelles in a solution knowledge of the N_{agg} is essential, which from the SAXS data is 212.[16] This gives 1.31 × 10^{20} micelles, and a ratio of 0.87 mM [micelles]: 0.70 mM [αhp]. For accuracy, the N_{agg} values were calculated from the DLS measurements and this is shown in Section **5.1.4.2**.

Initially the calculations were all based on a 1:1 ratio of micelles to substrate. However, the minimum amount of required water meant this was not achievable for the smaller water pools. So, as in the earlier example, it was necessary to work out the amount of AOT from this minimum water volume. The quantity of AOT was, as previously mentioned, allowed to vary among the different water pools. Additions of AOT for a given w, adjusts only the number of micelles and does not significantly alter the water pool size, or its properties.[7]

5.1.3.2 Sample Preparation for the Dynamic Light Scattering Measurements

For examining the dimensions of the micelles using DLS, the preparation procedure varied from that given in Section **5.1.3** and was much more demanding. Typically 10 ml solutions of each water pool (w = 0, 2, 5, 15, 20, 25, and 30) were prepared. Each of the solutions was then diluted by a minimum factor of 10, with some requiring higher dilutions, as this was dependent on the viscosity of the original solution (see dilutions Section **5.1.4.1**). A combination of sonication, centrifuge, and syringe filtration using 0.02 μm Whatman Anotop™ Plus filters was performed. On occasion this process was carried out multiple times to achieve the monodispersity required for consistent DLS measurements. The centrifuge for the smaller volumes was a Heraeus, Labofuge 200 used at its maximum running speed of 5300 rpm for approximately 1 hour.

5.1.4 Dynamic Light Scattering

Brownian motion refers to the random motion of particles in a fluid and occurs as a result of collisions with nearby molecules. The amount of movement by the particles differs according to their size and large particles move slower following collision, than smaller ones. The technique of dynamic light scattering (or photon correlation spectroscopy) measures the Brownian motion of the particles and from this calculates the size of the molecules in the sample. It relies on interpreting the variation in scattered laser light from its interaction with particles of different sizes, as the motion of the particles alters the degree of scattering. It is imperative to calculate this initial size data correctly since, other factors such as volume, and number distributions are normally calculated from this.

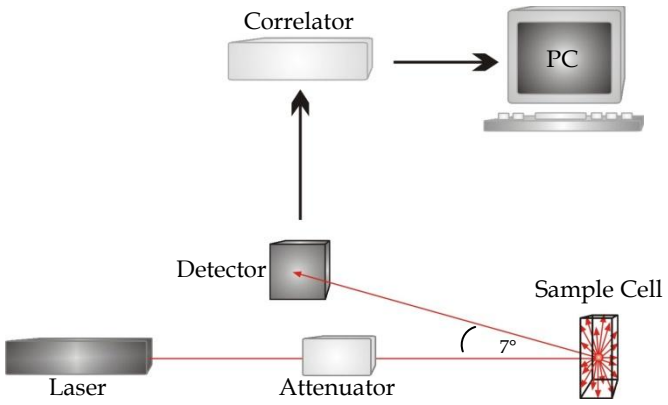

Figure 5.3 A schematic of the Malvern Instruments Zetasizer Nano S series spectrometer used for DLS measurements. This model is capable of measuring in the range 0.6 nm-6 µm, to determine the size of particles in solution.

A Malvern Instruments Zetasizer Nano S series spectrometer was used for the DLS measurements and its main components are shown in Figure 5.3. The following section outlines how a DLS measurement was carried out. In the DLS instrument a He-Ne laser (633 nm) passes through an attenuator to adjust its intensity. The sample, contained in a clear walled disposable polystyrene cuvette (10 × 10 × 45 mm, approximate volume 1.25 ml) is illuminated with the He-Ne laser. The laser is scattered off the particles in the sample, and the light that is back scattered at an angle of 173 ° to the incident beam is measured. This is called non-invasive back scatter (NIBS) detection. NIBS is preferred for DLS measurements for several reasons; it reduces

multiple scattering, allows higher concentrations to be measured, and decreases the interference from larger particles, such as dust, which tend to scatter forwards. The detected signal continues through to a digital correlator, which compares the scattering intensity at successive time intervals, to create a correlation function. For larger particles, the intensity of radiation varies more slowly than that for the smaller particles. This information then passes to a PC hosting the Zetasizer software, which derives the required size data. The Zetasizer program uses algorithms to extract decay rates from a correlation plot. From this, the rate of variation in intensity is determined and a size distribution is created. The duration of this scanning process is typically a few minutes, though the preparation of a sample of adequate quality is more time consuming.

The result from a DLS experiment is a fitted correlation curve that includes all the information regarding the translational diffusion of the particles in the sample. Given that the diffusion coefficient (D) is proportional to the lifetime of the exponential decay of the correlation curve, its value can be calculated. The relationship between the size of the particle and its speed due to Brownian motion is defined by the Stokes-Einstein equation,

$$d_H = \frac{k\mathrm{T}}{3\pi\eta D} \quad [5.4]$$

The hydrodynamic diameter (d_H) of the micelles can accordingly be derived from the values of D. In this work the measurements were conducted at a temperature (T) of 298 K, with an equilibration time of approximately 60 seconds to ensure Brownian motion was measured. In Equation [5.4], k is the Boltzmann constant, and the viscosity (η) of the micelle solutions was assumed to be that of the organic phase, isooctane (0.480 cP).[17]

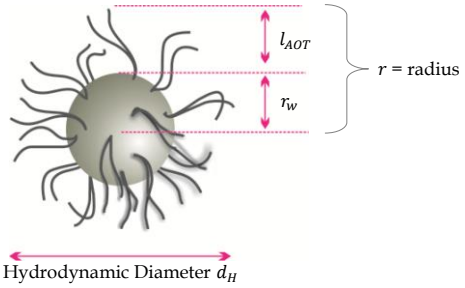

Figure 5.4 The 3D structure of a reverse micelle. The labelled features include the hydrodynamic diameter d_H, as calculated by DLS, the length of an AOT molecule, l_{AOT} = 12 Å,[11] and the radius of the water pool, r_w.

The particle size measured from DLS is the diameter of a spherical particle plus any extensions to the particle that diffuse with a common speed. For a reverse micelle system this includes the core of the micelle in addition to the surface structure, specifically here, the non-polar tails (see Figure 5.4).

An ideal solution consists of non-interacting dispersed hard spheres. Therefore, assuming the viscosity of isooctane requires that all the original micelle solutions be adequately diluted to correctly model the size of the particles.[18] The upper limit to the solution viscosity is empirically set as 3.0 cP. While fluids with higher viscosities (frequently known as non-Newtonian) can be measured, the particle-particle interactions must be accounted for as they can alter the diffusion of particles and the result is no longer derived from free Brownian motion. For the range of micelles investigated here, a spherical structure as illustrated in Figure 5.4 is supported.[5]

5.1.4.1 Dilution Factors and Viscosities

The infinite dilution limiting value (D_0), for the diffusion coefficient is given by,

$$D = D_0 (1 + \alpha\emptyset) \quad [5.5]$$

where α is the inter-particle interaction, and $\emptyset$ the volume fraction of the dispersed phase. When measuring Brownian motion D should $\approx D_0$ to ensure that the inter-particle interactions are negligible and this can be confirmed by calculating the volume fraction of the dispersed phase. The volume fraction of i species (i = water, AOT) was calculated using, $\emptyset_i = c_i v_i$, where c_i and v_i are the molar concentration and molar volume of i species respectively. $\emptyset_{ws} = \emptyset_w + \emptyset_s$, can be applied to sum the fractions of the water ($\emptyset_w$), and surfactant ($\emptyset_s$), to yield the total volume fraction of the dispersed phase ($\emptyset_{ws}$). The molar volume of AOT was taken as 3.93×10^{-4} m^3 mol^{-1}, and obtained from $\frac{M_R}{\rho} = v_{\mathrm{AOT}}$, whilst the molar volume of water was 1.8×10^{-5} m^3 mol^{-1}. Recalling that the original solutions were diluted by a factor of at least 10 for use with DLS, and the greatest volume fractions result from the micelles with the largest concentration of AOT, w = 2 determines the upper limit of $\emptyset_{ws}$. For a water pool size of 2, $\emptyset_{ws}$ = ((2.78 $\times 10^3$/10) $\times 1.8 \times 10^{-5}$) + ((1.39 $\times 10^3$/10) $\times 3.93 \times 10^{-4}$) = 0.06, and 0.60 for the original solution. Since the spherical shape of the aggregates remains unchanged up to $\emptyset_{ws}$ = 0.3,[19] all the diluted samples fall within this limit. All but one of the $\emptyset_{ws}$ values for the

original (neat) solutions are also below 0.3. The exception occurs for the neat dilution factor ($\emptyset_{ws}$ = 0.6) for a water pool size of 2, as shown in the example.

Concentrated AOT microemulsions ($\emptyset_{ws} > 0.6$) and hard sphere models (dilute samples) constitute two very different types of structure. Dense microemulsions ($\emptyset_{ws} > 0.6$) are affected by interactions between aggregates. For these solutions convergence of the correlation function as measured by DLS is much slower than in the hard sphere equivalent. The slower relaxation can be attributed to the collective motion of aggregates, with the inter-particle interactions altering the dynamics of these micelles. Normally, this is influential at volume fractions of well beyond $\emptyset_{ws}$ = 0.6[20] so does not effect the DLS work undertaken here. However, it remains important to note that the structure of the dense solution in w = 2 may alter the behaviour of the micelles in the later TRIR studies.

DLS states that for high concentrations of the particles in solution, the sample viscosity should be measured and the measured value used, rather than assuming the viscosity of the solvent. Considering that the dispersed phase volume fraction was maintained sufficiently low for all the micelle solutions produced, the following is true, $D \approx D_0$. The viscosity of a random diluted sample was measured, and the viscosity difference between this and that of pure isooctane was within error, so $D \approx D_0$ was confirmed as a valid assumption.

Viscosities of the solutions for the TRIR experiments were measured using an Ostwald viscometer, situated in a temperature controlled bath set to 298 K. The time elapsed for each liquid to pass through the glass capillary was recorded along with the density of the solution. The relative relationship of the measured times were compared to that of deionised water as a standard,

$$\eta = \frac{\rho}{\rho_0} \times \frac{t}{t_0} \eta_0 \quad [5.6]$$

Here η_0 = 0.8904 cP,[21] ρ_0= 995.64 kg m^{-3}, t_0 = 92.44 s, whilst ρ and t were measured for each solution. Repeats were performed for consistency, and there was little deviation (approximately 0.5 s) between the times recorded. The viscosity of isooctane was also measured using the Ostwald viscometer to test its accuracy and yielded, 0.481 cP at 298 K, which is consistent with the literature value of 0.480 cP.[17]

The variation in the viscosities of the micelle solutions is surprising (refer to Table 5.1). When doubling the water pool size from 15 to 30, for a fixed amount of AOT, the viscosity of the solution is shown to increase significantly. This suggests maintaining a fixed amount of AOT for the micelle solutions does not guarantee a negligible increase in viscosity, as may be anticipated. Solutions of 0.46 M and 0.19 M AOT were both prepared for w = 15, to evaluate the effect of altering the AOT concentration on the viscosity of the solution. Clearly, the increase in the viscosity, when changing the water pool size is greater than that from changing the amount of AOT. Given that a constant concentration of AOT still notably alters the viscosity of the micelle solution, it seems reasonable to vary the concentration of AOT among the different water pool solutions. Ideally, additional TRIR scans would have been performed for all the solutions maintained at the same viscosity. Though maintaining a constant viscosity for the required reverse micelle solutions appears to not be a simple task, since there are many factors to consider.

Table 5.1 The viscosities of micelle solutions prepared with different water pool sizes for investigation with TRIR spectroscopy. The viscosity of w = 15 with [AOT] = 0.46 was measured for comparison and no field investigations were performed on this solution.

w	Conc. AOT / M	η / cP
2	1.39	10.5
5	0.56	3.68
15	0.19	0.70
15	0.46	2.49
30	0.46	7.75

5.1.4.2 The Hydrodynamic Radii and Size Distribution Plots

The results from the dynamic light scattering experiments on the micelle solutions of αhp in w = 2, 5, 15, 20, 25, and 30 are given in Table 5.2, along with the data for a sample made with AOT/isooctane in the absence of αhp or added water (i.e. w = 0). The results reveal a general increase in the micelle size with increasing w, as do the accompanying size distribution profiles, shown displaying the relative intensity of scattered light vs. the size of the particle (see Figure 5.5).

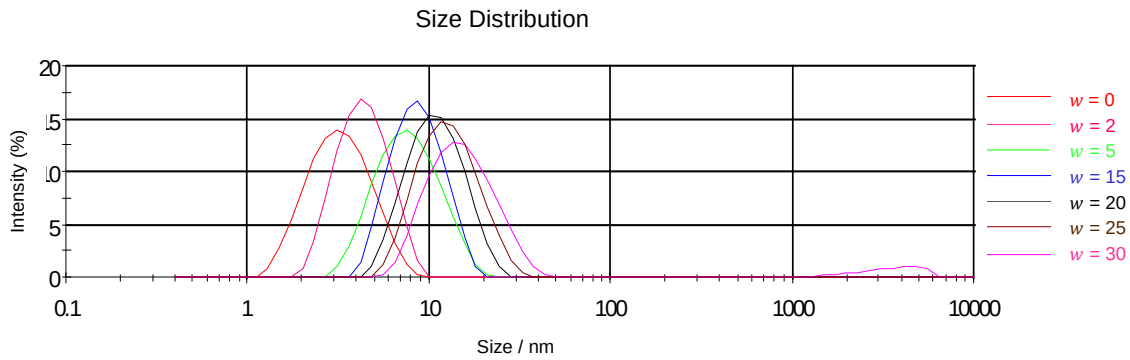

Figure 5.5 The size distribution profiles for w = 2, 5, 15, 20, 25, and 30 containing αhp. The water pool size for w = 0 was obtained without αhp.

All the distribution plots identify a single peak, with the exception of when w = 30 which features an additional peak occurring at 3369 nm. This is most likely attributed to interference from scattering by dust. The polydispersity index (PI) of each sample is also given in Table 5.2. The PI is derived from the spread of decay rates and the particle sizes around the average value and is normally used to compare the widths of the Gaussian distributions. Predictably, the PI for w = 30 is higher than for the other samples, due to the presence of the additional peak.

Based purely on geometrical considerations the hydrodynamic radius (r_H) may be described as the sum of $l_{AOT} + r_w$ (see Figure 5.4).[8] Therefore to obtain the diameter of the water pool (d_w), the length of the two AOT molecules must be deducted from the recorded d_H. The outcome of this is given in Table 5.2. Strictly, to predict the size of the water pool alone, the αhp must be accounted for in all the samples except the water pool of zero. This modifies d_w to equal $d_H - 2l_{AOT} - l_{\alpha hp}$, where the length of αhp ($l_{\alpha hp}$) is approximated as being 9 Å across.[†] However, since the concentration of micelles in some of the samples, i.e. the lower water pools, far exceed the concentration of αhp, only the AOT molecules are assumed to be influential to the diameter.

The measured data for d_w differs significantly from that obtained using SAXS.[16] All the values from SAXS are consistently lower by a minimum of 1 nm, and more than 3 nm at their largest. This 3 nm deviation occurs when w = 5, the d_w approximated for this is indicative of a much larger water pool. The literature values of d_w from a combination of DLS and NMR techniques in the final column of Table 5.2 are analogous to the SAXS data, and so differ from the recorded result similarly to that

[†] Estimated from the bond lengths in αhp

already described. A number of factors could contribute to the difference in the water pool size noted from this work, compared to that in literature, including the initial water pool calculations, the preparation procedure, the d_w approximations, or even the technique. To eliminate the possibility of the technique causing the variation, the results were also compared with literature DLS values.

The correlation between the d_H values recorded here, and d_H DLS literature values, is closer than the aforementioned SAXS data. While the literature d_H values were reported for empty micelles, the values here included a contribution to the diameter from the αhp molecules. This should be more influential to the average diameter for the larger water pools as the ratio of micelles to αhp approaches 1:1. Consequently, a true comparison with the literature can only be performed on empty micelles, as the introduction of differing molecules depending on size, and polarity, amongst other factors, may alter the properties and structure of the water pool.[5]

Ideally comparisons with literature would be performed on the empty micelles, however, the length of time dedicated to producing solutions of adequate monodispersity to acquire these results meant that was unfeasible. Furthermore it was unnecessary, since the original purpose was to determine the distance in the water pool approximately, with the inclusion of the αhp/mhp molecules. The measurement for w = 5 containing mhp is shown in Table 5.3, and the diameter for this water pool agrees better with the literature SAXS and DLS/NMR data.

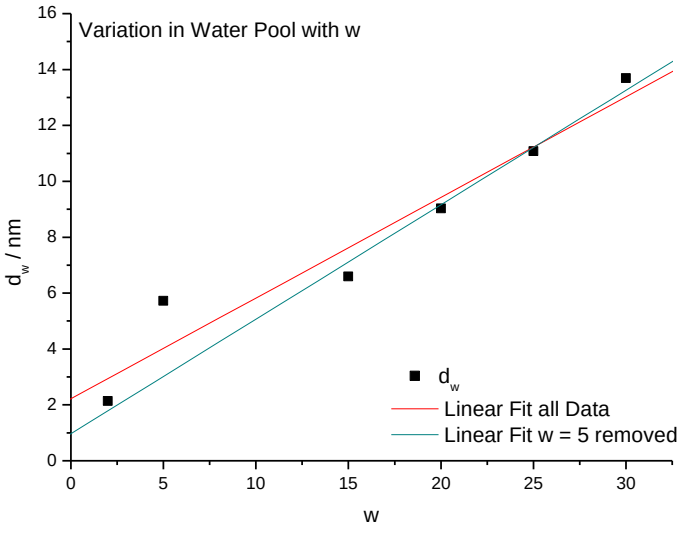

Linear Regression for all Data:

Y = 2.22127 + 0.3601 * X

Value	Error
2.22127	± 0.88155
0.3601	± 0.04626

R	SD	N	P
0.96854	1.14329	6	0.00147

Linear Regression w =5 removed

Y = 0.96932 + 0.40961 * X

Value	Error
0.96932	± 0.43664
0.40961	± 0.02104

R	SD	N	P
0.99607	0.45178	5	2.95926E-4

Figure 5.6 The linear variation of water pool diameter, d_w, with water pool, w, for the micelles containing αhp. The trend is shown with and without the anomalous data for $w = 5$.

Table 5.2 The hydrodynamic diameters from the DLS measurements on the varying water pool solutions containing αhp. The literature results in red show values obtained from the trend in hydrodynamic radius with water pool size, and are therefore approximated and not measured results. All the literature (Lit) values are included for empty reverse micelles of water/AOT/isooctane. The w = 0 result was recorded in the absence of αhp. The z-average is the most consistent diameter generated.

w	Peak 1 (% intensity, width) / nm	z – average	PDI	Peak 2 (% intensity, width) / nm	d_w / nm	(SAXS) $d_{w\ (Lit)}$ / nm[12]	(DLS) $d_{H\ (Lit)}$ / nm[9]	(DLS and NMR) $d_{w\ (Lit)}$ / nm[5]
0	3.415 (100 %, 1.333)	2.909	0.137	-	1.015	0.78	3.6	0.9
2	4.537 (100 %, 1.426)	4.187	0.058	-	2.137	1.40	5.0	1.5
5	8.126 (100 %, 3.206)	7.042	0.122	-	5.726	2.34	7.2	2.4
15	8.994 (100 %, 2.917)	7.946	0.115	-	6.594	5.44	-	5.4
20	11.43 (100 %, 4.012)	10.09	0.113	-	9.03	7.01	10.4	7.0
25	13.48 (100 %, 5.060)	11.72	0.141	-	11.08	8.56	-	8.6
30	16.09 (94 %, 6.635)	-	0.240	3369 (6.0 %, 1201)[†]	13.69	10.12	-	10.2

Table 5.3 The hydrodynamic diameter from the DLS measurement on the w = 5 solution containing mhp. The Lit values are explained in Table 5.2.

w	Peak 1 (% intensity, width) / nm	z – average	PDI	Peak 2 (% intensity, width) / nm	d_w / nm	(SAXS) $d_{w\ (Lit)}$ / nm[12]	(DLS) $d_{H\ (Lit)}$ / nm[9]	(DLS and NMR) $d_{w\ (Lit)}$ / nm[5]
5	6.124 (100 %, 2.513)	5.045	0.176	-	3.724	2.34	7.2	2.4

[†] Due to dust

The w = 0 result measures the natural water content in the AOT/isooctane mix, and contributes 1.0 nm to all the water pool diameters. The majority of the water is expected to originate from wet AOT, as opposed to the isooctane, so dilution of the neat solutions with isooctane should not alter this value significantly. For w = 0, d_w was measured to be $\approx$ 0.2 nm higher than that observed in the literature.

The variation of d_w with w, is expected to show a linear trend. Figure 5.6 shows that d_w (αhp) vs. w does exhibit a near linear relationship. Exclusion of the data point from the water pool of 5 reveals a lower deviation from the fit, as is supported by the standard deviation (SD) and correlation function (R). The overall linear enlargement of the water pool diameter, with w, suggests that the calculations in Section **5.1.3.1**, do increase the size of water pool relative to the last quite consistently. Though, evidently, the d_w for the w = 5 is higher than the trend and more in line with the value expected for when w = 11.

Notably, the larger water pools w = 15-30 demonstrate near perfect linearity with d_w. Thus it appears that the lower water pools of < 10, may need to account for a staggered packing of AOT. This is documented to increase the outer wall of the reverse micelle by up to 3 Å, giving 15 Å as opposed to the assumed 12 Å.[9] However, on doing so, the size of the boundary layer was overestimated, generating a d_w of less than zero, when w = 0. This indicates an intermediate thickness between the two, may be present for when w = 2, while the w = 5 diameter cannot reliably be adjusted to predict the thickness of the micelle wall. The possibility of an increased boundary layer is considered again in Section **5.1.5.1** when estimating the RP separation in the micelles.

Initially for the preparation of the micelle solutions, literature N_{agg} values from SAXS[16] data were used to predict the concentration of the micelles. This data now seems to be in disagreement with the diameters obtained from the DLS measurements. Therefore, the N_{agg} values were calculated for determining the Poisson distributions for the αhp (and mhp) among the micelles. N_{agg} was estimated using two methods, both of which stem from the calculated value of d_w. In solution the AOT molecule adopts a truncated conal shape. The tip of the cone is the surfactant head and the tail extends out to produce a V shape (see Figure 5.7).[10] From this, a crude model to calculate N_{agg} can be constructed. This requires both the surface area of a sphere ($4\pi r^2$), and the maximum cross sectional area (A) of the AOT molecule, $\approx$ 55 Å^2.[22]

$$N_{agg} = \frac{4\pi r^2}{A} \quad [5.7]$$

This model assumes a close packing of the AOT and no overlap of the polar head groups. Under these conditions, the ratio given in Equation [5.7] yields the minimum aggregation number.

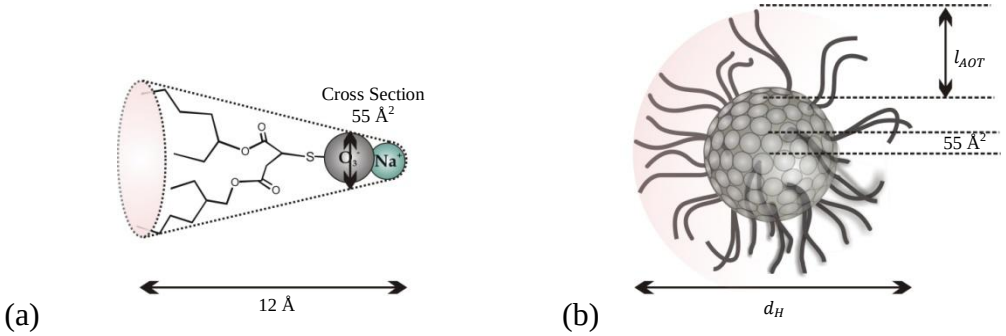

(a) (b)

Figure 5.7 (a) The Cone Shape adopted by AOT. The length of AOT is 12 Å, whilst the head group occupies a maximum cross sectional area of 55 Å^2. (b) The assumed close packing of the polar heads with their maximum cross section indicted by the small circles, over the total surface area of the water core.

An alternative method is to calculate N_{agg} from the relationship in Equation [5.8].[9]

Table 5.4 The N_{agg} values, calculated *via* Equations [5.7], and [5.8]. The third column shows the literature values derived from SAXS data.[16] The corresponding values for mhp are highlighted in the bottom row.

w	N_{agg} [5.7]	N_{agg} [5.8]	N_{agg} SAXS
0	6	-	12
2	26	85	32
5	187	655	64
15	248	334	212
20	466	643	322
25	701	950	468
30	1070	1490	658
5	79	180	64

$$r_w = \left(\frac{90 w_0 N_{agg}}{4\pi}\right)^{1/3} \quad [5.8]$$

This equation is derived from the NMR chemical shifts of water and was originally used to calculate the r_w. It has since found regular use in literature.[8] Both sets of values for N_{agg} are included in Table 5.4 for comparison with the literature SAXS data. Quite predictably, the calculated N_{agg} values are in general larger than the SAXS data. A plot of the N_{agg} vs. w (see Figure 5.8) yields a 3rd order polynomial for all the datasets shown in Table 5.4, including the literature.

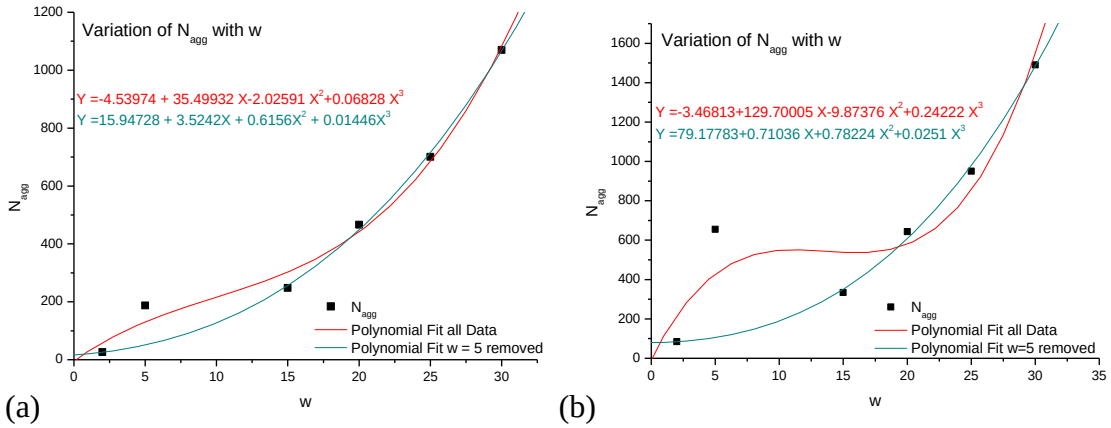

Figure 5.8 Plots to show the variation of N_{agg} with water pool, w, for the micelles containing αhp. Plots (a) and (b) use N_{agg} values from Equations [5.7], and [5.8] respectively. The trends are shown with and without the anomalous data for a $w = 5$.

Likewise to the earlier assessment of d_w, the plots are shown with and without the data point for w = 5, where again the removal of 5 improves correlation. On removal of the w = 5 point, it appears that the data may additionally fit a 2nd order curve. However the fit is marginally better for the 3rd order polynomial given in Figure 5.8 and this is also consistent with the exhibited literature trend.

Since the trends in both sets of calculated N_{agg} values follow the correct relationship, it is difficult to confirm which method offers a realistic representation of the actual N_{agg}; therefore both were used in the following section.

5.1.4.3 Poisson Distribution Plots

According to the Poisson distribution for the individual solutions, the probability of locating one substrate molecule in a micelle is highest when the concentration of the micelles equal that of the substrate. This is unsurprising, given that the calculation is based on random events. There is a difficulty in maintaining an identical substrate to micelle concentration that is, the minimum amount of water required to solubilise αhp. This is particularly limiting for lower water pools, where a large concentration of AOT is usually necessary to achieve the desired water pool ratio. For these solutions, the probability of finding a molecule, in the micelle, at any one time, for a set concentration of AOT can be determined from the Poisson distribution.

The plots in Figures 5.9, are based on the estimated values of N_{agg} in Table 5.4, using Equations [5.2] and [5.3]. Clearly from both distribution plots, for the 0.7 mM αhp, there is a high probability of finding the molecule in the micelle for water pools of w = 30, and w = 15. The probability is lower for the water pool of 5 and negligible for a water pool of 2. To attain the highest probability when w = 2, an AOT concentration of 45 (plot (a)) or 20 mM (plot (b)) would be required, depending on the assumed N_{agg} value.

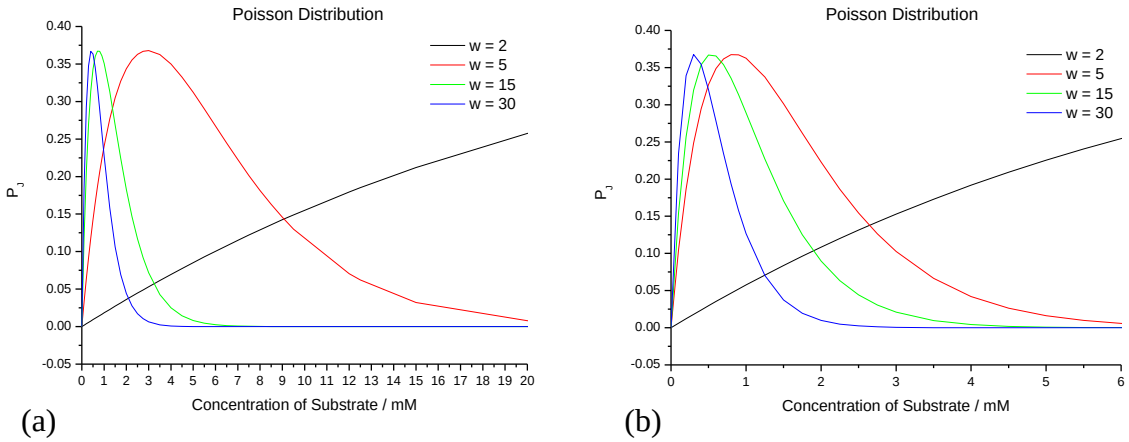

Figure 5.9 Plots to show the Poisson distribution of αhp molecules among the micelles for the calculated values of N_{agg}. (a) Shows the data from Equation [5.7] and (b) Is from Equation [5.8].

Considering that mhp is liquid, the solubility constraint due to the water was no longer an issue. That said, higher concentrations of the mhp, than αhp were required for

a sufficiently large kinetic trace, owing to the lower IR absorption by the resulting benzoyl radical. Evidently the water pool diameter for mhp contained in the micelles for when w = 5, is also lower than that obtained for αhp. Therefore the plots used for αhp were not appropriate to model the probability distribution for mhp among the micelles. Alternative plots, with different concentrations of AOT to those used for αhp, were created to determine the maximum probability. Two concentrations of mhp were chosen, 9 mM (Equation [5.8]) and 20 mM (Equation [5.7]), which correspond to the peaks in the two Poisson distribution plots for when w = 5. Both these TRIR studies along with those of αhp are discussed in the next section.

5.1.5 Magnetic Field Effects of Radical Pairs in Micelle Solutions

The magnetic field effects and kinetics of RPs encased in micelles have received considerable attention.[23, 24] Some examples of the investigations on neutral RPs (in micelles) in low fields were described briefly in Chapter **1**. Despite providing a more realistic model of cellular systems than conventional micelles, there are fewer reports on the field effects and the kinetics of RPs in reverse micelles.[25] In these structures and as illustrated in Figure 5.2, the hydrophobic wall surrounds a micropool of water. This allows enzymatic activity in host proteins (modelled by reverse micelles) to be recreated *in vitro*. Thus the biological literature on studying enzymes and proteins incorporated into these systems is extensive.[3, 22]

The influence of micelle confinement on the recombination kinetics of the RP is common to both micelles and reverse micelles. Broadly, for an encapsulated RP, the decay of the pair proceeds in two distinguishable steps. The first step typically occurs within one microsecond and can be attributed to the g-pair, intra-micelle RP recombination. Whereas the second step, can extend over tens or hundreds of microseconds and is from the inter-micelle recombination of the f-pairs. Likewise these separable kinetics should be evident in the current work, if the RP is indeed located in the water pool of the reverse micelle. In addition, an attraction of the reverse micelle over conventional micelles is the ability to expand the size of the water pool over a wider range. This alters the timeframe between geminate reencounters for the RPs in the different water pools and should reveal very different kinetics for the two extremes of water pool (w = 2, 30) tested here.

The generation of a magnetic field effect is strongly dependent on the timescale of spin-state evolution, as well as the lifetime of the RP.[26] A given SCRP will require

longer to develop an LFE than a MFE, due to the different rates of spin-state evolution. Any process capable of interrupting the g-phase of the pair can alter the extent of S-T mixing and accordingly the field effect. Importantly, f-pairs have also been confirmed to produce field effects and alterations therein can additionally affect the extent of spin mixing.[27] As discussed, the LFE should develop through interplay of the hfc and the applied field, while the MFE is driven by the strength of the external field. Therefore manipulating the conditions that can control both of these field effects is crucial in exploring the respective mechanisms involved.

Previous TRIR investigations on αhp in isotropic solution have highlighted changes the size of the LFE in relation to the MFE, which arise from the time varying composition of the f-pairs.[25] Integrating the predominantly second order kinetic curve over early integration periods revealed the greatest magnitude LFE and lowest MFE, which gradually reversed over time to give a decrease and increase respectively. It was proposed that this gave insight into the nature of the f-pair lifetimes. The changes were interpreted from the relative diffusion rates of the possible f-pair combinations, where the symmetrically similar and larger benzoyl radicals were suggested to recombine later in time. This rationalises the recorded reduction in the LFE. If g-pairs and f-pairs show the same field dependence then a comparable change would be anticipated for both and under this condition the integrations would increase/decrease equally for both field effects. This model is considered further in this and the subsequent section relating to the viscosity studies.

5.1.5.1 The Recombination Kinetics and Magnetic Field Dependence of Radical Pairs in the AOT Reverse Micelle Solutions

The kinetic decays for 0.7 mM αhp photolysed in micelles of varying water pool sizes are displayed in Figure 5.10. Also included in the figure, for comparison, are the decay curves for the αhp radicals in solutions with viscosities of 6 (solvent mix) and 59 cP (cyclohexanol). Notably the RP in the water pool of 5 exhibits the longest decay over the 40 μs recording time and the kinetic curves for the water pools of 2, 5, and 30 all decay more slowly than the RP in cyclohexanol. This suggests the RPs in these solutions were successfully encapsulated in the micelles, as the recorded viscosities of all the micelle solutions are far lower than the 59 cP of cyclohexanol. Therefore these RPs could not be located in the bulk phase, as they would have generated much faster decays, more comparable to that occurring in the 6 cP solution. Refer to Table 5.1 for the corresponding viscosity measurements.

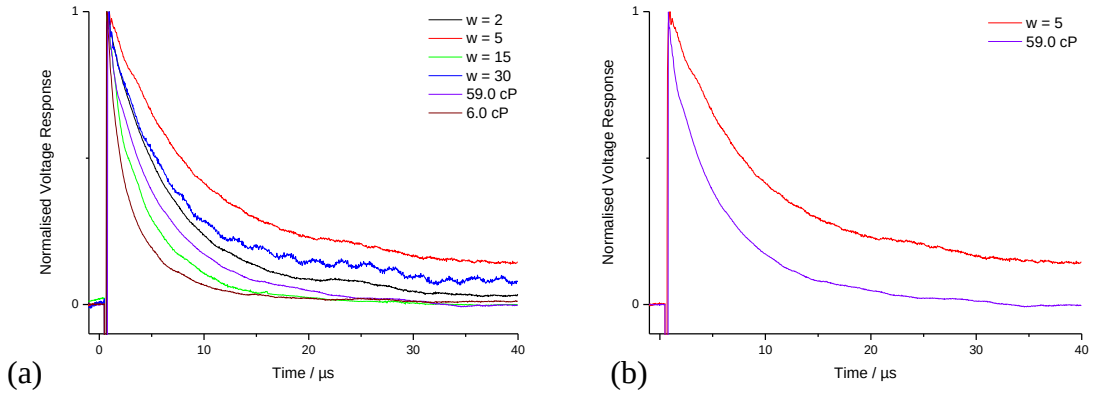

Figure 5.10 (a) The kinetic traces for the recombination of 0.7 mM αhp radicals contained in varying sized reverse micelles. The decay traces in water pools of w = 2, 5, 15 and 30 are compared with those in solutions of cyclohexanol (59 cP), and cyclohexanol/propan-2-ol (6.03 cP). (b) Shows the possible separation of g- and f-pair kinetics. The normalised voltage scale in both plots represents the concentration of the radicals.

Further confirmation that the αhp was contained in the micelle was visual. On occasions where the molecules were not in the micelle, occurring when the solution was prepared with both phases at once and not *via* injection, some αhp would settle at the bottom of the flask. This proves could not be located in the isooctane in any of the solutions tested since there was no evidence of residual precursor. It is important to note that the solubility of the RP is most likely quite different to the precursor and may still be located in the bulk phase.

The kinetic curves for the water pools, 2, 5 and 30, are quite different from those in cyclohexanol, in which the RP principally undergoes uncorrelated (f-pair) second order recombination. In the micelle systems, there is some evidence for the two kinetic processes described earlier. From approximately 10 µs onward, a slow decaying component dominates the kinetic trace (see Figure 5.10 (b)). This decay is incomplete during the recording period shown. Based on the majority of studies of RPs in micelles it further seems reasonable to propose that the RP is in the water pool and the observed kinetics reflect an extended geminate period followed by the slower f-pair decay for the radicals that escape from the micelle. What is difficult to explain is the length of the geminate period, which appears much longer than is typically observed ($<$ 1 µs) for RPs trapped in micelles.[25]

As the water pool diameter in the reverse micelles is reduced, the intervals between geminate reencounters increase. This should, provided there is sufficient RP separation to overcome the electron exchange energy, also increase the probability of geminate recombination in these smaller water pools. Accordingly, this should decrease the number of f-pairs escaping the micelle and simultaneously increase the rate at which escape occurs. It is therefore anticipated that the smaller water pools should reveal a more distinct difference in the two kinetic rates, over that occurring for the same RP in the larger water pools. While there appears to be no obvious trend among the water pools in Figure 5.10, it may be proposed that $w = 5$ and $w = 2$ loosely obey the prediction. However, the proximity of the geminate RP obtained through the DLS measurements must also be addressed when interpreting the recorded kinetics.

For $w = 2$, the altered behaviour of the polar head groups of the AOT may limit access to the water pool. The length of the outer wall in the micelles with $w < 10$ is, as previously mentioned, recorded to be 15 Å as opposed to the assumed 12 Å. This additional length has been attributed to a staggered arrangement of the AOT molecules that eases with increased water content.[9] By accounting for the possibility of a staggered boundary layer approximately 1.5 nm would remain for the water core, which would be rigid from hydrogen bonding and therefore unlikely to contain the αhp, whose size may be averaged as closer to 9 Å in length. This indicates that the αhp may be located among the water at the interface and therefore able to escape the micelle faster, and hence give rise to the witnessed radical decay, which less convincingly reveals signs of separated kinetics (compare with $w = 5$ and $w = 30$) or the expected increase in the g-pair recombination. The reason for the slower decay (*cf.* 59 cP) is most likely due to the high viscosity (10.5 cP) of the solution in combination with the initial location at the micelle interface, rather than from successful encapsulation in the water pool.

Clearly the viscosity of the solutions is an additional factor when discussing the rate of f-pair recombination and will, in part, govern the ability of the radicals to diffuse through the solution. From micelle dynamics and the structure of the ternary system, there are three main pathways for f-pair recombination; diffusion through the Stern/Guoy-Chapman layer, micelle coalescence or exchange of the AOT monomers. The latter two depend on the number of and distance between the micelles in solution, and both of these will influence the speed of exchange. Micelle coalescence, which replaces the entire water pool of the micelles is slow in comparison to single AOT exchange and can therefore be considered negligible in the present study. The

contribution to escape from AOT exchange and escape through the boundary layer, however, occur within microseconds and are relevant to timescale of interest. The hindrance to RP diffusion can, from the mentioned factors, increase quite dramatically from the bulk solution and depends on both the number of micelles (size and consequent viscosity) and the initial location of the RP as already suggested for when w = 2.

w = 15 was prepared based on the minimum amount of water. It has a lower viscosity (0.70 cP) than any of the other micelle solutions and was measured to evaluate the importance of the viscosity on the RP decay (see Table 5.1). From Figure 5.10 it appears that the kinetics in the w = 15 solution are more indicative of that from f-pairs, encountered in isotropic solution rather than the separable kinetics expected in the micelles. Notably the RP decays slower than in the solution of 6.03 cP viscosity, which indicates the RPs have spent some time in the micelles. However, the predominantly f-pair decay suggests escape from this micelle is faster than for when w = 5 or 30. This implies that the viscosity of the solution not only influences the rate of f-pair decay, but also escape from the micelle. Once freed from the micelles the f-pairs can recombine rapidly, as there is less opposition to radical diffusion than in the higher viscosity micelle solutions.

Considering the maximum possible RP separation from the DLS measurements, the size of αhp (or mhp), and the bulk water properties of the core for a $w > 3$, the water pool of 5 should be sufficient to allow spin-state mixing. This pool size should also enhance the frequency of RP reencounter (compared to that in a larger water pool), and the average RP lifetime, as already demonstrated. For this pool size the minimum value of d_w is estimated as ≈ 4.2 nm for the micelle containing αhp and ≈ 2.4 nm for those with mhp. These values assume an outer wall of 15 Å and account for the size of the substrate. Both of these pool sizes allow the RP to access the required $>$ 1 nm separation to overcome the electron exchange energy.

The resulting magnetic field traces for the w = 5 and w = 30, along with 0.7 mM αhp in cyclohexanol are given in Figure 5.11. A subtle increase in the magnitude of the LFE is observed for the RP contained in the micelles for which the w = 5 over that occurring when the w = 30, while the generated MFEs remain equal and appear to saturate within the field range. Based on the observed kinetics, an obvious difference in the field dependence between the two water pools was anticipated, when considering RP diffusion should occur more readily in the larger pools and reencounter less

frequently. However, the efficiency of S-T mixing for the RP contained in these two water pools may vary. In the smaller water pool the chance of reencounter increases. Though reencounter in the triplet state may be higher than that for the RP in the larger water pool, which despite colliding less frequently may react more efficiently. This is one possible explanation for the comparable field dependence recorded.

An unexpected finding is that there is a significant reduction in the size of the MFE between the result in cyclohexanol and those recorded for the reverse micelles. The hint of an increase in the LFE and clear decrease in the MFE is difficult to explain for the w = 5. Rather an increase in both would be anticipated if the RP were effectively prevented from diffusing, since this should enhance the extent of spin-state mixing, at least for early times. The enhanced geminate period, as suggested by the kinetics does not appear to have induced a greater amount of singlet recombination, following S-T mixing and has revealed only negligible growth in the size of the LFE.

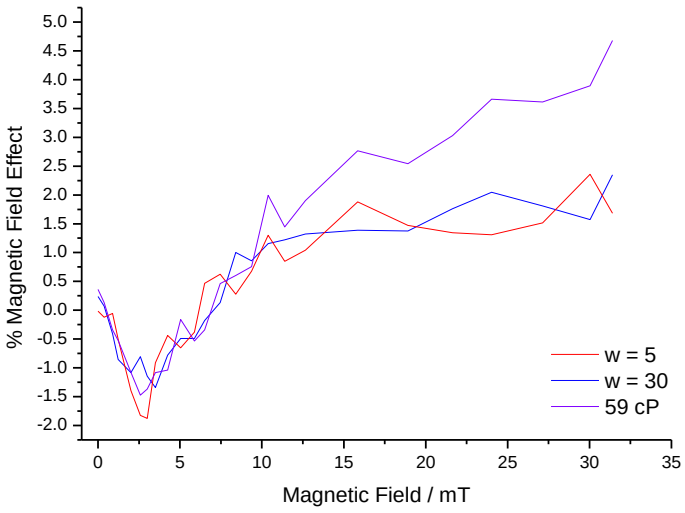

Figure 5.11 The magnetic field traces for the recombination of αhp RPs contained in reverse micelles of w = 5, and 30, compared with the result in cyclohexanol. For the micelle solutions, the LFE is larger when w = 5 and the MFEs are comparable.

In the micelle the extended geminate phase should also increase the influence of incoherent spin relaxation. Accordingly, if random relaxations were enhanced there would be a greater loss of spin correlation and a higher field would be required for saturation of the MFE. Quite convincingly however, the MFE plateaus, indicating that

the limit in spin-state mixing from the removal of the $T_{\pm}$ sub-levels has already occurred. This now suggests that the result may be an observation of the increased influence of the geminate stage on the LFE/MFE ratio. By viewing the time dependence of the relative magnetic field effects, this possibility can be explored. The corresponding field traces for the w = 5 kinetic curve integrated at different times after the laser flash, are displayed in Figure 5.12. Over time this appears to show an increase in the magnitude of the LFE, while the MFE shows a reduction, importantly both these changes are small. The amount of associated noise in the signals with the varying time integrations does not disregard the possibility that, within error, the results are approximately equivalent. Thus it appears the field effects from the g- and f-pairs remain constant with time. This supports the separation of g- and f-pair contributions to the field effect, with the observed field result being dominated by the g-pair effects. At later integrations the MARY dependence may resemble that in homogeneous solutions, generating the expected increase in the MFE. This however, could not be confirmed since the integrations beyond 6 μs were far too noisy for any useful interpretation.

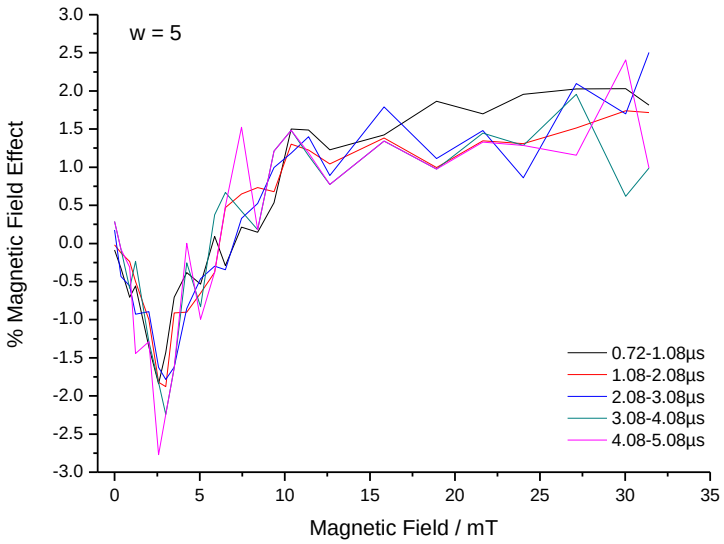

Figure 5.12 The magnetic field traces for the αhp RP in the w = 5 reverse micelle solution, with the kinetic curve integrated over the specified time intervals.

The MARY curves for the water pools of w = 2, and 15 are shown in Figure 5.13. It was originally anticipated that the most frequent recombination and greatest effect of spin-state mixing would occur in a smaller water pool size, hence why w = 2 was pursued. However, from the magnetic field trace and the kinetic curve data for w = 2

there are three reasons to suggest that the RP does not reside in the water pool. Firstly, there is an inadequate distance of approximately 0.64 nm in the pool, to allow spin mixing to occur. If the RP were in the core, the hydrogen bonded nature of the water in this size pool would effectively bind the RP in the centre. Consequently a far reduced decay rate would be anticipated in the kinetics, since the majority of g- and f-pair recombination would be prevented. This is not observed. Secondly, the solution is viscous. At 10.5 cP, it should sufficiently hinder diffusion of the RP to allow field effects of this magnitude to be recorded (*cf.* with the 7.2 cP solution in Figure 5.17). This leads on to the third point; the MFE is clearly larger than that recorded in the other micelle water pools of w = 5 and 30. This is strongly suggestive that the αhp is actually located at the micelle boundary, or perhaps more likely in the AOT tails. Naturally, since the tails are flexible and mobile, they would release the RP rapidly. The RP recombination should therefore be governed by the rate of inter-micelle collision and the viscosity of the solution.

w = 15 reveals the predicted MARY trend, where both the LFE and the MFE are reduced, due to the shorter overall lifetime of the RP (refer to Figure 5.13 (b)). The MFE saturation relative to that occurring in cyclohexanol is again lower, which is in agreement with the other water pool field dependences.

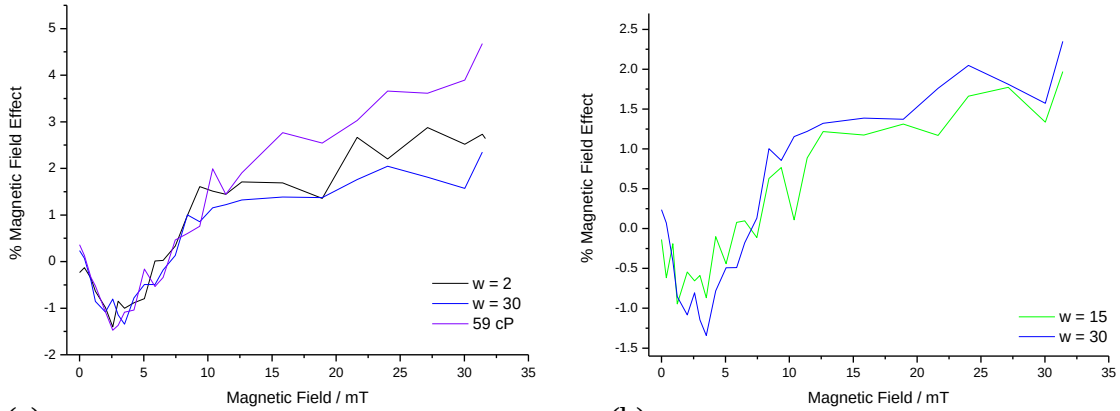

Figure 5.13 The magnetic field trace for the recombination of αhp radicals contained in water pool of (a) w = 2 compared with w = 30, and cyclohexanol. (b) w = 15, compared with w = 30.

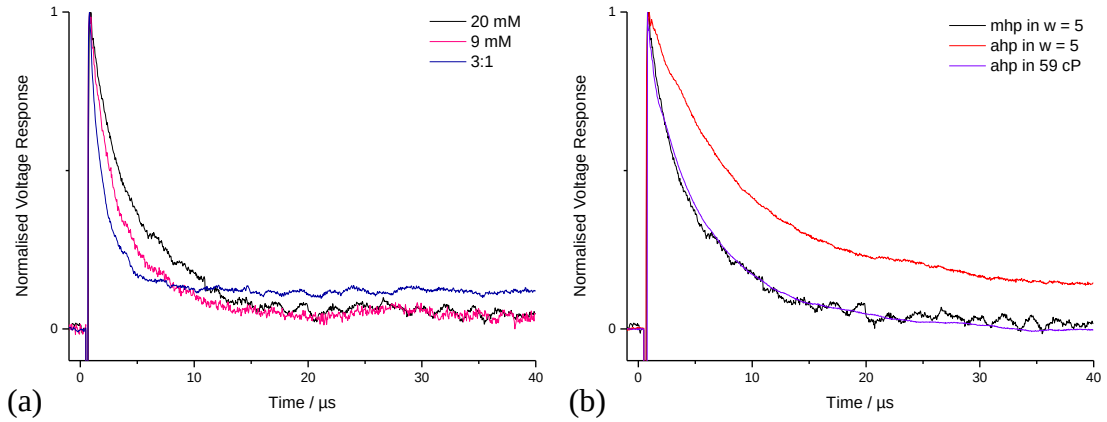

Figure 5.14 (a) The kinetic traces for the recombination of differing concentrations of mhp contained in a reverse micelle solution of w = 5. This includes the result from a 3:1 ratio of mhp to micelle concentration. (b) Comparison of the decay curve of 20 mM mhp from (a) with αhp in w = 5, and αhp in a high viscosity solvent. The normalised voltage scale in both plots represents the concentration of the radicals

To test the influence of the RP on the recorded field effect, αhp was replaced with mhp in the micelle solutions. As discussed earlier, both molecules differ only in the *para*-substituted moiety on the benzene ring. This makes mhp both smaller and less capable of hydrogen bonding, refer to Figure 5.1 for the structures. The generated RP from both precursors possess the same average hyperfine coupling. Therefore spin mixing should evolve at the same rate, limiting any difference in the field dependence to be a result of the RP structure since their environments should also be similar.

Evidently αhp in the w = 5 generated the longest RP lifetime, and for this reason w = 5 was likewise used for the mhp studies. The RP decays for mhp are shown in Figure 5.14. The kinetics were measured for varying substrate concentrations as indicated. Firstly to determine the minimum concentration required for an adequate signal, and secondly, to probe for any differences in the kinetics, given that each of the concentrations corresponds to a maximum in the Poisson probability distribution (for the two N_{agg} estimations). Importantly, the 20 and 9 mM solutions have a comparable viscosity. Therefore any kinetic variations can be attributed to the distributions of mhp among the micelles, as the water pool in both is also identical.

Clearly the 20 mM decays more slowly than the 9 mM and both signals are noisier than those for αhp, despite the much larger concentrations used. For these

curves, there is no evidence of a separation in the g- and f-pair recombination processes and the RP kinetics parallel, or are lower than that encountered for αhp in highly viscous cyclohexanol (see Figure 5.14 (b)). The comparatively fast decays in these solutions would suggest this RP is situated in a different position to the earlier αhp pair. The corresponding magnetic field traces for mhp yielded no discernable field effects and the outcome was similar for all the time integrations, and concentrations tested. An example of this is shown in Figure 5.15, where the field dependence appears to be random.

The kinetic curve for the 20 mM mhp decays at a similar rate to the αhp in cyclohexanol, which may imply a relatively long lived RP, though this is clearly not verified by the resulting field data. Additionally the decay from a solution prepared with an excess of mhp per micelle, in a 3:1 ratio as calculated from the Poisson distribution, was recorded (Figure 5.14 (b)). The 3:1 ratio reveals a faster initial decay and an absorbance level that remains above zero, even for longer times ($>$ 40 μs). This trace exhibits the trend originally expected for the smaller water pools, where the two kinetic processes are clearly distinguishable. However the RP decay in this case never returned to zero, indicating either the formation of a product molecule with an absorption in the range of the benzoyl moiety, or an extremely long lived f-pair decay for the few pairs that escape the micelle. It was anticipated that this may give insight into the location of the RP. Since if the RP was in the water pool, the f-pair encounter would be rapid in this low viscosity environment and the decay would be complete earlier in time than either the 9 or 20 mM solutions. Despite the obviously faster initial decay, the absence of a field effect implies the RP for mhp was not located in the water pool.

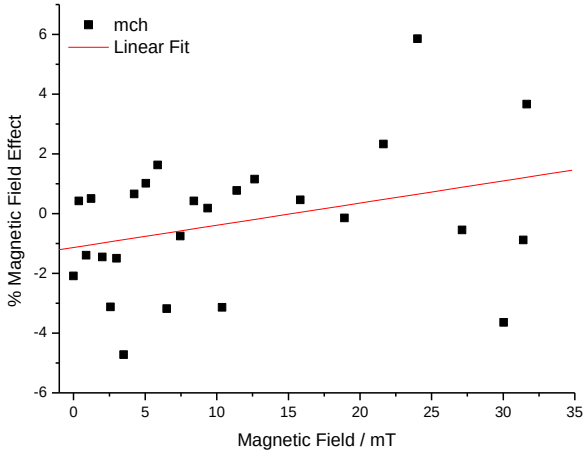

Figure 5.15 The magnetic field trace for the recombination of 20 mM mhp radicals contained in a micelle solution of w = 5.

5.2 The Variation in the Magnetic Field Dependence with Viscosity and Hydrogen Bonding

In the earlier section the αhp was effectively encased using reverse micelles. In this section the solvent cage is responsible for restricting RP diffusion. The lifetime of a RP in an isotropic solution is primarily governed by the viscosity of the solvent and control of this can enhance the lifetime of the RP in the cage, and consequently the extent of spin-state mixing. Furthermore, the competitive kinetic processes occurring in homogeneous solution are less complex than those in the reverse micelles and should enable easier interpretation of the results. This work explores the effect of viscosity on the generation of the LFE and MFE in solutions of increasing viscosity and the possibility that hydrogen bonding may also extend the RP lifetime.

5.2.1 Viscosity

Table 5.5 shows the solvent mixtures formed from increasing % volumes of propan-2-ol added to cyclohexanol, along with their measured viscosities, which were calculated using Equation [5.6]. The viscosity sharply decreases on addition of the propan-2-ol to cyclohexanol and thereafter follows a near linear relationship for increasing volumes of propan-2-ol. Accordingly a similar trend would be expected among the kinetic curves, where the drop in the RP lifetime would be much greater between the cyclohexanol and 25 % propan-2-ol, than for the remaining solutions.

Table 5.5 The viscosities for solutions containing varying % volumes of cyclohexanol and propan-2-ol. All viscosities were measured using an Ostwald viscometer at 25 °, or in the case of the cyclohexanol a Brookfield viscometer.

Cyclohexanol	Propan-2-ol	η / cP
0	100	2.0
25	75	3.2
50	50	6.0
75	25	7.2
100	0	59.0

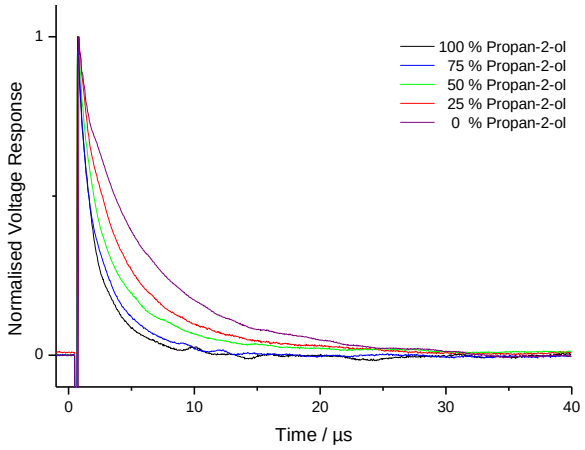

Figure 5.16 The kinetic traces for the recombination of 2 mM αhp radicals in solutions of cyclohexanol with propan-2-ol added by % volume.

The corresponding decay curves for the RP in the different solution mixes are shown in Figure 5.16. The decay time of the f-pairs gradually increases with increasing viscosity. This confirms that in the viscous solutions the solvent molecules behave as a more effective barrier to RP diffusion. Consequently both the g- and f-pair stages of the RP are likely to have been extended, first by hindered escape from the cage, which is thereafter followed by slower f-pair recombination. Unlike the reverse micelle solutions the solvent mix is homogeneous and opposition to radical diffusion under this condition continual.

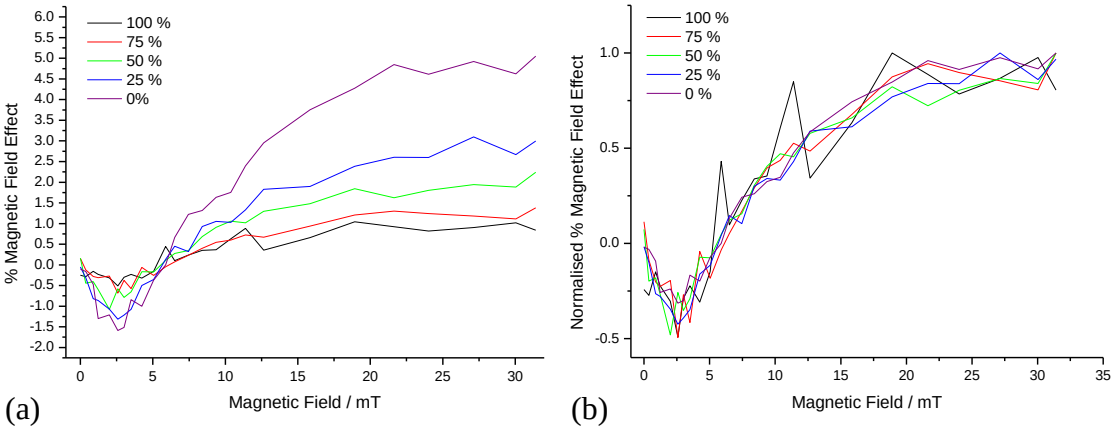

Figure 5.17 (a) Shows the magnetic field traces for the recombination of 2 mM αhp in solutions of altered viscosity, by % volume of propan-2-ol added to cyclohexanol (refer to Table 5.5). All MARY curves are the result of integrating between 60-90 % of the total kinetic curve. (b) Is the same data normalised to the MFE.

The differing lifetimes should likewise be evident in the overall magnitude of the magnetic field dependence. Here, a longer lived RP should enhance both the LFE and the MFE, while the short lived pairs may only develop the MFE. LFEs are reported to be more sensitive to the lifetime of the RP and it is therefore worth noting that as the RP decay shortens, the likelihood of observing an LFE may also decrease. The MARY curves for the mixed solvents in Figure 5.17 reveal a weaker magnitude MFE and LFE with decreasing viscosity, as more radicals rapidly escape the geminate cage before spin-state mixing. Surprisingly a LFE is still detectable even in the very low viscosity, of the 100 % propan-2-ol solution. This solution also demonstrates a very shallow MFE, though both effects are very weak.

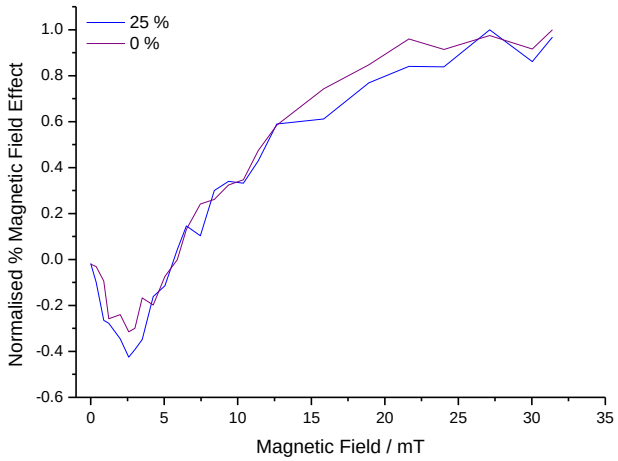

Figure 5.18 The normalised magnetic field traces for the recombination of 2 mM αhp in solutions of cyclohexanol, and 25 % propan-2-ol by volume added to cyclohexanol. Both results are from integrating between 60-90 % of the total kinetic curve.

Clearly the size of the MFE for cyclohexanol (59 cP) is far greater than that in the next highest viscosity solution (7.2 cP). However, from this figure the relative LFEs do not necessarily exhibit an equivalent change. Normalisation of the data to the MFE in Figure 5.17 (b), confirms the rate of achieving the MFE is comparable among all the solvent mixes. On closer inspection of the results, there is an indication of an increase in the relative size of the LFE for the 25 % propan-2-ol solution, from that occurring in pure cyclohexanol (see Figure 5.18). The LFE appears to have increased in relation to the MFE, not to the extent observed in the micelle solutions, which shows a plateau in the MFE and an obvious difference. Importantly in this case, the varying contributions from noise between the traces may equally account for the marginal differences

observed. Therefore, most consistently, the development of the LFE and MFE are proposed to remain unchanged across the solutions of different viscosity. This leads to a final point in that the relaxation occurring appears to be negligible, since the rate of achieving the MFE is comparable for all the solutions despite the longer geminate pair lifetime in the more viscous solutions.

5.2.2 Hydrogen Bonding

Previous work has highlighted the possibility that hydrogen bonding between the solvent and a RP may prolong the RP lifetime. To further test this theory, solvents of high viscosity with little/no propensity for hydrogen bonding, and sufficient polarity to solubilise αhp were sought. This was in itself challenging given that most viscous solutions are normally hydrogen bonded, or non-polar oils and which are unable to solubilise αhp or similar molecules required for this study. Consequently the use of hydrogen bonded solvents was unavoidable, as no solvent or solvent mix could fulfil all the aforementioned criteria. Solvent mixtures inclusive of cyclohexanol were used in an attempt to examine the effects of hydrogen bonding.

Given the demonstrated importance of the viscosity of the solution, it was necessary to use solvent mixtures maintained at an adequate viscosity to reveal a sizeable field effect, in both the LFE and MFE. Simultaneously, this viscosity needed to be attainable on addition of the second solvent, which may vary quite significantly in its viscosity depending on its structure. The chosen value was 7.2 cP. In addition to the hydrogen bonding studies this should further probe for a potentially unusual LFE rise in comparison to the MFE, which was hinted at, but unconfirmed from the earlier viscosity studies (Figure 5.18). By using the same precursor and viscosity, any difference in the observed effects should be a result of the solvent mixtures used. Table 5.6 details the % volumes of the solutions required to achieve a viscosity of 7.2 cP, which were all measured using an Ostwald viscometer.

While dichloromethane and acetonitrile should exhibit no effects from hydrogen bonding, the tendency for cyclohexanol to form hydrogen bonds may far outweigh any effect from these additional solutions. It is also reasonable to propose that as the size of the solvent chain increases for the alcohols, the extent of hydrogen bonding would decrease. Beyond these suggestions it is difficult to predict the likely outcome of the MARY curves. Ideally, the solvents would have been sufficiently viscous to measure the field dependence among them. However, the degree of noise and the low magnitude

field effects observed in the neat solutions (see for example 100 % propan-2-ol in Figure 5.17 (a)) made it impossible to compare the results accurately.

Table 5.6 Cyclohexanol containing varying % volumes of the solvents as listed, to make a homogeneous solution with viscosity of approximately 7.2 cP.

Cyclohexanol	Solvent 2	Solvent 2
75	Ethanol	25
75	Propan-1-ol	25
75	Propan-2-ol	25
54	Butan-1-ol	46
40	Butan-2-ol	60
86	Acetonitrile	14
84	Dichloromethane	16

The resulting magnetic field traces for these data sets show that the different solvents mixes do not achieve the same MFE (see Figure 5.19). Cyclohexanol is again used for comparison. The solutions of propan-2-ol, propan-1-ol and ethanol all possess approximately the same viscosity and were therefore used in the same volume ratios. Quite clearly the overall magnitude of the MFE and LFE is lower for ethanol, than for the other two alcohols, of which propan-2-ol reveals marginally larger field effects.

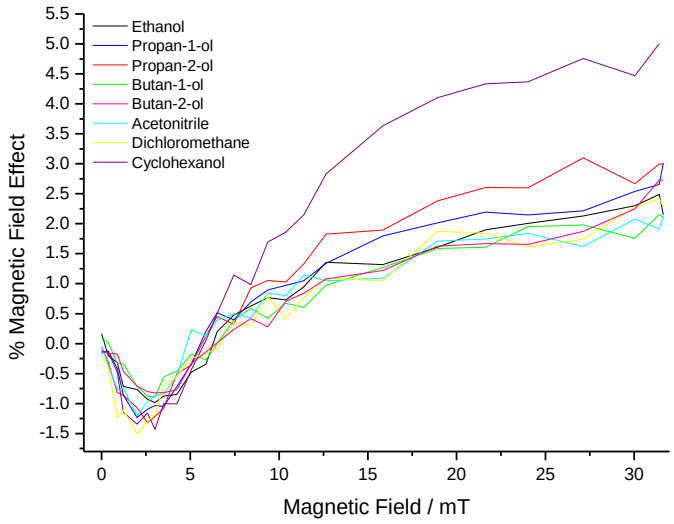

Figure 5.19 The magnetic field traces for αhp in the mixed solvents of 7.2 cP as indicated in Table 5.6, compared with the result in neat cyclohexanol. All the results are from integrating between 1-3 μs of the kinetic curve.

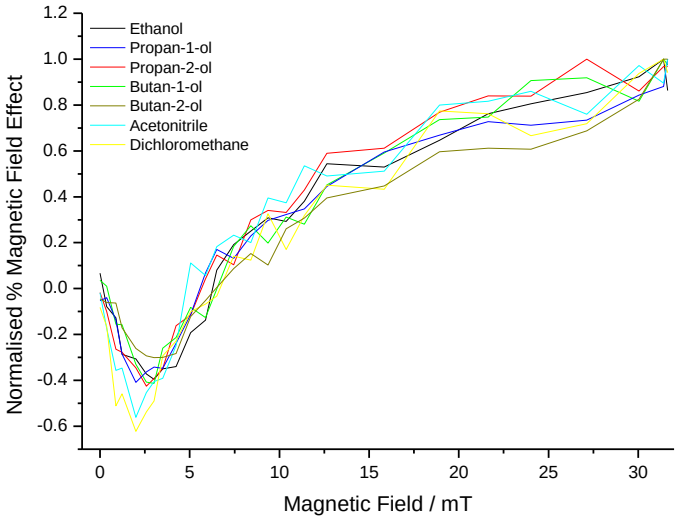

Figure 5.20 The normalised magnetic field traces for αhp in the mixed solvents of 7.2 cP as indicated in Table 5.6. All the results are from integrating between 1-3 μs of the kinetic curve.

All the generated MFEs are similar, excluding the propan-2-ol and propan-1-ol values which appear greater. Normalisation of the data (in Figure 5.20) reveals a surprisingly large relative LFE for the solutions containing dichloromethane and acetonitrile, which were both specifically chosen for their inability to form hydrogen bonds.

Table 5.7 The Hildebrand[28] and Reichardt[29] parameters for the solvents investigated.

Solvent	δ / MPa^{½}	E_T / kcal mol^{-1}
Ethanol	26.2	51.9
Propan -1-ol	24.3	50.7
Propan-2-ol	23.5	48.4
Butan-1-ol	23.3	49.7
Butan-2-ol	23.1	47.1
Acetonitrile	24.1	45.6
Dichloromethane	20.2	40.7
Cyclohexanol	23.3	49.7

Evidently, it is the properties of the additional solvents in the solution mixes that give rise to this unusual behaviour. While it is understood that the field effect still includes a contribution from cyclohexanol, it was anticipated that this result could be

rationalised by parameters that measure the degree of interaction between the molecules in solution. Two such parameters; the Hildebrand (δ), and Reichardt (E_T) parameters are given in Table 5.7.[29] δ is a measure of the extent of hydrogen bonding, while E_T is a measure of the solvent polarity.

To identify if a trend was present among the solvents used and the resulting low field dependence, the maximum % LFE was plotted against the two parameters in Table 5.7 (see Figure 5.21). Both (a) and (b) reveal a loosely linear relationship. Conversely these plots would imply the solvents exhibiting a lower polarity or less hydrogen bonding stabilise the RP and generate a larger magnitude LFE. This opposes the anticipated result, where the more polar/hydrogen bonded solutions would be expected to interact better with the RP and thus extend its lifetime. The general trends from both the plots are, however, rather unconvincing and subject to a considerable error.

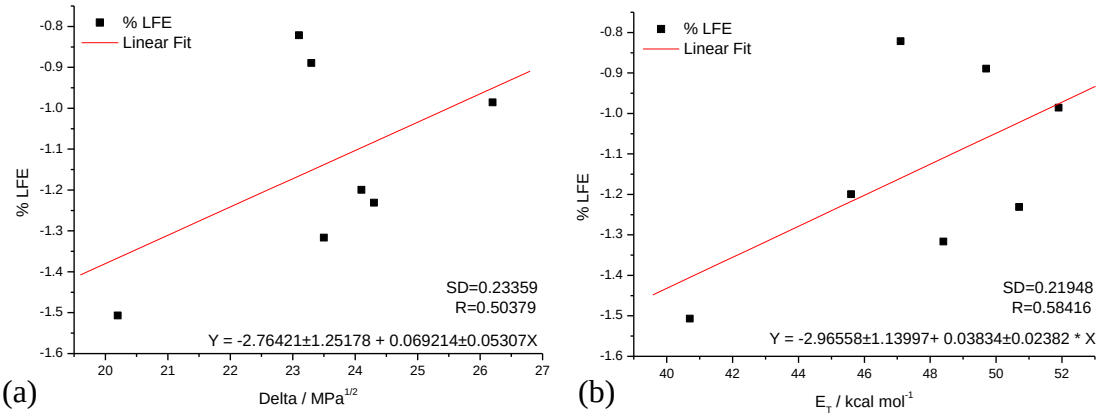

Figure 5.21 The variation of the % LFE from Figure 5.19 with (a) the Hildebrand parameter, δ, and (b) the Reichardt parameter, E_T, for solvents added to cyclohexanol to make the 7.2 cP solutions.

Previous work (as described earlier Section **5.1.5**) has attributed changes in the LFE/MFE ratio to be from the composition of the RPs at any one integration period of the kinetic curve.[27] All the curves were integrated between the same integration window and therefore allow the relevance of this model to be explored for the investigated solvent mixtures. If the average RP lifetime in a particular solution is short, there will be fewer longer lived pairs and the RP would be comparatively less able to develop the LFE at the same rate as it does the MFE. Butan-2-ol and ethanol generate the weakest relative LFEs. By viewing the corresponding kinetic traces (Figure 5.22), it is apparent

that these solvents mixtures also reveal the fastest RP decays, so behave in a manner that is in agreement with the prediction. Furthermore the noise level in these two MARY traces is similar, which makes this assessment of the lifetimes all the more convincing.

The largest normalised LFEs arise from both the dichloromethane and acetonitrile; however the kinetic traces indicate that the LFE should develop faster for propan-1ol, then propan-2-ol, in that order. As with all these MARY curves, it is again essential to consider the relative noise level in the acetonitrile and dichloromethane scans, which are among the highest recorded. This may contribute to the apparently large LFE in relation to the remaining solutions, and to the MFE. Comparison of propan-1-ol with ethanol reveals only a negligible increase in the LFE/MFE ratio for the former, while the RP decays would support the change to be much greater. There are a range of noise levels in the field dependences, which makes investigating the composition model difficult on the current datasets. For the field traces without such a large margin for error; butan-2-ol and propan-1-ol, the anticipated trend is followed. The δ, and E_T values for both of these added solvents, also reveal there should be less interaction between the solvent molecules in butan-2-ol and accordingly with the RP. This may lead to the shorter RP lifetime in the butan-2-ol solution mix.

In any case the relationship between the LFE/MFE and the influence of hydrogen bonding remains unresolved for present work and further investigations are clearly required.

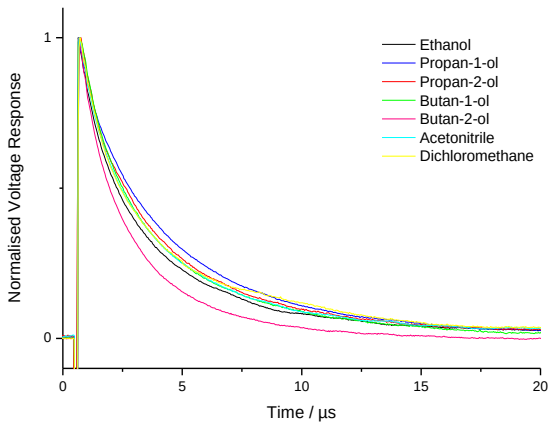

Figure 5.22 The kinetic traces for the recombination of 2 mM αhp radicals in the solutions of cyclohexanol with different solvents, added by % volume, as indicated in Table 5.6.

5.3 Conclusions and Future Work

The work in this chapter has probed the effects of changing the RP environment on its recombination kinetics and magnetic field dependence. The first section revealed long RP lifetimes when the RP was effectively encased in the water pool of varying sized reverse micelles. The lifetime of the RP was clearly extended over that achievable in highly viscous solvents, suggesting the substrate was, at least to some extent, successfully encapsulated.

The field effects showed only a marginal increase in the magnitude of the LFE for the RP in a water pool that had approximately 4.2 nm (w = 5) available for diffusion, over that occurring with a diffusion distance of 12.8 nm (w = 30). With a smaller water pool, reencounter is more frequent and should generate a greater field effect in both the MFE and LFE. However for these two water pools the LFE and MFE were near equivalent. For the smallest water pool (w = 2), the approximate separation distance of the RP reduces to 0.64 nm. This should have revealed a long RP decay with no observable field effect. Conversely, the increased strength of the hydrogen bonding in this size water pool, most likely excluded the RP from entering the pool. Accordingly the field trace for this w = 2 solution resembled those recorded for the RP in homogeneous solutions of a comparable viscosity.

A significant reduction in the size of the MFE was noted between the result in viscous homogeneous cyclohexanol and that recorded for the reverse micelles. The MFE in the micelles was also demonstrated to saturate at much lower field strengths than for the homogeneous solutions. This is proposed to be due to the increased geminate lifetime of the RP influencing the LFE/MFE ratio. The different time integrations of the kinetic curves supported this to be the case. The effect of the viscosity of the micelle solution clearly influenced the recombination kinetics and for the observation of a sizeable field effect in these reverse micelles is it is necessary control both the viscosity from the amount of AOT/water and the micelle size. Though, the latter appears not to influence the magnitude of the field effect to the extent of the viscosity of the solution.

Further tests in homogeneous solution confirmed that the magnitude of the magnetic field effects (MFE and LFE), increased with increasing viscosity. This supports the idea that the solvent viscosity directly affects the RP lifetime and that longer lived RPs are selectively removed at lower viscosities. Solutions of 7.2 cP viscosity were probed for the effects of hydrogen bonding. However, noise levels in the

data inhibited a detailed interpretation of the results. For those scans with a smaller margin for error, the results revealed the anticipated relationship with respect to the RP lifetimes and the interaction between the molecules in solution. Attempts were made to establish an overall trend through the solvent properties, though no convincing trend was present.

Further work on the micelles would include investigating other similar photoinitiators, in the water pool of 5 to confirm the LFE/MFE ratio. Also to investigate alternative molecules with the potential for hydrogen bonding with the water in the pool, as the attempts in this work were unsuccessful. For the mhp micelle solution, it would be beneficial to determine the location of the mhp using an appropriate technique, since the absence of a field effect suggests it was not located in the water pool. Equally it may be worthwhile investigating a larger pool size. Since for the present work, the separation accessible in the $w = 5$ pool after the inclusion of the two precursor molecules (separately) varied by a few nm.

Clearly the work with the viscosity of 7.2 cP also requires examination, and would ideally use neat solvents rather than a solvent mix, to identify if the LFE/MFE relationship still differs. Alternatively, if continuing with using solvent mixes solvents with extremely low and high Hildebrand/Reichardt parameters should be studied, to determine if a definite linear relationship can be established.

References

1 B. C. Vink and J. R. Woodward, *Journal of the American Chemical Society*, 2004, **126** (51), 16730.

2 B. C. Vink, *Time Resolved Infrared Studies of Weak Magnetic Field Effects on Radical Pair Reactions*, University of Leicester, Thesis, 2007.

3 R. Bru, A. Sánchez-Ferrer and F. García-Carmona, *Biochemical Journal*, 1995, **310** (3), 721, and references therein.

4 P. Somasundaran, *Encyclopedia of Surface and Colloid Science*, Second Edition, CRC Press, Taylor and Francis Group.

5 K. D. Tapas and M. Amarnath, *Advances in Colloid and Interface Science*, 1995, **59**, 95, and references therein.

6 R. A. Day, B. H. Robinson, J. H. R. Clarke and J. V. Doherty, *Journal of the Chemical Society, Faraday Transactions 1*, 1978, **75**, 132.

7 J. J. Silber, A. Biasutti, E. Abuin and E. Lissi, *Advances in Colloid and Interface Science*, 1999, **82**, 189.

8 H. B. Bohidar and M. Behboudnia, *Colloids and Surfaces A: Physicochemical and Engineering Aspects*, 2001, **178**, 313.

9 A. Maitra, *The Journal of Physical Chemistry*, 1984, **88** (21), 5122.

10 H. F. Eicke and V. Arnold, *Journal of Colloid and Interface Science*, 1974, **46**, 101.

11 M. Zulauf and H. F. Eicke, *The Journal of Physical Chemistry*, 1979, **83** (4), 480.

12 G. Zundel, *Hydration and Intermolecular Interaction*, Academic Press, New York, 1969.

13 J. H. Fendler, *Membrane mimetic chemistry*, Wiley Interscience; New York, 1982.

14 S. E. Friberg, *Microemulsions: Structure and Dynamics*, CRC Press, 2009.

15 S. S. Atik and J. K. Thomas, *Journal of the American Chemical Society*, 1980, **103**, 3543.

16 A. Amararene, M. Gindre, J.-Y. Le Huérou, W. Urbach, D. Valdez and M. Waks, *The American Physical Society, Physical Review E*, 2000, **61**, (1), 682.

17 Landolt-Börstein, IV / 25, Viscosity of Pure Organic Liquids and Binary Liquid Mixtures.

18 K. Kurumada, A. Shioi and M. Harada, *Journal of Physical Chemistry*, 1996, **100**, 1020.

19 M. Kotlarchyk, S.-H. Chen, J. S. Huang and M. W. Kim, *Physical Review A*, 1984, **29**, 2054.

20 M. Kotlarchyk, E. Y. Sheu and M. Capel, *Physical Review A*, 1992, **46**, 928.

21 D. R. Lide, *Handbook of Chemistry and Physics*, CRC Press, 2003 - 2004.

22 E. P. Melo, P. Fojan, J. M. S. Cabral and S. B. Petersen, *Chemistry and Physics of Lipids*, 2000, **106**, 181.

23 U. E. Steiner and T. Ulrich, *Chemical Review*, 1989, **89**, 51.

24 R. W. Eveson, C. R. Timmel, B. Brocklehurst, P. J. Hore and K. A. Mclauchlan, *International Journal of Radiation Biology*, 2000, **76** (11), 1509.

25 U. E. Steiner, in *Magnetic Field Dependent Reactions in Reverse Micellar Systems in: Structure and Reactivity in Reverse Micelles*, ed. M.-P. Pileni, Elsevier Science Publishers, Amsterdam, 1989, p. 156.

26 C. R. Timmel and K. B. Henbest, *Royal Society of London Transactions Series A*, 2004, **362**, 2573.

27 J. R. Woodward, T. J. Foster, A. T. Salaoru and C. B. Vink, *Physical Chemistry Chemical Physics*, 2008, **10** 4020.

28 A. F. M. Barton, *Handbook of solubility parameters and other cohesion parameters* CRC Press, 1991.
29 C. Reichardt, *Chemical Review*, 1994, **94**, 2319.

6. Conclusions

This thesis describes work conducted in varying applied magnetic fields, to probe reactions involving radicals and radical pairs (RPs). The RPs investigated are neutral, formed from commercial photoinitiators, and contain a benzoyl moiety and all of the field strengths used in the current work indicate that spin-state mixing for the RP should evolve at a rate that is dominated by the hyperfine coupling mechanism, as discussed in Chapter **1**.

In particular, it can be considered that a focus of this thesis has been on studying biological systems, either directly by catecholamine mediated interactions with the transferrin iron binding, or indirectly by monitoring the kinetics and magnetic field effects (MFEs) of radical pair (RP) reactions in reverse micelles. The latter, like most micelle microencapsulation investigations, are regarded as simple models for biological systems, so they allow the affect of a magnetic field and the reaction kinetics to be examined in a biologically relevant environment. This, in addition to exploring the unexpected photochemistry of the BAPO photoinitiator in solutions containing alcohol or water, broadly summarises the three main results chapters.

Originally, as detailed in Chapter **2**, the aim was to develop a commercial step scan spectrometer to monitor magnetic field effects. Following numerous modifications, the purchased spectrometer was found to be incapable of detecting any of the tested radical intermediates, even at relatively high concentrations of the precursor molecule. This is most likely a consequence of the poor power of the globar source, in combination with the method of data acquisition. Other developments were also sought by adapting the existing TRIR spectrometer, to collect the RP kinetic decay data with a zero background signal. This was pursued by converting the optics in the setup to match a Michelson interferometer. However, the noise level in the final readings inhibited any further work with this system, and the original setup was used to collect all the magnetic affect on reaction yield (MARY) and kinetic data contained in this thesis, most of which is included in Chapter **5**.

At physiological pH, catecholamines are well reported to assist pathogenic growth by sequestering the iron from the normally inaccessible iron binding proteins, transferrin and lactoferrin. Chapter **3** follows the EPR study of the iron(III) binding in the proteins upon exposure to catecholamines (norepinephrine, epinephrine, dopamine and synthetic inotrope dobutamine), to gain insight into the mechanistic route for iron

capture. The characteristic di-peak EPR spectrum of transferrin is transformed in the presence of the stress hormones; this generates a new peak which is most consistent with the iron binding to the catecholamine. The resulting peak is similar in shape and position to that observed for the catecholamines binding an iron(III) centre, as is confirmed using inorganic salts. This documents the first direct observation of a change in the ferric iron binding status on addition of the catecholamines.

Importantly the binding affinity of the catecholamines for ferric iron is far weaker than that of either transferrin or lactoferrin, and it is for this reason suggested that direct iron abstraction from transferrin cannot occur. Further investigations to compliment the EPR transferrin iron binding studies were undertaken using the techniques of urea-polyacrymide gel electrophoresis (urea-PAGE) and densitometry which followed Fe(II) evolution. Both of these identified iron(III) reduction to accompany the loss of iron from the metalloproteins. This pathway of iron capture by ferric iron reduction is entirely reasonable given that transferrin has a far reduced affinity for iron(II).

To confirm the mechanism and model the behaviour of bacterial ferrous uptake systems, the effects of ferrozine (iron(II) sink) on the transferrin iron binding EPR spectra were also examined. The presence of ferrozine was shown to promote faster and more extensive removal of the iron from transferrin, suggesting iron theft should be enhanced in the presence of bacteria. It also appears, from the current work, that catecholamines encompass the key features of siderophores and ferric reductases, both of which are essential to capture and use or store iron in bacteria. From all the developments in Chapter **3** the catecholamines are proposed to behave in a pseudo-siderophore manner.

The work in Chapter **3** is not only significant from a mechanistic viewpoint but also diagnostically. Since catecholamines are used widely in hospitals to support critically ill patients, the ability of pharmacologically administered catecholamine concentrations to visibly alter the iron binding status of the transferrin in human serum (as shown in this work), has demonstrated links with increased virulence. This implicates iron theft from the transferrin or lactoferrin as a potential source of bacterial infection and accordingly highlights the role of EPR as a diagnostic technique. Evidently this still requires extensive testing and the work given in Chapter **3** is only the initial stage.

Chapter **4** focuses on uncovering the identities of the previously unobserved radicals that are produced when BAPO is irradiated in alcohol- or water- containing

solutions. The new photochemistry was first revealed through the differing magnetic field effects for the RPs, formed upon the photolysis of MAPO and BAPO in cyclohexanol solution. The MAPO photoinitiators demonstrated the expected low field effect (LFE), consistent with α-cleavage, whilst BAPO showed only a very weak conventional MFE. This unusual photochemistry for BAPO was initially probed using TREPR spectroscopy, and clearly identified the presence of two additional doublets arising from at least two radical species, in addition to the traditional RP. The origin of these peaks was unknown. However by employing different alcohols and observing the effect on the TREPR data, plausible reaction mechanisms were constructed. This was followed by performing DFT calculations on the structures to estimate their hyperfine coupling constants, and evaluate the likelihood of formation by comparing these calculated values with the recorded spectroscopic data. A combination of the procedures described generated the three possible radical structures that are proposed to give rise to the additional EPR signals. Further work on this would entail investigation of the likely pathways and methods to determine the identity of the radicals produced. One method of doing this may be through resolving the small hyperfine couplings, using ENDOR, or attaching alternative species to the resulting radicals.

The final chapter examines the effects of changing the RP microenvironment on its recombination kinetics and magnetic field dependence, in fields of $\leq$ 37 mT. This chapter is split into two parts; the first is concerned with investigating RPs in AOT reverse micelles (heterogeneous solution) and the second in homogenous solution. The micelle studies revealed long RP lifetimes when the pairs were effectively encased in the water pools of varying sized reverse micelles. Accompanying size information was gathered by dynamic light scattering measurements to determine the approximate separation distance available to the RP in the reverse micelles. It was found that for a separation difference of up to 8 nm (approximate difference between the smallest, w = 5, and the largest, w = 30, pool) there was negligible effect on the resulting magnetic field trace. This is surprising given that the recombination kinetics were found to be both slower in the smaller water pools and reveal a biphasic decay.

A further important observation is the reduction in the overall magnitude of the MFE between the result in viscous homogeneous cyclohexanol and that recorded for the reverse micelles. This is most likely attributed to the increased geminate lifetime of the RP influencing the LFE/MFE ratio, whereas in homogeneous solutions this would predominantly be governed by the f-pair decay. While the viscosity of the micelle

solution is shown to influence the recombination kinetics in the reverse micelles, the complexity of the competing kinetics processes of the encased RP make it more difficult to fully interpret. It is, however, confirmed for the solvent mixtures in the second section of Chapter **5**. In this section the absolute magnitude of the magnetic field effects (MFE and LFE) correlate well with the viscosity of the homogeneous solutions. This supports the idea that the solvent viscosity directly affects the RP lifetime and that longer lived RPs are selectively removed at lower viscosities. Other experiments performed to link the RP lifetimes to an increase in the size of the field effect, were attempted through varying the hydrogen bonding ability of the solutions containing the RP. This proved fairly unsuccessful and only loosely obeyed the prediction whereby the more hydrogen bonded solutions extended the lifetime of the RP and accordingly the field effect.

Future studies, to develop the work given in Chapter **5**, would involve determining the exact location of the precursor molecule in the reverse micelles, and examining the influence of hydrogen bonding by using non-hydrogen bonded benzoyl photoinitiators.

Appendix

Publications

R. Shergill, M. Haberler, C. B. Vink, H. V. Patten and J. R. Woodward, *Physical Chemistry Chemical Physics*, 2009, **11**, 7248.

R. Shergill, S. M. Sandrini, J. Woodward, R. Muralikuttan, R. D. Haigh, M. Lyte and P. P. E. Freestone, *Journal of Bacteriology*, 2010, **192** (2), 587.

Additional Responsibilities

Graduate Teaching Assistant (GTA)